UNIVERSITY OF GLASGOW

Some novel developments in high-resolution NMR spectroscopy

by

Smita Odedra

A thesis submitted in fulfilment of the requirements
for the degree of Doctor of Philosophy

in the
School of Chemistry
College of Science and Engineering

November 2014

Declaration of Authorship

I declare that, except where explicit reference is made to the contribution of others, that this thesis is the result of my own work and has not been submitted for any other degree at the University of Glasgow or any other institution.

Signed: _____

Date: _____

This thesis was typeset with LaTeX using a template created by Sunil Patel [1]. NMR spectra were processed using Bruker XWin-NMR. Figures were created using Stone Create, Plot, CrystalMaker and Wolfram Mathematica. The data for most simulations presented here were calculated using home-written FORTRAN programs – these programs were written by myself or adapted from code written by previous members of the Wimperis group. A number of simulations were carried out using the SpinDynamica code for Wolfram Mathematica [2] – usage is specified in figure captions.

The following publications have arisen from this work:

- *Use of composite refocusing pulses to form spin echoes* by S. Odedra and S. Wimperis [3]
- *Improved background suppression in ^1H MAS NMR using composite pulses* by S. Odedra and S. Wimperis [4]
- *Imaging of the B_1 distribution and background signal in a MAS NMR probehead using inhomogeneous B_0 and B_1 fields* by S. Odedra and S. Wimperis [5]
- *Dual-compensated antisymmetric composite refocusing pulses for NMR* by S. Odedra, M.J. Thrippleton and S. Wimperis [6]

Parts of Reference [3] appear in Chapter 2; the work published in References [4] and [5] appears in Chapter 3; and Chapter 4 is based on the work in Reference [6].

"The world was young and I was young and the experiment was beautiful. It satisfied everything that I wanted to see."

Isidor I. Rabi

Abstract

The radiofrequency (rf) pulses used in NMR are subject to a number of imperfections, such as those resulting from the inhomogeneity of the rf field or an offset of the transmitter frequency from exact resonance. In spin-echo experiments, these imperfections yield spectra with reduced signal intensity and distorted phase. Composite pulses, which have tailored bandwidth properties with respect to experimental frequency parameters such as the rf field strength or resonance offset, offer a route to improving the amplitude of the spin-echo signal. However, the symmetry of the pulse sequence must be carefully considered to prevent the introduction of phase errors into the spin-echo signal.

Here, composite pulses will be studied as a means to improving one of the most common techniques for ^{1}H background suppression in MAS NMR, the "Depth" sequence. Novel composite 180° pulses will be presented for this application and verified experimentally. The composite pulse Depth experiment yields spectra with improved amplitude of the ^{1}H signals of interest, while successfully maintaining good suppression of background signals.

Novel families of dual-compensated 180° composite pulses for $I = 1/2$ will also be designed for use in NMR spin-echo experiments. These pulses are capable of simultaneously compensating for resonance offset and rf inhomogeneity problems. Crucially, unlike many composite pulses that have been presented before, these new pulses have the correct symmetry properties to form a spin echo without phase distortion.

Composite pulses have found wide usage in solution-state NMR, and although in principle the same pulses can be applied in solid-state NMR experiments, complications can arise under magic angle spinning (MAS). The effects of MAS on composite pulse performance will be explored both through computer simulations and ^{31}P experiments.

Finally, on a different theme, we will investigate spin-locking of half-integer quadrupolar nuclei in solids. Spin-locking is an important feature of many NMR experiments, yet the complex behaviour observed for quadrupolar nuclei is not fully understood. Using the theoretical model introduced by Ashbrook and Wimperis, we will investigate the far off-resonance case of spin-locking for $I = 3/2$ and $I = 5/2$ nuclei.

Acknowledgements

Firstly, I must thank the other members of the Wimperis Group: Nicole and Akiko, for providing inspiration, wisdom, biscuits and help over the years, and Steve for good ideas and patience. Thanks to Hernan for assistance in my early days with the spectrometer and for always being jolly. I am thankful to Michael Thrippleton for contributing to the theory in Chapter 4, David Adam for time on the solution-state NMR spectrometers at Glasgow and Sharon Ashbrook for time on the NMR spectrometer in St. Andrews. Thank you John Griffin for introducing me to *multizg* and sharing cake fantasies and cat stories. I am very grateful to Scott Sneddon for incredible support and zesty friendship. Finally, a big thanks to Colin Reilly for helping to keep our office spick and span and cheerful!

Contents

In memory of Dr. Andy Parkin

Chapter 1

Introduction

1.1 A brief history of NMR

1.1.1 Beginnings

The evolution of quantum theory in the 1920s paved the way for the discovery of nuclear magnetic resonance (NMR) as the concept of spin was developed. Stern and Gerlach's eminent experiment in 1922 [7] examined the behaviour of a beam of silver atoms passing through a magnetic field: they observed a discrete number of deflected beams, rather than a continuous range of deflection, confirming that the particles possessed an intrinsic angular momentum of certain quantised values. In 1925, Uhlenbeck and Goudsmit proposed the concept of an electron spinning around its own axis, with angular momentum and a magnetic dipole moment resulting from the spinning electrical charge [8]. Pauli had first suggested in 1924 that nuclei possess spin in his explanation for the origin of hyperfine splittings in atomic optical spectra [9]. He went on to formulate a theoretical framework of spin angular momentum in 1927.

The nuclear spin was first observed by Stern, Frisch and Estermann in 1933 [10, 11] after they adapted their equipment to measure the magnetic moment of the proton in a beam of hydrogen molecules, although their measurement had low accuracy.

Rabi's theory of the magnetic resonance method was published in 1937 [12], explaining that an atom will be reoriented by a gyrating magnetic field. The probability of this reorientation is dependent on the frequency of the field's rotation, and is largest when

this frequency is equal to the Larmor frequency. By adding to Stern's technique a loop of wire to produce an oscillating radiofrequency (rf) field over the atomic beam, Rabi and his group observed the flipping of spins as an absorption on their atomic-beam detector when the field was tuned to the Larmor frequency. Rabi was awarded a Nobel Prize in 1944 for his efforts.

Two groups independently demonstrated NMR in the bulk phase almost simultaneously in 1946 – Bloch, Hansen and Packard at Stanford University and Purcell, Torrey and Pound at Harvard University. Bloch, who had gained experience in rf techniques during his wartime research at Harvard's Radar Research Laboratory, deduced that the macroscopic nuclear magnetisation of a sample could be tipped away from its equilibrium position along the z axis by the resonant absorption of rf energy. A coil placed along the x or y axis would then be able to detect the electrical signal generated by the precession of the magnetisation about the magnetic field. In January 1946, the group succeeded in detecting their first NMR signal from a sample of water.

Purcell, Torrey and Pound had meanwhile taken up the challenge of detecting the transition between nuclear magnetic energy levels as a side project while working at the MIT Radiation Laboratory and writing up a series of books. After arranging to use a large magnet at Harvard University for their experiments, the group observed their first signal in a solid sample of paraffin wax. Purcell and Bloch shared the Nobel Prize in 1952.

1.1.2 Pulsed Fourier transform NMR

In the early days of NMR, continuous wave (CW) methods were used, varying either the magnetic field strength of an electromagnet or the frequency of the rf radiation. As the field is swept, absorption signals are observed one frequency at a time as the resonance condition is met. The main disadvantage of CW NMR is that high-resolution spectra can only be obtained with a slow scan, with the sweep rate restricted in order to probe individual transitions.

Lowe and Norberg were the first to apply the Fourier transform (FT) to the NMR signal following an rf pulse [13]. However, it was Ernst and Anderson who realised the full potential the Fourier transform method could bring to NMR, and the technique gained

popularity after their 1966 paper [14] was published. By simultaneously exciting nuclei over a range of resonance frequencies, and using the Fourier transform to separate their nuclear induction signals, pulsed FT NMR provided a route to obtain high-resolution spectra without the time constraints inherent in CW NMR. In addition, this gave the opportunity of acquiring multiple scans as well as opening up the possibility of performing more complex NMR experiments. As described by Freeman [15], "We can lead the spins through an intricate dance, carefully programmed in advance, to enhance, simplify, correlate, decouple, edit or assign the NMR spectra."

1.2 Nuclear magnetism

The nucleus of an atom possesses four fundamental properties: mass, electric charge, magnetism and spin. Although the latter two properties do not affect the overall chemical or physical properties of a substance, they are of vital importance to the technique of NMR, providing an invaluable insight into the structure and dynamics of chemical systems.

The magnitude of the spin angular momentum, **I**, associated with a nucleus is given by

$$| \mathbf{I} | = \hbar \sqrt{I(I+1)} \tag{1.1}$$

where the associated spin quantum number I may be zero, half-integer or integer. The value of I for a particular isotope is dependent on its nuclear structure and can be rationalised using the nuclear shell model. Nuclei with non-zero spin can be studied with NMR.

The spin angular momentum vector **I** is spatially quantised – the projection of **I** onto the z axis of a three-dimensional coordinate system gives the z component of **I**,

$$I_z = m_I \hbar, \tag{1.2}$$

where the azimuthal quantum number m_I has $2I + 1$ values in integral steps between

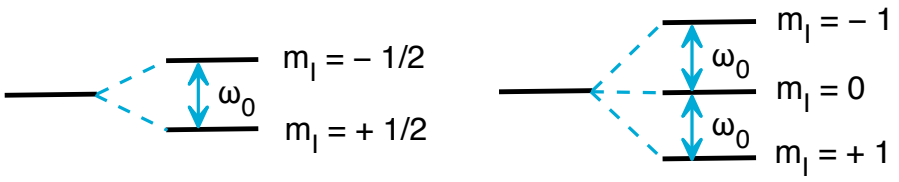

(a) $I = 1/2$ (b) $I = 1$

FIGURE 1.1: The Zeeman interaction lifts the degeneracy of the $2I + 1$ states in the presence of a static magnetic field. Energy levels are separated by the Larmor frequency, ω_0.

$-I$ and $+I$. In nuclei with non-zero spin, the nuclear magnetic dipole moment is proportional to the spin angular momentum,

$$\boldsymbol{\mu} = \gamma \mathbf{I} \tag{1.3}$$

where the gyromagnetic ratio γ is constant for a given nucleus. The magnitude of the nuclear magnetic dipole moment is therefore

$$| \boldsymbol{\mu} | = \gamma \hbar \sqrt{I(I+1)} \tag{1.4}$$

and it is also spatially quantised so that

$$\mu_z = \gamma m_I \hbar \tag{1.5}$$

In the absence of a magnetic field, the $2I + 1$ orientations of the spin I nucleus are degenerate. However, when a magnetic field B_0 is applied, which is defined as acting along the z axis of the laboratory frame, the Zeeman interaction lifts the degeneracy, as can be seen in Figure 1.1.

Each NMR-active isotope possesses a different Larmor frequency – this fundamental property allows us to distinguish between different isotopes, making NMR spectroscopy an important method for materials characterisation.

The Hamiltonian for an isolated spin in a static, uniform magnetic field is given by

$$H_z = -\mu_z B_0. \tag{1.6}$$

Combining Equations 1.5 and 1.6,

$$H_z = -\gamma\hbar I_z B_0. \tag{1.7}$$

The eigenfunctions of H_z are the energies associated with these different states:

$$E_z = -\gamma\hbar m_I B_0. \tag{1.8}$$

The transition energy between enery levels $\Delta m_I = \pm 1$ is

$$\Delta E = \gamma\hbar B_0 \tag{1.9}$$

or in frequency units,

$$\omega_0 = \gamma B_0 \tag{1.10}$$

expressed in units of rad s^{-1}. This is known as the Larmor frequency. The spin magnetisation may exist in two types of state depending on the value of Δm_I, which is known as the coherence order and denoted by the symbol p. States with $p = 0$ are populations of energy levels, while coherent superpositions between the energy levels, termed coherences, are characterised by $p > 0$. Depending on the number of energy levels between which the state of coherence occurs, coherences are known as single-quantum coherences ($p = \pm 1$), double-quantum coherences ($p = \pm 2$) and so on.

1.3 The vector model

According to Bloch, a macroscopic sample containing many identical, non-interacting spins can be considered classically in terms of a bulk magnetisation vector in three-dimensional space, providing a simple geometrical insight into the NMR experiment. In an ensemble of spin $I = 1/2$ nuclei at thermal equilibrium in a magnetic field, there is a population difference between the spin states according to the Boltzmann distribution:

$$N_{\text{upper}}/N_{\text{lower}} = \exp(-\Delta E/\mathrm{k}T) \tag{1.11}$$

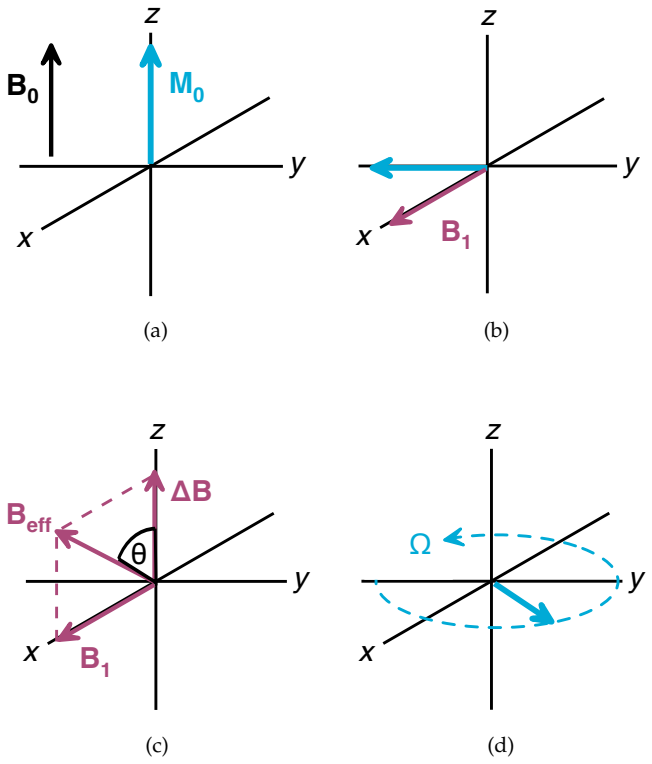

FIGURE 1.2: The vector model. (a) Bulk magnetisation vector $\mathbf{M_0}$ aligned with $\mathbf{B_0}$ in the rotating frame at thermal equilibrium. (b) A 90° pulse applied along the rotating frame x axis has the effect of tilting the magnetisation vector until it lies along the $-y$ axis. (c) An off-resonance pulse causes rotation around the effective radiofrequency field, B_{eff}. (d) After the pulse is turned off, the magnetisation vector undergoes free precession in the xy plane with angular frequency $\Omega = \omega_0 - \omega_{\text{rf}}$.

This gives rise to a stationary net magnetisation which can be represented by a vector $\mathbf{M}$. This vector aligns with the magnetic field $\mathbf{B_0}$ along the z axis of the laboratory frame, as can seen in Figure 1.2(a).

If a linearly oscillating radiofrequency pulse is applied with a frequency, ω_{rf}, close to the Larmor frequency, the pulse will interact with the nuclear spins in the sample, causing the bulk magnetisation vector to reorientate. In order to simplify the understanding of this interaction, the concept of a rotating reference frame is used. The radiofrequency field $\boldsymbol{B_1}$ is applied so that the magnetic field $2B_1 \cos(\omega_{\text{rf}} t)$ oscillates perpendicular to the $\boldsymbol{B_0}$ field. This field can be decomposed into two circularly polarised counter-rotating components:

$$\begin{aligned} \boldsymbol{B_1}(t) &= 2B_1 \cos(\omega_{\text{rf}} t)\boldsymbol{x} \\ &= B_1\{[\cos(\omega_{\text{rf}} t)\boldsymbol{x} + \sin(\omega_{\text{rf}} t)\boldsymbol{y}] + [\cos(-\omega_{\text{rf}} t)\boldsymbol{x} + \sin(-\omega_{\text{rf}} t)\boldsymbol{y}]\} \end{aligned} \tag{1.12}$$

In the rotating frame, the x and y axes rotate at an angular frequency ω_{rf} around the z axis. In this frame, the component of the B_1 field rotating at $+\omega_{\text{rf}}$ appears as a static field orthogonal to B_0, while the component rotating at $-\omega_{\text{rf}}$ does not significantly affect the nuclear spins.

If the pulse is applied on-resonance ($\omega_0 = \omega_{\text{rf}}$) along the rotating frame x axis, it will cause the bulk magnetisation vector $\mathbf{M}$ to precess in the rotating frame yz plane with frequency $\omega_1 = |\gamma B_1|$, as is shown in Figure 1.2(b).

The flip angle or nutation angle is the angle through which B_1 rotates the magnetisation vector during time τ_{rf} , and is defined as

$$\begin{aligned} \beta &= \omega_1 \tau_{\text{rf}} \\ &= \gamma B_1 \tau_{\text{rf}} \end{aligned} \tag{1.13}$$

The phase of the pulse, ϕ, describes the axis along which the pulse is applied in the rotating frame. The notation β_ϕ is therefore used to describe a pulse of flip angle β and phase ϕ. Viewed from the origin along the rotation axis, positive rotations are clockwise about a given axis. Thus a $90^\circ_{0^\circ}$ pulse will cause a magnetisation vector aligned with the z axis to rotate until it lies along the $-y$ axis.

This picture is modified when considering an off-resonance pulse where $\omega_0 \neq \omega_{\text{rf}}$ [16]. In the rotating frame, the apparent Larmor precession frequency is given by

$$\Omega = \omega_0 - \omega_{\text{rf}} \tag{1.14}$$

where Ω is known as the resonance offset frequency. The reduced field along the z axis is given by

$$\Delta B = -\Omega/\gamma \tag{1.15}$$

The vectorial sum of the orthogonal fields $\mathbf{\Delta B}$ and $\mathbf{B_1}$ is the net effective field, $\mathbf{B_{eff}}$, as shown in Figure 1.2(c). It is about this axis that the magnetisation precesses during an off-resonance pulse. The magnitude of this effective field is given by

$$B_{\text{eff}} = \sqrt{(\Delta B)^2 + (B_1)^2} \tag{1.16}$$

while the tilt angle θ of the field with respect to the z axis is

$$\theta = \tan^{-1}(B_1/\Delta B) \tag{1.17}$$

After a pulse, the magnetisation precesses with angular frequency Ω around the rotating frame z axis. This is illustrated in Figure 1.2(d).

This "free precession" is damped by two different relaxation processes which act to return the magnetisation vector to its initial thermal equilibrium state, that is, aligned with B_0 along the z axis. Spin-lattice relaxation, also known as longitudinal relaxation, occurs with a time constant T_1 and involves the return of the z component to its equilibrium value. This requires spins to flip to attain the original Boltzmann population difference. Spin-spin relaxation, or transverse relaxation, involves the decay of magnetisation in the xy plane to zero with time constant T_2. This occurs by the randomisation of phases of individual spins.

1.4 Signal detection

By applying an rf pulse that is not exactly 180° (or an integer multiple of 180°) to the thermal equilibrium state, longitudinal magnetisation ($p = 0$) is converted to transverse magnetisation ($p = \pm 1$). The resulting precession of bulk magnetisation about the rotating frame z-axis induces an electromotive force in the receiver coil [17, 18] – this current is the time-domain NMR signal, known as the free induction decay (FID). After preamplification, this signal is "mixed down" with the carrier frequency to produce a frequency which is the difference of the two. This allows the spectrometer to deal with only a small range of frequencies, regardless of what nucleus is being observed. This shifting of the frequencies is equivalent to viewing the detection in the rotating frame, as described in Section 1.3. Further information on this procedure can be found in References [19] and [20].

The bulk magnetisation evolves according to $\exp(i\Omega t)$, where Ω is the frequency of the evolution in the rotating frame. The signal can be written,

$$s(t) = C\exp(i\Omega t) = C\cos(\Omega t) + iC\sin(\Omega t) \tag{1.18}$$

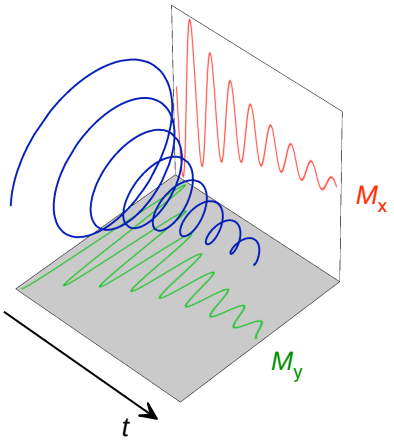

FIGURE 1.3: The precession of the tip of the bulk magnetisation as it decays in time is illustrated by the blue curve. The real and imaginary signal components measured by quadrature detection are represented by the projections shown in red and green.

where C describes the overall amplitude of the coherence, which can be time-dependent to take into account relaxation effects. Figure 1.3 illustrates the precession of the the tip of the bulk magnetisation vector with time, with a decay of the form $\exp(-t/T_2)$. In order to distinguish $+\Omega$ from $-\Omega$, i.e., to determine the sense of precession, both the real and imaginary terms of Equation 1.18 must be measured. This is achieved using quadrature detection: two phase-sensitive detectors are set 90° out of phase with each other, and the two FIDs detected are treated as the real and imaginary components of the complex time-domain signal, corresponding to the x- and y-components of the transverse magnetisation in the rotating frame.

The real and imaginary components are sampled simultaneously at time intervals of Δ seconds. According to the Nyquist theorem, the resulting spectrum will have a frequency range in Hz of $SW = 1/\Delta$. All signals and noise that lie outwith the range of $-SW/2$ and $SW/2$ will be "folded in" or "aliased", hence will appear within this frequency window. The bandwidth of detection is restricted using digital filtering to prevent this [21].

1.5 Fourier transform NMR

A typical FID is a sum of many sinusoidal waves of different frequencies, phases and amplitudes. Converting this complicated signal into the frequency-domain NMR spectrum greatly aids interpretation of the signals.

Modifying Equation 1.18, the time-domain signal of a single frequency Ω is given by,

$$s(t) = C\exp(i\Omega t)\exp(-t/T_2)\exp(i\phi). \tag{1.19}$$

Here, C is an overall scaling factor of the coherence, $\exp(-t/T_2)$ accounts for the relaxation and $\exp(i\phi)$ is an arbitrary phase factor dependent on instrumental influences.

The Fourier transform takes the analytical form,

$$S(\omega) = \int_0^\infty s(t)\exp(-i\omega t)\,\mathrm{d}t. \tag{1.20}$$

Assuming $T_2 = \infty$ and $\phi = 0$ in Equation 1.19, the time-domain signal is converted to a frequency-domain spectrum $S(\omega)$ that has an amplitude proportional to C when $\omega = \Omega$ and that is zero for all other frequencies. In practice, the FID decays to zero from relaxation processes ($T_2 \neq \infty$) and the resulting complex spectrum comprises a real and an imaginary component,

$$S(\omega) = C[A(\omega) + iD(\omega)] \tag{1.21}$$

where

$$A(\omega) = \frac{R}{R^2 + (\omega - \Omega)^2} \tag{1.22}$$

and

$$D(\omega) = \frac{-(\omega - \Omega)}{R^2 + (\omega - \Omega)^2} \tag{1.23}$$

represent absorptive and dispersive Lorentzian functions centred at frequency Ω. Here, $R = 1/T_2$ is the rate constant in Hz for transverse relaxation. These lineshapes are illustrated in Figure 1.4.

The absorptive lineshape has a full-width at half-height equal to $2R = 2/T_2$ in rad s^{-1} and an intensity of $1/R$. The dispersive lineshape has width at half-height of $\sim 7.5R$ rad s^{-1} and a peak intensity of $1/2R$. Owing to the more desirable characteristics of the absorptive lineshape, usually only the real part of the spectrum is shown.

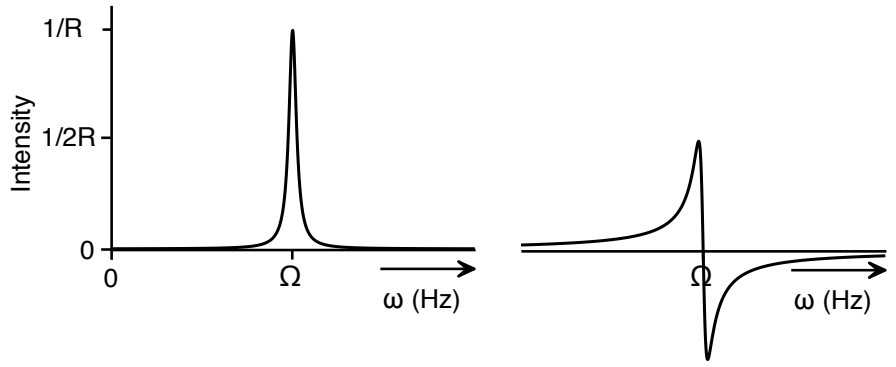

(a) Absorptive Lorentzian lineshape (b) Dispersive Lorentzian lineshape

FIGURE 1.4: The absorptive and dispersive Lorentzian lineshapes that comprise the real and imaginary components of an NMR spectrum obtained by Fourier transformation of a complex time-domain signal recorded using quadrature detection.

1.6 Phase correction

1.6.1 Zeroth-order phase correction

The arbitary phase factor ϕ in Equation 1.19 arises as although the two orthogonal signals acquired by quadrature detection are labelled as the x- and y-components of the magnetisation, there is no way of ensuring these correspond to the same axis system used to define the phase of the rf pulses. As a result, mixing of the absorptive and dispersive components of $S(\omega)$ occurs. There is a simple solution to this: multiplying the spectrum by $\exp(i\phi_{\text{corr}})$, where ϕ_{corr} is a phase correction, will produce the desired spectrum if we set $\phi_{\text{corr}} = -\phi$. A single phase correction is applied to the whole spectrum – this is a zeroth-order correction. This process of *phasing* the spectrum is carried out by manually altering ϕ_{corr} until a satisfactory absorption lineshape is achieved.

1.6.2 First-order phase correction

Sometimes the zeroth-order phase correction does not bring all the lines in the spectrum into phase. In some cases, a first-order phase correction can be used to improve the spectrum. In the case of a simple one-pulse experiment, a 90° pulse rotates the bulk magnetisation vector to the $-y$ axis when on-resonance, but an increasing amount of x-magnetisation is created as the transmitter frequency is moved off-resonance. Phase errors arising from the "dead time" – the unavoidable time delay between the rf pulse

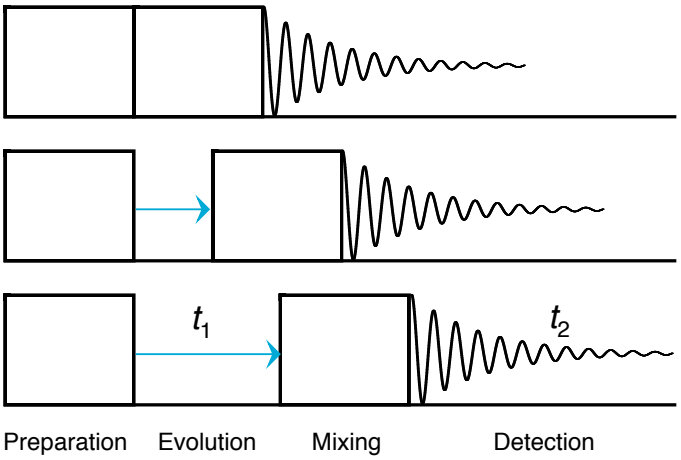

FIGURE 1.5: Schematic diagram showing the stages of a two-dimensional NMR experiment.

and start of the aquisition of the FID – also contribute to this problem. Since this phase error is approximately proportional to the offset, a frequency-dependent phase correction, $\phi_{\text{corr}} = k\Omega$ can compensate for this. The use of a small first-order correction can be effective if spectral lines are sharp. However, baseline distortions can result from applying a first-order correction to broad lines, and for more complicated experiments there may not be a simple relationship between the phase of the peaks and their offset frequencies [20, 22, 23].

1.7 Two-dimensional NMR

Two-dimensional NMR, where intensity is plotted as a function of two frequencies, has opened up the field to a vast number of experiments since it was first proposed by Jeener in 1971 and given a full theoretical treatment by Aue, Bartholdi and Ernst in 1976 [24].

A two-dimensional experiment comprises of four key stages: preparation, evolution, mixing and detection, as illustrated in Figure 1.5. During the preparation period, equilibrium magnetisation is converted into a particular coherence either by one simple pulse or a more complicated series of pulses and delays. This coherence does not need to be directly observable – multiple-quantum coherences can be created. Section 1.8 will describe methods of coherence selection. Next, the spins are allowed to precess during

the evolution period t_1. The coherence is then transformed into observable $p = -1$ coherence during the mixing period, which is measured during the detection period, t_2. The experiment is then repeated, incrementing the duration of the t_1 period. The evolution of the magnetisation in t_1 modulates either the amplitude or phase, or both, of the signal in t_2. After the two-dimensional dataset, $s(t_1, t_2)$, has been double Fourier transformed with respect to both time domains, a two-dimensional frequency spectrum S results. A peak at (Ω_1, Ω_2) represents a coherence evolving at frequency Ω_1 in the indirect dimension which was transformed into a $p = -1$ coherence with frequency Ω_2.

1.8 Coherence selection

During an NMR experiment, rf pulses will convert equilibrium magnetisation (characterised by a coherence order $p = 0$) into other coherence orders. In general, a 90° pulse will create all possible coherence orders allowed within the spin system, while a 180° pulse inverts the sign of a coherence from p to $-p$. It is possible to select particular shifts in coherence orders at pulses in an experiment, while other signals are cancelled. This is achieved through the use of pulsed magnetic field gradients [25] or with a method known as phase cycling [26].

The application of a pulsed field gradient creates an inhomogeneity in the main magnetic field, causing coherences to dephase. This dephasing can be reversed by applying a second field gradient. By judicious choice of the duration, strength and position of the two gradients within a pulse sequence, rephasing only occurs for desired coherences. This method of coherence selection will not be considered further or used in this work – for further information, the reader is directed to References [20] and [25].

Phase cycling involves varying the phases of the rf pulses and the receiver phase over a number of transients, with undesired signals summing to zero on completion of the whole cycle. The two rules of phase cycling allow the design of a sequence that will achieve the required coherence pathway:

1. For selecting a coherence change of Δp, the receiver phase ϕ_{Rx} must be incremented by $-\Delta p \phi$ where ϕ is the phase of the pulse. This matches the phase shift

of the receiver with the phase shift of the coherence undergoing a change in coherence order of Δp. Over the course of the phase cycle, undesired coherences will experience different phase shifts and be eliminated.

2. A phase cycle with N steps of $360^\circ / N$ will select, along with the desired pathway, coherences changes of $\Delta p \pm nN$, where n is an integer.

These rules can be applied to each pulse in a sequence where a particular change in coherence order is required, and the individual phase cycles can be nested together to obtain an overall cycle for the whole pulse sequence.

A coherence transfer pathway diagram illustrates the desired coherence changes occuring in an experiment, and will be encountered throughout this thesis (for example, Figure 2.6). All pathways diagrams must start with the population state $p = 0$, because the spin system at thermal equilibrium consists of longitudinal I_z magnetisation. At the end of a pulse sequence, $p = -1$ coherence is detected.

Chapter 2

Theoretical Background

2.1 The density matrix

Quantum mechanical theory states that an individual spin can be expressed as a wavefunction $\psi(t)$ which can be represented as a linear combination of the elements of an orthonormal set of basis functions ϕ_i:

$$\psi(t) = \sum_i c_i(t)\phi_i, \tag{2.1}$$

where $c_i(t)$ are time-dependent coefficients. The total nuclear magnetisation in a macroscopic sample is the sum of contributions of each spin contained within it. However, to calculate the state of a bulk sample by summing each individual contribution would be impractical, considering the abundance of nuclear spins present. An alternative approach is to use density matrix (also known as density operator) theory.

The density operator, $\rho(t)$, is defined as the outer product of the wavefunction and its conjugate,

$$\rho(t) = \overline{|\psi(t)\rangle\langle\psi(t)|}, \tag{2.2}$$

where the overbar denotes an average over the whole ensemble of spins. Its name stems from the probability density concept in the Born interpretation of quantum mechanics.

If we consider a single spin $I = 1/2$ nucleus in a superposition of the α ($m_I = +1/2$) and β ($m_I = -1/2$) eigenstates of the Zeeman Hamiltonian (i.e., in the Zeeman basis

set), $|\psi(t)\rangle$ and $\langle\psi(t)|$ are given by

$$|\psi(t)\rangle = c_\alpha(t)|\alpha\rangle + c_\beta(t)|\beta\rangle \tag{2.3}$$

$$\langle\psi(t)| = c_\alpha^*(t)\langle\alpha| + c_\beta^*(t)\langle\beta| \tag{2.4}$$

where $c_\alpha^*(t)$ and $c_\beta^*(t)$ are the complex conjugates of the coefficients $c_\alpha(t)$ and $c_\beta(t)$.

The matrix form of an operator Q can be written using a set of basis functions such that the element $Q_{i,j}$ in row i and column j is

$$Q_{i,j} = \langle i|Q|j\rangle. \tag{2.5}$$

The matrix elements of the density operator are therefore given by

$$\begin{aligned} \rho_{i,j}(t) &= \langle\phi_i|\rho(t)|\phi_j\rangle \\ &= \overline{c_i^*(t)c_j(t)} \end{aligned} \tag{2.6}$$

The density operator for the spin $I = 1/2$ case may therefore be represented in matrix form as

$$\begin{aligned} \rho(t) &= \begin{pmatrix} \langle\alpha|\,\rho(t)|\alpha\rangle & \langle\alpha|\,\rho(t)|\beta\rangle \\ \langle\beta|\,\rho(t)|\alpha\rangle & \langle\beta|\,\rho(t)|\beta\rangle \end{pmatrix} \\ &= \begin{pmatrix} \overline{c_\alpha(t)c_\alpha^*(t)} & \overline{c_\alpha(t)c_\beta^*(t)} \\ \overline{c_\beta(t)c_\alpha^*(t)} & \overline{c_\beta(t)c_\beta^*(t)} \end{pmatrix} \\ &= \begin{pmatrix} \rho_{11} & \rho_{12} \\ \rho_{21} & \rho_{22}. \end{pmatrix} \end{aligned} \tag{2.7}$$

The major advantage of this approach is that the ensemble averaging is accounted for *within* the density operator, and so the bulk magnetisation can be calculated directly from it:

$$M_x = \frac{1}{2}\gamma N(\rho_{2,1} + \rho_{1,2}) \tag{2.8}$$

$$M_y = \frac{1}{2}\gamma iN(\rho_{2,1} - \rho_{1,2}) \tag{2.9}$$

$$M_z = \frac{1}{2}\gamma N(\rho_{1,1} - \rho_{2,2}). \tag{2.10}$$

The diagonal elements, $\rho_{i,i}$, of the density matrix relate to the probabilities of the spins being found in the corresponding eigenstates, thus they correspond to the populations of these states. The off-diagonal elements, $\rho_{i,j}$, correspond to coherent superpositions of the eigenstates and are termed coherences.

2.1.1 The reduced density matrix

At equilibrium, the ensemble averages $\overline{c_\alpha(t)c_\beta^*(t)}$ and $\overline{c_\beta(t)c_\alpha^*(t)}$ are equal to zero. This fits with what we know from experiment – there is no net spin polarisation in the transverse plane perpendicular to the magnetic field. We can thus write the equilibrium density operator as,

$$\rho_{\text{eq}} = \begin{pmatrix} n_\alpha/N & 0 \\ 0 & n_\beta/N \end{pmatrix} \tag{2.11}$$

where n_α and n_β are the equilibrium populations and N is the total number of spins [20]. The equilibrium populations can be calculated using the Boltzmann distributions as described in Equation 1.11, giving

$$n_\alpha = \frac{1}{2}N\exp(-E_\alpha/kT) \tag{2.12}$$

$$n_\beta = \frac{1}{2}N\exp(-E_\beta/kT). \tag{2.13}$$

Since the energies of a spin in either state interacting with the magnetic field are much smaller than the thermal energy kT, the exponential terms can be approximated to $\exp(x) = 1 + x$ using a power series expansion. We can then write,

$$n_\alpha = \frac{1}{2}N\left(1 + \frac{\gamma\hbar B_0}{2kT}\right) \tag{2.14}$$

$$n_\beta = \frac{1}{2}N\left(1 - \frac{\gamma\hbar B_0}{2kT}\right) \tag{2.15}$$

by substituting E_α and E_β for $\pm\gamma\hbar m_I B_0$ as defined in Equation 1.8.

It follows from this that the average population $n_{\text{av}} = \frac{1}{2}(n_\alpha + n_\beta)$ equals $\frac{1}{2}N$ and the population difference $\Delta n = n_\alpha - n_\beta$ is given by $\gamma\hbar B_0/2kT$. Rewriting the populations of the two states in terms of deviations from the average, we can then express the density

matrix as

$$\rho_{eq} = \frac{1}{N}\begin{pmatrix} n_{\text{av}} + \frac{1}{2}\Delta n & 0 \\ 0 & n_{\text{av}} - \frac{1}{2}\Delta n. \end{pmatrix} \tag{2.16}$$

This can in turn be written in terms of the operators E and I_z:

$$\begin{aligned} \rho_{eq} &= \frac{n_{\text{av}}}{N}\begin{pmatrix} 1 & 0 \\ 0 & 1 \end{pmatrix} + \frac{\Delta n}{N}\begin{pmatrix} \frac{1}{2} & 0 \\ 0 & -\frac{1}{2} \end{pmatrix} \\ &= \frac{n_{\text{av}}}{N}E + \frac{\Delta n}{N}I_z. \end{aligned} \tag{2.17}$$

Since the matrix E does not correspond to any observable magnetisation, the first term can be discarded, allowing us to write the reduced density matrix as

$$\sigma = \frac{\Delta n}{N}I_z. \tag{2.18}$$

Finally, the constant $\frac{\Delta n}{N}$, which defines the total size of the equilibrium magnetisation, is dropped since we are only interested in how the signal evolves with time rather than its absolute value. The reduced density matrix is then simply given by

$$\sigma = I_z. \tag{2.19}$$

This provides the starting point for calculations involving density matrix theory. The matrix representations of the spin angular momentum operators I_x, I_y and I_z are given in Appendix A for spin $I = 1/2, 3/2$ and $5/2$.

2.2 Time evolution of the density matrix

The time evolution of the density operator can be related to the Hamiltonian with the Liouville-von Neumann equation:

$$\begin{aligned} \frac{\mathrm{d}}{\mathrm{d}t}\,\sigma(t) &= -i[H, \sigma(t)] \\ &= -iH\sigma(t) + i\sigma(t)H. \end{aligned} \tag{2.20}$$

This may be solved for the density operator to give

$$\sigma(t) = U(t)\sigma(0)U^{-1}(t) \tag{2.21}$$

where the propagator, $U(t)$, represents the Hamiltonian acting between $t = 0$ and $t = t$. If the Hamiltonian is time-independent, the propagator is $U = \exp(-iHt)$ so that

$$\sigma(t) = \exp(-iHt)\sigma(0)\exp(+iHt). \tag{2.22}$$

From Equation 2.22 it is apparent that if we know the inital density operator, $\sigma(0)$, and the interaction Hamiltonian, H, we can calculate the density operator at any point in time, t.

More generally, the propagator is given for a time-dependent case by

$$U(t) = \hat{T}\exp\{-i\int_0^t H(t)\,\mathrm{d}t\}, \tag{2.23}$$

where the Dyson time-ordering operator, $\hat{T}$, ensures that the exponential function is calculated correctly when the Hamiltonians at different times do not commute. Methods of calculating the evolution of the density matrix with a time-dependent Hamiltonian will be covered in Sections 4.2.1 and 5.2.

The value of an observable is obtained from the expectation value of the corresponding operator, Q. This is found by taking the trace (the sum of the diagonal elements) of the matrix product of the adjoint operator $Q^\dagger$ with the density operator at time t,

$$\overline{\langle\psi(t)|Q|\psi(t)\rangle} = \mathrm{Tr}\{\sigma(t)Q^\dagger\} \tag{2.24}$$

2.3 Product operator basis set

It is often more convenient to work with an alternative basis set rather than expressing the density operator in the Zeeman Hamiltonian basis set. The product operator formalism offers a rigorous quantum mechanical insight into the outcome of an NMR experiment, yet retains the intuitive nature of the vector model. Since it was described in

a review by Sørensen et al. in 1983[27], it has proved popular in studies of spin $I = 1/2$ nuclei, particularly for its ability to describe weakly J-coupled spin systems.

2.3.1 Operators for a single spin

For an isolated spin $I = 1/2$ nucleus, the product operator basis set comprises of four operators:

$$\tfrac{1}{2}E \quad I_x \quad I_y \quad I_z. \tag{2.25}$$

The first of these is half the identity operator, while the latter three spin angular momentum operators correspond to the x-, y- and z-components of the magnetisation. The density operator can be written as a sum of the contribution of each of these:

$$\sigma(t) = a_x(t)I_x + a_y(t)I_y + a_z(t)I_z \tag{2.26}$$

To determine how the density operator evolves with time, we first consider the free precession Hamiltonian,

$$H_{\text{free}} = \Omega I_z \tag{2.27}$$

and the Hamiltonians for a pulse about about the x- and y-axes:

$$H_{\text{x-pulse}} = \omega_1 I_x \tag{2.28}$$

$$H_{\text{y-pulse}} = \omega_1 I_y. \tag{2.29}$$

Taking the example of an x-pulse of duration t_p, we can use the solution of the Liouville-von Neumann equation to get

$$\begin{aligned} \sigma(t_p) &= \exp(-i\omega_1 t_p I_x) I_z \exp(+i\omega_1 t_p I_x) \\ &= \exp(-i\beta I_x) I_z \exp(+i\beta I_x), \end{aligned} \tag{2.30}$$

where the equilibrium density matrix is $\sigma(0) = I_z$ and the flip angle is $\beta = \omega_1 t_p$. The relation

$$\exp(-i\beta I_x) I_z \exp(+i\beta I_x) \equiv I_z \cos\beta - I_y \sin\beta \tag{2.31}$$

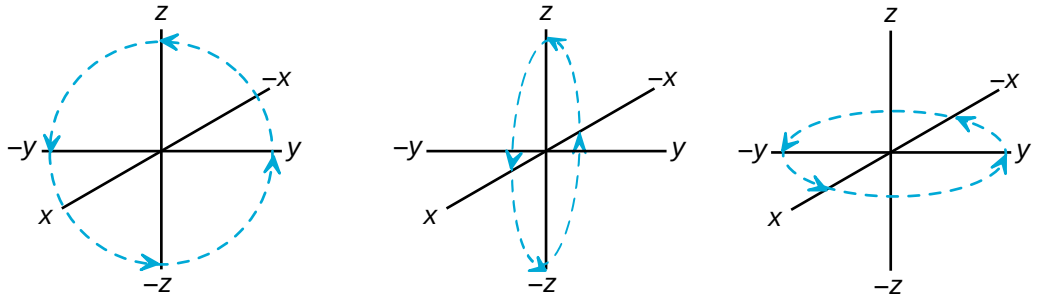

FIGURE 2.1: Diagrams illustrating the transformation of the product operators under (a) an x pulse, (b) a y pulse and (c) free precession at a resonance offset Ω.

can then be used to solve the equation, giving

$$\sigma(t_p) = I_z \cos\beta - I_y \sin\beta. \tag{2.32}$$

This result is exactly analogous to what we would expect from the vector model – a rotation of I_z by an angle β about the x-axis has taken place.

Summarising the effect of pulses of flip angle β on the three angular momentum operators, we have:

$$\begin{aligned} I_x &\xrightarrow{\beta_x} I_x & \qquad I_x &\xrightarrow{\beta_y} I_x\cos\beta - I_z\sin\beta \\ I_y &\xrightarrow{\beta_x} I_y\cos\beta + I_z\sin\beta & \qquad I_y &\xrightarrow{\beta_y} I_y \\ I_z &\xrightarrow{\beta_x} I_z\cos\beta - I_y\sin\beta & \qquad I_z &\xrightarrow{\beta_y} I_z\cos\beta + I_x\sin\beta \end{aligned}$$

while the effect of free precession for time t at a resonance offset Ω is given by

$$\begin{aligned} I_x &\xrightarrow{\Omega t} I_x\cos\Omega t + I_y\sin\Omega t \\ I_y &\xrightarrow{\Omega t} I_y\cos\Omega t - I_x\sin\Omega t \\ I_z &\xrightarrow{\Omega t} I_z. \end{aligned}$$

The sign conventions used in these rotations are clear in the diagrams in Figure 2.1

2.3.2 Product operators for two spins

For a system of two weakly J-coupled spin $I = 1/2$ nuclei labelled I and S the 16 operators of the basis set can be obtained by taking the products of the four operators

of each spin, as shown in Table 2.1.

TABLE 2.1: Product operators for two spins I and S. The factor of two is a normalisation constant.

		$\frac{1}{2}E$	S_x	S_y	S_z
$2\times$	$\frac{1}{2}E$	$\frac{1}{2}E$	S_x	S_y	S_z
$2\times$	I_x	I_x	$2I_xS_x$	$2I_yS_y$	$2I_xS_z$
$2\times$	I_y	I_y	$2I_yS_x$	$2I_yS_y$	$2I_yS_z$
$2\times$	I_z	I_z	$2I_zS_x$	$2I_zS_y$	$2I_zS_z$

I and S can be the same or different nuclear species. The rules for calculating the evolution of coupled spins can be found elsewhere [20, 27, 28].

2.4 Spherical tensor operator basis set

Although useful for describing experiments on spin $I = 1/2$ nuclei, the product operator basis set becomes inconvenient for representing higher coherence orders relevant for quadrupolar nuclei. Instead, the tensor operator basis set proves useful in the case of quadrupolar spin systems. This basis set will be employed in Chapter 6.

Müller et al. published the expansion of the density operator using irreducible spherical tensor operators, $T_{l,p}$, in 1987 [29]:

$$\sigma(t) = \sum_{l=0}^{2l} \sum_{p=-l}^{l} a_{l,p}(t) T_{l,p}. \tag{2.33}$$

A nucleus with spin quantum number I has a basis set of $(2I+1)^2$ operators, $T_{l,p}$, where l is the rank and p is the order. The rank, l, can take values $0, 1, 2 \ldots 2I$, whilst for a given rank the order, p, ranges from $-l$ to $+l$ in integer steps of 1. The matrix representation of each tensor operator has non-zero elements along a single diagonal. The order, p, represents the coherence order, thus $p = \Delta m_I$. Tensor operators with $p = 0$ therefore represent population states; $p = \pm 1$ represent single-quantum coherences, and so on.

The rank can be understood by relating them to the relative phases of the non-zero components of the operator matrices. For a given coherence order, the lowest rank describes operators with all components in-phase. Matrices of the next higher order

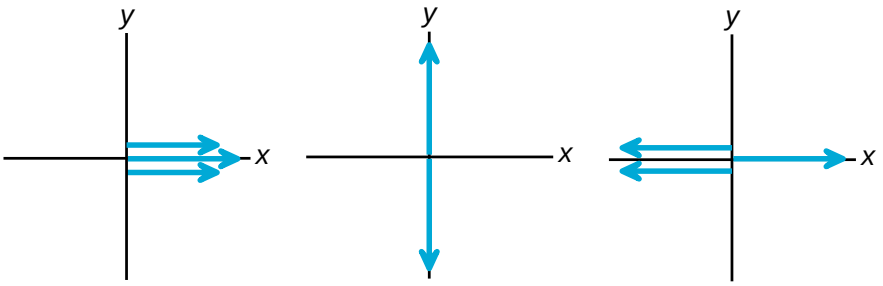

(a) $T_{1,-1}$ (b) $T_{2,-1}$ (c) $T_{3,-1}$

FIGURE 2.2: Vector model diagrams of some $p = -1$ tensor operators [30].

have singly-antiphase components – that is, the first half of the components have one sign, and the second half have the opposite sign. The components of the next higher orders are doubly antiphase, then triply antiphase, and so on. The tensor operators of rank $p = -1$ can be represented by vector model illustrations as shown in Figure 2.2.

As the density matrix is Hermitian,

$$\sigma_{i,j}(t) = \sigma^*_{j,i}(t) \tag{2.34}$$

if the tensor $T_{l,p}$ is present with amplitude a, then the tensor $T_{l,-p}$ is also present with amplitude $(-1)^p a^*$.

The matrix representations of the irreducible spherical tensor operators for spin $I = 3/2$ and $I = 5/2$ can be found in Appendix B.

2.5 Internal interactions

As described in Section 1.2, the Zeeman interaction is responsible for lifting the degeneracy of the energy levels of a nucleus. As well as this coupling of the spin angular momentum to the external magnetic field, the spins within a sample sense subtly different local fields according to their specific chemical environments, i.e., depending on their proximity to other electrons and nuclei. These internal interactions play a pivotal role in determining the appearance of an NMR spectrum, providing a rich range of information that secures NMR's role as an indispensable tool for analysis. The following sections will introduce these interactions.

2.5.1 Chemical shift interaction

The resonant frequency of a nucleus is dependent on its Larmor frequency, an intrinsic property for a particular isotope, and the strength of the external magnetic field it is exposed to. The magnetic field B_0 is also responsible for causing circulation of electrons in their atomic or molecular orbitals. This motion produces an induced magnetic field, B_{in}, which either opposes or augments the external field. The effective field at the nucleus is then,

$$B = B_0 - B_{\text{in}} = B_0(1 - \sigma), \tag{2.35}$$

modifying the Larmor frequency defined in Equation 1.10 to,

$$\omega = |\gamma B_0|(1 - \sigma), \tag{2.36}$$

where σ is the shielding. Although producing only a small change, a detectable shift in the frequency of the peaks may be observed under high-resolution NMR.

As the shielding has the properties of a second-rank Cartesian tensor, it can be represented by a 3×3 matrix. This is also true of the dipolar interaction (Section 2.5.2), J-coupling (Section 2.5.3) and the quadrupolar interaction (Section 2.5.4). The definition of the tensor in a suitable frame of reference (the principal axis system, or PAS) ensures that the matrix is diagonal and the tensor can then be defined by three principal values. For shielding, these quantities are defined as $\sigma_{\text{XX}}^{\text{PAS}}$, $\sigma_{\text{YY}}^{\text{PAS}}$ and $\sigma_{\text{ZZ}}^{\text{PAS}}$ and are associated with the PAS X, Y and Z axes, respectively. The shielding tensor in its PAS can be written in matrix form as,

$$\sigma = \begin{pmatrix} \sigma_{\text{XX}}^{\text{PAS}} & 0 & 0 \\ 0 & \sigma_{\text{YY}}^{\text{PAS}} & 0 \\ 0 & 0 & \sigma_{\text{ZZ}}^{\text{PAS}} \end{pmatrix}. \tag{2.37}$$

These values may be used to define an isotropic component of the shielding tensor, σ_{iso}, an anisotropy, Δ, and an asymmetry parameter, η:

$$\sigma_{\text{iso}} = \frac{1}{3}(\sigma_{\text{XX}}^{\text{PAS}} + \sigma_{\text{YY}}^{\text{PAS}} + \sigma_{\text{ZZ}}^{\text{PAS}}) \tag{2.38}$$

$$\Delta = \sigma_{\text{ZZ}}^{\text{PAS}} - \sigma_{\text{iso}} \tag{2.39}$$

$$\eta = \frac{\sigma_{YY}^{PAS} - \sigma_{XX}^{PAS}}{\Delta}. \tag{2.40}$$

NMR frequencies are not measured in absolute terms. Instead, they are expressed as chemical shifts – a frequency difference with regard to a reference sample. In order to have chemical shift values that are independent of the external magnetic field strength, the value is also divided by the resonance frequency of the reference peak. Thus the chemical shift, δ_{iso} is given by,

$$\delta_{iso} = \frac{\omega_0 - \omega_0^{ref}}{\omega_0^{ref}} = \frac{\sigma_{iso}^{ref} - \sigma_{iso}}{1 - \sigma_{iso}^{ref}}. \tag{2.41}$$

In order to make the values more convenient, the ratio is multiplied by 10^6, and the chemical shifts quoted in 'parts per million' (ppm).

The chemical shift can also be defined by three principal values in its PAS, allowing the isotropic chemical shift, δ_{iso}, the chemical shift anisotropy, Δ_{CS} , and the chemical shift asymmetry, η_{CS} to be defined as:

$$\delta_{CS} = \frac{1}{3}(\delta_{XX}^{PAS} + \delta_{YY}^{PAS} + \delta_{ZZ}^{PAS}) \tag{2.42}$$

$$\Delta_{CS} = \delta_{ZZ}^{PAS} - \delta_{iso} \tag{2.43}$$

$$\eta_{CS} = \frac{\delta_{YY}^{PAS} - \delta_{XX}^{PAS}}{\Delta_{CS}}. \tag{2.44}$$

The observed chemical shift in an NMR spectrum, δ, is the sum of the isotropic and anisotropic components:

$$\delta = \delta_{iso} + \frac{1}{2}\,\Delta_{CS}(3\cos^2\theta - 1 + \eta_{CS}\sin^2\theta\cos 2\phi) \tag{2.45}$$

where θ and ϕ are the polar angles that define the orientation of the B_0 field with respect to the PAS of the chemical shielding tensor.

The rapid tumbling motion of molecules in solution state is responsible for averaging out the anisotropic contribution to the chemical shift to zero. Therefore, only δ_{iso} determines the shift of the peaks in a solution-state spectrum.

In solids, the anisotropic components of Equation 2.45 play a large part in determining the characteristic width and shape of the spectrum. For a single crystal, only one frequency arises from one particular orientation and a sharp line is seen in the spectrum for each distinct spin. However, in the more common case of a powdered solid, all orientations are simultaneously present, giving rise to a powder pattern comprising of a sum of the contributions of each crystallite in the sample. The restricted motion within the solid sample prevents the averaging achieved in solution state.

2.5.2 The dipolar interaction

Dipolar coupling is a through-space interaction that provides an important route to understanding correlations between spins. Each spin generates a magnetic field orientated parallel to the nuclear spin vector. Two nuclei I and S that are located close to each other will experience each other's magnetic field. The effective magnetic field at one spin will therefore depend on the orientation of both magnetic dipoles. The dipolar interaction Hamiltonian is:

$$H_{\mathrm{D}} = \omega_{\mathrm{D}}^{\mathrm{PAS}} \left(\mathbf{I} \cdot \mathbf{S} - \frac{3(\mathbf{I} \cdot \mathbf{r})(\mathbf{S} \cdot \mathbf{r})}{r^2} \right) \tag{2.46}$$

where the strength of the interaction depends strongly on the distance between the spins (r) as well as the gyromagnetic ratios according to the dipole-dipole coupling constant, defined as

$$\omega_{\mathrm{D}}^{\mathrm{PAS}} = \frac{-\mu_0 \gamma_I \gamma_S \hbar}{4\pi r^3} \tag{2.47}$$

in units of radians per second.

In high magnetic fields, the secular approximation can be made and the orientation dependence is given by

$$\omega_{\mathrm{D}} = \omega_{\mathrm{D}}^{\mathrm{PAS}} \frac{1}{2} (3\cos^2 \theta_{IS} - 1) \tag{2.48}$$

where θ_{IS} is the angle between the axis connecting the two spins and the applied magnetic field B_0. Unlike the chemical shielding tensor, the dipolar coupling tensor is traceless and its isotropic value is therefore zero. It is always axially symmetric ($\eta = 0$). In an isotropic solution, the orientations of the nuclear spins are rapidly exchanged by rotational Brownian motion and the dipolar interaction is therefore averaged out during

the timescale of an NMR experiment. However, it does contribute to relaxation processes and is important in experiments involving the nuclear Overhauser effect (NOE) [16, 31].

In a powdered solid, dipolar coupling is a significant broadening mechanism, leading to a Pake doublet lineshape in a powder of isolated pairs of spin $I = 1/2$ nuclei [32]. In a sample with numerous dipolar-coupled spins, the NMR spectrum will be a broad Gaussian lineshape [33].

2.5.3 J-coupling

J-coupling, also known as scalar coupling, is a through-bond interaction arising from the interaction between electrons, which are spin $I = 1/2$ particles, with nuclear spins [22, 34]. A bonding orbital containing two electrons will be spin paired according to the Pauli principle ($\cdot \uparrow\downarrow \cdot$). If we introduce a nuclear spin on one side, the overall energy will be lower if the nuclear spin is polarised in the same direction as the electron close to the nucleus ($\uparrow \uparrow\downarrow \cdot$) than if it is aligned antiparallel to it ($\downarrow \uparrow\downarrow \cdot$). If another nuclear spin is then introduced, the energy is again minimised if it is aligned antiparallel to the first nuclear spin ($\uparrow \uparrow\downarrow \downarrow$). This indirect interaction via the electrons perturbs the nuclear spin Hamiltonian. J-coupling is strongest for directly-bonded nuclear spins, but can also be detected over two or three bonds.

The Hamiltonian for J-coupling between spins I and S is given by

$$H_{\mathbf{J}} = 2\pi\, \mathbf{I} \cdot \mathbf{J}_{IS} \cdot \mathbf{S} \tag{2.49}$$

The second-rank tensor $\mathbf{J}_{IS}$ describes the J-coupling and as the interaction is given with units of Hz a factor of 2π appears in the equation above.

In an isotropic liquid, the second-rank tensor $\mathbf{J}_{IS}$ is averaged out by the rapid tumbling motion and the remaining isotropic component is given by the average of the diagonal elements of the matrix,

$$J_{IS} = \frac{1}{3}(J_{XX} + J_{YY} + J_{ZZ}). \tag{2.50}$$

Solution-state NMR spectra often contain complicated splitting patterns owing to this J-coupling interaction, and these can be exploited for determining molecular structure from a spectrum.

In solids, the J-coupling is usually much smaller than the other interactions, so resolved J-coupled multiplets are an uncommon feature of spectra. The anisotropic component of the J-coupling tensor is present in solids and anisotropic liquids, but its contribution is usually small enough to be overlooked.

2.5.4 The quadrupolar interaction

Quadrupolar nuclei are those which have spin quantum number, I, greater than a half. They possess an electric quadrupole moment, eQ, which arises from the non-spherical distribution of charge in the nucleus. The charge distribution in the nucleus can be described as a series of multipoles: the monopole, or point charge, is the zeroth-order term; the electric-dipole is the first-order term (which is equal to zero for a nucleus, as are all other odd-order electric terms); and the second-order term is the electric quadrupole moment [35]. This is illustrated in Figure 2.3(a). Although there is little experimental evidence of higher order terms owing to their much smaller effect in perturbing electrostatic interactions, Abragam [36] wrote that "There is no reason, however, to doubt their existence."

The quadrupolar interaction arises when the quadrupole moment couples to the electric field gradient (EFG) created by the surrounding electron density at the nucleus. Figure 2.3(b) shows the quadrupole in two different orientations surrounded by point charges. It is apparent that the electrostatic energy will vary according to orientation, and the second orientation shown is more energetically favourable. In contrast, a spin $I = 1/2$ nucleus only has a monopole component, thus would not have an orientation dependence in the same field gradient.

The EFG can be represented by a diagonal tensor $\mathbf{V}$ corresponding to the principal axis system. The tensor is traceless,

$$V_{XX} + V_{YY} + V_{ZZ} = 0 \tag{2.51}$$

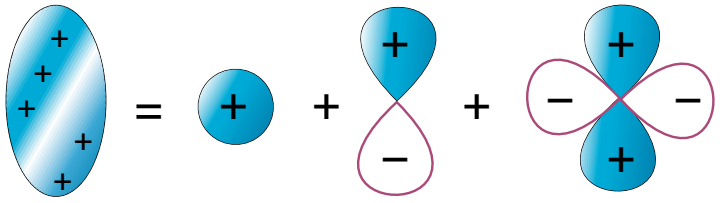

(a) Nuclear charge distribution broken down as a series of multipoles

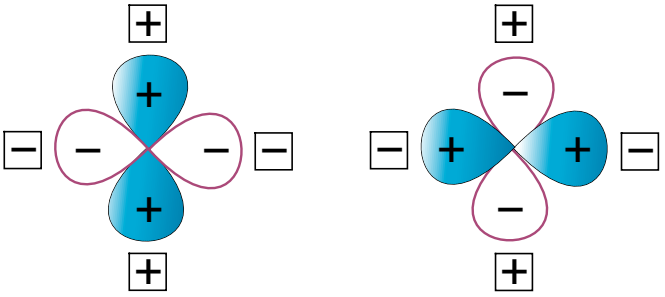

(b) Orientation dependence of the nuclear quadrupole moment

FIGURE 2.3: (a) The charge distribution in a nucleus can be expanded as a series of multipoles where the zeroth-order term is the total charge, the dipolar term is zero and the the quadrupolar term is only possessed by spins $I > 1/2$. (b) The quadrupolar interaction arises from the orientation-dependent coupling of the quadrupolar moment to the electric field gradient. Here, the quadrupole moment surrounded by point charges will be more energetically favourable in the second orientation shown.

and the three principal tensor elements are ordered

$$V_{XX} \geq V_{YY} \geq V_{ZZ} \tag{2.52}$$

in a principal axis system (PAS) where $\mathbf{V}$ is diagonal. The EFG anisotropy can be characterised by q and η, where q, the magnitude of the EFG is given by

$$q = V_{ZZ}/e \tag{2.53}$$

where e is the electric charge, and the asymmetry parameter η is given by

$$\eta = \frac{V_{XX} - V_{YY}}{V_{ZZ}} \tag{2.54}$$

and can take values between 0 and 1. The magnitude of the interaction between the nuclear quadrupole moment and the principal field gradient V_{ZZ} is expressed as C_Q,

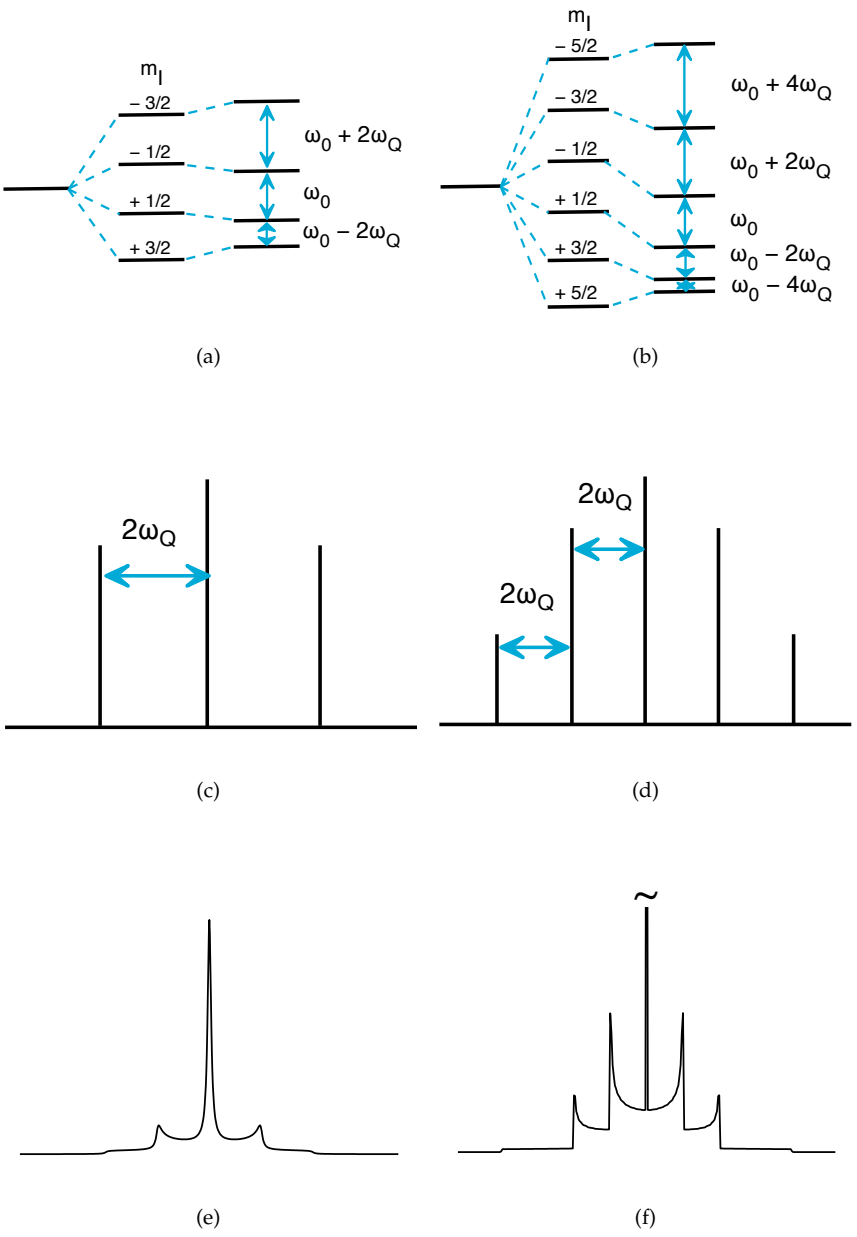

FIGURE 2.4: For spin $I = 3/2$ (a, c, e) and $I = 5/2$ (b, d, f): Perturbation of the Zeeman energy levels by the first-order quadrupolar interaction (a and b); Simulations of the resulting single crystal NMR spectra (c and d) and powder spectra (e and f) with $\eta = 0$.

the quadrupolar coupling constant:

$$C_Q = \frac{e^2 q Q}{h}. \tag{2.55}$$

The quadrupolar frequency in the PAS is often used instead of C_Q, and is defined as

$$\omega_Q^{\mathrm{PAS}} = \frac{3\pi C_Q}{2I(2I-1)} \tag{2.56}$$

in units of rad s^{-1}.

Assuming axial symmetry ($\eta = 0$), the quadrupolar Hamiltonian is

$$H_{\text{quad}} = \frac{\omega_Q^{\text{PAS}}}{2}(3\cos^2\theta - 1)\{I_z^2 - \frac{1}{3}I(I+1)\} \tag{2.57}$$

where θ is the angle the Z axis of the principal axis system makes to the z axis of the rotating or laboratory frame. The corresponding eigenvalues give the energy level splittings,

$$E_Q = \omega_Q\{m_I^2 - \frac{1}{3}I(I+1)\} \tag{2.58}$$

where the quadrupolar splitting parameter ω_Q is defined as

$$\omega_Q = \frac{\omega_Q^{\text{PAS}}}{2}(3\cos^2\theta - 1) \tag{2.59}$$

This perturbation of the Zeeman energy levels is illustrated in Figure 2.4(a) for $I = 3/2$ and Figure 2.4(b) for $I = 5/2$. The NMR spectrum of a single crystal for spin $I = 3/2$ therefore consists of three transitions with frequencies of $\omega_0 + 2\omega_Q$, ω_0 and $\omega_0 - 2\omega_Q$ (Figure 2.4(c)) while the spectrum for spin $I = 5/2$ consists of five non-degenerate transitions separated by $2\omega_Q$ (Figure 2.4(d)). In a powdered sample, all orientations of $\mathbf{V}$ with respect to B_0 are simultaneously present in different crystallites. According to Equation 2.59, this will result in a range of values for ω_Q. The overlap of different transitions gives rise to a powder pattern, as shown in Figures 2.4(e) and 2.4(f). For half-integer spins, the transition between energy levels $m_I = \pm 1/2$ (known as the central transition) is not affected by the quadrupolar interaction to first order. In contrast, the other transitions (satellite transitions) are significantly broadened by the quadrupolar interaction, to the extent that they can be difficult to observe.

2.6 Magic angle spinning

Magic angle spinning (MAS) is a widely used technique in solid-state NMR that helps to remove the broadening interactions discussed in previous sections. By spinning the sample rapidly at an angle of 54.74° with respect to the applied magnetic field, a considerable improvement in resolution can be achieved [13, 37, 38]. If the spinning rate

is fast compared to the size of the anisotropy, the broad static powder pattern can be reduced to a single sharp line at the isotropic chemical shift. Slower spinning produces a spectrum containing a set of spinning sidebands, which flank both sides of the centre-band [19, 39].

Practically, MAS NMR experiments involve packing a powdered solid into a MAS rotor. Rotors are available in different sizes, with smaller rotors allowing faster spinning but larger rotors offering an increased sample volume and thus greater sensitivity. In this thesis, rotors have been used with diameters of 4 mm (which allow spinning between around 4 and 15 kHz) and 2.5 mm (around 20 to 35 kHz). As the cap of a rotor features fins, it acts as a turbine to spin the whole rotor when jets of air are directed at it within the probe.

We have seen that internal interactions are most conveniently described in their principal axis system (PAS). As the Zeeman interaction aligned parallel to B_0 is the dominant interaction, all internal interactions must be rotated to this frame of reference, known as the laboratory frame. To simplify the description of a rotation, Hamiltonians are expressed in spherical tensor form,

$$H = \sum_{l=0}^{2} \sum_{m=-l}^{+l} (-1)^m A_{l,m} T_{l,-m} \tag{2.60}$$

where $T_{l,-m}$ is an irreducible spherical tensor describing the spin component and $A_{l,m}$ is a tensor which describes the spatial component of a certain interaction. The rank of the tensor, l, takes values $l = 0, 1, 2$ while the order of the tensor can take values $m = -l, -l+1, \ldots, l-1, l$.

In order to give a description of MAS, we must transform the irreducible spherical tensor A which describes the spatial part of the interaction from the principal axis system (A^{P}) to the laboratory frame (A^{L}) via the intermediate rotor frame (A^{R}). A rotation of a spatial tensor can be described in terms of the Euler angles $\Omega = \{\alpha, \beta, \gamma\}$. We can define a rotation operator $R(\alpha, \beta, \gamma)$ which is a product of three successive rotations:

$$R(\alpha, \beta, \gamma) = R_\gamma R_\beta R_\alpha = \exp(-i\gamma I_{z''}) \exp(-i\beta I_{y'}) \exp(-i\alpha I_z) \tag{2.61}$$

Each of these operations defines a new coordinate system for the next rotation. The three rotations are:

1. A rotation of angle α about the z-axis, giving coordinate axes x', y', z'
2. A rotation of angle β about the y'-axis, giving coordinate axes x'', y'', z''
3. A rotation of angle γ about the z''-axis, giving coordinate axes x''', y''', z'''

Owing to the unitary properties of R, Equation 2.61 can be equivalently expressed with the rotations taking place with respect to a single axis frame [19]:

$$R(\alpha, \beta, \gamma) = \exp(-i\alpha I_z) \exp(-i\beta I_y) \exp(-i\gamma I_z). \tag{2.62}$$

In order to describe MAS, we require a rotation from the PAS to the rotor frame, $R(\alpha_{PR}, \beta_{PR}, \gamma_{PR})$, followed by a rotation from the rotor frame to the lab frame, $R(\alpha_{RL}, \beta_{RL}, \gamma_{RL})$. Figure 2.5 illustrates these two successive transformations. β_{PR} describes the angle between the z-axis of the interaction tensor principal axis system and the spinning axis, while β_{RL} describes the angle between the rotor axis and the static magnetic field, $\mathbf{B_0}$. The value of α_{RL} varies with the rotation of the rotor according to $\alpha = -\omega_R t$, where ω_R is the spinning frequency. γ_{RL} is the phase of the rotor and can be arbritrarily set to zero.

The operator R can be described by a Wigner D-matrix. A double-frame transformation acting on a spherical tensor A^{P} from the PAS to the rotor frame (PR) and then from the rotor frame to the laboratory frame (RL) can be written

$$A^{\mathrm{L}}_{l,n} = \sum_{m=-l}^{l} \sum_{m'=-l}^{l} D^{l}_{m,n}(\alpha_{\mathrm{RL}}, \beta_{\mathrm{RL}}, \gamma_{\mathrm{RL}}) D^{l}_{m',m}(\alpha_{\mathrm{PR}}, \beta_{\mathrm{PR}}, \gamma_{\mathrm{PR}}) A^{\mathrm{P}}_{l,m'}. \tag{2.63}$$

The Wigner D-matrix elements can be reduced to exponentials that are dependent on α and γ and a reduced Wigner d-matrix element that depends only on β:

$$D^{l}_{m',m}(\alpha, \beta, \gamma) = \exp(-im'\alpha)\, d^{l}_{m'm}(\beta) \exp(-im'\gamma) \tag{2.64}$$

The reduced Wigner rotation matrix elements can be found tabulated elsewhere [40, 41].

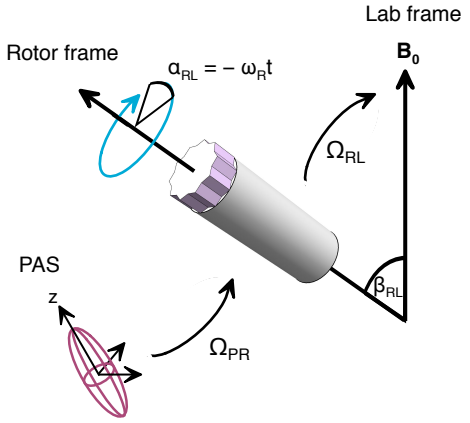

FIGURE 2.5: To understand the theory of MAS, we require a rotation from the PAS to the rotor frame, described by the Euler angles Ω_{PR}, followed by a rotation from the rotor frame to the lab frame, described by the Euler angles Ω_{RL}. The rotor is inclined at $\beta_{\mathrm{RL}} \approx 54.74^\circ$ relative to the laboratory frame and spun rapidly under magic angle spinning. The angle α_{RL} describes the time-dependent phase of the rotor.

The anisotropic components of an interaction are contained within the rank-2 ($l = 2$) terms of a spherical tensor. For a second-rank tensor, the D-matrix elements transformed from P to R to L are

$$D^2_{m',n}(\Omega_{\mathrm{PL}}) = \sum_{m=-2}^{2} D^2_{m,n}(\Omega_{\mathrm{RL}}) D^2_{m',m}(\Omega_{\mathrm{PR}}) \tag{2.65}$$

Focusing on the term $D^2_{m,n}(\Omega_{\mathrm{RL}})$ in Equation 2.65 which takes us from the rotor frame to the lab frame, and remembering that $\gamma_{RL} = 0$ we can write using Equation 2.64:

$$\begin{aligned} D^2_{m,n}(\Omega_{\mathrm{PR}}) &= \exp(-im\alpha_{\mathrm{RL}})\, d^2_{m,n}(\beta_{\mathrm{RL}}) \exp(-in\gamma_{\mathrm{RL}}) \\ &= \exp(-im\alpha_{\mathrm{RL}})\, d^2_{m,n}(\beta_{\mathrm{RL}}) \end{aligned} \tag{2.66}$$

If we average the time-dependent part of Equation 2.66 over one rotor period, $t_R = 2\pi/\omega_R$, we find

$$\frac{1}{t_R}\int_0^{2\pi/\omega_R} \exp(im\omega_R t)\, \mathrm{d}t = \begin{cases} \frac{2\pi}{\omega_R t_R} = 1 & \text{if } m = 0 \\ \frac{\cos(m2\pi) + i\sin(m2\pi) - 1}{im\omega_R t_R} = 0 & \text{if } m = \pm 1, \pm 2, \ldots \end{cases} \tag{2.67}$$

When $m = 0$, the time-dependent part equals 1 after a complete rotor period. When $m = \pm 1, \pm 2, \ldots$, the time-dependent part equals zero. The five terms in Equation 2.65

are thus reduced to one term:

$$D^2_{m',n}(\Omega_{\mathrm{PL}}) = D^2_{0,n}(\Omega_{\mathrm{RL}})D^2_{m',0}(\Omega_{\mathrm{PR}}) \tag{2.68}$$

which corresponds to A^{L}_{2n} in Equation 2.63. Under the high-field secular approximation, the only non-zero terms of the matrix are along its diagonal. Since we therefore only need consider the A^{L}_{20} term, Equation 2.68 then becomes

$$D^2_{m',0}(\Omega_{\mathrm{PL}}) = D^2_{0,0}(\Omega_{\mathrm{RL}})D^2_{m',0}(\Omega_{\mathrm{PR}}). \tag{2.69}$$

The orientation dependence of the $D^2_{0,0}$ term is the $l = 2$ Legendre polynomial, $\frac{1}{2}(3\cos^2\theta - 1)$. When the rotor is spun at the magic angle $\beta_{\mathrm{RL}} = \tan^{-1}\sqrt{2} \approx 54.74^\circ$, the term $D^2_{m'0}(\Omega_{\mathrm{PL}})$ evaluates to zero. In this way, magic angle spinning is capable of averaging a second-rank interaction to zero after one rotor period.

If data points are acquired at integer multiples of t_R, a Fourier transform of the resulting FID will reduce a powder pattern to a single line at the isotropic chemical shift. If the data points are not acquired only at nt_R and the spinning rate is not larger than the anisotropic interaction, then the $m = \pm 1$ and $m = \pm 2$ terms in Equation 2.65 lead to oscillatory evolution of the density matrix. This corresponds to the experimental observation of rotary echoes in the FID spaced by t_R s and spinning sidebands in a MAS NMR spectrum separated by $1/t_R = \omega_R/2\pi$ Hz.

2.7 The spin echo

An NMR signal will decay after an excitation pulse owing to inhomogeneous effects that cause different spins in a sample to precess at different rates. In solution-state NMR, this dephasing can result from the effect of an inhomogenous B_0 field, where different volumes of the sample will have different precession frequencies according to the field they experience. This dephasing can be reversed by using a spin-echo pulse sequence.

The spin echo can also remedy phase distortions seen in spectra with broad resonances caused by anisotropic interactions in solid-state NMR. Transverse magnetisation will evolve at different rates according to the orientation of different crystallites in a powder

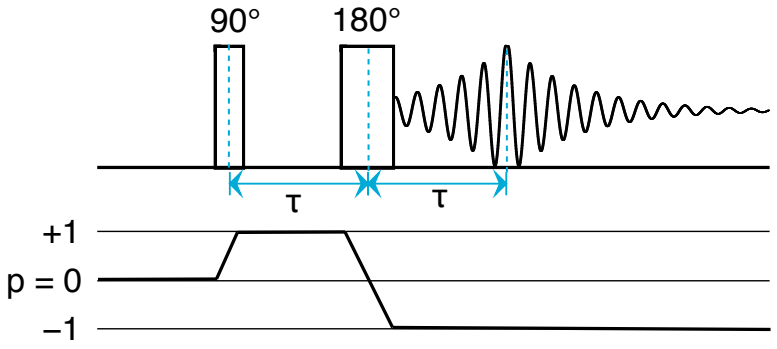

FIGURE 2.6: Pulse sequence and coherence transfer pathway diagram of a spin-echo experiment.

sample. Large broadening interactions will be characterised by rapidly decaying FIDs, but FIDs cannot be acquired immediately after a pulse, and a significant part can be lost during the "dead time" between the pulse and acquisition. As a result, different spins will acquire different phases by the time aquisition begins, leading to distorted lineshapes in the frequency domain. In cases where the dead time is small and the signal decays slowly, a first-order phase correction (Section 1.6) can improve the spectrum. However, this method is not suitable if the FID decays rapidly and the dead time is relatively long. Instead, a spin echo can be used to refocus the dephasing magnetisation such that all homogeneous components of the broad line will have the same phase. The Hahn or Carr-Purcell echo, $90^\circ_{0^\circ} - \tau - 180^\circ_{0^\circ} - \tau$, is used for lines broadened by chemical shift anisotropy or heteronuclear dipolar coupling [42, 43], while the solid echo sequence, $90^\circ_{0^\circ} - \tau - 90^\circ_{90^\circ} - \tau$, is used for lines broadened by quadrupolar coupling or homonuclear dipolar coupling [44, 45]. The latter sequence will not be considered further here.

A spin-echo pulse sequence and coherence transfer pathway are shown in Figure 2.6. A 90° pulse is used to excite single-quantum coherence. A 180° pulse is applied after duration τ, using Exorcycle phase cycling to select the coherence order change $\Delta p = -2$ (see Section 2.8). After a further period of free precession of duration τ a spin echo is formed. In MAS experiments, the τ period is usually equal to an integer number of rotor periods.

The mechanism of echo formation may be revealed by considering a vector model picture of the experiment. Figure 2.7 illustrates the paths followed by the tips of three vectors shown in green, red and blue, each having a different precession frequency.

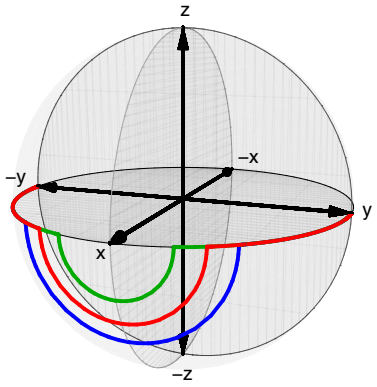

FIGURE 2.7: "Grapefruit plot" showing the trajectories of magnetisation vectors during the $\tau - 180° - \tau$ part of a echo pulse sequence. Each vector starts at the $-y$ axis following the application of a 90° excitation pulse but these vectors fan out during the first τ period according to their different precession frequencies (green – fast, red – slower, blue – slowest). After a 180° and another free precession period for time τ, the vectors are all refocused along the y axis.

Each of the vectors is initially aligned along the $-y$-axis following the application of a $90°_{0°}$ excitation pulse. During the free precession period, τ, the vectors begin to fan out in the xy plane. A $180°_{0°}$ pulse then rotates each vector about the x-axis to its mirror image position in the xy plane, thus moving the "fast" spins behind the "slow" spins. After another period of free precession of equal length to the first, all vectors are aligned together, or refocused, along the y-axis.

2.8 Exorcycle

Exorcycle is the name given to the phase cycle which selects the coherence pathway shown in Figure 2.6 and was in fact the first published example of a phase cycle [26, 46]. It was developed by Bodenhausen et al. to remove artefacts they observed in two-dimensional spin-echo spectra that they dubbed "ghosts" and "phantoms" [47, 48]. These effects arise as a consequence of imperfections in the radiofrequency pulses, such as inhomogeneity of the B_1 field and an offset of the transmitter from resonance. By incrementing the phase of the refocusing pulse by 90° while the receiver phase is incremented by 180° (see Table 2.2), Exorcycle retains signal that undergoes a change in coherence order of $\Delta p = -2$ during the 180° pulse and discards the component that will not echo.

TABLE 2.2: The Exorcycle phase cycle.

Pulse phase	Receiver phase
0°	0°
90°	180°
180°	0°
270°	180°

Using the product operator formalism (as described in Section 2.3) we can examine the effect of pulse errors and show that Exorcycle is able to correct the phase of the magnetisation in some cases [3]. A magnetisation vector which acquires after time t a phase $\phi = \Omega t$ can be written $I_x \cos\phi + I_y \sin\phi$. To form a spin echo, the phase must be reversed by applying a $180^\circ_{0^\circ}$ pulse:

$$I_x \cos\phi + I_y \sin\phi \xrightarrow{180^\circ_{0^\circ}} I_x \cos\phi - I_y \sin\phi. \tag{2.70}$$

The phase of the magnetisation after the pulse is, as desired,

$$\tan^{-1}\left(\frac{-\sin\phi}{\cos\phi}\right) = \tan^{-1}(-\tan\phi) = -\phi. \tag{2.71}$$

A perfect spin echo will be formed after another period of free precession t.

2.8.1 Flip angle misset

Flip angle errors are a common pulse imperfection arising from the inhomogeneity of the B_1 field strength, which is an unavoidable consequence of the design of the rf coil. The variation of the B_1 field strength is responsible for a distribution of nutation frequencies across the sample. This leads to a decrease in signal amplitude as the nominal flip angle is not attained by all spins in the sample. Errors in the size of the flip angle also arise from poor pulse calibration. If we consider a refocusing pulse that has a general flip angle β,

$$I_x \cos\phi + I_y \sin\phi \xrightarrow{\beta^\circ_{0^\circ}} I_x \cos\phi + I_y \sin\phi \cos\beta + I_z \sin\phi \sin\beta = A \tag{2.72}$$

then the phase of the magnetisation vector is

$$\tan^{-1}\left(\frac{-\sin\phi\cos\beta}{\cos\phi}\right) = \tan^{-1}(-\tan\phi\cos\beta) \tag{2.73}$$

which is only equal to $-\phi$ if $\beta = 180^\circ$. The amplitude of the signal, given by

$$\sqrt{\cos^2\phi + \sin^2\phi\cos^2\beta}, \tag{2.74}$$

depends both on the phase ϕ and flip angle β, and there may be considerable signal cancellation in an inhomogeneous B_1 field. In addition, the imperfect refocusing pulse also creates unwanted I_z magnetisation.

Using Exorcycle phase cycling, step A is repeated with the phase of the refocusing pulse advanced by 90° each time, giving:

$$I_x\cos\phi + I_y\sin\phi \xrightarrow{\beta^\circ_{90^\circ}} I_x\cos\phi\cos\beta - I_z\cos\phi\sin\beta + I_y\sin\phi = B \tag{2.75}$$

$$I_x\cos\phi + I_y\sin\phi \xrightarrow{\beta^\circ_{180^\circ}} I_x\cos\phi + I_y\sin\phi\cos\beta - I_z\sin\phi\sin\beta = C \tag{2.76}$$

$$I_x\cos\phi + I_y\sin\phi \xrightarrow{\beta^\circ_{270^\circ}} I_x\cos\phi\cos\beta + I_z\cos\phi\sin\beta + I_y\sin\phi = D \tag{2.77}$$

With each step the receiver step is incremented by 180°, which is equivalent to adding and subtracting the steps A – D alternately, giving

$$A - B + C - D = 2I_x\cos\phi(1-\cos\beta) - 2I_y\sin\phi(1-\cos\beta). \tag{2.78}$$

The phase of the magnetisation once phase-cycled is therefore

$$\tan^{-1}\left(\frac{-\sin\phi(1-\cos\beta)}{\cos\phi(1-\cos\beta)}\right) = \tan^{-1}(-\tan\phi) = -\phi \tag{2.79}$$

and so a spin echo with perfect phase will be formed. The averaged amplitude of the magnetisation vector is

$$(1-\cos\beta)/2 \tag{2.80}$$

and so no longer varies according to ϕ. The signal intensity does retain a dependence on the flip angle β – this property is exploited in the "Depth" technique introduced in Chapter 3.

2.8.2 Off-resonance pulse errors

As described in Section 1.3, there are two effects of applying an rf pulse off-resonance: the rotation axis is tilted towards the z-axis and the effective flip angle increases. We can model the former problem by considering a $180^\circ_{0^\circ}$ pulse with a rotation axis tilted up towards the z-axis by an angle Δ. The rotation about this tilted axis is equivalent to a Δ rotation about the rotating-frame y-axis, followed by a 180° rotation about the x-axis and finally a Δ rotation about the rotating-frame $-y$-axis

$$I_x \cos\phi + I_y \sin\phi \xrightarrow{\Delta_{90^\circ}} \xrightarrow{180^\circ_{0^\circ}} \xrightarrow{\Delta_{270^\circ}} I_x \cos\phi \cos 2\Delta + I_z \cos\phi \sin 2\Delta - I_y \sin\phi = E \quad (2.81)$$

The phase of the magnetisation following this is

$$\tan^{-1}\left(\frac{-\sin\phi}{\cos\phi\cos 2\Delta}\right) = \tan^{-1}\left(\frac{-\tan\phi}{\cos 2\Delta}\right) \quad (2.82)$$

which is only equal to $-\phi$ if $\Delta = 0$. A perfect spin echo will therefore not form if the pulse is not on resonance. Again, the signal amplitude is dependent on both ϕ and β – in this case it is given by

$$\sqrt{\cos^2\phi\cos^2 2\Delta + \sin^2\phi}, \quad (2.83)$$

Exorcycle can again be used to correct the phase problem. The remaining steps of the phase cycle are:

$$I_x \cos\phi + I_y \sin\phi \xrightarrow{\Delta_{180^\circ}} \xrightarrow{180^\circ_{90^\circ}} \xrightarrow{\Delta_{0^\circ}} -I_x \cos\phi + I_y \sin\phi \cos 2\Delta + I_z \sin\phi \sin 2\Delta = F \quad (2.84)$$

$$I_x \cos\phi + I_y \sin\phi \xrightarrow{\Delta_{270^\circ}} \xrightarrow{180^\circ_{180^\circ}} \xrightarrow{\Delta_{90^\circ}} I_x \cos\phi \cos 2\Delta - I_z \cos\phi \sin 2\Delta - I_y \sin\phi = G \quad (2.85)$$

$$I_x \cos\phi + I_y \sin\phi \xrightarrow{\Delta_{0^\circ}} \xrightarrow{180^\circ_{270^\circ}} \xrightarrow{\Delta_{180^\circ}} -I_x \cos\phi + I_y \sin\phi \cos 2\Delta - I_z \sin\phi \sin 2\Delta = H \quad (2.86)$$

Summing these according to the varying receiver phase, we have

$$E - F + G - H = 2I_x \cos\phi(1 + \cos 2\Delta) - 2I_y \sin\phi(1 + \cos 2\Delta) \quad (2.87)$$

and the phase of the magnetisation is

$$\tan^{-1}\left(\frac{-\sin\phi+\cos 2\Delta)}{\cos\phi+\cos 2\Delta)}\right)=\tan^{-1}(-\tan\phi)=-\phi \tag{2.88}$$

A perfect spin echo will be formed, but the signal amplitude is reduced to

$$(1+\cos 2\Delta)/2. \tag{2.89}$$

2.8.3 Rotation axis errors in the xy-plane

Another possible source of imperfection of the refocusing pulse is when the rotation axis of the pulse deviates from the correct position but remains in the xy-plane. This does not occur with simple 180° refocusing pulses, but is relevant in experiments using composite pulses, as we will see in Section 2.10. We can model the problem by considering a $180^\circ_{0^\circ}$ pulse with a rotation axis tilted by an angle of Δ' towards the y-axis. This is equivalent to a Δ' rotation about the $-z$-axis, followed by a $180^\circ_{0^\circ}$ pulse and finally a Δ' rotation about the z-axis. In this case, the four steps of Exorcycle yield:

$$I_x\cos\phi+I_y\sin\phi \xrightarrow{\Delta'_{-z}} \xrightarrow{180^\circ_{0^\circ}} \xrightarrow{\Delta'_z} I_x\cos(\phi-2\Delta')-I_y\sin(\phi-2\Delta')=I \tag{2.90}$$

$$I_x\cos\phi+I_y\sin\phi \xrightarrow{\Delta'_{-z}} \xrightarrow{180^\circ_{90^\circ}} \xrightarrow{\Delta'_z} -I_x\cos(\phi-2\Delta')+I_y\sin(\phi-2\Delta')=J \tag{2.91}$$

$$I_x\cos\phi+I_y\sin\phi \xrightarrow{\Delta'_{-z}} \xrightarrow{180^\circ_{180^\circ}} \xrightarrow{\Delta'_z} I_x\cos(\phi-2\Delta')-I_y\sin(\phi-2\Delta')=K \tag{2.92}$$

$$I_x\cos\phi+I_y\sin\phi \xrightarrow{\Delta'_{-z}} \xrightarrow{180^\circ_{270^\circ}} \xrightarrow{\Delta'_z} -I_x\cos(\phi-2\Delta')+I_y\sin(\phi-2\Delta')=L \tag{2.93}$$

The overall result of this experiment is,

$$I-J+K-L=4I_x\cos(\phi-2\Delta')-4I_y\sin(\phi-2\Delta') \tag{2.94}$$

and the phase of the magnetisation is therefore

$$\tan^{-1}\left(\frac{-\sin(\phi-2\Delta')}{\cos(\phi-2\Delta')}\right)=-(\phi-2\Delta') \tag{2.95}$$

which is the same as the phase yielded by the experiment without any phase cycling. It is clear that Exorcycle is unable to help in this case, and a perfect spin echo will not form if the additional phase $2\Delta'$ varies as a function of B_1 field strength or the resonance offset.

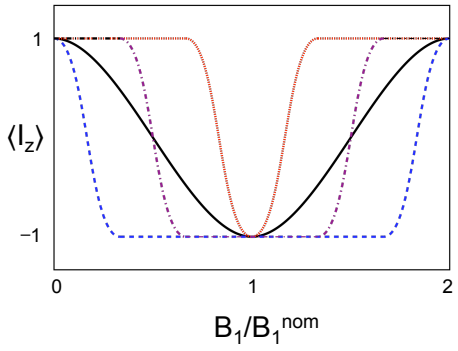

FIGURE 2.8: Inversion profiles showing I_z magnetisation inverted as a function of normalised B_1 field strength for a simple 180° pulse (black), a narrowband composite pulse (red), a passband composite pulse (purple) and a broadband composite pulse (blue).

2.9 Composite pulses: an introduction

As seen in Section 2.8, selection of the echo coherence pathway using Exorcycle corrects phase imperfections in the refocusing pulse but cannot compensate for loss of signal amplitude arising from resonance offset or B_1 inhomogeneity. One method that can be used to help overcome this is the use of composite pulses. A composite pulse is a contiguous sequence of rf pulses of varying flip angle and phase, which has the overall effect of a simple rf pulse but possesses compensatory mechanisms to limit the deleterious effects of pulse imperfections.

Composite pulses have been adopted in a wide range of experiments in both solid- and liquid-state NMR, compensating for the effects of B_1 inhomogeneity and resonance offset. Figure 2.8 illustrates typical inversion profiles for composite pulses that are broadband, passband and narrowband [49] with respect to radiofrequency field strength compared to a simple 180° inversion pulse (black solid line.) Narrowband sequences (shown by the red dotted line) invert magnetisation over only a narrow range of field strengths, and have found use in spatial localisation in imaging experiments. Passband sequences (purple) show characteristics of both a narrowband and broadband sequence. These have been used to achieve enhanced suppression of background signal when implemented in the Depth sequence in ^{1}H NMR ([4], Chapter 3). Broadband composite pulses have been employed to compensate for variations in field strength and resonance offset, and much research has been carried out in devising such sequences ([3, 6], Chapter 4).

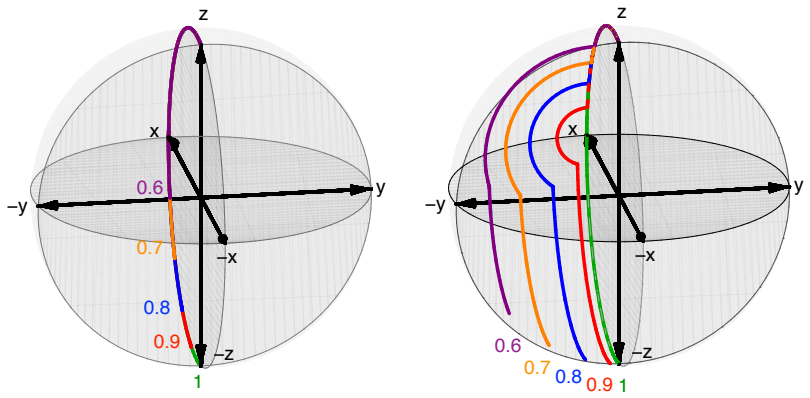

(a) 180° pulse with rf inhomogeneity errors. (b) LF pulse with rf inhomogeneity errors.

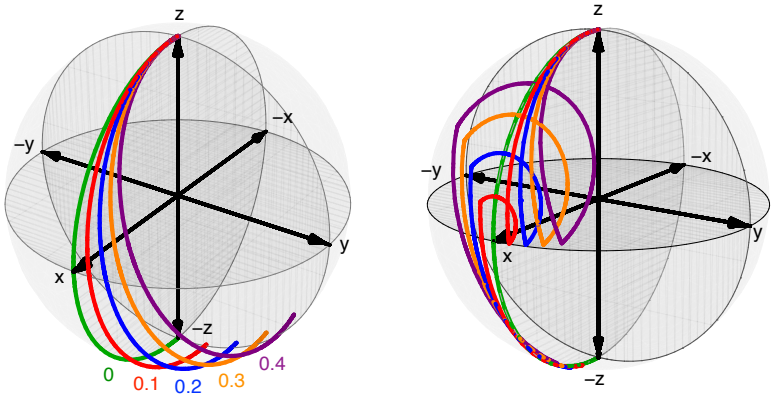

(c) 180° pulse with offset errors. (d) LF pulse with offset errors.

FIGURE 2.9: "Grapefruit plots" showing the trajectories of magnetisation vectors under a simple $180^\circ_{90^\circ}$ inversion pulse (a and c) and the LF composite pulse, $90^\circ_{90^\circ}180^\circ_{0^\circ}90^\circ_{90^\circ}$ (b and d). The rf error was $B_1/B_1^{\text{nom}} = 1, 0.9, 0.8, 0.7, 0.6$ in (a) and (b). In (c) and (d), the normalised offsets are $\Delta B/B_1 = 0, 0.1, 0.2, 0.3, 0.4$. Simulated with Spin Dynamica [2].

2.9.1 Levitt's inversion pulse

The first composite pulse was devised by Levitt in 1978, who at the time was an undergraduate in the Freeman laboratory at Oxford University [50, 51]. His broadband inversion sequence, $90^\circ_{90^\circ}180^\circ_{0^\circ}90^\circ_{90^\circ}$, was designed with the spin-echo phenomenon on his mind [52]:

> "It occurred to me that the vector picture used to explain the formation of spin echoes could be tipped on its side to predict a refocusing effect for radiofrequency inhomogeneity, while still generating a net 180-degree rotation of the nuclear spins."

To help visualise the error compensation provided by the composite pulse, Figure 2.9 illustrates the trajectories of magnetisation vectors subjected to B_1 inhomogeneity and resonance offset effects under a simple 180° pulse and Levitt's inversion pulse sequence (henceforth referred to as "LF"). In Figure 2.9(a), the B_1 field strength is reduced to 90%, 80%, 70% and 60% of its nominal value. The flip angle of the nominal 180° pulse shortens accordingly, and it is clear that the efficiency of the 180° pulse as an inversion pulse is severely compromised in the presence of radiofrequency strength errors. The performance of LF with regard to the same levels of B_1 error is shown in Figure 2.9(b). During the first $90^\circ_{90^\circ}$ element of the composite pulse, the vectors are rotated towards the x axis but fall short of reaching it owing to their reduced nutation frequencies. A $180^\circ_{0^\circ}$ pulse then causes nutation around the x axis, moving each vector approximately to its mirror image location about the xy plane. The final element of the composite pulse, another $90^\circ_{90^\circ}$ pulse, rotates the vectors by the same angle as the first pulse, carrying them much closer to the $-z$ axis than a simple pulse is able to.

The LF pulse also compensates for errors arising from resonance offset. Figures 2.9(c) and 2.9(d) show the effect of increasing the normalised offset, $\Delta B/B_1$. For a simple pulse, the rotation takes place about a tilted field as described in Section 1.3, and the inversion pulse leaves the vector further from the $-z$ axis as the offset increases. With the LF pulse, the first element carries the vectors close to the xy plane. The $180^\circ_{0^\circ}$ pulse then rotates the vectors to a position with approximately reversed y and z coordinates. The final $90^\circ_{90^\circ}$ pulse then brings the vectors almost into focus along the $-z$ axis.

2.10 Use of composite pulses to form spin echoes

A myriad of composite pulses have been suggested since Levitt's initial discovery [3, 49, 51, 53–67]. However, despite initial excitement for broadband composite pulses, it was soon found that often the pulse sequences gave poor results for refocusing transverse (xy) magnetisation in a spin-echo experiment, with phase distortions arising even with the correct phase cycling [3, 68]. This problem occurs as the overall rotation axis of the pulse varies with the field strength. It was shown in Section 2.8 that Exorcycle is unable to correct phase distortions if they arise from a rotation of the overall pulse rotation axis in the xy-plane.

Following this finding, a number of composite pulses termed *phase-distortionless* or *constant-rotation* sequences were introduced [49, 56, 58–62, 69]. In addition to maintaining an overall flip angle over a broad range of rf field strengths or resonance offset, these sequences have rotation axes that are nearly constant over a large range.

In this section, it is demonstrated that the symmetry of the composite pulse must be considered if a perfect spin echo is to be formed. Many of the early broadband composite pulses are unsuitable for use as a refocusing pulse in a spin-echo experiment, including many of the so-called phase-distortionless variety. We can write a composite pulse of N number of elements,

$$(\beta_1)_{\phi_1}\ (\beta_2)_{\phi_2} \ldots (\beta_N)_{\phi_N} \tag{2.96}$$

We will examine the properties of two types of composite pulse:

1. Symmetric composite pulses, where the flip angles are $\beta_1 = \beta_N, \beta_2 = \beta_{N-1}$, etc. and the phases are $\phi_1 = \phi_N, \phi_2 = \phi_{N-1}$, etc.

2. Antisymmetric composite pulses, where the flip angles are $\beta_1 = \beta_N, \beta_2 = \beta_{N-1}$, etc. and the phases are $\phi_1 = \phi_0 + \phi_{1'}, \phi_2 = \phi_0 + \phi_{2'}, \ \ldots \phi_{N-1} = \phi_0 - \phi_{2'}, \ \phi_N = \phi_0 - \phi_{1'}$, where the central pulse (if any) has the base phase ϕ_0

and show that antisymmetric composite pulses should be used in spin-echo experiments.

2.10.1 Symmetric composite pulses

We will prove that an on-resonance symmetric pulse has an overall rotation axis in the xy-plane [60, 70]. The propagator U for a symmetric sequence of three off-resonance rotations,

1. β about an axis with phase ϕ in xy-plane and tilted up towards the z-axis by Δ

2. β' about an axis with phase ϕ' in xy-plane and tilted up towards the z-axis by Δ

3. β about an axis with phase ϕ in xy-plane and tilted up towards the z-axis by Δ

is given by

$$\begin{aligned} U = &\exp[-i\beta(I_x\cos\phi\cos\Delta + I_y\sin\phi\cos\Delta + I_z\sin\Delta)] \\ &\times \exp[-i\beta'(I_x\cos\phi'\cos\Delta + I_y\sin\phi'\cos\Delta + I_z\sin\Delta)] \\ &\times \exp[-i\beta(I_x\cos\phi\cos\Delta + I_y\sin\phi\cos\Delta + I_z\sin\Delta)] \end{aligned} \tag{2.97}$$

The inverse propagator is obtained by reversing the order and making all rotations negative, giving

$$\begin{aligned} U^{-1} = &\exp[i\beta(I_x\cos\phi\cos\Delta + I_y\sin\phi\cos\Delta + I_z\sin\Delta)] \\ &\times \exp[i\beta'(I_x\cos\phi'\cos\Delta + I_y\sin\phi'\cos\Delta + I_z\sin\Delta)] \\ &\times \exp[i\beta(I_x\cos\phi\cos\Delta + I_y\sin\phi\cos\Delta + I_z\sin\Delta)] \end{aligned} \tag{2.98}$$

If the overall rotation axis of U lies in the xy-plane, then a 180° (or π) rotation of U^{-1} about z should give U:

$$\begin{aligned} \exp(-i\pi I_z)\,U^{-1}\exp(i\pi I_z) = &\exp[-i\beta(I_x\cos\phi\cos\Delta + I_y\sin\phi\cos\Delta - I_z\sin\Delta)] \\ &\times \exp[-i\beta'(I_x\cos\phi'\cos\Delta + I_y\sin\phi'\cos\Delta - I_z\sin\Delta)] \\ &\times \exp[-i\beta(I_x\cos\phi\cos\Delta + I_y\sin\phi\cos\Delta - I_z\sin\Delta)] \end{aligned} \tag{2.99}$$

Equation 2.99 is only equal to U if $\Delta = 0$, that is, if the pulses are applied on-resonance. There are no particular constraints on the rotation axis for an off-resonance symmetric composite pulse. This result can be extended to symmetric pulses of any number of elements, N.

2.10.2 Antisymmetric composite pulses

We will now prove that an antisymmetric composite pulse with a base phase $\phi = 0$ has an overall rotation axis constrained to the xz-plane both on- and off-resonance. The propagator U for an antisymmetric sequence of three off-resonance rotations,

1. β about an axis with phase ϕ in xy-plane and tilted up towards the z-axis by Δ
2. β' about an axis with phase ϕ' in xz-plane and tilted up from the x-axis towards the z-axis by Δ

3. β about an axis with phase $-\phi$ in xy-plane and tilted up towards the z-axis by Δ

is given by

$$\begin{aligned} U = &\exp[-i\beta(I_x\cos\phi\cos\Delta - I_y\sin\phi\cos\Delta + I_z\sin\Delta)] \\ &\times \exp[-i\beta'(I_x\cos\phi\Delta + I_z\sin\Delta)] \\ &\times \exp[-i\beta(I_x\cos\phi\cos\Delta + I_y\sin\phi\cos\Delta + I_z\sin\Delta)] \end{aligned} \tag{2.100}$$

The inverse propagator is

$$\begin{aligned} U^{-1} = &\exp[i\beta(I_x\cos\phi\cos\Delta + I_y\sin\phi\cos\Delta + I_z\sin\Delta)] \\ &\times \exp[i\beta'(I_x\cos\phi\Delta + I_z\sin\Delta)] \\ &\times \exp[i\beta(I_x\cos\phi\cos\Delta - I_y\sin\phi\cos\Delta + I_z\sin\Delta)] \end{aligned} \tag{2.101}$$

A 180° rotation of U^{-1} about y should give U if the rotation axes of U and U^{-1} lies in the xz-plane:

$$\begin{aligned} \exp(-i\pi I_z)\,U^{-1}\exp(i\pi I_z) = &\exp[-i\beta(I_x\cos\phi\cos\Delta - I_y\sin\phi\cos\Delta + I_z\sin\Delta)] \\ &\times \exp[-i\beta'(I_x\cos\phi\Delta + I_z\sin\Delta)] \\ &\times \exp[-i\beta(I_x\cos\phi\cos\Delta + I_y\sin\phi\cos\Delta + I_z\sin\Delta)] \end{aligned} \tag{2.102}$$

Thus all antisymmetric composite pulses with a base phase $\phi_0 = 0°$ have an overall rotation axis that lies in the xz-plane for all resonance offsets. Since Exorcycle can correct for problems with the spin-echo phase that arise from errors in the overall flip angle or deviations of the rotation axis in the xz-plane, it is clear that an antisymmetric pulse should be used to compensate for refocusing pulse imperfections in a spin-echo experiment.

2.10.3 Analysis using quaternions

The overall rotation axes and flip angles of a composite pulse can be determined using the quaternion formalism, outlined in Appendix C, as set out by Counsell et al. [70]. These have been plotted as a function of normalised B_1 field strength, B_1/B_1^{nom}, and normalised offset, $\Delta B/B_1^{\text{nom}}$, for a number of composite pulses shown in Table 2.3. The

TABLE 2.3: Broadband composite pulses used in simulations in Figure 2.10 and 2.11

Pulse	Sequence	Type	Reference
LF	$90^\circ_{0^\circ}\ 180^\circ_{90^\circ}\ 90^\circ_{0^\circ}$	Sym	[50, 51]
TS	$180^\circ_{120^\circ}\ 180^\circ_{240^\circ}\ 180^\circ_{120^\circ}$	Sym	[56, 71]
BB_1	$180^\circ_{104.5^\circ}\ 360^\circ_{313.4^\circ}\ 180^\circ_{104.5^\circ}\ 180^\circ_{0^\circ}$	Asym	[49]
F_1	$180^\circ_{46.6^\circ}\ 180^\circ_{255.5^\circ}\ 180^\circ_{0^\circ}\ 180^\circ_{104.5^\circ}\ 180^\circ_{313.4^\circ}$	Anti	[62]
TPG	$180^\circ_{256^\circ}\ 180^\circ_{52^\circ}\ 180^\circ_{0^\circ}\ 180^\circ_{128^\circ}\ 180^\circ_{0^\circ}\ 180^\circ_{232^\circ}\ 180^\circ_{0^\circ}\ 180^\circ_{308^\circ}\ 180^\circ_{104^\circ}$	Anti	[60]
OW	$180^\circ_{53^\circ}\ 180^\circ_{30^\circ}\ 180^\circ_{304^\circ}\ 180^\circ_{142^\circ}\ 180^\circ_{255^\circ}\ 180^\circ_{309^\circ}\ 180^\circ_{0^\circ}\ 180^\circ_{51^\circ}\ 180^\circ_{105^\circ}\ 180^\circ_{218^\circ}\ 180^\circ_{56^\circ}\ 180^\circ_{330^\circ}\ 180^\circ_{307^\circ}$	Anti	[3]
LT	$90^\circ_{135^\circ}\ 270^\circ_{45^\circ}\ 90^\circ_{135^\circ}$	Sym	[50, 51, 56]
W	$90^\circ_{0^\circ}\ 270^\circ_{45^\circ}\ 360^\circ_{0^\circ}$	Asym	[72]
SP	$60^\circ_{180^\circ}\ 300^\circ_{0^\circ}\ 60^\circ_{180^\circ}$	Anti + Sym	[69]

rotation axes are defined by ϕ, the angle of the axis measured in the xy plane away from the x-axis, and θ, the angle of the rotation axis from the z-axis towards the x-axis. The overall flip angle is given by β.

The results for two symmetric sequences which compensate for B_1 inhomogeneity, LF and TS, are plotted in Figure 2.10. Although achieving a flip angle of 180° over a greater bandwidth than a simple pulse, both of these pulses show variation in ϕ in the presence of a B_1 error as the rotation axis rotates in the xy-plane. BB_1, which is an asymmetric phase-distortionless pulse, has proved popular owing to its greater bandwidth and stable rotation axis [63]. In these plots it is clear to see that the overall rotation axis remains along the x-axis across its usable bandwidth. However, both ϕ and θ vary as the B_1 error increases further. All of these composite pulses will reintroduce phase distortions in a spin-echo experiment, as Exorcycle is unable to correct for problems arising from variations in ϕ.

The antisymmetric sequences F_1, TPG and OW, in contrast, only show variation in θ but not ϕ as their overall rotation axes are confined to the xz-plane. These provide excellent compensation for B_1 inhomogeneity and can be used to successfully with Exorcycle phase cycling in a spin-echo experiment.

The composite pulses W, LT and SP were designed to compensate for off-resonance effects. Their overall flip angles and rotation axes as a function of $\Delta B/B_1^{\text{nom}}$ can be

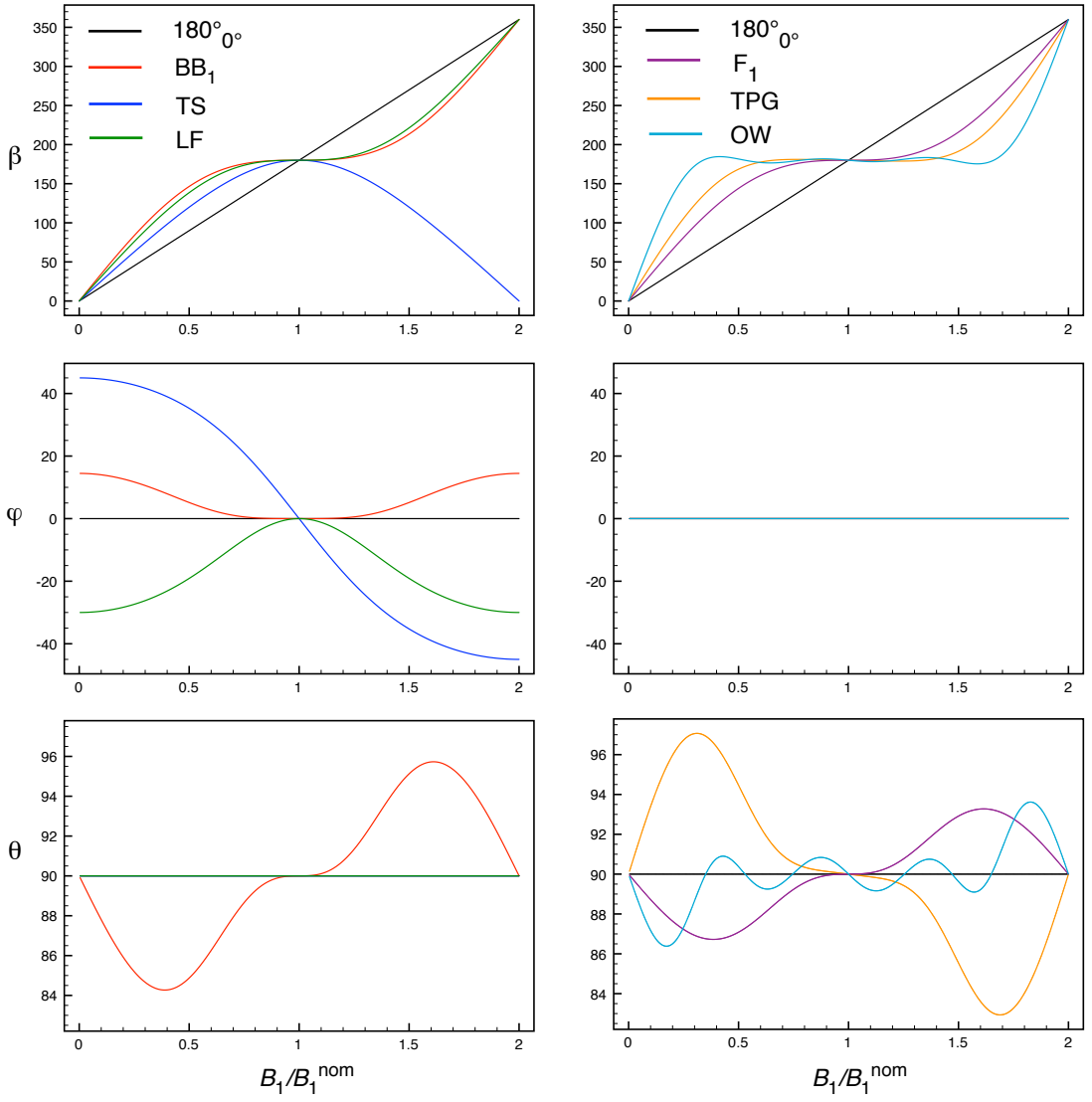

FIGURE 2.10: Overall flip angle (β) and rotation axes plotted as a function of normalised B_1 field strength, B_1 / B_1^{nom}. The rotation axes are defined by ϕ, the angle of the axis measured in the xy plane away from the x-axis, and θ, the angle of the rotation axis from the z-axis towards the x-axis. The pulse sequences can be found in Table 2.3.

found in Figure 2.11. LT can be described as a symmetric phase-distortionless pulse, as its rotation axis remains along the rotating-frame x-axis across a certain bandwidth. W is an asymmetric pulse, and although it has a favourable bandwidth evident in the plot showing overall flip angle, β, the angle ϕ deviates from 0° as the offset changes. SP is a symmetric as well as an antisymmetric sequence and shows the favourable property of having its rotation axis confined to the xz-plane only.

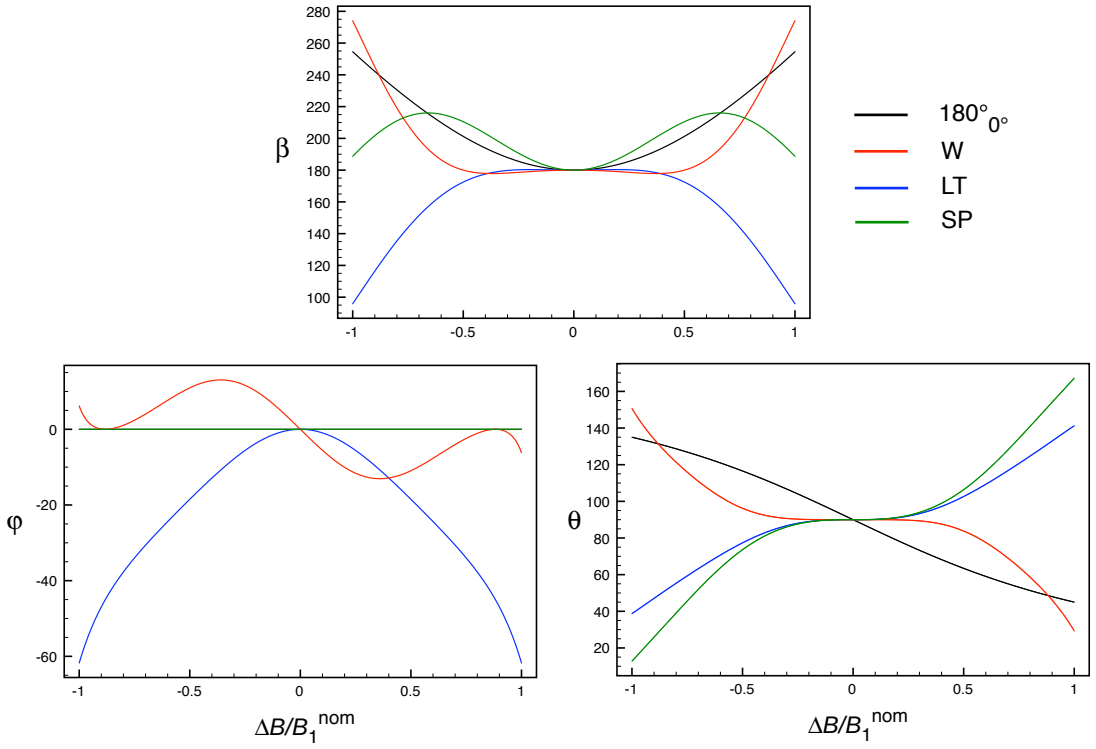

FIGURE 2.11: Overall flip angle (β) and rotation axes plotted as a function of normalised offset, $\Delta B/B_1^{\text{nom}}$. The rotation axes are defined by ϕ, the angle of the axis measured in the xy plane away from the x-axis, and θ, the angle of the rotation axis from the z-axis towards the x-axis. The pulse sequences can be found in Table 2.3.

2.10.4 Multiple refocusing

It should be mentioned that it is possible to use an on-resonance symmetric broadband composite 180° pulse to form a spin echo with perfect phase as long as one forms two consecutive spin echoes with the same composite pulse. In this case, any error in the spin-echo phase caused by the first composite pulse will be automatically corrected by the second. Levitt and Freeman have discussed this in the context of a multiple-echo train formed with the composite pulse LF, where there is correction of the magnetisation phase on even-numbered echoes [73]. However, this self-correction breaks down off resonance where the composite pulse is no longer a rotation in the xy plane.

Hwang and Shaka have shown that the second spin echo formed by any refocusing element – symmetric, antisymmetric or asymmetric – has perfect phase as long as the coherence pathway is selected independently for each of the two identical refocusing elements. This result applies both on and off resonance. They have named this observation "excitation sculpting" [74].

However, neither of these important results is relevant in the present context; if one wishes to correct for pulse imperfections in a simple spin-echo experiment then one should not double the possible sources of imperfection by using two refocusing pulses.

Chapter 3

Background suppression in ^{1}H MAS NMR

3.1 Introduction

3.1.1 The ^{1}H background problem and solutions

^{1}H experiments have long been crucial in solution-state NMR owing to the high sensitivity and high natural abundance of the nucleus, as well as its ubiquitous presence in organic compounds. The importance of ^{1}H NMR of solids has also grown as developments in methodology, spectrometer hardware and probe designs have enabled the possibility of recording high-resolution spectra. Overcoming the strong homogeneous dipolar interactions in a proton-rich sample which lead to broad, featureless spectra has been the main challenge of solid-state ^{1}H NMR. Various approaches have been used to achieve this – rapid MAS, effective decoupling techniques, sophisticated two-dimensional experiments and isotopic dilution of samples with deuterium have all proved useful strategies to enhancing resolution [75–81].

An additional common problem encountered in ^{1}H MAS NMR spectra is the presence of a significant broad "background" signal, which arises from protons located outside the rotor. These background protons are found either as water on surfaces of the static components of the probehead (i.e., on the stator block) or are protons present within the materials used in the probehead construction (e.g., glues and capacitors). The signal

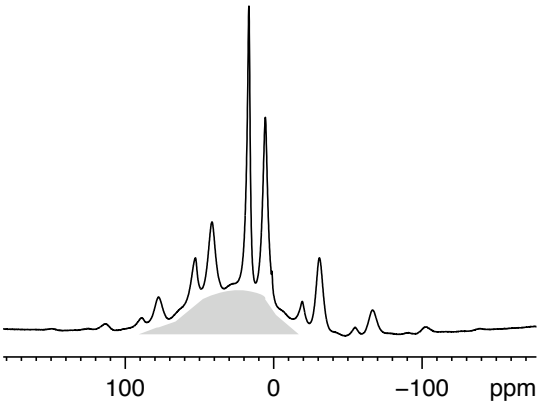

FIGURE 3.1: ^{1}H MAS NMR spectrum of deuterated oxalic acid dihydrate obtained with a simple 90° excitation pulse (14,286 Hz MAS rate, 90° pulse duration of 2.1 μs.)

from these protons can overlap and obscure signals from the sample, and is particularly problematic when studying samples with a low ^{1}H concentration, such as nominally perdeuterated biological or inorganic materials.

Figure 3.1 shows a typical example of such a spectrum blighted by a strong background signal. The sample used was nominally perdeuterated oxalic acid dihydrate, which gives rise two signals in the spectrum: carboxylic acid protons at 17 ppm and water protons at 6 ppm. Spinning sidebands are observed, separated by the MAS frequency of 14.3 kHz. The background protons give rise to a broad, unsightly hump of a signal, highlighted in grey.

A number of methods exist for removing this background signal. An obvious method involves recording two spectra – one of the sample, and a second of an empty probe-head, and then mathematically subtracting the background spectrum. However, since the presence of the sample alters the electronic properties of the resonance circuit, the two spectra will need separate phasing and arbitrary scaling. As pointed out by Chen et. al. [82], in many cases it is difficult to distinguish the background signal from broad signals from the sample, and errors can be made in removing the desired signal as well as the background. In addition, this method is time-consuming as two spectra with roughly equal signal-to-noise ratios must be recorded instead of one.

Recently, several new methods have been suggested for background suppression. Chen

and coworkers' technique is based on the the fact that, being far from the coil, the effective flip angle for background protons is small and the excitation regime is approximately linear [82]. They proposed acquiring two spectra with different pulse lengths (e.g., 90° and 180°) separated by the relaxation delay. The second spectrum will contain only the background signal but with an intensity greater by a factor of two. Halving the intensity of the second spectrum and subtracting it from the first yields a background-free spectrum. Jaeger and Hemman [83] suggested an approach named Elimination of Artefacts in NMR Spectroscopy (EASY), also based on the fact that the background spins have a much smaller flip angle than the sample. Following a 90° pulse exciting both the sample and background spins (first transient), a second 90° pulse is applied immediately after the complete T_2 decay of the FID (second transient). Provided that T_1 is longer than T_2, the second transient contains only the background signal, which can be subtracted using phase cycling.

One of the most popular and well-known approaches for ^{1}H background suppression is the Depth pulse sequence. Originally developed for in vivo NMR spectroscopy using surface coils, the Depth sequence excites a spatially localised signal by exploiting the variation in B_1 field strength with distance of spins from the rf coil [84–86]. The sequence was first applied to the problem of background suppression in ^{1}H MAS NMR by Cory and Ritchey, who used a 90° pulse followed by two 180° pulses phase cycled according to the Exorcycle scheme [26, 46]. As described in Section 2.8.1, Exorcycle suppresses signal associated with imperfect 180° pulses and the selected signal has a strong dependence on the flip angle, β [87, 88]. For a pulse sequence with initial pulse β followed by N refocusing pulses 2β, the overall dependence of the the signal on the flip angle is given by

$$\sin^{2N+1}\beta \tag{3.1}$$

With Cory and Ritchey's method, signal is only acquired with full intensity from spins in the centre of the rf coil, where the the B_1 field has its nominal value, while background spins, which experience a very weak B_1 field are not detected.

White and coworkers have proposed a background suppression method for MAS NMR based on the same principle as Cory and Ritchey [89]. Instead of using Exorcycle to achieve spatial localisation of the signal, they employed a narrowband composite 90°

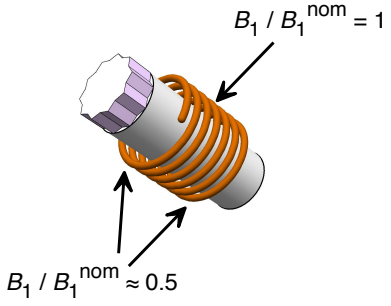

FIGURE 3.2: The B_1 field created by a solenoid drops to approximately half its nominal value at each end of the coil. As a result, spins in the sample will experience a range of radiofrequency field strengths depending on their position in the rotor.

pulse, $90^\circ_{0^\circ}\ 90^\circ_{90^\circ}\ 90^\circ_{180^\circ}\ 90^\circ_{270^\circ}$, that had been used earlier to eliminate unwanted signals in solution-state NMR spectra [90]. Feng and Reimer suggested a modification to Cory and Ritchey's implentation of Depth, employing a long initial excitation pulse instead of a 90° pulse. This results in dephasing of the background coherences and extends the applicability of the Depth sequence to situations where the difference in B_1 field strength between the inside and outside of the coil is small.

3.1.2 Radiofrequency inhomogeneity effects on the Depth sequence

One drawback of the Cory-Ritchey Depth sequence is that, compared with a conventional 90° aquisition, there is a significant decrease in the desired signal intensity of the sample spins. This occurs as a result of the sequence being *too* spatially selective. If we consider the B_1 field generated along the axis of a solenoidal coil, we find that the B_1 field drops to about half of its nominal value at each end of the coil [91, 92] as illustrated in Figure 3.2. Since the rotor is longer than the coil, it is clear that there will be a range of flip angles across the sample and signal will only be selected from the centre of the rotor. If $\beta = 90^\circ$ in the centre of the sample, then at the end of the coil $\beta = 45^\circ$. From Equation 3.1, $\sin^5\beta = 0.18$ with $\beta = 45^\circ$, and so theoretically only 18% of the maximum possible amplitude of the magnetisation will be excited at the end of the coil in the $N = 2$ Cory-Ritchey Depth sequence.

We have seen in Section 2.9 that composite pulses are able to compensate for the effects of B_1 inhomogeneity. In this Chapter we will explore the applicability of composite pulses to the Depth sequence to improve the method for background suppression in ^1H

MAS NMR. Passband pulses seem to offer the most suitable B_1 response for this particular problem. They are locally narrowband around $B_1 \approx 0$, thus will excite little signal from the background, and locally broadband for $B_1 \approx B_1^{\text{nom}}$, helping to excite spins within the region of coil. With the features of a narrowband pulse, it is possible that better suppression of the background signal could be achieved with a single composite 180° pulse compared with the simple $N = 2$ Depth sequence.

3.1.3 Refocusing pulse symmetry

In the Cory-Ritchey Depth pulse sequence, the refocusing pulses are simple 180° pulses. The rotation axis of a $180^\circ_{0^\circ}$ pulse is along the x-axis when on resonance, while off resonance the axis deviates from the x-axis yet remains in the xz plane. If the flip angle of the refocusing pulse deviates from 180° or the rotation axis deviates away from the x-axis, a phase error will be introduced into the spin-echo signal. As described in Section 2.8, selection of the coherence transfer pathway with Exorcycle phase cycling cancels this phase error and a spin-echo signal with perfect phase is obtained.

It is important that the phase of the NMR signal remains undistorted if an acceptable spectrum is to be obtained. For this reason, it is vital to consider the symmetry of the composite refocusing pulses to be used in the Depth sequence. In Section 2.10 it was demonstrated that symmetric composite pulses have overall rotation axes that deviate in the xy plane as a function of B_1 and offset, while those of asymmetric composite pulses are not constrained to lie in any particular plane of the rotating frame. A phase error will be reintroduced in the spin-echo signal by such pulses, even if Exorcycle is implemented. As we are aiming to achieve satisfactory background suppression using just a single refocusing pulse, the multiple refocusing method described in Section 2.10.4 is not an option for removing phase errors. An antisymmetric pulse must therefore be used, as Exorcycle is able to remove phase errors arising from deviations of the overall rotation axis in the xz-plane [3, 4].

3.2 Passband composite pulses

3.2.1 Existing passband composite pulses

A number of passband 90° and 180° composite pulses have been published. Wimperis designed several composite 90° pulses using average Hamiltonian theory [49, 93], including the sequences

$$\mathrm{R}_1 = 360^\circ_{262.8^\circ}\ 360^\circ_{97.2^\circ}\ 90^\circ_{0^\circ} \tag{3.2}$$

$$\mathrm{PB}_1(90^\circ) = 360^\circ_{93.6^\circ}\ 720^\circ_{266.4^\circ}\ 360^\circ_{93.6^\circ}\ 90^\circ_{0^\circ} \tag{3.3}$$

These pulses have similar passband excitation profiles when used on an initial state of z magnetisation. They differ when used on an initial state of transverse y magnetisation, with the longer sequence $\mathrm{PB}_1(90^\circ)$ providing better phase behaviour. Since we shall be applying this sequence as an excitation pulse at the start of the Depth sequence, the shorter sequence R_1 will be used.

Passband composite 180° pulses have been designed by Cho et al. [94, 95], which we designate with the names Cho-7 and Cho-9 according to the length of the sequences:

$$\text{Cho-7} = 180^\circ_{285^\circ}\ 180^\circ_{195^\circ}\ 180^\circ_{45^\circ}\ 180^\circ_{90^\circ}\ 180^\circ_{45^\circ}\ 180^\circ_{195^\circ}\ 180^\circ_{285^\circ} \tag{3.4}$$

$$\text{Cho-9} = 180^\circ_{90^\circ}\ 180^\circ_{105^\circ}\ 180^\circ_{270^\circ}\ 180^\circ_{255^\circ}\ 180^\circ_{0^\circ}\ 180^\circ_{255^\circ}\ 180^\circ_{270^\circ}\ 180^\circ_{105^\circ}\ 180^\circ_{90^\circ} \tag{3.5}$$

Wimperis has introduced several sequences [49, 93], including

$$\mathrm{T}_1 = 360^\circ_{255.5^\circ}\ 360^\circ_{104.5^\circ}\ 180^\circ_{0^\circ} \tag{3.6}$$

$$\mathrm{PB}_1(180^\circ) = 360^\circ_{97.2^\circ}\ 720^\circ_{262.8^\circ}\ 360^\circ_{97.2^\circ}\ 180^\circ_{0^\circ} \tag{3.7}$$

However, these passband 180° pulses are all either symmetric (Equations 3.4 and 3.5) or asymmetric (Equations 3.6 and 3.7), making them unsuitable for refocusing transverse magnetisation without producing a phase error. This motivated the search for passband 180° composite pulses with antisymmetric phases schemes.

3.2.2 Novel passband composite pulses

Several methods have been used to derive novel passband refocusing pulses [4]. If we take an asymmetric 90° composite pulse, and append to it a time-reversed version of itself with phases that are mirrored about the x-axis, we obtain an antisymmetric 180° pulse. For example, if R_1 (Equation 3.2) is time-reversed and mirrored, we get $90^\circ_{0^\circ}\ 360^\circ_{262.8^\circ}\ 360^\circ_{97.2^\circ}$. Appending this altered sequence to R_1 gives the new passband 180° pulse,

$$\mathrm{APB}_1 = 360^\circ_{262.8^\circ}\ 360^\circ_{97.2^\circ}\ 180^\circ_{0^\circ}\ 360^\circ_{262.8^\circ}\ 360^\circ_{97.2^\circ} \tag{3.8}$$

Alternatively, we can derive an antisymmetric 180° composite pulse from a symmetric 180° sequence. Using Equation 6 from Reference [62],

$$\phi'_j = -(-1)^j\phi_j - \sum_{k=1}^{j-1}(-1)^k 2\phi_k \tag{3.9}$$

we can convert the symmetric phase scheme of Cho-7 (Equation 3.4) into the antisymmetric "toggling frame" (see Section 4.2.1) phase scheme to give,

$$\mathrm{APB}_2 = 180^\circ_{105^\circ}\ 180^\circ_{195^\circ}\ 180^\circ_{45^\circ}\ 180^\circ_{0^\circ}\ 180^\circ_{315^\circ}\ 180^\circ_{165^\circ}\ 180^\circ_{255^\circ} \tag{3.10}$$

Finally, noting that a sequence consisting of an odd number of 180° pulses with a central pulse of $180^\circ_{0^\circ}$ will produce an overall $180^\circ_{0^\circ}$ composite pulse, we can conduct a numerical search using a simple computer program to find a sequence of pulses that most closely matches a target function which is passband with respect to the B_1 field. Source code in Fortran for the computer program used can be found in Appendix D. The target function can be defined to search for pulses of different bandwidths, but the closeness of the best match found can be limited by the number of pulses in the sequence. Searching for a passband pulse with a broader bandwidth than the other sequences presented here, we found it necessary to have a composite pulse composed of seven 180° elements. Using this approach, the following sequence was found

$$\mathrm{APB}_3 = 180^\circ_{192^\circ}\ 180^\circ_{315^\circ}\ 180^\circ_{241^\circ}\ 180^\circ_{0^\circ}\ 180^\circ_{119^\circ}\ 180^\circ_{45^\circ}\ 180^\circ_{168^\circ} \tag{3.11}$$

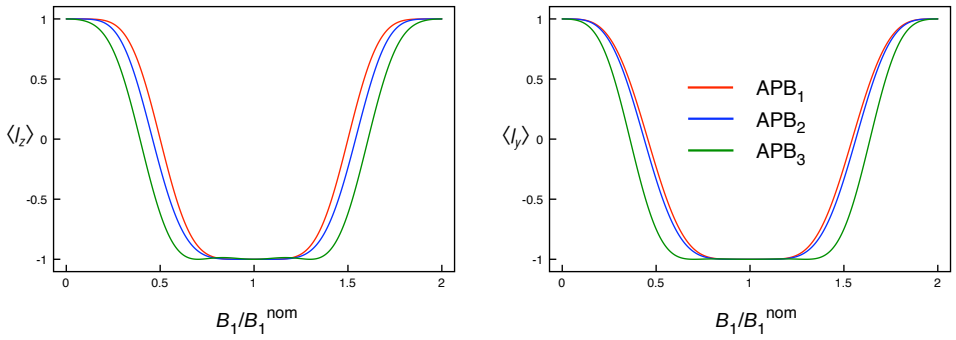

(a) $I_z \rightarrow -I_z$ (b) $I_y \rightarrow -I_y$

FIGURE 3.3: Simulated $I_z \rightarrow -I_z$ and $I_y \rightarrow -I_y$ inversion profiles for the APB$_n$ antisymmetric passband composite pulses as a function of the normalised B_1 field strength, B_1 / B_1^{nom}

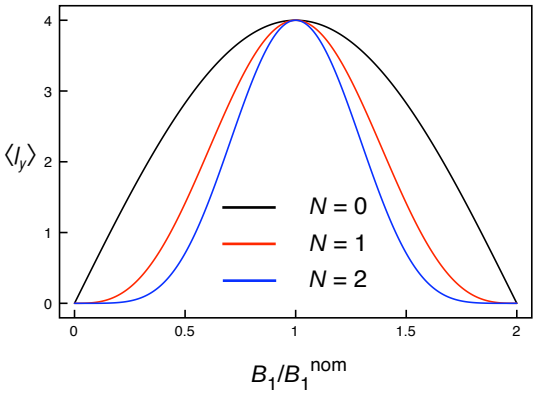

FIGURE 3.4: Simulations of the performance of the original Cory-Ritchie Depth sequence, comprising a 90° pulse followed by N 180° pulses, with each refocusing pulse phase cycled independently according to the Exorcycle scheme. The desired in-phase magnetization component $\langle I_y \rangle = \text{Tr}\{\sigma^{\text{final}} I_y\} / \text{Tr}\{I_y^2\}$ is plotted as a function of the normalised B_1 field strength, B_1 / B_1^{nom} ($\langle I_x \rangle = 0$ for all sequences). Each sequence corresponds to a $4N$-step phase cycle and thus at the nominal field strength the result will be $\sigma^{\text{final}} = 4^N I_y$; the results have been normalised to the $N = 1$ curve to enable comparison of the bandwidth of each sequence.

Figure 3.3 shows the $I_z \rightarrow -I_z$ and $I_y \rightarrow -I_y$ inversion profiles for the three new APB$_n$ antisymmetric passband composite 180° pulses as a function of norrmalised B_1 field strength. APB$_1$ and APB$_2$ have similar bandwidths, while APB$_3$ has been designed to be locally broadband over a wider range of B_1 values than it is locally narrowband.

3.3 Simulations of the Depth sequence

Figure 3.4 shows simulations of the original Cory-Ritchey Depth sequence, comprising a 90° pulse followed by N 180° pulses. An initial state $\sigma^{\text{initial}} = I_z$ was used. The phase of each refocusing pulse was incremented through the four steps of Exorcycle and the resulting magnetisations summed appropriately over the $4N$ steps. The desired in-phase magnetisation component is plotted as a function of the normalised B_1 field strength. Each sequence corresponds to a $4N$-step phase cycle and thus at the nominal field strength the result will be $\sigma_{\text{final}} = 4^N I_y$; here, the results have been normalised to the $N = 1$ result to enable comparison of the bandwidth of each sequence. It can be seen that, with increasing N, the signal becomes more localised to a narrower range of B_1/B_1^{nom}. In particular, although there is little signal excited (as desired) for $B_1/B_1^{\text{nom}} < 0.25$, the $N = 2$ sequence is poor at exciting magnetisation with high amplitude across the range $0.5 \leq B_1/B_1^{\text{nom}} \leq 1.0$, which corresponds to the range of B_1 fields expected to occur within the coil.

The effect of the symmetry of the refocusing pulse on the resultant phase of the magnetisation is shown in Figure 3.5. The performance of various passband composite 180° pulses has been simulated, with an initial state $\sigma^{\text{initial}} = -I_y$ (the magnetisation created by a perfect $90^\circ_{0^\circ}$ pulse on an equilibrium state I_z) and incorporating the Exorcycle phase cycle. The resulting in-phase magnetisation component $\langle I_y \rangle$ and the out-of-phase component $\langle I_x \rangle$ are plotted as a function of normalised field strength B_1/B_1^{nom}.

Figure 3.5(a) shows the I_y and I_x magnetisation created by the symmetric passband sequences Cho-7 and Cho-9, as well as by the asymmetric sequences T_1 and $PB_1(180^\circ)$. The $\langle I_y \rangle$ profiles of the Cho-7, Cho-9 and T_1 sequences are passband over a similar range of B_1/B_1^{nom}. For each of these sequences, little I_x magnetisation is created close to B_1^{nom}, but as the field strength deviates from the nominal value, a significant I_x component results. The passband composite pulse $PB_1(180^\circ)$ shows the best phase behaviour of these sequences, though some out-of-phase magnetisation is still created at B_1 field strengths away from the nominal value. The I_y and I_x profiles of the antisymmetric sequences APB_1, APB_2 and APB_3 as well as for the Cory-Ritchey sequence with $N = 1$ are shown in Figure 3.5(b). It can be seen that even in the presence of B_1 inhomogeneity, these sequences do not create any unwanted out-of-phase I_x magnetisation. These antisymmetric sequences therefore yield ideal phase behaviour and will be most suitable

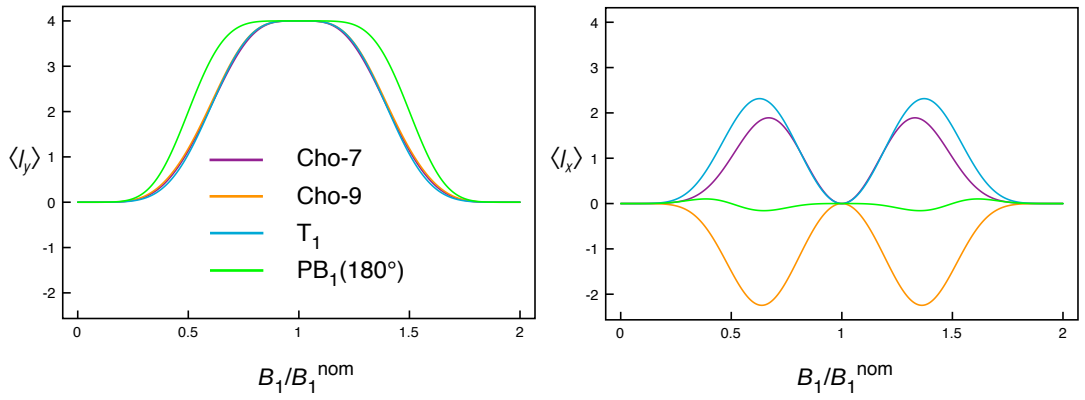

(a) $N = 1$ Depth sequence with symmetric and asymmetric composite pulses.

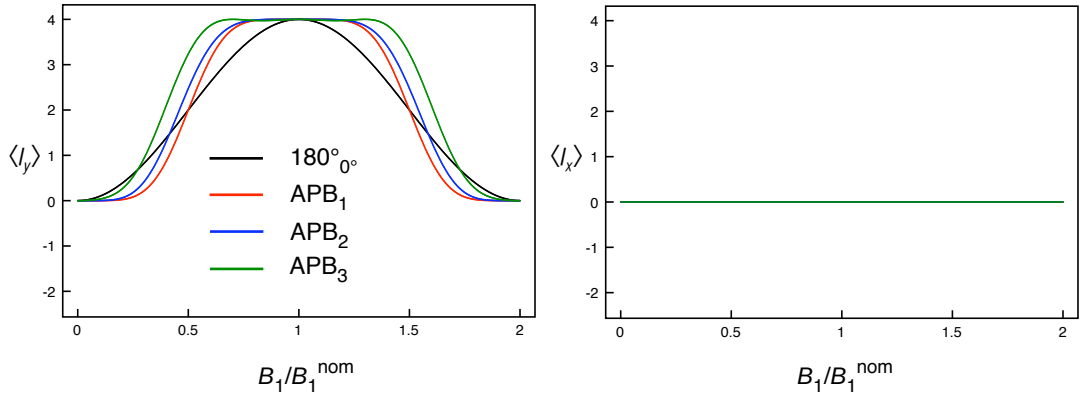

(b) $N = 1$ Depth sequence with antisymmetric composite pulses.

FIGURE 3.5: Simulations showing the effect of the symmetry of a refocusing pulse on the spin-echo phase. The performance of various passband composite 180° pulses as a function of normalised B_1 field strength has been simulated, with an initial state $\sigma^{\text{initial}} = -I_y$ and incorporating Exorcycle.

for background suppression experiments. From this point onwards, we will therefore only consider the antisymmetric passband sequences APB_1, APB_2 and APB_3.

Figure 3.6 shows simulations of the performance of these antisymmetric passband refocusing pulses in an $N = 1$ Depth pulse sequence in combination with a variety of excitation pulses. An initial state $\sigma^{\text{initial}} = I_z$ was used and the Exorcycle phase cycle was followed for the refocusing pulse. Both the $\langle I_y \rangle$ and $\langle I_x \rangle$ profiles are shown as a function of B_1/B_1^{nom}. Figure 3.6(a) shows simulations of the Depth sequence implemented using a simple 90° excitation pulse followed by a single antisymmetric passband refocusing pulse. The use of a simple 180° refocusing pulse (which is both symmetric and antisymmetric) corresponds, of course, to the $N = 1$ Cory-Ritchey sequence. The simulations in Figure 3.6(b) use the passband excitation pulse R_1 (Equation 3.2) , while those

in Figure 3.6(c) use the broadband excitation pulse $\mathrm{BB}_1(90^\circ)$ of Reference [49],

$$\mathrm{BB}_1(90^\circ) = 180^\circ_{97.2^\circ}\ 360^\circ_{291.5^\circ}\ 180^\circ_{97.2^\circ}\ 90^\circ_{0^\circ}. \tag{3.12}$$

The small out-of-phase $\langle I_x \rangle$ magnetization components that appear in Figures 3.6(b) and 3.6(c) arise from the composite excitation pulse used but are of such low amplitude that they are unlikely to cause a problem in experimental practice. It can be seen that the use of antisymmetric passband refocusing pulses in the Depth pulse sequence yields much better excitation of transverse magnetization across the range $0.5 \leq B_1/B_1^{\mathrm{nom}} \leq 1.0$ than the $N = 1$ or $N = 2$ Cory-Ritchey sequence, while still suppressing excitation for low B_1 field strengths, $B_1/B_1^{\mathrm{nom}} \leq 0.25$. In terms of achieving uniform excitation across the range $0.5 \leq B_1/B_1^{\mathrm{nom}} \leq 1.0$, it is worth noting that the use of broadband excitation sequences, as in Figure 3.6(c) , is preferable to the use of passband excitation sequences, as in Figure 3.6(b) .

If the use of a Depth pulse sequence with a single passband composite 180° pulse is to be recommended in preference to the widely used $N = 2$ Cory-Ritchey sequence (with two simple 180° pulses) then it is important to compare the quality of signal suppression at low B_1 field strengths that the methods achieve. Figure 3.7 shows the expectation value of the I_y magnetisation resulting from various Depth sequences plotted on a logarithmic scale for values of B_1/B_1^{nom} up to 0.5. An initial state $\sigma^{\mathrm{initial}} = I_z$ and a simple 90° excitation pulse were used in the simulations. At low nominal field strengths, a single composite APB_1 pulse exceeds the degree of signal suppression achieved by the $N = 2$ Cory-Ritchey sequence by one or two orders of magnitude. A single APB_2 composite pulse results in a similar degree of suppression to the $N = 2$ Cory-Ritchey sequence, while the APB_3 is approximately two orders of magnitude less effective, although it still achieves better suppression than the $N = 1$ Cory-Ritchey sequence.

Passband 180° pulses are known to be highly sensitive to the presence of a resonance offset, Ω [49, 93, 95]. However, off-resonance effects are unlikely to be significant in ^{1}H MAS NMR as we can expect that the ^{1}H nutation frequency will be large, maybe 100-200 kHz, and the ^{1}H spectral range fairly small, maybe 10-15 kHz at most (in diamagnetic solids), even at the highest B_0 field strengths. The off-resonance behaviour of the new passband Depth sequences is investigated in Figure 3.8 where the $\langle I_{xy} \rangle = (\langle I_x \rangle + \langle I_y \rangle)^{1/2}$ profiles have been simulated with offset parameters $\Delta B/B_1^{\mathrm{nom}}$ of $-0.05, 0$ and

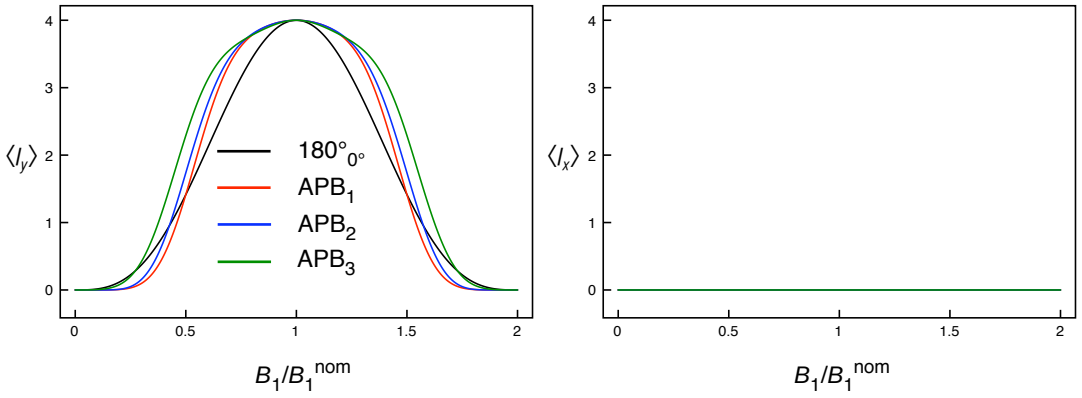

(a) $N = 1$ Depth sequence with simple 90° excitation pulse.

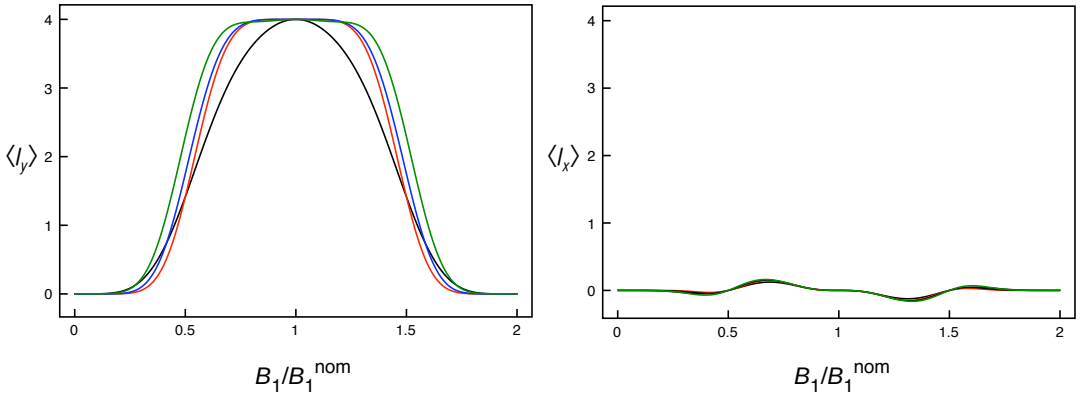

(b) $N = 1$ Depth sequence with passband 90° excitation pulse.

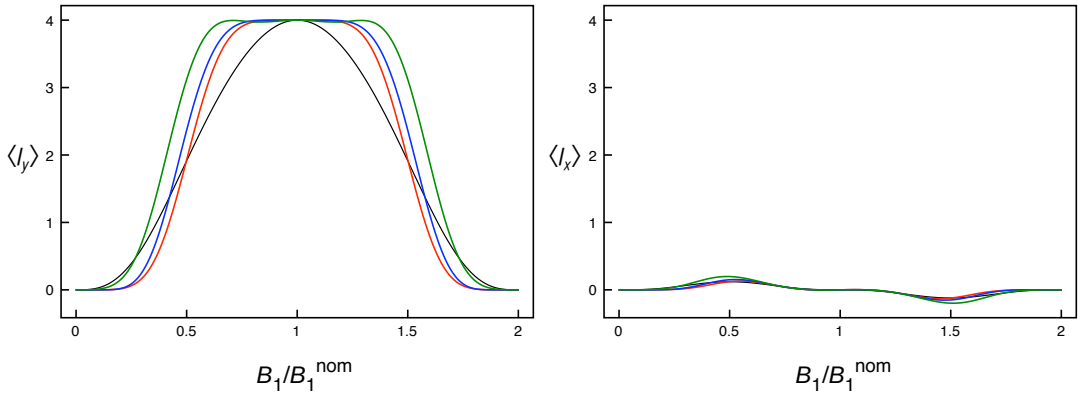

(c) $N = 1$ Depth sequence with broadband 90° excitation pulse.

FIGURE 3.6: Simulations of the performance of the antisymmetric APB$_n$ passband refocusing pulses in a Depth pulse sequence when used in combination with different types of excitation pulses: a simple 90° pulse, the passband pulse R$_1$ (Equation 3.2) and the broadband pulse BB$_1$(90°) (Equation 3.12) with an initial state $\sigma^{\text{initial}} = I_z$ and incorporating Exorcycle.

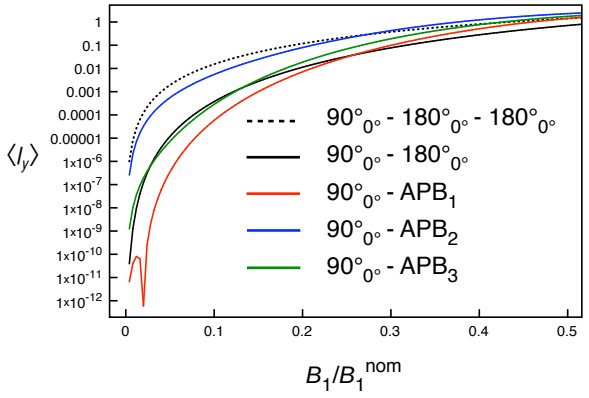

FIGURE 3.7: The expectation value of the I_y magnetisation resulting from various depth sequences plotted on a logarithmic scale for values of B_1/B_1^{nom} up to 0.5. An initial state $\sigma^{\text{initial}} = I_z$ and a simple 90° excitation pulse were used.

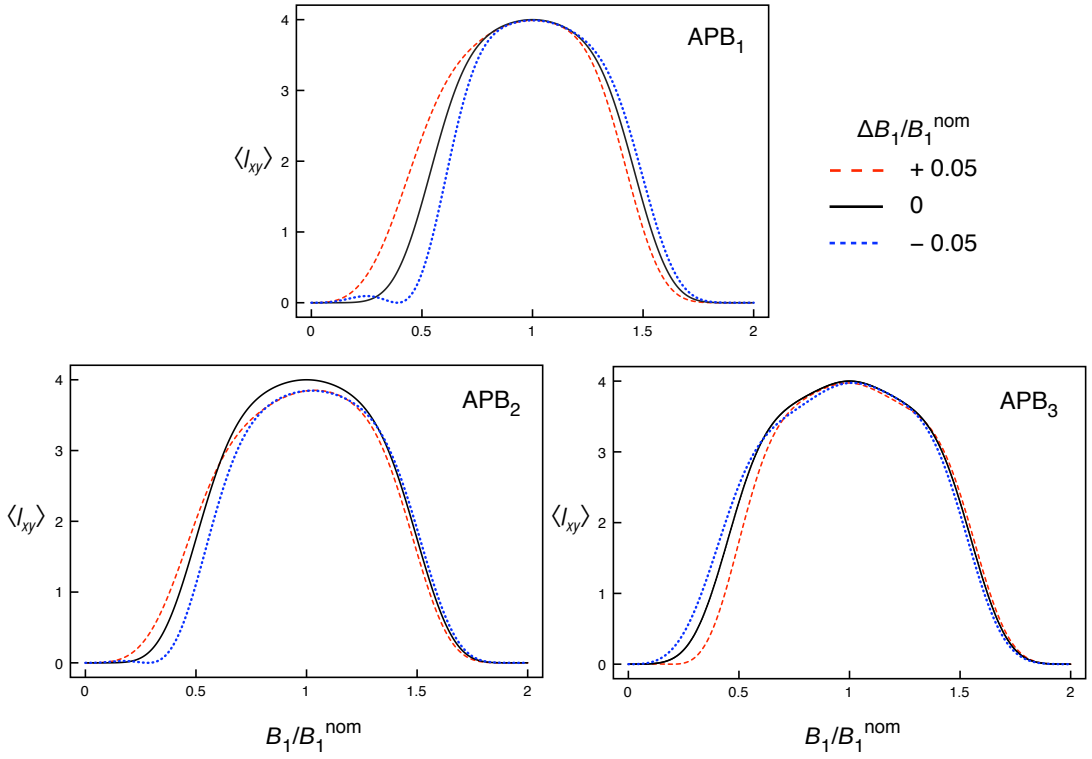

FIGURE 3.8: The expectation value of the I_{xy} magnetisation in a Depth sequence as a function of B_1/B_1^{nom}. The simulations have been carried out at resonance offsets corresponding to offset parameters of $\Delta B/B_1^{\text{nom}}$ of $-0.05, 0$ and $+0.05$, where $\Delta B = -\Omega/\gamma$. An initial state $\sigma^{\text{initial}} = I_z$ and a simple 90° excitation pulse were used.

$+0.05$, where $\Delta B = -\Omega\gamma$. An initial state $\sigma^{\text{initial}} = I_z$ and a simple 90° excitation pulse were used in the simulations. All three Depth sequences hold their passband character well across this small range of offsets, with perhaps the sequence based on the composite pulse APB_3 providing the best off-resonance performance.

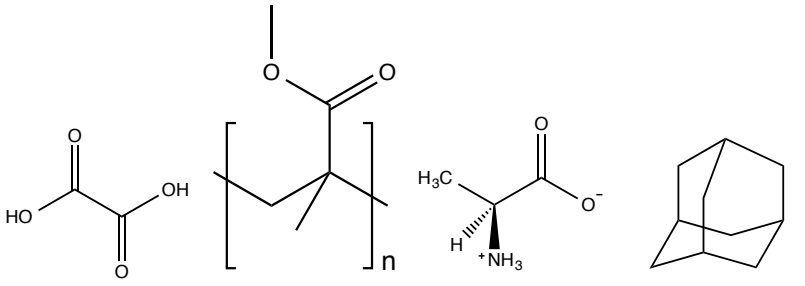

(a) Oxalic acid (b) PMMA (c) L-alanine (d) Adamantane

FIGURE 3.9: Molecular structures of the compounds used in the experimental parts of this Chapter. Nominally perdeuterated forms of oxalic acid dihydrate and PMMA were used to reduce the dipolar broadening seen in the spectra.

3.4 Experiments

Experiments were performed on either a Bruker Avance 400 MHz spectrometer equipped with a widebore 9.4 T magnet and a 4-mm MAS probe or a Bruker Avance III 600 MHz spectrometer equipped with a widebore 14.1 T magnet and a 2.5-mm MAS probe. Alanine, nominally perdeuterated poly(methyl methacrylate) (PMMA) and nominally perdeuterated oxalic acid dihydrate were chosen for study; the low ^{1}H concentrations in the PMMA (1% relative abundance) and oxalic acid dihydrate (4% relative abundance) result in a very noticeable background signal in their ^{1}H MAS NMR spectra, arising from protons present in the probe. Figure 3.9 shows the molecular structure of all the compounds used in this Chapter. On the 4-mm probe at 400 MHz, the calibrated 90° pulse length for ^{1}H was 2.1 μs, corresponding to a nutation frequency, $\nu_1 = |\gamma B_1|/2\pi$ of 120 kHz. On the 2.5-mm probe at 600 MHz, the calibrated 90° pulse duration was found to be 1.65 μs, indicating a radiofrequency field strength of 150 kHz.

For the $N = 2$ Cory-Ritchey depth sequence, the 16-step phase cycle given in Reference [87] was used. In our other Depth sequences, based on a single spin echo, another 16-step phase cycle was used, comprising a 4-step Exorcycle nested with the 4-step CYCLOPS. This gives the 16-step phase cycle shown in Table 3.1.

Figure 3.10 shows ^{1}H MAS NMR spectra of nominally perdeuterated oxalic acid dihydrate, recorded at a MAS rate of 14286 Hz. The water protons have a 6 ppm and the carboxylic acid protons a 17 ppm chemical shift. The spectrum recorded with a simple 90° pulse (Figure 3.10(a)) shows a distinct broad signal at 25 ppm arising from "background" protons in the probehead. Figure 3.10(b) shows the spectrum resulting from

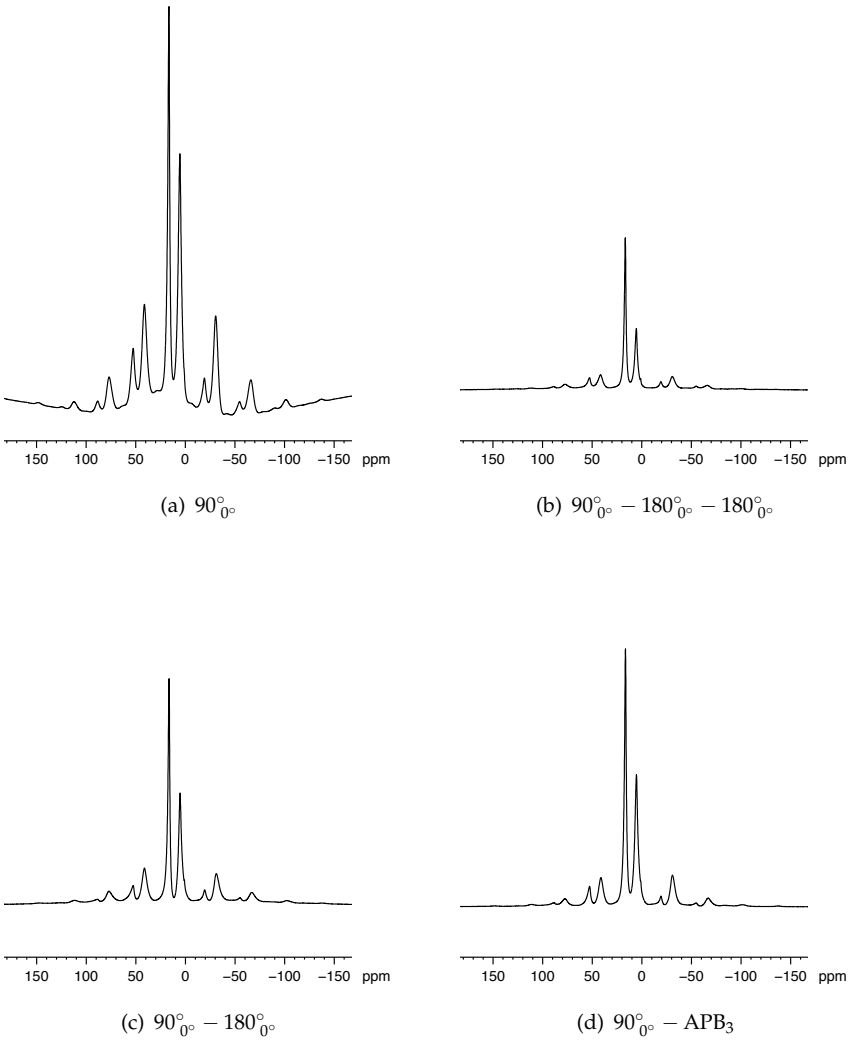

(a) $90^\circ_{0^\circ}$ (b) $90^\circ_{0^\circ} - 180^\circ_{0^\circ} - 180^\circ_{0^\circ}$

(c) $90^\circ_{0^\circ} - 180^\circ_{0^\circ}$ (d) $90^\circ_{0^\circ} - \mathrm{APB}_3$

FIGURE 3.10: ^{1}H (400 MHz) MAS NMR spectra of deuterated oxalic acid (14286 Hz MAS rate, 90° pulse length of 2.1 μs, relaxation interval of 120 s, averaging of 16 transients).

the original Cory-Ritchey Depth sequence with two 180° refocusing pulses ($N = 2$). Although the background signal has been removed effectively with this sequence and the baseline improved (owing to the use of a spin echo), significant loss of signal from the sample has also occurred. By implementing an $N = 1$ Cory-Ritchey Depth sequence (Figure 3.10(c)), a greater amount of signal from the sample can be retained. Figure 3.10(d) shows the spectrum obtained using the Depth sequence with a single passband composite refocusing pulse, APB_3. In addition to the successful removal of the background signal from the spectrum, it can be seen that greater signal is obtained from the oxalic acid dihydrate when compared with Figure 3.10(c). Very similar results to those in Figure 3.10(d) were obtained with Depth sequences incorporating the

TABLE 3.1: The 16-step phase cycling scheme (Exorcycle + CYCLOPS) used for sequences based on a single spin echo. The notation here lists the phases in units of 90° (as used by default by the NMR software) and so $0 = 0°$, $1 = 90°$, $2 = 180°$ and $3 = 270°$.

Excitation pulse	Refocusing pulse	Receiver phase
0 0 0 0 1 1 1 1	0 1 2 3 1 2 3 0	0 2 0 2 1 3 1 3
2 2 2 2 3 3 3 3	2 3 0 1 3 0 1 2	2 0 2 0 3 1 3 1

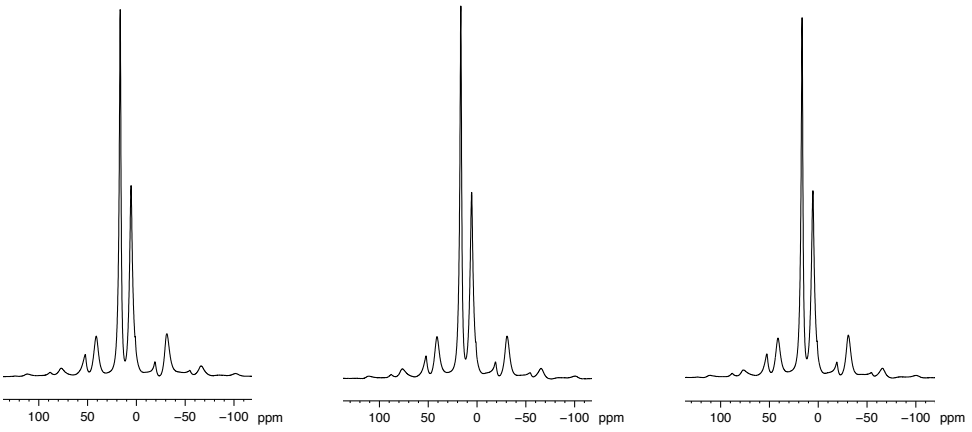

(a) $\Delta B/B_1^{\text{nom}} = 0$ (b) $\Delta B/B_1^{\text{nom}} = +0.05$ (c) $\Delta B/B_1^{\text{nom}} = -0.05$

FIGURE 3.11: ^{1}H (400 MHz) MAS NMR spectra of deuterated oxalic acid (14286 Hz MAS rate, 90° pulse length of 2.1 μs, relaxation interval of 120 s, averaging of 16 transients). Spectra recorded with a Depth sequence of a simple 90° excitation pulse followed by a passband refocusing pulse, APB_1 with transmitter offsets of (a) 0 Hz, (b) +6250 Hz and (c) −6250 Hz.

passband composite pulses APB_1 and APB_2.

The on- and off-resonance performances of the new passband composite pulse Depth sequences are compared in Figure 3.11, where again ^{1}H MAS NMR spectra of nominally perdeuterated oxalic acid dihydrate, recorded at a MAS rate of 14286 Hz, are shown. A Depth sequence with a single composite refocusing pulse, APB_2, was used and yielded an essentially identical result with the transmitter offset in the middle of the two ^{1}H centreband resonances (Figure 3.11(a)) and with the transmitter offset by either +6250 Hz Figure 3.11(b) or −6250 Hz (Figure 3.11). The transmitter offsets used here correspond to the offset parameters $\Delta B/B_1^{\text{nom}} = \pm 0.05$ which were used in the simulations in Figure 3.8, which are typical for ^{1}H NMR. The similarity of the spectra shown here demonstrates the robustness of the composite pulse performance under this range of offsets.

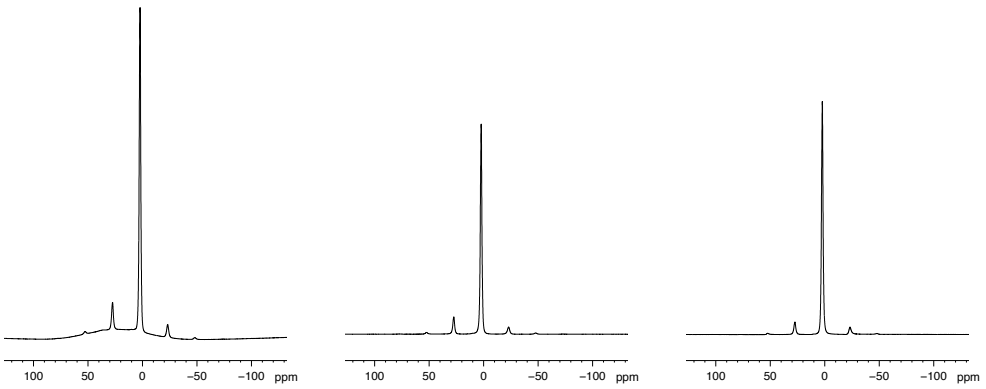

(a) $90^\circ_{0^\circ}$ (b) $90^\circ_{0^\circ} - \mathrm{APB}_1$ (c) $\mathrm{BB}_1(90^\circ) - \mathrm{APB}_1$

FIGURE 3.12: ^{1}H (400 MHz) MAS NMR spectra of deuterated PMMA (14286 Hz MAS rate, 90° pulse length of 2.1 μs, relaxation interval of 120 s, averaging of 16 transients).

Figure 3.12 shows ^{1}H MAS NMR spectra of nominally perdeuterated PMMA, recorded at a MAS rate of 10 kHz. At this B_0 field strength and MAS frequency, only a single unresolved ^{1}H centreband resonance is observed, at a shift of 2.5 ppm, corresponding to the CH_2 and two different CH_3 sites visible in Figure 3.9(b) [96, 97]. The spectrum recorded with a simple 90° pulse (Figure 3.12(a)) shows a distinct broad signal at 25 ppm arising from "background" protons in the probehead. The Depth sequence with a simple 90° excitation pulse followed by the composite refocusing pulse APB_1 was used to record the spectrum shown in Figure 3.12(b), while in Figure 3.12(c) a slightly greater signal was obtained using a sequence comprising the broadband composite 90° pulse $\mathrm{BB}_1(90^\circ)$ as an excitation sequence followed by APB_1 as the refocusing sequence. Both passband composite pulse Depth sequences can be seen to have successfully removed the unwanted background signal.

As an example of ^{1}H MAS at faster spinning rates, Figure 3.13 shows ^{1}H MAS NMR spectra of L-alanine, recorded at a MAS rate of 20 kHz. Figure 3.9(c) shows the molecular structure of L-alanine. Three ^{1}H resonances are resolved: the NH_3 protons give rise to the signal at 8.5 ppm, the CH proton is at 3.8 ppm and the CH_3 protons appear at 1.3 ppm [98–100]. The spectrum recorded with a simple 90° pulse (Figure 3.13(a)) has a poor baseline but shows no immediately apparent sign of any background signal owing to the much higher concentration of ^{1}H spins in this sample. Figure 3.13(b) shows the spectrum resulting from the original $N = 2$ Cory-Ritchey Depth sequence. Although the baseline has been improved (owing to the spin echo), significant loss of signal from the sample has also occurred. Figure 3.13(c) shows the spectrum obtained

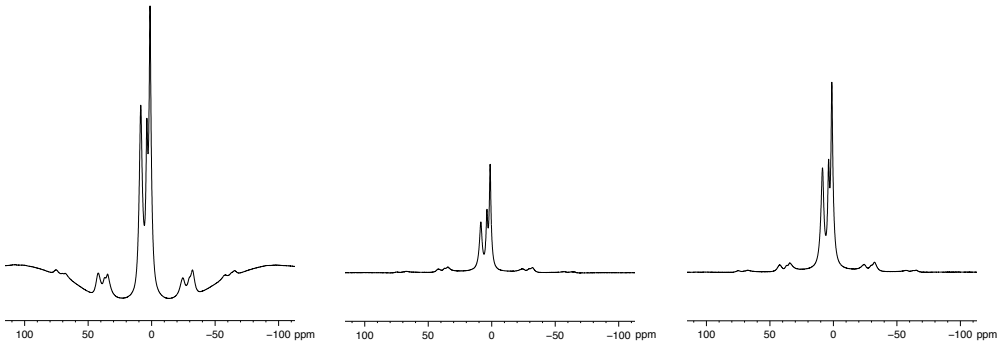

(a) $90^\circ_{0^\circ}$ (b) $90^\circ_{0^\circ} - 180^\circ_{0^\circ} - 180^\circ_{0^\circ}$ (c) $90^\circ_{0^\circ} - \mathrm{APB}_1$

FIGURE 3.13: ^{1}H (600 MHz) MAS NMR spectra of L-alanine (20 kHz MAS rate, 90° pulse length of 1.65 μs, relaxation interval of 3 s, averaging of 16 transients).

using the Depth sequence with a simple 90° excitation pulse and a single passband composite refocusing pulse APB_1. It can be seen that much greater signal is obtained when compared with Figure 3.13(b).

3.5 Imaging of the B_1 distribution and background signal in a MAS probehead

To gain insight into the actual B_1 distribution and origin of the background signal, a two-dimensional correlation experiment employing inhomogeneous B_0 and B_1 fields can be used [5]. The experiment allows the range of B_1 fields across the sample to measured, as well as across the background spins, so that any overlap between the two distributions can be judged. By using the room-temperature shim coils to generate a linear z gradient in the B_0 field, the experiment can be performed on any NMR spectrometer and MAS probehead. The method can also be combined with Depth pulse techniques for background suppression, allowing their performance to be more rigorously evaluated.

3.5.1 B_0 and B_1 correlation on a MAS probehead

The B_1 distribution of an NMR probehead can be measured using a two-dimensional nutation experiment performed on a spin $I = 1/2$ nucleus with a relatively narrow

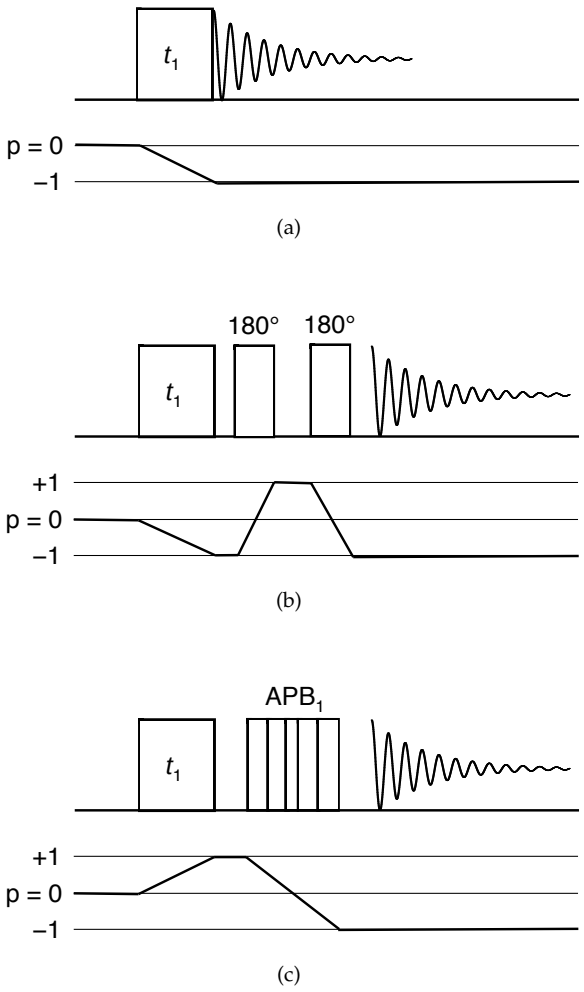

FIGURE 3.14: Pulse sequences and coherence transfer pathway diagrams employed for imaging the B_1 field distribution in a MAS NMR probe using inhomogeneous B_0 and B_1 fields. (a) Basic two-dimensional nutation experiment. (b) Nutation experiment incorporating CoryRitchey Depth pulse sequence. (c) Nutation experiment incorporating passband Depth sequence utilising the antisymmetric composite 180 pulse APB_1. All experiments are performed in the presence of the B_0 gradient along the z axis.

spectral range, such as ^{1}H. The duration of a radiofrequency pulse is incremented, forming the t_1 period of a two-dimensional experiment yielding the pulse sequence shown in Figure 3.14(a), and the resulting free induction decays subjected to a two-dimensional Fourier transformation. The resulting two-dimensional spectrum has the conventional ^{1}H spectrum in the F_2 dimension and the distribution of $\nu_1 = |\gamma B_1| / 2\pi$ nutation frequencies in the F_1 dimension. In addition, a linear B_0 gradient is applied along either the $+z$ or $-z$ axis (i.e., parallel or antiparallel to B_0 itself) during the nutation experiment. The aim of this is to create a second dimension with spatial resolution so that the distribution of the B_1 field can be correlated with its spatial origin within the sample.

The room-temperature shim coils were used to generate the linear z gradient – with

this approach, the experiment can be applied on any MAS probe and any NMR spectrometer. The shim coils generate only relatively weak magnetic field gradients, so the z gradient is used because it will be stronger than the linear x or y shim gradients. The low strength of the B_0 gradient is a problem because solid-state ^{1}H resonances are generally very broad and the gradient must produce a significant further broadening if acceptable spatial resolution is to be obtained. Our sample was chosen with this in mind: adamantane (Figure 3.9(d)) is highly mobile and in the solid each molecule is able to rotate rapidly within its lattice position, giving a relatively narrow ^{1}H resonance. In addition, further narrowing is achieved with MAS. The application of MAS in the presence of a B_0 gradient has the effect that, for the sample and rotor, gradient components orthogonal to the spinning axis will be averaged, leaving only the component along the spinning axis. This effective B_0 gradient will be parallel with the strongest component of the B_1 gradient (along the axis of the solenoidal radiofrequency coil), giving rise to the situation described in Reference [101] and [102], where correlated B_0 and B_1 gradients result in retention of high-resolution NMR spectra despite the spatial resolution. Note, however, that this only applies to the spinning sample and not to the background spins, which are static and so will yield a lineshape that is broadened in both dimensions by the B_0 and B_1 gradients.

The B_1 field will drop from $\sim$100 kHz in the centre of the radiofrequency coil to $\sim$0 kHz for the background spins. Thus, the B_1 gradient will be very strong compared to the B_0 gradients that we can produce on the shim coils ($<$ 1 kHz across the dimensions of the MAS rotor). This means that, as in Reference [102], we can ignore the effect of the B_0 gradient during the pulse to a first approximation and hence during the t_1 period. Therefore, we can interpret the two-dimensional spectrum as representing the B_1 gradient image in the F_1 dimension correlated with the B_0 gradient image in the F_2 dimension.

This experiment can be used to make a critical assessment of the performance of simple and composite Depth pulse methods for ^{1}H background suppression in a MAS probe. Appending two 180° pulses phase cycled according to Exorcycle scheme to the imaging method described here yields the pulse sequence in Figure 3.14(b), which will be used to examine the Depth sequence as implemented by Cory and Ritchey. Combining one of our passband composite pulses for background suppression with the two-dimensional method yields the pulse sequence in Figure 3.14(c).

3.5.2 Experimental details

Experiments were performed on a Bruker Avance 400 MHz spectrometer equipped with a widebore 9.4 T magnet and a 4-mm MAS probe. Adamantane was packed conventionally to fill a 4-mm zirconia MAS rotor (with Kel-F cap) completely. Figure 3.9(d) shows the structure of adamantane, which possesses two inequivalent ^{1}H sites. These are not resolved here, and a single peak is seen at 1.8 ppm. The calibrated 90° pulse length for ^{1}H was 1.95 μs, corresponding to an apparent nutation frequency, $\nu_1 = |\gamma B_1|/2\pi$, of 128 kHz. The MAS rate used was 10 kHz. The ^{1}H MAS linewidth for adamantane in the absence of a B_0 gradient was 460 Hz. The B_0 gradient was applied by increasing the linear z shim current up to its maximum permitted value in either the positive or negative sense. This yielded a ^{1}H MAS linewidth for adamantane of 2070 Hz. Two-dimensional nutation spectra were recorded by incrementing the excitation pulse through 96 steps of 2.0 μs, yielding an F_1 spectral width (with a real Fourier transform with respect to t_1) running from 0 to 250 kHz. A four-step CYCLOPS phase cycling was used. When Depth pulses were appended to the nutation sequence, a truncated 16-step phase cycle was used for the original Cory-Ritchey sequence as described in Table 1 of Reference [87], while a 16-step Exorcycle + CYCLOPS phase cycle was used for the passband sequences, as described in Table 3.1. The passband composite 180° pulse used in the passband depth sequence was APB_1 from Equation 3.8.

3.5.3 Results

The ^{1}H MAS NMR spectrum of adamantane obtained in the absence of the B_0 gradient is shown in Figure 3.15(a). The spectrum appears to consist of a single resonance at 1.9 ppm, with a linewidth (full-width at half-height) of 460 Hz. The application of the B_0 gradient broadens the line to 2070 Hz, as shown in Figure 3.15(b).

Two-dimensional ^{1}H MAS nutation spectra of adamantane, recorded with the pulse sequence shown in Figure 3.14(a), are shown in Figure 3.16. In the spectrum in Figure 3.16(a), recorded with the linear z shim current set to its maximum positive value, it can be seen that the ^{1}H nutation rate is $\nu_1 \approx 150$ kHz in the centre of the sample (corresponding to the centre of the radiofrequency coil). Since the B_0 gradient spreads the signal along the F_2 dimension according to its spatial z coordinate, while the B_1 field

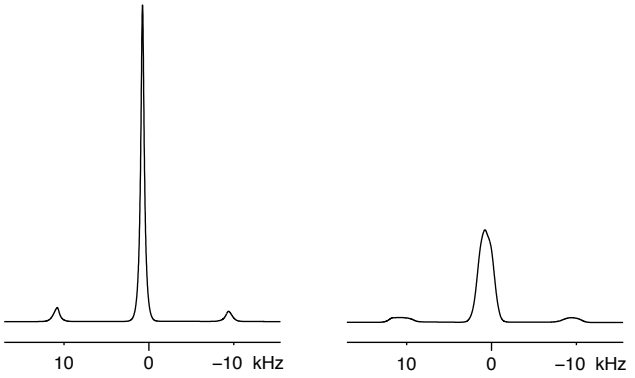

(a) Without B_0 gradient

(b) With B_0 gradient generated using room-temperature z shim

FIGURE 3.15: ^{1}H (400 MHz) MAS NMR spectra of adamantane (10 kHz MAS rate, 90° pulse length of 1.95 μs, relaxation interval of 10 s, four-step CYCLOPS phase cycle applied). The full linewidth at half-height in (a) is 460 Hz, while in (b) the application of a B_0 gradient broadens this to 2070 Hz.

of the coil decreases from the centre towards the two ends of the sample, an inverted V-shaped lineshape results for the sample (see the expansion in Figure 3.16(b)). The signal from the very top and bottom of the rotor exhibits a nutation rate ν_1 of around 10-30 kHz on either side of the maximum in the F_2 dimension. Spinning sidebands from the adamantane sample are also visible in Figure 3.16(a).

A spatially distinct background signal is also apparent in Figure 3.16(a), appearing as a broad signal corresponding to a nutation rate ν_1 in the range 10-30 kHz. Corresponding to ^{1}H nuclei in materials used in the probehead, the background spins will be mainly located below the MAS rotor, perhaps being excited and detected by electronic components further down in the probe body. These background spins experience a much lower average B_1 field than those within the rotor. With reversal of the direction of the B_0 gradient, the position of the background signal is moved from the high-frequency side of the rotor in F_2 (see Figure 3.16(a)) to the low-frequency side (Figure 3.16(c)). From the sample dimensions and orientation, we can estimate that our B_0 gradient strength is 200 Hz mm^{-1} along the z-axis. The apparent shift of the background signal maximum upon reversing the z gradient direction is 25 kHz (i.e., the background signal maximum is shifted about 12.5 kHz by the gradient), consistent with the background signal originating roughly 12.5 kHz/(200 Hz mm^{-1}) = 62.5 mm below the centre of the sample (which is not shifted by the B_0 gradient). Although the precise value should be viewed with caution (the B_0 gradient will not be linear over all space), this would

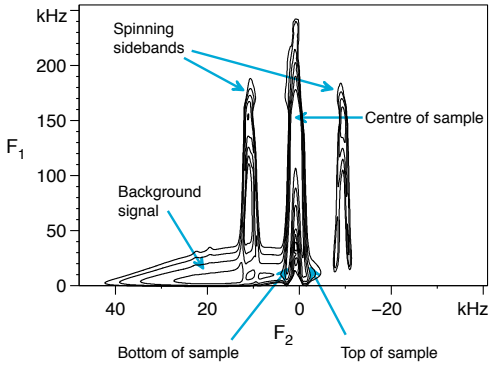

(a) z shim set to maximum positive value

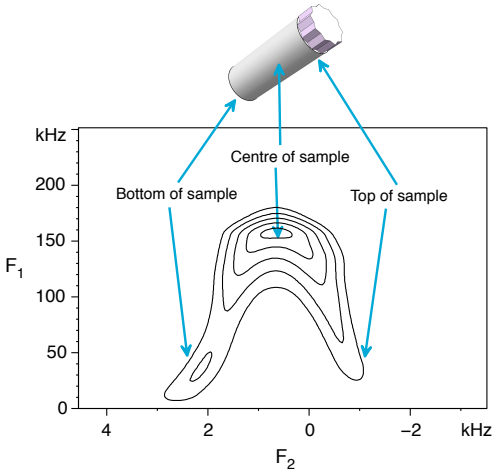

(b) Expansion of centreband region

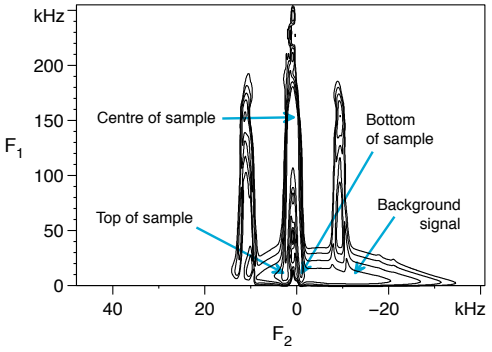

(c) z shim set to maximum negative value

FIGURE 3.16: Two-dimensional ^{1}H (400 MHz) nutation spectra of adamantane. Spectra were recorded with the pulse sequence shown in Figure 3.14(a) by averaging 16 transients for each of the 96 t_1 increments of 2 μs for the excitation pulse. In (a), the linear z shim has been set to its maximum positive value, while in (b) an expansion of the centreband adamantane signal is shown. In (c), the B_0 gradient has been reversed by adjusting the room-temperature z shim current to its maximum negative current.

appear to confirm that electronic components situated well below the coil, rotor and stator assembly play a significant role in acquiring the background ^{1}H signal, with the signal itself perhaps originating from the polymers used in the construction of some of these components, e.g., the capacitors.

The nutation spectrum shown in Figure 3.17(a) was acquired with the original Cory-Ritchey Depth sequence for background suppression appended to the normal nutation pulse sequence, as shown in Figure 3.14(a). Comparing this spectrum with that in Figure 3.16(a), the successful elimination of the background signal is evident. The F_1 projections of two-dimensional nutation experiments acquired without background

suppression sequences (Figure 3.14(a)) and with the Cory-Ritchey (Figure 3.14(b)) and passband Depth (Figure 3.14(c)) sequences appended are compared in Figure 3.17(b). The projections show the signal amplitude as a function of the B_1 field and can thus be used to assess the effectiveness of the Depth sequences for removing background signals. In addition to the adamantane signal with a maximum in its B_1 distribution at $\nu_1 \approx 150$ kHz, the conventional nutation experiment shows a significant signal originating from the background with a broad range of low nutation frequencies in the range 10-30 kHz. Appending the Cory-Ritchey Depth sequence yields a projection that is free of any background signal. However, a distinct drop in signal intensity is also evident for the sample.

As described in Section 3.1.2, with the use of passband composite pulses in the Depth sequence we hoped to achieve effective suppression of the background signal using only a single refocusing pulse. Using this approach, greater signal intensity can be obtained from the sample owing to the compensation for the B_1 inhomogeneity of the coil. The simulations in Figure 3.7 have confirmed that implementing the Depth sequence using a single passband composite pulse achieves a greater degree of suppression of the background than the original Cory-Ritchey Depth sequence with two simple 180° pulses. Figure 3.17(b) also shows the F_1 projection of the nutation experiment with passband Depth appended using the sequence APB_1. Compared with the original Cory-Ritchey Depth sequence, more signal is excited across the B_1 range experienced by the sample within the coil, while successful removal of the background is still achieved.

One significant point to be noted from the spectra in Figures 3.16 and 3.17 is that the B_1 inhomogeneity seems to be very severe at the two ends of the sample, which lie outside the radiofrequency coil, with ν_1 dropping as low as 10 kHz in our results. Consequently, the low nutation rates of the packed sample at each end of the rotor actually overlap with the nutation rate range of the background signal. As a result, although the passband composite pulse method improves the signal-to-noise ratio for the Depth sequence, it is clearly not possible to retain the full signal intensity from the sample if the background is removed using any method that exploits the B_1 distribution of signals.

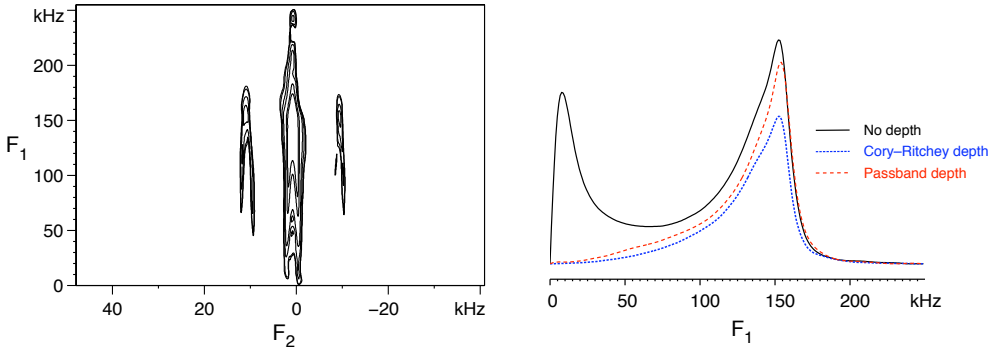

FIGURE 3.17: (a) Two-dimensional ^{1}H (400 MHz) nutation spectrum of adamantane, incorporating the Cory-Ritchey background suppression method. Spectrum recorded with the pulse in Figure 3.14(b) by averaging 16 transients for each of 96 t_1 increments of 2 μs for the excitation pulse. (b) Comparison of the F_1 projections of two-dimensional nutation spectra with no Depth background suppression, with Cory-Ritchey background suppression, and with passband Depth suppression using the antisymmetric composite 180° pulse APB_1

3.6 Conclusions

The $N = 2$ Cory-Ritchey Depth sequence is a popular method employed in ^{1}H MAS NMR to suppress the broad background signal that arises from ^{1}H nuclei located outside the MAS rotor. However, compared to a simple 90° excitation pulse, the signal amplitude arising from the sample is greatly reduced. It seems that the majority of this signal loss is due to the non-uniform excitation that this sequence provides as a function of B_1 across the range $0.5 \leq B_1/B_1^{nom} \leq 1.0$, which corresponds to the range of B_1 fields expected to occur within the coil (see Figure 3.2). Three novel antisymmetric passband refocusing pulses have been introduced – the inclusion of these in the Depth sequence compensates for the B_1 inhomogeneity experienced by the sample.

Another possible source of signal loss in some samples is significant transverse relaxation during the spin echo intervals within the Depth sequence. As expected, therefore, the $N = 1$ Cory-Ritchie Depth sequence yields more signal than the $N = 2$ sequence (compare Figures 3.10(b) and 3.10(c)), both because of the more uniform excitation in the range of B_1 fields generated within the coil (see Figure 3.4) and the shorter free-precession intervals used. However, it must be noted that the degree of signal suppression predicted for the $N = 1$ Cory-Ritchey sequence for $B_1/B_1^{nom} \leq 0.25$, corresponding to spins outside the radiofrequency coil, is two or three orders of magnitude lower than that predicted for the $N = 2$ sequence (see Figure 3.7).

Use of an antisymmetric passband composite 180° pulse in a single spin-echo Depth sequence yields greater signal than the $N = 1$ Cory-Ritchey sequence (compare Figures 3.10(c) and 3.10(d)) owing to the more uniform excitation across the range $0.5 \leq B_1 / B_1^{\text{nom}} \leq 1.0$, corresponding to the range of B_1 fields expected to occur within the coil (see Figure 3.6). However, if the passband refocusing pulse APB_1 or APB_2 is used then the degree of signal suppression for $B_1 / B_1^{\text{nom}} \leq 0.25$ (i.e., the background suppression) is predicted to be as good as or better than that achieved with the widely used $N = 2$ Cory-Ritchey sequence (see Figure 3.7). In experimental practice, little difference was observed between the performances of the three APB_n passband pulses, with all typically yielding about twice the signal-to-noise ratio of the $N = 2$ Cory-Ritchey sequence (compare Figures 3.10(b) and 3.10(d) or Figures 3.13(b) and 3.13(c)).

The combination of a passband or broadband composite 90° pulse with a passband 180° is predicted to provide more uniform excitation near to B_1^{nom} than use of a simple 90° pulse in such a combination (see Figure 3.6). In practice, we found that only broadband composite 90° pulses yielded any further signal enhancement in ^{1}H MAS (compare Figures 3.12(b) and 3.12(c)). The disappointing performance of passband 90° pulses when combined with passband 180° pulses in this application is likely to be a consequence of their overall excitation profile being rather narrow when compared with the range of B_1 field strengths expected inside the solenoidal radiofrequency coil. We would also express some caution about the use of broadband composite 90° pulses, such as $\text{BB}_1(90^\circ)$, in this application as, although the degree of signal suppression for $B_1 / B_1^{\text{nom}} \leq 0.25$ is predicted to be similar to that of the $N = 2$ Cory-Ritchey sequence for the combination of $\text{BB}_1(90^\circ)$ and APB_1, for the sequences APB_2 and APB_3 it is predicted to be significantly worse. The results in Figure 3.8 demonstrate that the passband Depth sequences proposed in this work are sufficiently robust with respect to resonance offset for general use in ^{1}H MAS NMR. This is a consequence of both the small ^{1}H spectral range (likely to be at most 10-15 kHz) and the high ^{1}H nutation frequencies used in modern ^{1}H MAS NMR (maybe 100-200 kHz). With other nuclides, resonance offset and, if present, quadrupolar interactions are likely to be more of a problem, as a result of both wider spectral ranges and lower nutation rates.

Two-dimensional nutation experiments were used to allow the spatial distribution of the B_1 field to be mapped. The principal origin of the background signal in the 4-mm probe used in this Chapter was found to be located well below the coil, rotor and stator

assembly. Appending the Depth sequence to the nutation experiment clearly demonstrated the removal of the background signal, while the use of the passband Depth sequence achieved greater signal excitation from within the sample (see Figure 3.17(b). It was also found that the nutation rates of the sample at either end of the rotor overlaps with the range of nutation rates of the background signal. As a consequence, it can be realised that it is not possible to retain the full signal intensity from the sample if the background is to be removed using any method that exploits the distribution of B_1 strengths.

Chapter 4

Dual-compensated antisymmetric composite refocusing pulses

4.1 Introduction

As described in Section 2.9, different composite pulses are used when different bandwidth properties with respect to experimental frequency parameters are required. Two of the most common pulse imperfections encountered in NMR are the spatial inhomogeneity of the radiofrequency field strength B_1, which leads to a distribution of nutation frequencies across the sample, and the finite magnitude of ω_1 with respect to typical resonance offsets in the spectrum. Much of the effort in composite pulse design has therefore been in creating sequences which are broadband with respect to the nutation frequency ω_1 or the resonance offset Ω.

Broadband composite 180° pulses have always been of particular interest as both inversion of longitudinal (z) magnetisation and refocusing of tranverse (xy) magnetisation are very sensitive to the common pulse imperfections. However, the early enthusiasm for such pulses was rather diminished when it was realized that they often do not show an advantage over simple 180° pulses when used for refocusing of transverse magnetisation, as is required when forming a conventional (or Hahn) spin echo. Many composite pulses, including Levitt's popular $90^\circ_{90^\circ}\ 180^\circ_{0^\circ}\ 90^\circ_{90^\circ}$, produce a spin-echo signal with a phase that is sensitive to the value of ω_1 and Ω, owing to the dependence of the overall rotation axis on these parameters.

Phase distortionless or constant-rotation composite pulses have both overall flip angles and rotation axes that are almost constant over a certain range of either ω_1 or Ω. However, the problem with such pulses is that their bandwidths are not nearly large enough for the imperfections that are commonly encountered in practical NMR spectroscopy. It seems that there are no short phase-distortionless composite 180° pulses that can compensate for a B_1 field that drops to less than half its nominal value across the volume of the sample, or for a resonance offset parameter, $|\Omega|/\omega_1^{\mathrm{nom}} = \Delta B/B_1^{\mathrm{nom}}$, of 1 or greater, yet both these situations occur frequently in experimental practice. In addition, most composite 180° pulses designed to compensate for B_1 inhomogeneity have a poor performance with respect to resonance offset, often much worse than that of a simple 180° pulse. As a result, there will always be either parts of the sample or signals with offsets that are outside the usable bandwidths of even the best so-called phase-distortionless composite pulses and an unwanted phase shift in the echo signal will nonetheless result.

As explained in Section 2.10, the overall rotation axis of an antisymmetric composite pulse lies in a fixed vertical plane of the rotating frame (the xz plane if the central pulse has phase 0°). Using Exorcycle phase cycling, the use of an antisymmetric refocusing pulse will produce an echo signal with constant phase for all values of ω_1 and Ω. As with any other phase-distortionless composite pulse, the effective bandwidth of an antisymmetric broadband pulse may not be sufficient to cover the full range of the relevant instrumental imperfection but, unlike a symmetric or asymmetric composite 180° pulse, it will not introduce any phase distortion into the spin echo.

In this Chapter, novel antisymmetric broadband composite 180° pulses will be introduced [6]. These pulses are designed to be *dual compensated* - that is, compensated simultaneously for both resonance offset and inhomogeneity of the radiofrequency field. Only one dual-compensated composite pulse of this phase symmetry has been presented in the literature before, in an appendix to Reference [60] without any verifying simulations or experiments. Interestingly, we will show here that this sequence belongs to one of the two families of dual-compensated 180° pulses presented here. These new dual-compensated pulses will be designed analytically, with the aid of a graphical interpretation of average Hamiltonian theory, and experimentally verified. These composite pulses can also be incorporated into two-dimensional experiments containing spin-echo

elements, and we demonstrate their inclusion in ^{31}P refocused-INADEQUATE experiments.

4.2 Theory and composite pulse design

4.2.1 Average Hamiltonian theory

Section 2.2 gave the solution for the evolution of the density matrix acted on by a time-independent Hamiltonian. The use of average Hamiltonian theory has been used extensively in NMR to evaluate cases where the Hamiltonian is time-dependent [103–105], and has been described in several works in the context of composite pulse design [6, 56, 59].

Written in the rotating frame of reference, the Hamiltonian during the radiofrequency pulse, either simple or composite, can be considered as the sum of two parts, H^{nom} and V:

$$H = H^{\text{nom}} + V \tag{4.1}$$

$$H^{\text{nom}} = \omega_1^{\text{nom}}(I_x \cos\phi(t) + I_y \sin\phi(t)) \tag{4.2}$$

where H^{nom} describes the interaction of the ideal or nominal radiofrequency field with a spin system with total angular momentum operator $\mathbf{I}$. The radiofrequency field produces a nominal nutation frequency ω_1^{nom} and has phase $\phi(t)$. This phase is constant during a single pulse and so piecewise-constant during a composite pulse; if the composite pulse consists of N pulses then $\phi(t)$ has the value ϕ_n during the nth pulse. The duration of the nth pulse is τ_n. The sequence is then completely specified by the N phases ϕ_n and the N pulse durations τ_n, with the overall duration T equal to $T = \tau_1 + \tau_2 + \ldots + \tau_N$.

The operator V describes the deviation of the actual pulse Hamiltonian H from the nominal behaviour described by H^{nom}. Here, we are interested in two possible forms of the perturbation V:

1. V arises from a deviation of the true nutation frequency ω_1 from its nominal value ω_1^{nom}, as caused for example by a spatial inhomogeneity of the radiofrequency

field across the sample:

$$V^{\text{inh}} = (\omega_1 - \omega_1^{\text{nom}})(I_x \cos\phi(t) + I_y \sin\phi(t)) \tag{4.3}$$

2. V arises from an offset Ω of the rotating frame frequency from exact resonance:

$$V^{\text{off}} = \Omega I_z \tag{4.4}$$

The time evolution of the spin system during the pulse is described by the propagator $U(t)$ and is written

$$U(t) = \hat{T} \exp\{-i \int_0^t H(t')\, \mathrm{d}t'\}, \tag{4.5}$$

where $\hat{T}$ is the Dyson time-ordering operator. $U(t)$, like $H(t)$, can be separated into two parts describing ideal behaviour and a perturbation,

$$U(t) = U^{\text{nom}}(t) U^{V}(t) \tag{4.6}$$

where

$$U^{\text{nom}}(t) = \hat{T} \exp\{-i \int_0^t H^{\text{nom}}(t')\, \mathrm{d}t'\} \tag{4.7}$$

$$U^{V}(t) = \hat{T} \exp\{-i \int_0^t \tilde{V}(t')\, \mathrm{d}t'\} \tag{4.8}$$

$$\tilde{V}(t) = U^{\text{nom}}(t)^{-1} V U^{\text{nom}}(t) \tag{4.9}$$

$\tilde{V}(t)$ is the full Hamiltonian in the interaction representation or "toggling frame" imposed by H^{nom}

The propagator $U^{\text{nom}}(t)$ describes the evolution of the spin system under the effect of the nominal radiofrequency field alone. Using the fact that $H^{\text{nom}}(t)$ is piecewise time-independent, Equation 4.7 can be written:

$$\begin{aligned} U^{\text{nom}}(t) = &\exp\{-i\omega_1^{\text{nom}} I_{\phi_n}(t - \tau_{n-1} - \ldots - \tau_1)\} \ldots \\ &\times \exp\{-i\omega_1^{\text{nom}} I_{\phi_2} \tau_2\} \exp\{-i\omega_1^{\text{nom}} I_{\phi_1} \tau_1\} \end{aligned} \tag{4.10}$$

where

$$\tau_1 + \ldots + \tau_{n-1} \leq t \leq \tau_1 + \ldots + \tau_n \tag{4.11}$$

$$I_{\phi_n} = I_x \cos\phi_n + I_y \sin\phi_n \tag{4.12}$$

The propagator $U^{\text{nom}}(t)$ consists of a series of $n-1$ *fixed rotations* with flip angles $\omega_1^{\text{nom}}\tau_1$, $\omega_1^{\text{nom}}\tau_2$, etc. and phases in the xy plane of ϕ_1, ϕ_2, etc. and a final *variable rotation* with phase ϕ_n. According to Equation 4.9, the order in which these rotations act on V is antichronological.

If the propagator $U^V(T)$ in Equation 4.6 were approximately equal to the identity operator, i.e. $U^V(T) \approx \mathbb{1}$, over a certain range of an experimental frequency parameter such as ω_1 or Ω, then the full propagator for the sequence $U(T)$ would approximate to the ideal propagator $U^{\text{nom}}(T)$ over that same range. In this case, providing the pulse durations and phases had also been chosen such that

$$U^{\text{nom}}(T) I_z U^{\text{nom}}(T)^{-1} = -I_z \tag{4.13}$$

then we would have derived a broadband composite 180° pulse.

As described by Tycko and coworkers [56, 59], a good way to achieve $U^V(T) \approx \mathbb{1}$ over a certain range of an experimental frequency parameter is to make a Magnus expansion of it:

$$U^V(T) = \exp\{-i(V^{(0)}T + V^{(1)}T + \ldots)\} \tag{4.14}$$

$$V^{(0)}T = \int_0^T \mathrm{d}t\ \tilde{V}(t) \tag{4.15}$$

$$V^{(1)}T = -\frac{i}{2}\int_0^T \mathrm{d}t_1 \int_0^{t_1} \mathrm{d}t_2\ [\tilde{V}(t_1), \tilde{V}(t_2)] \tag{4.16}$$

The sequence is broadband to Nth order if $V^{(n)} = 0$ for $0 \leq n \leq N$. As N becomes larger, the range over which $U^V(T) \approx \mathbb{1}$ also becomes larger, corresponding to an increasing bandwidth. The zeroth-order average Hamiltonian $V^{(0)}$ and the first-order Hamiltonian $V^{(1)}$ are the first two terms in a power series expansion of an exact average Hamiltonian. The terms $V^{\text{inh}(0)}$ and $V^{\text{off}(0)}$ are linear in $\omega_1 - \omega_1^{\text{nom}}$ and Ω, respectively, while $V^{\text{inh}(1)}$ and $V^{\text{off}(1)}$ are quadratic, and so on. Thus, by choosing the pulse

phases and durations in the composite sequence such that $V^{(0)}T = 0$, while simultaneously satisfying Equation 4.13, we will have designed a composite 180° pulse that is broadband to "zeroth-order" in the relevant experimental frequency parameter, either $\omega_1 - \omega_1^{\text{nom}}$ or Ω. If greater bandwidth is desired then this can be achieved by designing "first-order" broadband composite 180 pulses that satisfy $V^{(0)}T = V^{(1)}T = 0$.

4.2.2 Simple pulses

It is insightful to calculate the zeroth- and first-order Hamiltonian terms for simple radiofrequency pulse of duration τ_1 and phase ϕ_1 for the two perturbations described in Equations 4.3 and 4.4. For inhomogeneity of the rf field, we find:

$$\tilde{V}^{\text{inh}} = V^{\text{inh}} = (\omega_1 - \omega_1^{\text{nom}})I_{\phi_1} \tag{4.17}$$

$$V^{\text{inh}(0)}\tau_1 = (\omega_1 - \omega_1^{\text{nom}})\tau_1 I_{\phi_1} \tag{4.18}$$

$$V^{\text{inh}(1)}\tau_1 = 0 \tag{4.19}$$

For resonance offset, we calculate,

$$\begin{aligned}\tilde{V}^{\text{off}}(t) &= \exp\{+i\omega_1^{\text{nom}} I_{\phi_1} t\}\Omega I_z \exp\{-i\omega_1^{\text{nom}} I_{\phi_1} t\} \\ &= \Omega(I_z \cos\omega_1^{\text{nom}} t + I_{\phi_1+90^\circ} \sin\omega_1^{\text{nom}} t)\end{aligned} \tag{4.20}$$

$$V^{\text{off}(0)}\tau_1 = \frac{\Omega}{\omega_1^{\text{nom}}}\left(I_z \sin\omega_1^{\text{nom}}\tau_1 + I_{\phi_1+90^\circ}(1 - \cos\omega_1^{\text{nom}}\tau_1)\right) \tag{4.21}$$

$$V^{\text{off}(1)}\tau_1 = \frac{1}{2}\left(\frac{\Omega}{\omega_1^{\text{nom}}}\right)^2 I_{\phi_1}(\omega_1^{\text{nom}}\tau_1 - \sin\omega_1^{\text{nom}}\tau_1) \tag{4.22}$$

For the specific case of a simple 180° pulse ($\omega_1^{\text{nom}}\tau_1 = \pi$), Equations 4.21 and 4.22 become

$$V^{\text{off}(0)}\tau_1 = 2\frac{\Omega}{\omega_1^{\text{nom}}} I_{\phi_1+90^\circ} \tag{4.23}$$

$$V^{\text{off}(1)}\tau_1 = \frac{\pi}{2}\left(\frac{\Omega}{\omega_1^{\text{nom}}}\right)^2 I_{\phi_1} \tag{4.24}$$

4.2.3 Composite 180° pulses

We will consider composite 180° pulses composed of an odd number N of simple nominal 180° pulses:

$$180^\circ_{\phi_1^\circ}\ 180^\circ_{\phi_2^\circ} \ldots 180^\circ_{\phi_N^\circ} \tag{4.25}$$

By restricting the sequence to have this form, Equation 4.13 is satisfied for all possible phases $\{\phi_1, \phi_2 \ldots \phi_N\}$, leaving us free to choose these solely on the basis that they satisfy $V^{(0)}T = 0$ or $V^{(0)}T = V^{(1)}T = 0$. The exclusive use of 180° pulses also makes finding solutions for $V^{(0)}T = 0$ or $V^{(0)}T = V^{(1)}T = 0$ particularly simple and intuitive using a graphical interpretation, as we will see later.

For B_1 inhomogeneity, we find

$$V^{\mathrm{inh}(0)}T = (\omega_1 - \omega_1^{\mathrm{nom}})\tau \sum_{j=1}^{N} I_{\phi_j'} \tag{4.26}$$

$$V^{\mathrm{inh}(1)}T = \frac{i(\omega_1 - \omega_1^{\mathrm{nom}})^2\tau^2}{2} \sum_{j=1}^{N-1} \sum_{k=j+1}^{N} [I_{\phi_k'}, I_{\phi_j'}] \tag{4.27}$$

where τ is the duration of a simple 180° pulse. Note the prime on the phases in Equations 4.26 and 4.27. This indicates that these are the pulse phases transformed by the move to the interaction representation brought about by the fixed 180° rotations in $U^{\mathrm{nom}}(t)$. As described in Reference [62], these toggling frame phases are related to the pulse phases by

$$\phi_k' = (-1)^{k+1}\phi_k + \sum_{j=1}^{k-1}(-1)^{j+1}2\phi_j \tag{4.28}$$

For offset, we find

$$V^{\mathrm{off}(0)}T = 2\frac{\Omega}{\omega_1^{\mathrm{nom}}} \sum_{j=1}^{N} I_{\phi_j'+90^\circ+(j-1)180^\circ} \tag{4.29}$$

$$\begin{aligned} V^{\mathrm{off}(1)}\tau_1 =& \frac{\pi}{2}\left(\frac{\Omega}{\omega_1^{\mathrm{nom}}}\right)^2 \sum_{j=1}^{N} I_{\phi_j'} \\ & - 2i\left(\frac{\Omega}{\omega_1^{\mathrm{nom}}}\right)^2 \sum_{j=1}^{N-1} \sum_{k=j+1}^{N} [I_{\phi_k'+90^\circ+(k-1)180^\circ}, I_{\phi_j'+90^\circ+(j-1)180^\circ}] \end{aligned} \tag{4.30}$$

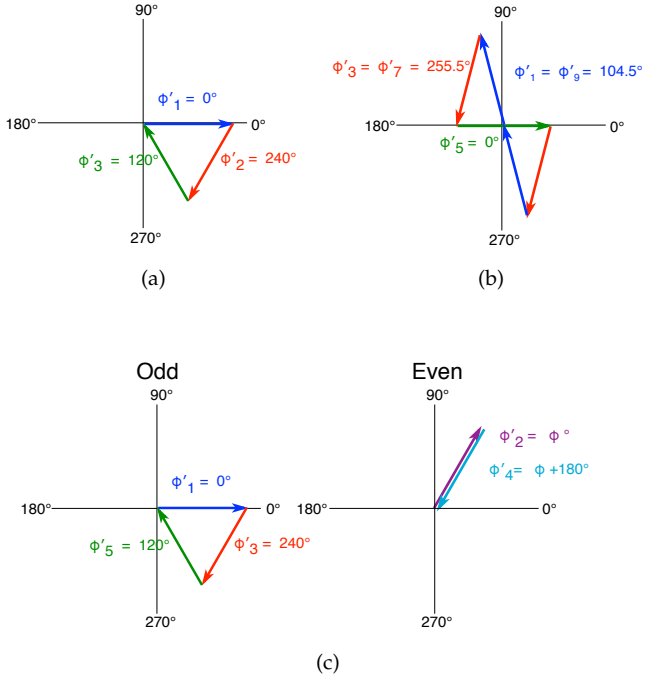

FIGURE 4.1: Graphical solution of the equations $V^{\mathrm{inh}(0)}T = 0$ and $V^{\mathrm{off}(0)}T = 0$ for the form of composite 180° pulse given in Equation 4.25. The contribution from each pulse is a transverse xy angular momentum operator of fixed length in the toggling frame relevant to B_1 inhomogeneity (Equation 4.26) or resonance offset (Equation 4.29). (a) Toggling-frame solution for three 180° pulses ($N = 3$); this corresponds to the symmetric composite pulse $180^\circ_{0^\circ}\ 180^\circ_{120^\circ}\ 180^\circ_{0^\circ}$ for B_1 inhomogeneity or $180^\circ_{0^\circ}\ 180^\circ_{300^\circ}\ 180^\circ_{0^\circ}$ for resonance offset. (b) Time-symmetric toggling-frame solution for five 180° pulses ($N = 5$); this corresponds to the antisymmetric composite pulse $180^\circ_{46.6^\circ}\ 180^\circ_{255.5^\circ}\ 180^\circ_{0^\circ}\ 180^\circ_{104.5^\circ}\ 180^\circ_{313.4^\circ}$ for B_1 inhomogeneity or $180^\circ_{46.6^\circ}\ 180^\circ_{75.5^\circ}\ 180^\circ_{0^\circ}\ 180^\circ_{284.5^\circ}\ 180^\circ_{313.4^\circ}$ for resonance offset. (c) Toggling-frame solution for five 180° pulses ($N = 5$) that ensures that $V^{\mathrm{inh}(0)}T = 0$ and $V^{\mathrm{off}(0)}T = 0$ simultaneously by having both the odd- and even-numbered vectors sum to zero separately; as the phase ϕ can take any value, this corresponds to the family of dual-compensated composite 180° pulses presented by Tycko and Pines, including the asymmetric sequence $360^\circ_{0^\circ}\ 180^\circ_{120^\circ}\ 180^\circ_{60^\circ}\ 180^\circ_{120^\circ}$.

The toggling-frame phases in Equations 4.29 and 4.30 are related to those in Equations 4.26 and 4.27 in a systematic fashion and we have emphasised this by writing all of them in terms of the primed phases of Equation 4.28.

4.2.4 Graphical solutions for $V^{\mathrm{inh}(0)}T = 0$ and $V^{\mathrm{off}(0)}T = 0$

Inspection of Equation 4.26 reveals that it is simply a summation of transverse angular momentum operators, which we can represent as vectors in an xy plane. Thus if we

choose $N = 3$ and

$$\phi_1' = 0^\circ$$
$$\phi_2' = 240^\circ$$
$$\phi_3' = 120^\circ$$

then the three vectors will sum to zero as shown in Figure 4.1(a) and we will have $V^{\mathrm{inh}(0)}T = 0$. These three toggling frame phases can be converted to actual pulse phases using Equation 4.28 and we find that $\phi = 0^\circ$, $\phi = 120^\circ$ and $\phi = 0^\circ$, yielding the well known broadband (for B_1 inhomogeneity) phase-distortionless composite 180° pulse $180^\circ_{0^\circ}\ 180^\circ_{120^\circ}\ 180^\circ_{0^\circ}$.

This is a time-symmetric composite pulse ($\tau_1 = \tau_N, \tau_2 = \tau_{N-1}$, etc. and $\phi_1 = \phi_N, \phi_2 = \phi_{N-1}$, etc.) yet its toggling frame phases are antisymmetric ($\phi_1' = \phi_0' + \phi_{1'}', \phi_2' = \phi_0' + \phi_{2'}' \ldots \phi_{N-1}' = \phi_0' - \phi_{2'}', \phi_N' = \phi_0' - \phi_{1'}'$). As explained earlier, we aim to derive novel antisymmetric composite refocusing pulses so that spin echoes can be formed which are free of phase distortion as long as the true echo pathway is selected. In order to obtain a composite pulse with antisymmetric phases, the choice of toggling frame phases must be *symmetric*.

If we choose $N = 5$, the five vectors will sum to zero if we select the time-symmetric phases

$$\phi_1' = \phi_5' = \cos^{-1}(-0.25) \approx 104.5^\circ$$
$$\phi_2' = \phi_4' = -\cos^{-1}(-0.25) \approx 255.5^\circ$$
$$\phi_3' = 0^\circ,$$

as shown in Figure 4.1(b). Converting these from the toggling frame to actual pulse phases using Equation 4.28, and then subtracting a constant phase 57.9° to make the central pulse $\phi_3 = 0^\circ$, we get:

$$\phi_1 = -\phi_5 = 46.6^\circ$$
$$\phi_2 = -\phi_4 = 255.5^\circ$$
$$\phi_3 = 0^\circ,$$

or the composite pulse 180° pulse $180^\circ_{46.6^\circ}\ 180^\circ_{255.5^\circ}\ 180^\circ_{0^\circ}\ 180^\circ_{104.5^\circ}\ 180^\circ_{313.4^\circ}$. This antisymmetric pulse, named F_1 in Reference [62], is broadband for B_1 inhomogeneity. Note that choosing the conjugate angle, $\cos^{-1}(-0.25) = 255.5$ is equivalent to using the mirror-image of the vector sequence shown in Figure 4.1(b), and generates the time-reversed sequence $180^\circ_{313.4^\circ}\ 180^\circ_{104.5^\circ}\ 180^\circ_{0^\circ}\ 180^\circ_{255.5^\circ}\ 180^\circ_{46.6^\circ}$, which we do not consider as a distinct sequence. The reversed sequence has the same performance with respect to B_1 inhomogeneity as its "forward" counterpart, while its offset performance is reversed with respect to the sign of the resonance offset.

Inspection of Equation 4.29 reveals that it too is simply a summation of transverse angular momentum operators. The only difference in this offset case is that the relationship between the toggling frame phases and the pulse phases is different from the inhomogeneity case: for offset there is an additional $+90^\circ$ phase shift of the toggling frame phases for the odd-numbered pulses and an additional -90° phase shift of the toggling frame phases for the even-numbered pulses. Regardless of this, we can still choose $N = 3$ as before and with $\phi'_1 + 90^\circ = 0^\circ, \phi'_2 = 240^\circ - 90^\circ, \phi'_3 + 90^\circ = 120^\circ$, the three vectors will sum to zero as shown in Figure 4.1(a), therefore $V^{\mathrm{off}(0)}T = 0$. Subtracting the additional phase shifts we find $\phi_1 = 30^\circ, \phi_2 = 90^\circ, \phi_3 = 150^\circ$ and then, using Equation 4.28 and after subtraction of a constant 30°, the actual pulse phases are found to be $\phi_1 = 0^\circ, \phi_2 = 300^\circ, \phi_3 = 0^\circ$. This is the broadband (for resonance offset) phase-distortionless composite 180° pulse $180^\circ_{0^\circ}\ 180^\circ_{300^\circ}\ 180^\circ_{0^\circ}$ (or equivalently $180^\circ_{0^\circ}\ 180^\circ_{60^\circ}\ 180^\circ_{0^\circ}$), which is one of a general series of symmetric solutions for $V^{\mathrm{off}(0)}T = 0$ given in Reference [59].

To derive a dual-compensated 180° pulse, we need to find a sequence that has $V^{\mathrm{inh}(0)}T = 0$ and $V^{\mathrm{off}(0)}T = 0$. As described by Tycko and coworkers using a theoretical framework similar to average Hamiltonian theory [58, 60], this can be done by noting that for the odd-numbered pulses the toggling frame phases for inhomogeneity and resonance offset differ only by a constant $+90^\circ$ and that for the even-number pulses the two toggling frames differ only by a constant -90°. Therefore, by ensuring that the angular momentum vectors for the odd-numbered pulses and for the even-numbered pulses separately sum to zero then a dual-compensated pulse should result. For example, with $N = 5$ and $\phi'_1 = 0^\circ, \phi'_2 = 240^\circ, \phi'_5 = 120^\circ$, and $\phi'_2 = \phi$ and $\phi'_4 = \phi + 180^\circ$ then both the odd- and even-numbered vectors will sum to zero as shown in Figure 4.1(c) and we will have $V^{\mathrm{inh}(0)}T = V^{\mathrm{off}(0)}T = 0$. As described by Tycko and coworkers, this generates an infinite family of composite 180° pulses as the phase ϕ is a free variable [58, 60]. These

five toggling frame phases can be converted to actual pulse phases using Equation 4.28 and, after subtraction of 120°, we find that $\phi_1 = 0°, \phi_2 = 120° - \phi, \phi_3 = 120° - 2\phi, \phi_4 = 300° - 3\phi$ and $\phi_5 = -4\phi$. With $\phi = 120°$ this gives the asymmetric dual-compensated 180° pulse $360°_{0°}\ 180°_{240°}\ 180°_{300°}\ 180°_{240°}$ (or equivalently $360°_{0°}\ 180°_{120°}\ 180°_{60°}\ 180°_{120°}$). With $\phi = 90°$ it gives the symmetric composite pulse $180°_{0°}\ 180°_{30°}\ 180°_{300°}\ 180°_{30°}\ 180°_{0°}$ (or equivalently $180°_{0°}\ 180°_{330°}\ 180°_{60°}\ 180°_{330°}\ 180°_{0°}$).

To obtain an antisymmetric dual-compensated 180° pulse it is clear that we need to have at least $N = 9$ so that the toggling-frame phases for both the odd- and even-numbered pulses can be symmetric, as shown for $N = 9$ in Figure 4.2(a). Thus with the toggling-frame phases $\phi'_1 = \phi'_9 = 104.5°, \phi'_3 = \phi'_7 = 255.5°, \phi'_5 = 0°$, and $\phi'_2 = \phi'_8 = \phi, \phi'_4 = \phi'_6 = \phi + 180°$ we can derive an antisymmetric pulse with $V^{\mathrm{inh}(0)}T = 0 = V^{\mathrm{off}(0)}T = 0$. Note that again there is a free phase variable ϕ, thereby generating an infinite family of composite 180° pulses (which we will call ASBO-9; ASBO stands for AntiSymmetric, for B_1 and Offset). These nine toggling frame phases can be converted to actual pulse phases using Equation 4.28 and, after subtraction of a constant phase to make the central pulse $\phi_5 = 0°$, we find that:

$$\begin{aligned}
\phi_1 &= -\phi_9 = 4\phi + \cos^{-1}(-0.25) = 4\phi + 104.5° \\
\phi_2 &= -\phi_8 = 3\phi + 2\cos^{-1}(-0.25) = 3\phi + 209° \\
\phi_3 &= -\phi_7 = 2\phi + \cos^{-1}(-0.25) = 2\phi + 104.5° \\
\phi_4 &= -\phi_6 = \phi + 180° \\
\phi_5 &= 0°
\end{aligned} \tag{4.31}$$

More antisymmetric dual-compensated pulses will exist with $N = 11$, $N = 13$, etc. Of these, however, only sequences with $N = 11$ can be derived in a closed form dependent on a single free phase variable ϕ as with the $N = 9$ case. The $N = 11$ solutions are shown in Figure 4.2(b), where the toggling-frame phases of the six odd-numbered pulses follow a time-symmetric pathway consisting of two equilateral triangles (to which we have added the free phase variable ϕ) and the toggling-frame phases of the five even-numbered pulses follow the same symmetric pathway as was used in Figure 4.1(b) and for the odd-numbered pulses in Figure 4.2(a). These toggling-frame phases correspond to the antisymmetric dual-compensated family of composite 180°

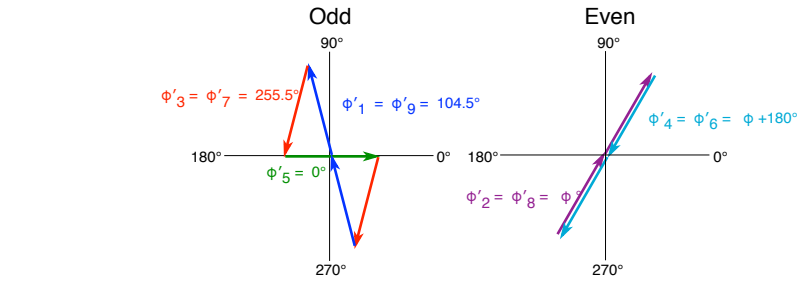

(a)

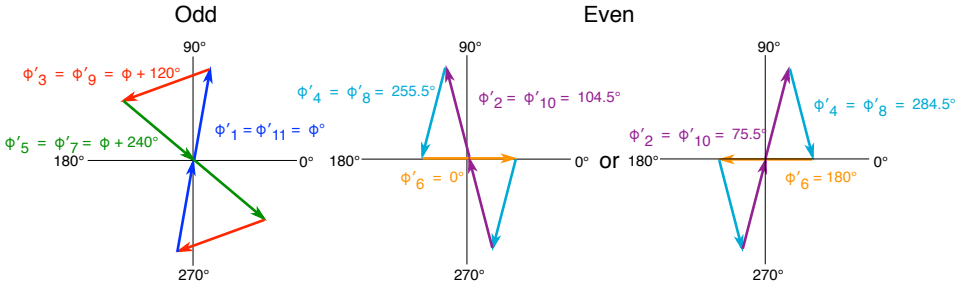

(b)

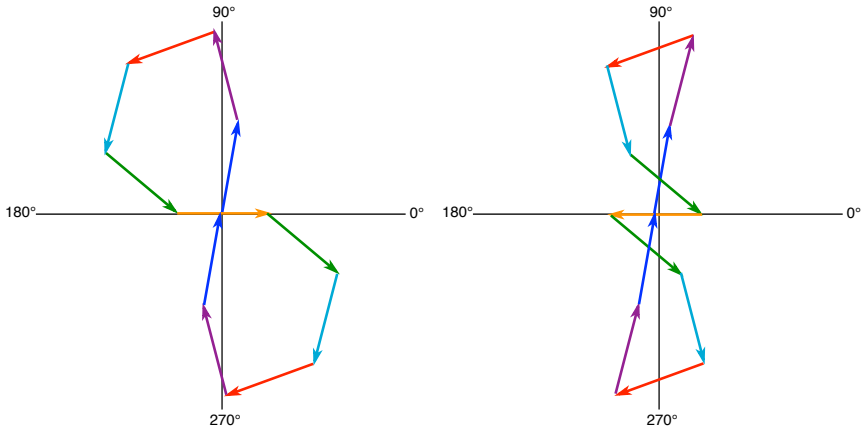

(c)

FIGURE 4.2: Graphical solution of the equations $V^{\mathrm{inh}(0)}T = 0$ and $V^{\mathrm{off}(0)}T = 0$ for the form of composite 180° pulse given in Equation 4.25. The contribution from each pulse is a transverse xy angular momentum operator of fixed length in the toggling frame relevant to B_1 inhomogeneity (Equation 4.26) or resonance offset (Equation 4.29). (a) Time-symmetric toggling-frame solution for nine 180° pulses ($N = 9$) that ensures that $V^{\mathrm{inh}(0)}T = 0$ and $V^{\mathrm{off}(0)}T = 0$ simultaneously; as the phase ϕ can take any value, this corresponds to the ASBO-9 family of antisymmetric dual-compensated composite 180° pulses generated by Equation 4.31. (b) Time-symmetric toggling-frame solution for eleven 180° pulses ($N = 11$) that ensures that $V^{\mathrm{inh}(0)}T = 0$ and $V^{\mathrm{off}(0)}T = 0$ simultaneously; as the phase ϕ can take any value and the even-numbered vectors can follow two inequivalent pathways, this corresponds to the ASBO-11 family of antisymmetric dual-compensated composite 180° pulses generated by Equation 4.32. (c) Combined odd and even pulse vectors showing an example of two inequivalent pathways given by $\phi = 80°$ for the ASBO-11 family.

pulses (which we will call ASBO-11):

$$\begin{aligned}
\phi_1 &= -\phi_{11} = 120^\circ - 5\phi \\
\phi_2 &= -\phi_{10} = 240^\circ - \cos^{-1}(-0.25) - 4\phi \\
\phi_3 &= -\phi_9 = 240^\circ - 2\cos^{-1}(-0.25) - 3\phi \\
\phi_4 &= -\phi_8 = 240^\circ - \cos^{-1}(-0.25) - 2\phi \\
\phi_5 &= -\phi_7 = 120^\circ - \phi \\
\phi_6 &= 0^\circ
\end{aligned} \tag{4.32}$$

In this case, the two conjugate angles, $\cos^{-1}(-0.25) = 104.5^\circ$ and $\cos^{-1}(-0.25) = 255.5^\circ$, produce distinct composite pulses, with different bandwidths with respect to both B_1 inhomogeneity and resonance offset. The two conjugate angles correspond to the two mirror-image vector pathways for the even-numbered toggling-frame phases shown in Figure 4.2(b). Combined with the odd-numbered pulse vector pathways, these produce different solutions for all values of the relative phase ϕ. Figure 4.2(c) shows an example of two such inequivalent pathways of combined odd and even toggling frame vectors for an $N = 11$ sequence where $\phi = 80^\circ$.

4.2.5 Higher-order terms

Derived in this way, the ASBO-9 and ASBO-11 dual-compensated pulse families satisfy the zeroth-order terms, $V^{\mathrm{inh}(0)}T = V^{\mathrm{off}(0)} = 0$. Using Equations 4.27 and 4.30, the first order average Hamiltonians can be evaluated. Since the toggling-frame phases are symmetric, the following relation holds:

$$[I_{\phi'_1}, I_{\phi'_2}] = -[I_{\phi'_{N-1}}, I_{\phi'_N}] \tag{4.33}$$

Taking into account the anticommutativity relation $[A, B] = -[B, A]$, the summation in Equation 4.27 evaluates to zero and therefore $V^{\mathrm{inh}(1)}T = 0$. For $V^{\mathrm{off}(1)}T = 0$, the operator part of the first term on the right-hand side of Equation 4.30 is identical to that in Equations 4.26, and will be equal to zero if $V^{\mathrm{inh}(0)}T = 0$. Owing to the symmetry of the toggling-frame phases, the second term also will equal zero. Thus, $V^{\mathrm{inh}(1)}T = V^{\mathrm{off}(1)}T = 0$.

However, when B_1 inhomogeneity and resonance offset are present simultaneously then there is a further first-order average Hamiltonian to consider. In this case, the perturbation V in Equation 4.1 is given by:

$$V^{\text{inh+off}} = V^{\text{inh}} + V^{\text{off}} \tag{4.34}$$

and we find to first-order,

$$V^{\text{inh+off}(1)}T = V^{\text{inh}(1)}T + V^{\text{off}(1)}T + V^{\text{inh,off}(1)}T \tag{4.35}$$

where the *inhomogeneity-offset cross term* is:

$$V^{\text{inh,off}(1)}T = -\frac{i}{2}\int_0^T \mathrm{d}t_1 \int_0^{t_1} \mathrm{d}t_2 \Big([\tilde{V}^{\text{inh}}(t_1), \tilde{V}^{\text{off}}(t_2)] + [\tilde{V}^{\text{off}}(t_1), \tilde{V}^{\text{inh}}(t_2)] \Big) \tag{4.36}$$

For the composite 180° pulse in Equation 4.25 we find

$$\begin{aligned} V^{\text{inh,off}(1)}T = &-\frac{2(\omega_1 - \omega_1^{\text{nom}})\Omega}{(\omega_1^{\text{nom}})^2} \Bigg(\sum_{j=1}^{N} I_{\phi'_j + 90^\circ + (j-1)180^\circ} \\ &+ \frac{\pi}{2} i \sum_{j=1}^{N-1} \sum_{k=j+1}^{N} [I_{\phi'_k}, I_{\phi'_j + 90^\circ + (j-1)180^\circ}] + [I_{\phi'_k + 90^\circ + (k-1)180^\circ}, I_{\phi'_j}] \Bigg) \end{aligned} \tag{4.37}$$

The first term in the large brackets on the right-hand side of this equation is identical to the operator term in Equation 4.29 and so will equal zero if $V^{\text{off}(0)}T = 0$. The second term (the sum of the two commutators) will be zero for a symmetric sequence of toggling-frame phases. Thus, on account of their symmetry properties, the ASBO-9 and ASBO-11 families of dual-compensated composite pulses are broadband up to first order, $V^{\text{inh}(0)}T = V^{\text{off}(0)}T = V^{\text{inh}(1)}T = V^{\text{off}(1)}T = V^{\text{inh,off}(1)}T = 0$.

4.2.6 ASBO composite pulses

It is possible to choose pulses in the ASBO-9 family that have pulse phases $\phi_1 = \phi_2$ (ASBO-9(7A)), $\phi_2 = \phi_3$ (ASBO-9(7B)), $\phi_3 = \phi_4$ (ASBO-9(7C)) or $\phi_4 = \phi_5 = \phi_6$ (ASBO-9(7D)). These "7-pulse" solutions are listed in Table 4.1. Although the duration of these sequences is, of course, still equal to 9 simple 180° pulses, it is possible that they could be more robust in experimental practice owing to the reduced number of phase shifts involved. Similarly, there are "9-pulse" solutions for the ASBO-11 series of composite

TABLE 4.1: Broadband composite pulses

Pulse	Sequence	ϕ $[\cos^{-1}(-0.25)]$	Ξ_{B_1}	Ξ_Ω
ASBO-9(7A)	$360^\circ_{162.4^\circ}\ 180^\circ_{313.4^\circ}\ 180^\circ_{284.5^\circ}\ 180^\circ_{0^\circ}\ 180^\circ_{75.5^\circ}\ 180^\circ_{46.6^\circ}\ 360^\circ_{197.6^\circ}$	104.5°	0.178	0.428
ASBO-9(7B)	$180^\circ_{46.6^\circ}\ 360^\circ_{255.5^\circ}\ 180^\circ_{75.5^\circ}\ 180^\circ_{0^\circ}\ 180^\circ_{284.5^\circ}\ 360^\circ_{104.5^\circ}\ 180^\circ_{313.4^\circ}$	255.5°	0.325	0.324
ASBO-9(7C)	$180^\circ_{46.6^\circ}\ 180^\circ_{75.5^\circ}\ 360^\circ_{255.5^\circ}\ 180^\circ_{0^\circ}\ 360^\circ_{104.5^\circ}\ 180^\circ_{284.5^\circ}\ 180^\circ_{313.4^\circ}$	75.5°	0.325	0.332
ASBO-9(7D)	$180^\circ_{104.5^\circ}\ 180^\circ_{29^\circ}\ 180^\circ_{104.5^\circ}\ 540^\circ_{0^\circ}\ 180^\circ_{255.5^\circ}\ 180^\circ_{331^\circ}\ 180^\circ_{255.5^\circ}$	180°	0.150	0.308
ASBO-9(B_1)	$180^\circ_{268.5^\circ}\ 180^\circ_{62^\circ}\ 180^\circ_{6.5^\circ}\ 180^\circ_{131^\circ}\ 180^\circ_{0^\circ}\ 180^\circ_{229^\circ}\ 180^\circ_{353.5^\circ}\ 180^\circ_{298^\circ}\ 180^\circ_{91.5^\circ}$	311°	0.485	0.228
ASBO-9(Ω)	$180^\circ_{176.5^\circ}\ 180^\circ_{173^\circ}\ 180^\circ_{320.5^\circ}\ 180^\circ_{288^\circ}\ 180^\circ_{0^\circ}\ 180^\circ_{72^\circ}\ 180^\circ_{39.5^\circ}\ 180^\circ_{187^\circ}\ 180^\circ_{183.5^\circ}$	108°	0.174	0.444
ASBO-11(B_1)	$180^\circ_{260^\circ}\ 180^\circ_{103.5^\circ}\ 180^\circ_{187^\circ}\ 180^\circ_{119.5^\circ}\ 180^\circ_{292^\circ}180^\circ_{0^\circ}\ 180^\circ_{68^\circ}\ 180^\circ_{240.5^\circ}\ 180^\circ_{173^\circ}\ 180^\circ_{256.5^\circ}\ 180^\circ_{100^\circ}$	188° [104.5°]	0.369	0.240
ASBO-11(Ω)	$180^\circ_{220^\circ}\ 180^\circ_{287.5^\circ}\ 180^\circ_{235^\circ}\ 180^\circ_{31.5^\circ}\ 180^\circ_{68^\circ}180^\circ_{0^\circ}\ 180^\circ_{292^\circ}\ 180^\circ_{328.5^\circ}\ 180^\circ_{125^\circ}\ 180^\circ_{72.5^\circ}\ 180^\circ_{140^\circ}$	52° [104.5°]	0.178	0.540
Simple	$180^\circ_{0^\circ}$	-	0.062	0.100
LF	$90^\circ_{90^\circ}\ 180^\circ_{0^\circ}\ 90^\circ_{90^\circ}$	-	0.046	0.096
TP	$360^\circ_{0^\circ}\ 180^\circ_{120^\circ}\ 180^\circ_{60^\circ}\ 180^\circ_{120^\circ}$	-	0.106	0.256
TPG	$180^\circ_{256^\circ}\ 180^\circ_{52^\circ}\ 180^\circ_{0^\circ}\ 180^\circ_{128^\circ}\ 180^\circ_{0^\circ}\ 180^\circ_{232^\circ}\ 180^\circ_{0^\circ}\ 180^\circ_{308^\circ}\ 180^\circ_{104^\circ}$	-	0.473	0.224

pulses but these would appear to be of lesser interest in view of the existence of the ASBO-9 family.

From the ASBO-9 and ASBO-11 families, the composite pulse sequences which are of most interest are those with the greatest bandwidths, either with respect to $\omega_1 = |\gamma B_1|$ or Ω. These were found by incrementing the free phase ϕ in steps of 1° from 0° to 360°, allowing for both $\cos^{-1}(-0.25) = 104.5^\circ$ and $\cos^{-1}(-0.25) = 255.5^\circ$ for ASBO-11. For each resulting composite pulse, the range of B_1/B_1^{nom} and $\Omega/\omega_1^{\text{nom}} = |\Delta B/B_1^{\text{nom}}|$ values where the echo amplitude retains $> 99.0\%$ of its full amplitude was calculated. For B_1 inhomogeneity, this range can be expressed as the fraction, Ξ_{B_1}, of the range of B_1/B_1^{nom} from 0 to 2 where the echo amplitude retains $> 99.0\%$ of its amplitude at B_1/B_1^{nom}. Thus Ξ_{B_1} can take values from 0 (no broadband properties) up to 1 (a hypothetical, perfect broadband pulse for B_1 inhomogeneity). For resonance offset, the performance of an antisymmetric pulse sequence is asymmetric with respect to $\Omega = 0$

(it is only symmetric for a symmetric sequence). Therefore, we calculate the range of offset parameters $\Omega/\omega_1^{\text{nom}}$ where the echo amplitude retains $> 99.0\%$ of its amplitude at $\Omega = 0$ for both positive and negative offsets and then assign to the offset figure of merit, Ξ_Ω, the smaller of the two values. Thus Ξ_Ω can take values from 0 (no broadband properties) up to ∞ (a hypothetical, perfect broadband pulse for resonance offset). A value of Ξ_Ω of, for example, 0.402 means that the spin-echo amplitude has $> 99.0\%$ of its full amplitude between $\Omega/\omega_1^{\text{nom}} = 0.402$ and $+0.402$ and that possibly, at one extreme of this range, the composite pulse might have an even broader bandwidth.

Table 4.1 gives the optimum ASBO-9 and ASBO-11 pulses for B_1 inhomogeneity (ASBO-9(B_1) and ASBO-11(B_1)) and resonance offset (ASBO-9(Ω) and ASBO-11(Ω)) found by this method, where their bandwidths are compared with the "7-pulse" ASBO-9 sequences mentioned above. Appendix E contains grapefruit plots of magnetisation vectors tracing out the path of each of these ASBO pulses as well as TPG. It is important to stress that all members of the ASBO-9 and ASBO-11 families of composite pulse are dual-compensated for B_1 inhomogeneity and offset and our computer search is merely for the purpose of identifying solutions with particular properties; indeed, the minimum values of Ξ_{B_1} and Ξ_Ω found in these families $\Xi_{B_1} = 0.142$ and $\Xi_\Omega = 0.224$ for ASBO-9 and $\Xi_{B_1} = 0.118$ and $\Xi_\Omega = 0.184$ for ASBO-11) are still greatly in excess of the values for a simple 180° pulse.

For comparison, Table 4.1 also lists some composite pulses from the literature, along with their Ξ_{B_1} and Ξ_Ω values, as well as a comparison with a simple 180° pulse. LF, the original broadband composite 180° pulse proposed by Levitt and Freeman is not of the phase-distortionless type and symmetric and so its Ξ_{B_1} and Ξ_Ω refocusing bandwidth values are even lower than those of the simple 180° pulse. The sequence $360^\circ_{0^\circ}\ 180^\circ_{120^\circ}\ 180^\circ_{60^\circ}\ 180^\circ_{120^\circ}$ (here designated TP), which has been discussed above in Section 4.2.4 [58, 60], was designed to be phase-distortionless and dual-compensated with respect to both B_1 inhomogeneity and offset Ω but its Ξ_{B_1} and Ξ_Ω values are significantly lower than, e.g., the ASBO-9(Ω) pulse. Finally, the 9-pulse antisymmetric composite 180° pulse $180^\circ_{256^\circ}\ 180^\circ_{52^\circ}\ 180^\circ_{0^\circ}\ 180^\circ_{128^\circ}\ 180^\circ_{0^\circ}\ 180^\circ_{232^\circ}\ 180^\circ_{0^\circ}\ 180^\circ_{308^\circ}\ 180^\circ_{104^\circ}$ (designated TPG here) was presented in Reference [60] without any verifying simulations or experiments yet can be seen to be similar to the sequence ASBO-9(B_1) and to yield similar Ξ_{B_1} and Ξ_Ω values. It in fact corresponds to the ASBO-9 family described by Equations 4.31 with $\phi \approx 308^\circ$. Composite pulses were derived in Reference [60] using "fixed point theory".

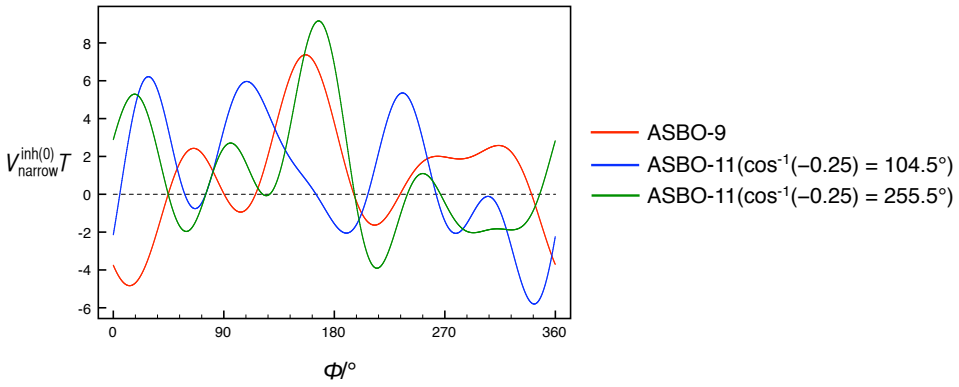

FIGURE 4.3: Plots of $V^{\text{inh}(0)}_{\text{narrow}}T = \omega_1\tau\sum_{j=1}^{N} I_{\phi_j}$ (here we set $\omega_1\tau = 1$) for ASBO-9 and ASBO-11 families of dual-compensated 180° pulses. Passband solutions exist where $V^{\text{inh}(0)}_{\text{narrow}}T = 0$.

4.2.7 Passband solutions

As described in Chapter 2, passband composite 180° pulses have B_1 inversion profiles that are locally narrowband for $B_1 \approx 0$ and locally broadband for $B_1 \approx B_1^{\text{nom}}$. It is worth examining the dual-compensated ASBO families for composite broadband 180° pulses simultaneously exhibit narrowband behaviour. A narrowband pulse has $H^{\text{nom}} = 0$ in Equation 4.1 and so there is no transformation into the toggling frame. For B_1 inhomogeneity, the zeroth-order average Hamiltonian in the narrowband region is simply given by

$$V^{\text{inh}(0)}_{\text{narrow}}T = \omega_1\tau\sum_{j=1}^{N} I_{\phi_j} \tag{4.38}$$

where the phases $\{\phi_j\}$ are the actual pulse phases rather than the toggling frame phases in Equation 4.26. As this is a real function for an antisymmetric sequence, $V^{\text{inh}(0)}_{\text{narrow}}T$ can be plotted as a function of ϕ in Equation 4.31 or 4.32 and the values of ϕ where $V^{\text{inh}(0)}_{\text{narrow}}T = 0$, which will correspond to passband solutions, can be read off. Figure 4.3 shows plots of these functions for the ASBO-9 and two ASBO-11 families. For the ASBO-9 family generated by Equation 4.31 there are six passband solutions between $\phi = 0$ and 360° and for the ASBO-11 family generated by Equation 4.32 there are six solutions forcos$^{-1}(-0.25) = 104.5°$ and eight for $\cos^{-1}(-0.25) = 255.5°$. The most promising of these sequences in terms of broadband B_1 performance (ASBO-9(PB_1) and ASBO-11(PB_1)) and broadband offset performance (ASBO-9(PΩ) and ASBO-11(PΩ)) are given in Table 4.2.

TABLE 4.2: Passband composite 180° pulses

Pulse	Sequence	ϕ $[\cos^{-1}(-0.25)]$	Ξ_{B_1}	Ξ_Ω
ASBO-9(PB_1)	$180^\circ_{26.5^\circ}$ $180^\circ_{149^\circ}$ $180^\circ_{64.5^\circ}$ $180^\circ_{160^\circ}$ $180^\circ_{0^\circ}$ $180^\circ_{220^\circ}$ $180^\circ_{295.5^\circ}$ $180^\circ_{211^\circ}$ $180^\circ_{333.5^\circ}$	340°	0.234	0.228
ASBO-9(PΩ)	$180^\circ_{104.5^\circ}$ $180^\circ_{119^\circ}$ $180^\circ_{284.5^\circ}$ $180^\circ_{270^\circ}$ $180^\circ_{0^\circ}$ $180^\circ_{90^\circ}$ $180^\circ_{75.5^\circ}$ $180^\circ_{241^\circ}$ $180^\circ_{255.5^\circ}$	108°	0.174	0.444
ASBO-11(PB_1)	$180^\circ_{165^\circ}$ $180^\circ_{27.5^\circ}$ $180^\circ_{130^\circ}$ $180^\circ_{81.5^\circ}$ $180^\circ_{273^\circ}$ $180^\circ_{0^\circ}$ $180^\circ_{87^\circ}$ $180^\circ_{278.5^\circ}$ $180^\circ_{230^\circ}$ $180^\circ_{332.5^\circ}$ $180^\circ_{195^\circ}$	207° [104.5°]	0.253	0.236
ASBO-11(PΩ)	$180^\circ_{190^\circ}$ $180^\circ_{263.5^\circ}$ $180^\circ_{217^\circ}$ $180^\circ_{19.5^\circ}$ $180^\circ_{62^\circ}$ $180^\circ_{0^\circ}$ $180^\circ_{298^\circ}$ $180^\circ_{340.5^\circ}$ $180^\circ_{143^\circ}$ $180^\circ_{96.5^\circ}$ $180^\circ_{170^\circ}$	58° [104.5°]	0.190	0.508

Note that because of the antisymmetry of the pulse phases none of these sequences will have $V^{\mathrm{inh}(1)}_{\mathrm{narrow}}T = 0$. They will have $V^{\mathrm{off}(0)}_{\mathrm{narrow}}T = 0$ but this is not a desirable feature; ideally, one would wish for broadband behaviour with respect to offset for $B_1 \approx 0$ but this is not possible.

4.3 Simulations

The performance of broadband composite 180° pulses in a spin-echo experiment was simulated assuming an initial state $\sigma^{\mathrm{initial}} = -I_y$ (the result of a perfect $90^\circ_{0^\circ}$ pulse on an I_z state). The pure echo signal was selected by incrementing the overall phase of the refocusing pulse through the four steps of the "Exorcycle" phase cycle [26, 46] and summing the resulting magnetisations appropriately over the four steps such that the ideal result should be $\sigma^{\mathrm{final}} = +I_y$. We then plotted the desired in-phase magnetisation component $\langle I_y \rangle = \mathrm{Tr}\{\sigma^{\mathrm{final}} I_y\}/\mathrm{Tr}\{{I_y}^2\}$ and (where necessary) the unwanted out-of-phase component $\langle I_x \rangle = \mathrm{Tr}\{\sigma^{\mathrm{final}} I_x\}/\mathrm{Tr}\{{I_x}^2\}$ as a function of B_1/B_1^{nom} (to study performance in the presence of B_1 inhomogeneity) or $\Delta B/B_1^{\mathrm{nom}}$(to study performance in the presence of a resonance offset), where $\Delta B = -\Omega/\gamma$ is the residual static field in the rotating frame, with the offset of the resonance from the transmitter frequency Ω and the gyromagnetic ratio γ.

The simulations shown in Figure 4.4 illustrate the effect of the symmetry of a composite 180° pulse on the phase of the refocused magnetisation as a function of normalised B_1

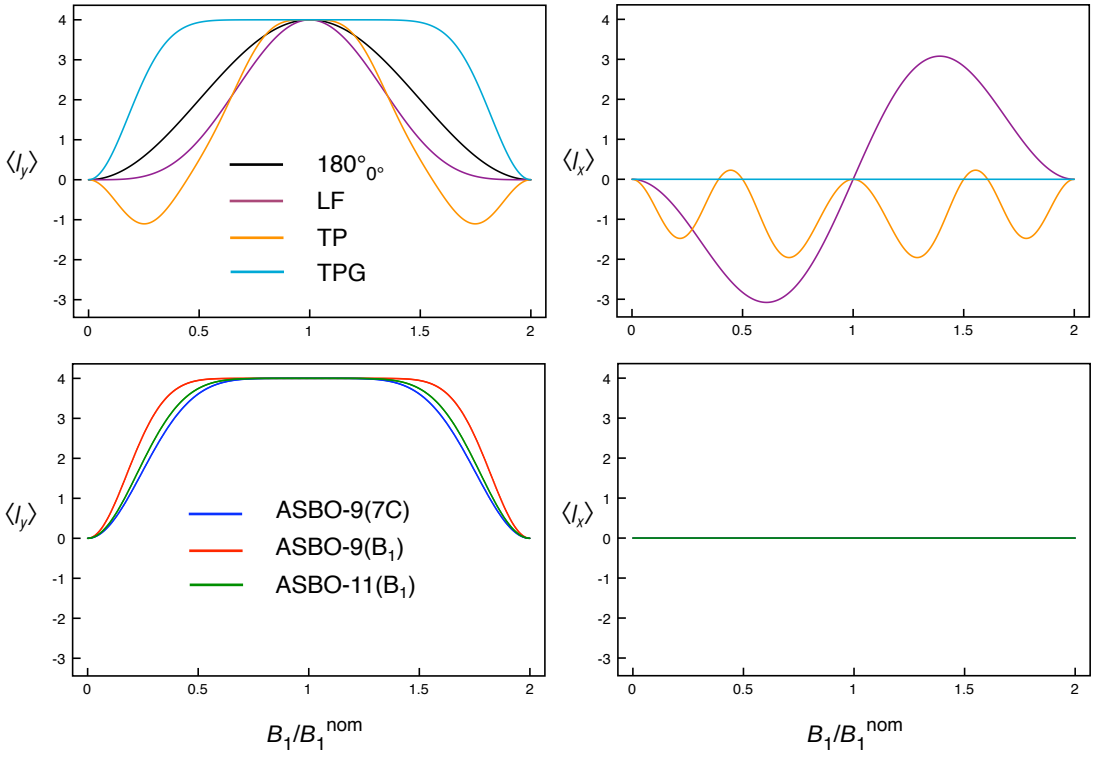

FIGURE 4.4: Simulations of the refocusing performance of broadband composite 180° pulses in a spin-echo experiment as a function of B_1/B_1^{nom} (to study performance in the presence of B_1 inhomogeneity). The simulations assume an initial state $\sigma^{\text{initial}} = -I_y$ and a refocusing pulse that has been subjected to the four steps of the Exorcycle phase cycle. (Top row) In-phase magnetisation component $\langle I_y \rangle$ and (b) the unwanted out-of-phase component $\langle I_x \rangle$ produced by a simple $180^\circ_{0^\circ}$ pulse and the composite pulses LF, TP and TPG (see Table 4.1). Only the simple refocusing pulse (which is technically antisymmetric) and the antisymmetric TPG sequence yield a zero out-of-phase component. (Bottom row) In-phase $\langle I_y \rangle$ and unwanted $\langle I_x \rangle$ spin-echo components produced by three of the new antisymmetric ASBO sequences (see Table 4.1). All of these antisymmetric ASBO sequences yield a zero out-of-phase component.

field strength, B_1/B_1^{nom}. The $\langle I_y \rangle$ magnetisation produced by a simple 180° pulse, as well as the broadband composite pulses LF, TP and TPG, has been simulated. When used as a refocusing pulse, the response of LF to B_1 inhomogeneity is in fact narrowband compared to the simple 180° pulse. TPG shows the most broadband response of these composite pulses. The symmetric sequence LF and the asymmetric composite pulse TP both give rise to an unwanted I_x magnetisation component in the presence of a B_1 inhomogeneity. Conversely, the simple 180° pulse and the antisymmetric TPG pulse sequence do not yield any unwanted I_x magnetisation when the B_1 field strength deviates from the nominal value. As was stated in Chapter 2, antisymmetric refocusing sequences are essential, as they will produce a spin echo with perfect phase.

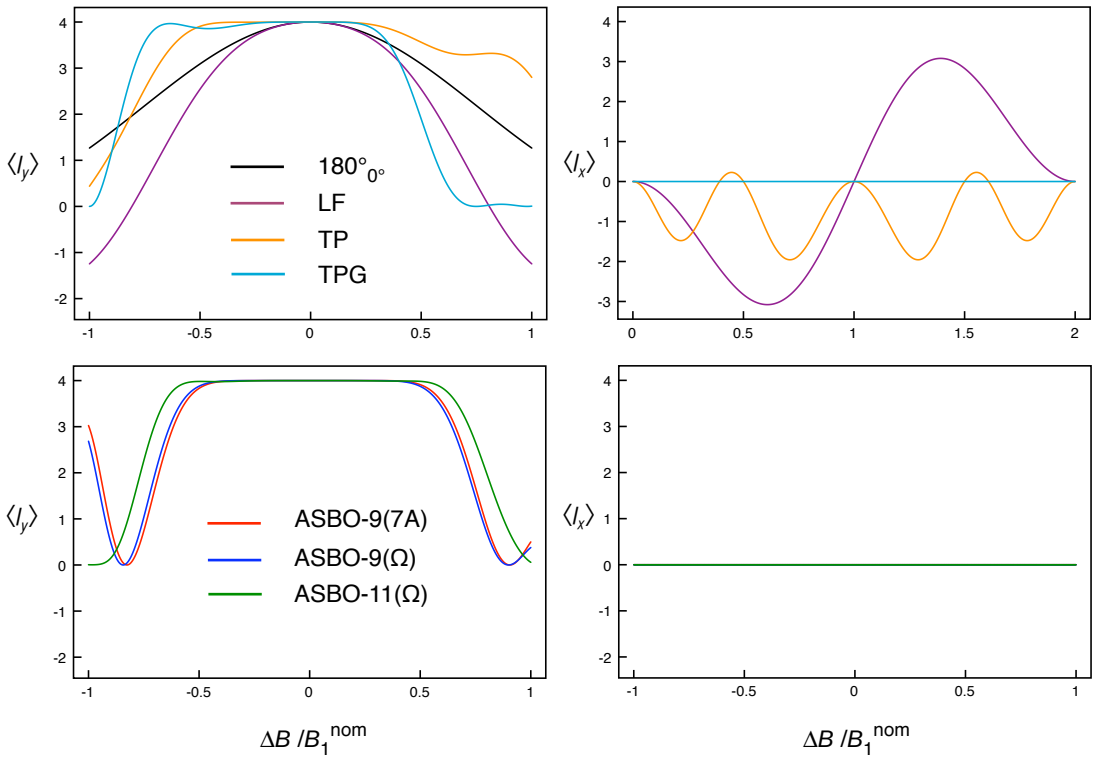

FIGURE 4.5: Simulations of the refocusing performance of broadband composite 180° pulses in a spin-echo experiment as a function of $\Delta B/B_1^{\text{nom}}$ (to study performance in the presence of resonance offset). The simulations assume an initial state $\sigma^{\text{initial}} = -I_y$ and a refocusing pulse that has been subjected to the four steps of the Exorcycle phase cycle. (Top row) In-phase magnetisation component $\langle I_y \rangle$ and (b) the unwanted out-of-phase component $\langle I_x \rangle$ produced by a simple $180°_{0°}$ pulse and the composite pulses LF, TP and TPG (see Table 4.1). Only the simple refocusing pulse (which is technically antisymmetric) and the antisymmetric TPG sequence yield a zero out-of-phase component. (Bottom row) In-phase $\langle I_y \rangle$ and unwanted $\langle I_x \rangle$ spin-echo components produced by three of the new antisymmetric ASBO sequences (see Table 4.1). All of these antisymmetric ASBO sequences yield a zero out-of-phase component.

Three of our novel antisymmetric dual-compensated composite pulses have also been simulated in Figure 4.4 as a function of B_1/B_1^{nom}: ASBO-9(7C), which shows the best response to B_1 inhomogeneity amongst the "7-pulse" solutions to the ASBO-9 family; ASBO-9(B_1), which has the greatest B_1 bandwidth of all our new composite pulses and is slightly more broadband than the existing pulse sequence TPG; and ASBO-11(B_1) – this sequence has the best performance in the presence of B_1 inhomogeneity in the 11-pulse set. Owing to the antisymmetric phase schemes of these pulse sequences, no out-of-phase I_x magnetisation is produced by any of these composite pulses.

The performance of a simple 180° pulse and various composite refocusing pulses with

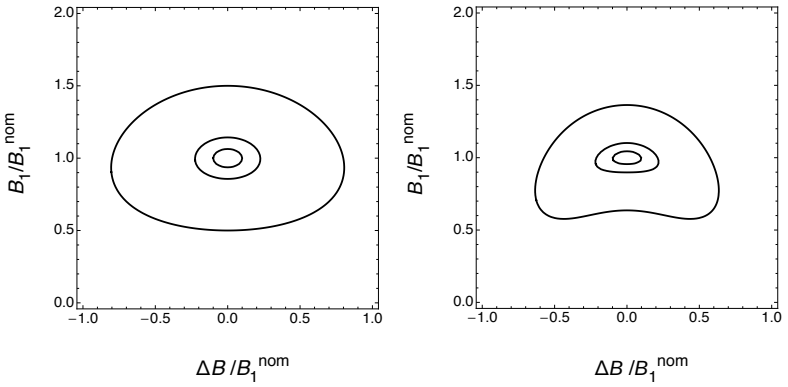

(a) $180^\circ_{0^\circ}$ (b) LF

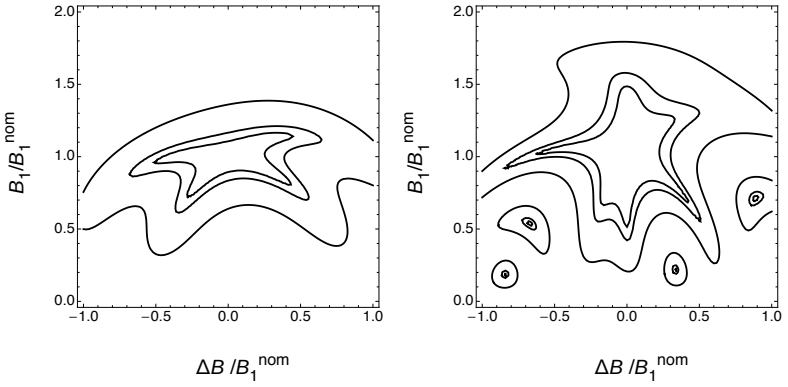

(c) TP (d) ASBO-9(B_1)

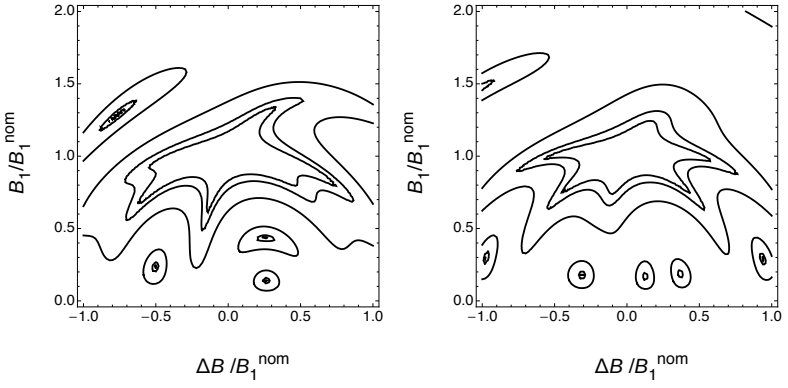

(e) ASBO-9(Ω) (f) ASBO-11(Ω)

FIGURE 4.6: Simulations of the in-phase $\langle I_y \rangle$ component yielded by various broadband composite 180°pulses in a spin-echo experiment as a function of B_1/B_1^{nom} and $\Delta B/B_1^{\text{nom}}$. The results are presented as a two-dimensional contour plot, with contours drawn at 99%, 95% and 50% of the maximum. The simulations assume an initial state $\sigma^{\text{initial}} = -I_y$ and a refocusing pulse that has been subjected to the four steps of the Exorcycle phase cycle. The LF and TP composite pulses are not antisymmetric and will also yield an unwanted out-of-phase $\langle I_x \rangle$ component (not shown).

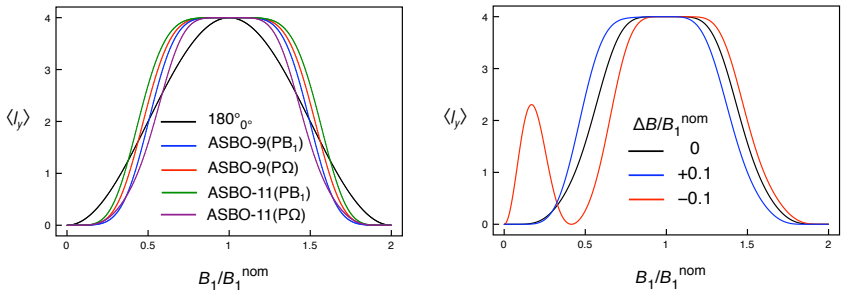

FIGURE 4.7: Simulations of the refocusing performance of passband ASBO pulses in a spin-echo experiment as a function of B_1/B_1^{nom} . The simulations assume an initial state $\sigma^{initial} = -I_y$ and a refocusing pulse that has been subjected to the four steps of the Exorcycle phase cycle. (a) In-phase magnetisation component $\langle I_y \rangle$ (the $\langle I_x \rangle$ component is zero) produced by a simple $180^\circ_{0^\circ}$ pulse and the passband composite pulses listed in Table 4.2). In (b), the performance of the passband sequence ASBO-11(PΩ) is simulated on resonance and at resonance offset parameters of $\Delta B/B_1^{nom} = +0.1$ and $\Delta B/B_1^{nom} = -0.1$.

respect to resonance offset is shown in Figure 4.5. As with the case of B_1 inhomogeneity, only the antisymmetric sequences do not produce any I_x magnetisation off-resonance. The composite pulses LF and TP will reintroduce phase distortions into the spectrum as out-of-phase I_x magnetisation results when the transmitter is not on resonance. The offset performance of three of the new dual-compensated 180° pulses are shown: ASBO-9(7A), the optimum "7 pulse" solution of the ASBO-9 set for compensating offset; ASBO-9(Ω), which performs very slightly better; and ASBO-11(Ω), which has the greatest bandwidth for resonance offset. These pulse sequences are all more broadband for offset than the dual-compensated pulses TP and TPG.

The dual-compensated nature of the ASBO composite pulses can be fully appreciated in the contour plots shown in Figure 4.6. The spin-echo experiment was simulated using a simple 180° pulse (Figure 4.6(a)) the composite refocusing pulses LF (Figure 4.6(b)), TP (Figure 4.6(c)), ASBO-9(B_1) (Figure 4.6(d)), ASBO-9(Ω) Figure 4.6(e)) and ASBO-11(Ω) (Figure 4.6(f)), and the resulting $\langle I_y \rangle$ contours at 99%, 95% and 50% plotted as a function of B_1/B_1^{nom} and $\Delta B/B_1^{nom}$. Note that the symmetric LF and asymmetric TP sequences will also yield unwanted I_x magnetisation, which we do not show here.

In Figure 4.7(a) the refocusing performance of the passband composite 180 pulses ASBO-9(PB_1), ASBO-9(PΩ). ASBO-11(PB_1) and ASBO-11(PΩ) is shown as a function of B_1/B_1^{nom}. These sequences show broadband behaviour near the nominal field strength, but are locally narrowband at low B_1/B_1^{nom} values. As indicated in Table 4.2 ASBO-11(PΩ) has

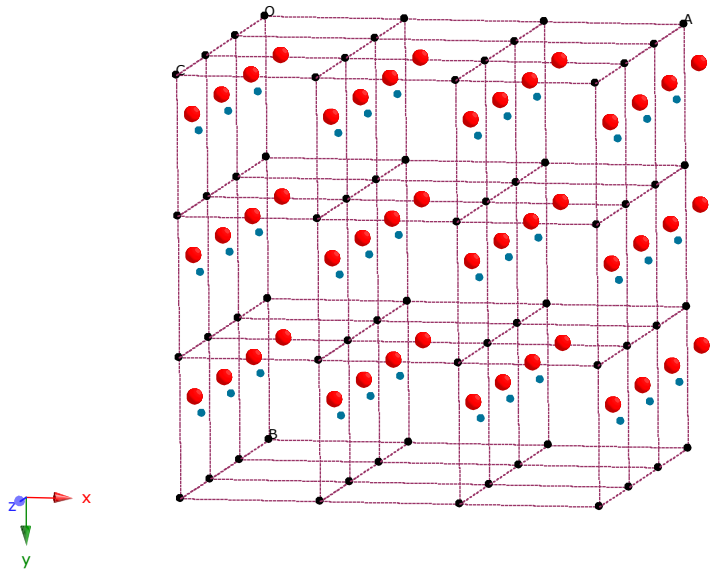

FIGURE 4.8: Crystal structure of BPO_4. Phosphorus atoms are shown in black, boron in blue and oxygen in red. The crystal structure was determined by Schulze [106].

the greatest value of Ξ_Ω of these sequences, indicating the best broadband offset performance. However, as shown in Figure 4.7(b) where this pulse sequence has been simulated with $\Delta B/B_1^{\text{nom}} = \pm 0.1$, it is not compensated for resonance offset in the narrowband region ($B_1/B_1^{\text{nom}} \sim 0.1$), as expected, despite being well compensated in the broadband region ($B_1/B_1^{\text{nom}} \sim 1$).

4.4 Experiments

4.4.1 ^{31}P solid-state NMR spin echoes

Experiments were performed on a Bruker Avance 400 NMR spectrometer equipped with a widebore 9.4 T magnet. The ^{31}P NMR spectrum of boron phosphate (BPO_4), which contains a single ^{31}P site (as shown in the crystal structure in Figure 4.8) was chosen as the subject of these experiments. This choice was made based on the current setup in our laboratory; other nuclei in both the solid and solution state and different probe designs are expected to yield equivalent results. The powdered solid sample was packed in a 4-mm MAS rotor, although the experiments were conducted without MAS.

The Larmor frequency was 162 MHz. The calibrated 90° pulse length for ^{31}P was 2.23 μs, corresponding to a nutation rate, $\nu_1 = |\gamma B_1|/2\pi$ of 112 kHz.

The pulse sequence used was a $90^\circ - \tau - R - \tau$ spin echo, where R is the simple or composite refocusing pulse. The τ interval was equal to 40 μs and timed from the centre of the 90° pulse to the centre of the R refocusing pulse and from the centre of the R pulse to the start of data acquisition. In all experiments, the four-step Exorcycle phase cycle was applied to the refocusing pulse R, and nested with four-step CYCLOPS, giving the overall phase cycle described in Table 3.1. The spectra recorded using the composite pulse ASBO-9(B_1) (solid line) are overlaid by the simple spin echo (dashed line) in Figure 4.9.

Figure 4.9(a) shows on-resonance spectra recorded with calibrated pulse durations. The spectrum recorded with a simple 180° pulse was phased and this same phase correction was applied to other on-resonance experiments. The solenoidal radiofrequency coil produces an inhomogeneous B_1 field; the composite pulse ASBO-9(B_1) compensates for this imperfection and yields a spin-echo signal with a greater amplitude than the simple 180° pulse.

To investigate the pulse performance in the presence of a resonance offset, the ^{31}P spin-echo spectrum was obtained with a simple 180° refocusing pulse with the transmitter offset by 22.4 kHz from the centre of the spectrum (corresponding to a normalised offset parameter $\Delta B/B_1^{\mathrm{nom}} = 0.2$ in Figure 4.9(b). The spectrum was phased and the same phase correction then applied to the other experiments performed with this offset. The simple spin echo yields a similar spectrum to its on-resonance counterpart. While the off-resonance composite pulse spectrum in Figure 4.9(b) shows a slight decrease in amplitude compared to the composite pulse spin echo in Figure 4.9(a), it still performs slightly better than the simple pulse.

To exacerbate the effect of B_1 inhomogeneity intentionally, the spin-echo experiments were repeated with the constituent elements of the refocusing pulses misset to 60% of their correctly calibrated durations (i.e., each 180° pulse element replaced with a 108° pulse). The results are shown in Figure 4.9(c). Here, the ASBO composite pulse echo clearly outperforms the simple echo, yielding a signal amplitude 40% greater than the simple echo.

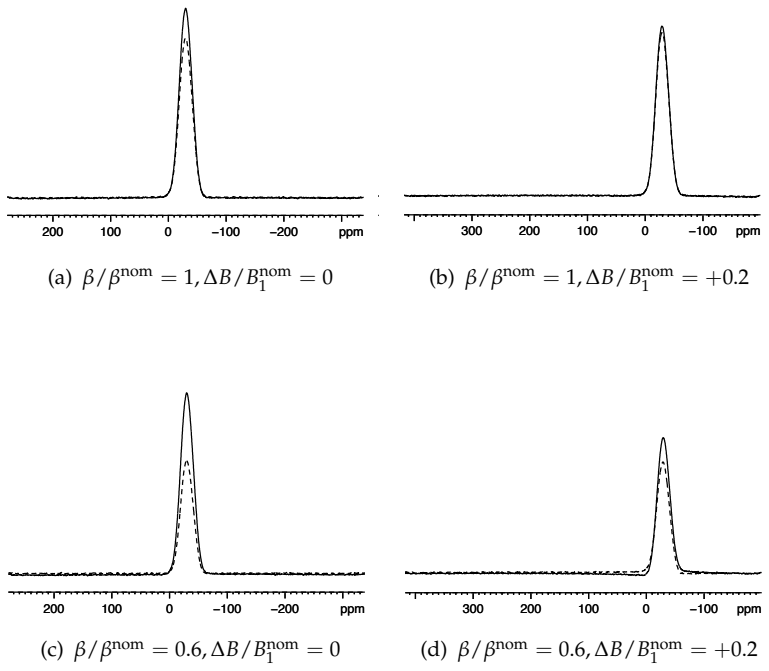

(a) $\beta/\beta^{\text{nom}} = 1, \Delta B/B_1^{\text{nom}} = 0$ (b) $\beta/\beta^{\text{nom}} = 1, \Delta B/B_1^{\text{nom}} = +0.2$

(c) $\beta/\beta^{\text{nom}} = 0.6, \Delta B/B_1^{\text{nom}} = 0$ (d) $\beta/\beta^{\text{nom}} = 0.6, \Delta B/B_1^{\text{nom}} = +0.2$

FIGURE 4.9: Static ^{31}P (162 MHz) NMR spin-echo spectra of solid BPO_4 (80 μs total echo interval, 90° pulse duration of 2.23 μs, spin-lattice relaxation interval of 600 s, four-step Exorcycle phase cycle applied to the refocusing pulse, 16 transients). Spectra shown in a dashed line were recorded with a simple 180° refocusing pulse, while those with a solid line used the dual-compensated pulse ASBO-9(B_1). The spectra in (a) were recorded on-resonance and with correctly calibrated pulse durations. In (b) and (d), the spectra were recorded 22.4 kHz off-resonance. In (c) and (d) the refocusing pulses were set to 60% of their correctly calibrated durations. The simple spin-echo spectra were phased for each offset frequency and these same phase corrections were applied to the composite pulse spectra.

In Figure 4.9(d), experiments were performed with an offset from resonance and with the refocusing pulse flip angles misset. Again, the composite pulse spectrum yields the greatest signal intensity. A small, unexpected phase error is apparent in the ASBO spectrum here. Repeating the simple echo sequence in Figure 4.9(a) again, it was found that the phase had changed during the timescale of the set of experiments which had been run sequentially over a total time of almost 2 days (for BPO_4 a 10 minutes interval was used between each transient, giving an experiment time of 160 minutes for a 16-scan spin-echo experiment). Rather than being a fault of the composite pulse sequence, this error is attributed to the instability of the NMR instrument over a time period, with unavoidable experimental effects arising for samples with long relaxation intervals.

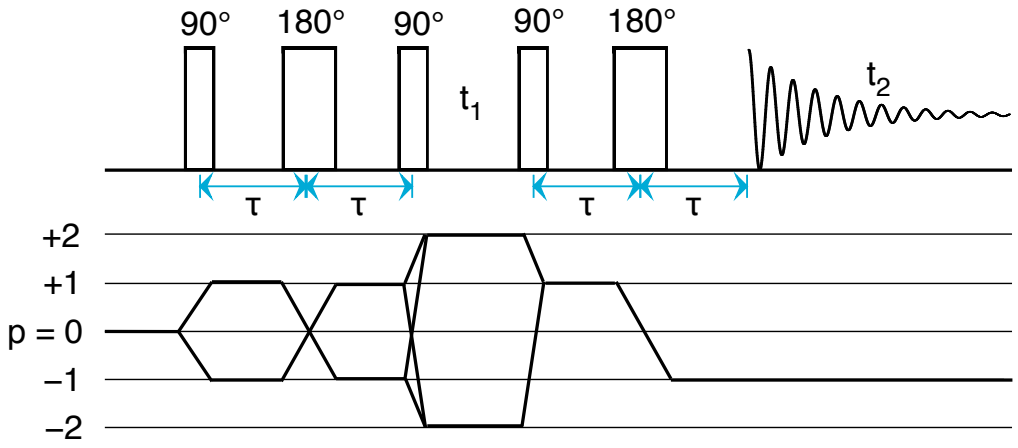

FIGURE 4.10: Pulse sequence and coherence transfer pathway diagram of the refocused INADEQUATE experiment.

4.4.2 Refocused INADEQUATE

In solid-state NMR, experiments examining through-bond J-couplings present a challenge as most solid compounds with restricted molecular motion possess strong dipolar couplings which obscure the much smaller J-couplings. However, the popular INADEQUATE experiment [107] from solution-state NMR has successfully been adapted for magic angle spinning experiments [108–110], allowing the observation of J-coupled sites in a two-dimensional experiment. The refocused INADEQUATE experiment [111] features an extra spin echo to obtain in-phase lineshapes, making it more suitable for experiments on solids where there is often insufficient resolution to observe the antiphase multiplets created by the original INADEQUATE experiment [112]. The refocused INADEQUATE experiment has been widely employed to study a range of materials [111, 113–117]. Fayon et al. have demonstrated the possibility of determining the P–O–P connectivities in inorganic pyrophosphate compounds such as $Zn_2P_2O_7$ and TiP_2O_7 via ^2J couplings [113, 118, 119]. Here, we will demonstrate that the ASBO family of dual-compensated composite pulses can be incorporated into the refocused INADEQUATE experiment to improve the signal amplitude. In this case the simple refocusing pulse is prone to deleterious effects of B_1 inhomogeneity and offset effects in two spin echoes during the experiment, manifesting as a loss of sensitivity in the two-dimensional spectrum.

Figure 4.10 shows the pulse sequence and coherence transfer pathway diagram for the

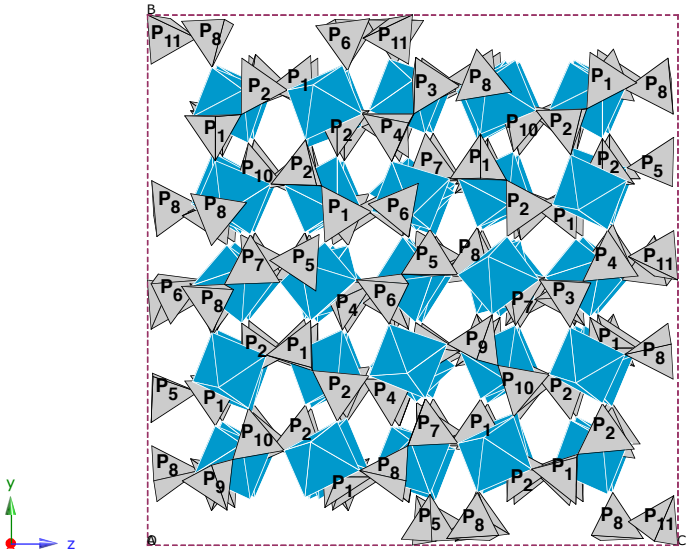

FIGURE 4.11: Unit cell of TiP_2O_7. PO_4 units are represented by grey tetrahedra while the TiO_8 units are represented by blue octahedra where each vertex corresponds to an oxygen. The crystal structure was determined by Norberg et al. [120]

refocused INADEQUATE experiment. After an initial 90° excitation pulse, the ^{31}P magnitsation is subjected to a spin echo which generates antiphase coherences through evolution under the J-coupling Hamiltonian. Theoretically, the best efficiency for generating this antiphase magnetisation is given by a spin-echo interval of $\tau = 1/(4J_{IS})$. The τ interval must be equal to an integer number of rotor periods, $\tau = n\tau_R$, so that the homonuclear dipolar couplings are removed by MAS. The antiphase coherences are converted by a 90° pulse into double-quantum (DQ) coherences between J-coupled nuclei, which evolves during the t_1 period at a frequency which is the sum of the single-quantum (SQ) frequencies of the two spins:

$$\omega_{\mathrm{DQ}} = \omega^I_{\mathrm{SQ}} + \omega^S_{\mathrm{SQ}} \tag{4.39}$$

Finally, these are converted back into antiphase coherences by a 90° pulse and transformed into in-phase coherence by the second spin echo before detection in the t_2 period.

Experiments were carried out on titanium pyrophosphate (TiP_2O_7), which was kindly provided by Dr. Gregory Tricot of Université de Lille Nord de France. The TiP_2O_7

TABLE 4.3: Assignment of the ^{31}P resonances for TiP_2O_7 [118, 120]

P site	δ_{iso}/ppm
P_1	−49.2
P_2	−49.5
P_3	−40.6
P_4	−44.5
P_5	−43.0
P_6	−40.4
P_7	−44.4
P_8	−38.6
P_9	−51.8
P_{10}	−52.6
P_{11}	−46.2

structure consists of corner-sharing distorted TiO_8 octahedra and PO_4 tetrahedra, giving rise to a structure with eleven crystallographically distinct phosphorus sites [120] as shown in Figure 4.11. The sample (a white powder) was packed in a 4-mm rotor and the calibrated 90° pulse length was 2.5 μs, corresponding to a nutation rate $\nu_1 = |\gamma B_1|/2\pi = 100$ kHz. A presaturation pulse train was prefixed to the pulse sequence shown in Figure 4.10, allowing a shortened relaxation interval of 1 s to be employed (using the full T_1 relaxation interval of approximately 3 minutes would render the experiment too long to be practical in our circumstances). Spectra were recorded at a MAS rate of $\omega_r/2\pi = 12.5$ kHz and with a rotor-synchronised spin-echo interval of $\tau = 8$ ms. Table 4.3 lists the eleven ^{31}P resonances observed in the NMR spectrum of TiP_2O_7 using the labeling of the phosphorus atom sites given by Norberg et al. [118**?**].

Figure 4.12 shows the first row of the two-dimensional INADEQUATE experiments. In Figure 4.12(a), a simple 180° pulse was used in both spin echoes, while in Figure 4.12(b) and Figure 4.12(c) each 180° pulse was replaced by a dual-compensated refocusing pulse from the ASBO family, either ASBO-9(B_1) or ASBO-9(7A). The difference in centreband signal intensity between the simple pulse INADEQUATE experiment, I_{SP}, and composite pulse echo experiments, I_{CP}, were examined for each line in the spectrum. These have been tabulated as a percentage change relative to the simple echo, $\{(I_{CP} - I_{SP})/I_{SP}\} * 100$ in Table 4.4. While the experiment using ASBO-9(B_1) is successful in increasing the signal amplitude of some of the peaks, P_1, P_2, P_9 and P_{10} actually decrease in intensity. This is unexpected, and alludes to problems in using

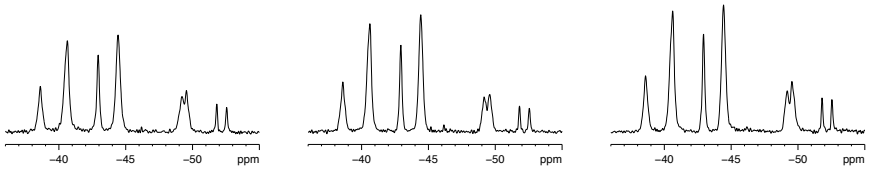

(a) $180^{\circ}_{0^{\circ}}$ (b) ASBO-9(B_1) (c) ASBO-9(7A)

FIGURE 4.12: ^{31}P (162 MHz) refocused INADEQUATE NMR spectra of solid TiP_2O_7 (8 ms total echo interval, 90° pulse duration of 2.5 μs, spin-lattice relaxation interval of 1 s with presaturation train, four-step Exorcycle phase cycle applied to the refocusing pulse, 64 transients). The first row of the two-dimensional experiment is shown using simple and composite refocusing pulses.

composite pulses in magic angle spinning experiments – this will be studied in detail in Chapter 5. As seen in Figure 4.6, antisymmetric pulses have asymmetric profiles with respect to the sign of the offset, which may explain why only the peaks with negative offset decrease in intensity. The results for the experiment using ASBO-9(7A) are more optimistic. Each peak shows an improvement in amplitude, with increases in intensity of up to one third using the composite pulse.

A full two-dimensional experiment was carried out using ASBO-9(7A), which showed the most promising results in Figure 4.12. The resulting spectrum is shown in Figure 4.13, along with F_1 and F_2 projections. Five pairs of double-quantum correlations are visible across the diagonal, indicating through-bond P–O–P connectivities in five distinct P_2O_7 units: (P_1–P_2), (P_3–P_4), (P_5–P_6), (P_7–P_8) and (P_9–P_{10}). An additional peak is seen on the diagonal at the single-quantum F_2 frequency of -44.5 ppm. Reference [118] addresses the origin of such anomalous diagonal peaks. The ASBO refocusing pulses were designed to compensate simultaneously for B_1 inhomogeneity and resonance offset effects to improve signal amplitude, and here we see they can be succesfully incorporated into two-dimensional experiments.

4.5 Conclusions

Novel antisymmetric broadband composite 180° pulses that are dual compensated, that is, compensated simultaneously for both resonance offset and inhomogeneity of the radiofrequency field, have been designed and evaluated. Using Exorcycle phase cycling to select the pure spin-echo signal, these refocusing pulses will produce no phase error

TABLE 4.4: Percentage change in signal intensity of each ^{31}P resonance in the TiP_2O_7 composite pulse INADEQUATE spectra shown in Figure 4.12(b) and Figure 4.12(c) compared to the simple INADEQUATE spectrum in Figure 4.12(a). $P_{11}$is not listed as its amplitude was not significantly above the noise level. P_3 and P_6 are listed under a single entry as they were not individually resolved; this was also the case for P_4 and P_7.

P site	ASBO-9(B_1) % change	ASBO-9(7A) % change
P_1	-3	$+13$
P_2	-10	$+21$
P_3 & P_6	$+19$	$+33$
P_4 & P_7	$+21$	$+31$
P_5	$+12$	$+27$
P_8	$+11$	$+24$
P_9	-6	$+21$
P_{10}	-6	$+28$

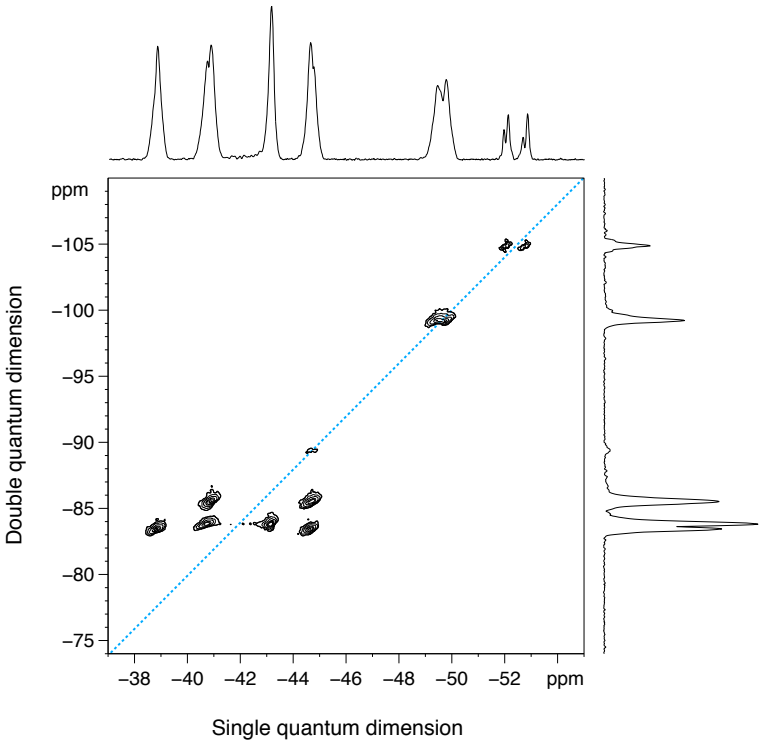

FIGURE 4.13: ^{31}P (162 MHz) two-dimensional refocused INADEQUATE NMR spectrum of solid TiP_2O_7 (8 ms total echo interval, 90° pulse duration of 2.5 μs, spin-lattice relaxation interval of 1 s with presaturation train, four-step Exorcycle phase cycle applied to the refocusing pulse, 64 transients). The refocusing pulse used was the dual-compensated pulse ASBO-9(7A).

across their entire bandwidth owing to the properties of pulses with antisymmetric phase schemes. This gives them advantage over phase-distortionless composite pulses in the literature – as most of these are based on symmetric or asymmetric phase shift schemes, they will introduce phase errors into spin-echo experiments.

The new antisymmetric composite pulses were designed using a graphical interpretation of average Hamiltonian theory, yielding an infinite family of 9-pulse refocusing sequences and an infinite family of 11-pulse sequences, all of which are dual-compensated to zeroth- and first-order. For applications where resonance offsets are small (e.g., ^{1}H NMR), the composite pulse ASBO-9(B_1) provides excellent compensation for B_1 inhomogeneity as well as good compensation for resonance offset. In cases where resonance offsets are larger (e.g., ^{13}C, ^{19}F, ^{31}P, ^{29}Si NMR), the composite pulses ASBO-9(7A), ASBO-9(Ω) and ASBO-11(Ω) could all be considered.

As well as verifying our new composite pulses with computer simulations, a number of ^{31}P experiments have been carried out. It has been shown that ASBO-9(B_1) outperforms a simple 180° refocusing pulse in a static spin-echo experiment, yielding an improvement in signal amplitude even in the presence of considerable pulse errors with deliberately large errors in flip angle and offset investigated. As an example of a two-dimensional application for these composite pulses, ASBO-9(7A) was included in the two spin-echo elements of the refocused INADEQUATE experiment, successfully showing the ability for compensation of B_1 inhomogeneity and offset effects.

Chapter 5

The effects of MAS on composite pulse performance

5.1 Introduction

A vast number of composite pulses have been designed for use in NMR experiments to compensate for imperfections in radiofrequency pulses, alleviating the common problems of B_1 inhomogeneity and resonance offset. In Chapter 2 we have shown that phase-antisymmetric refocusing pulses are the correct type to use when forming a spin echo [3], and in Chapter 4 introduced the new ASBO families of dual-compensated antisymmetric refocusing pulses. Composite pulses have been used widely in solution state NMR, and in principle the same pulse sequences can be employed in solid-state NMR applications. However, in solid-state NMR, there is the added complication that magic angle spinning introduces a time dependence to the internal interactions (chemical shift anisotropy, dipolar interactions and quadrupolar couplings) governing the offset of each crystallite over each rotor period. As a result, the resonance offset of each crystallite varies during the application of the radiofrequency pulses in MAS NMR. This may be overlooked if the pulse is of short duration and the change in offset is small during the pulse. However, we find that when the total duration of a composite pulse becomes comparable to the duration of the rotor period, the performance of the composite pulse is liable to deteriorate. In this Chapter, we investigate the effects of MAS on composite pulse performance in a spin echo. Computer simulations and ^{31}P

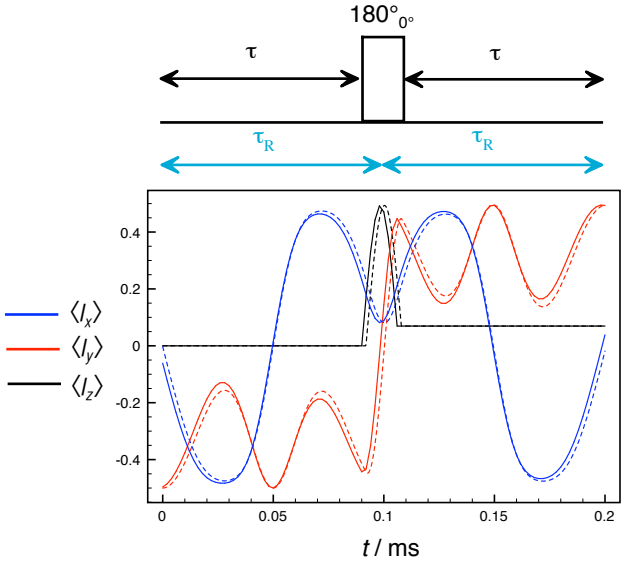

FIGURE 5.1: Simulation of a spin-echo sequence under MAS. The 90° pulse length used in the simulation was 6 μs, corresponding to a B_1 field strength of 41.67 kHz. Other parameters used in the simulation were $\nu_{\Delta CS}^{PAS} = \omega_{\Delta CS}^{PAS}/2\pi = 10$ kHz, $\nu_R = 10$ kHz, $\beta = 30°$, and $\phi = 0°$. The solid line simulation uses a time step which is too large to give a good approximation for the multi-step analysis of the evolution of the density matrix under MAS.

experiments will be carried out to investigate the ability of composite pulses to compensate for B_1 inhomogeneity and misset flip angles under MAS.

We note that Leppert et al. [121] introduced a number of composite 180° pulses designed specifically for MAS applications, and demonstrated their use in the TOSS (total suppression of spinning sidebands) experiment. However, the authors stated that their pulses were not expected to deliver optimal performance experimentally owing to their inability to compensate for non-ideal conditions such as B_1 field inhomogeneity. Since the application of these pulses is limited, we will not consider them further in this work.

5.2 Time dependence under MAS

As described in Section 2.5, resonances in solid-state NMR spectra are broadened by anisotropic interactions, with the most significant contributions from chemical shift anisotropy, dipolar couplings and for nuclei with spin $I \geq 1/2$, quadrupolar interactions. Most solid-state experiments are performed under MAS: by rapidly spinning the sample at the magic angle, a dramatic improvement in resolution can be achieved

(Section 2.6). In the simulations following, we will focus on a simple model system – an isolated spin $I = 1/2$ nucleus possessing a chemical shift anisotropy parameter, $\omega_{\Delta CS}^{PAS}(t)$, with a time-dependence governed by MAS.

As detailed in Section 2.2, the Liouville-von Neumann equation can be solved to calculate the time evolution of the density operator in cases where the Hamiltonian is time-independent. This is not the case under MAS, and so an alternative method must be used. Assuming that the time dependence of the Hamiltonian can be neglected on small timescales, the total experiment time can be broken down into small divisions and the evolution of the density matrix is calculated in successive time-independent steps [16, 122]. During each of these steps, the total Hamiltonian is given by

$$H = H_{CSA} \tag{5.1}$$

during periods of free precession or

$$H = H_{rf} + H_{CSA} \tag{5.2}$$

when an rf pulse is applied. The pulse Hamiltonian is

$$H_{rf} = \omega_1 I_x \tag{5.3}$$

(for a pulse with phase $\phi = 0^\circ$) and the CSA Hamiltonian is given by

$$H_{CSA} = \omega_{\Delta CS}(t) I_z \tag{5.4}$$

where the time-dependent chemical shift anisotropy is given by:

$$\omega_{\Delta CS}(t) = \frac{\omega_{\Delta CS}^{PAS}}{2}\{-\sqrt{2}\sin 2\beta \cos(\omega_R t + \xi) + \sin^2\beta \cos 2(\omega_R t + \xi)\} \tag{5.5}$$

Here, β is the angle between the spinning axis and the CSA tensor in its PAS and ξ is the initial phase about this axis. The magnitude of the CSA, $\omega_{\Delta CS}(t)$, will thus oscillate according to the rotor phase $\omega_R t$ where ω_R is the spinning rate and t is the time.

Figure 5.1 shows the evolution of x, y and z magnetisation as a single spin with initial state $-I_y$ (the result of a perfect 90° pulse on an inital state I_z) as it undergoes MAS during the spin-echo sequence $\tau - 180^\circ_{0^\circ} - \tau$. The 90° pulse length used in the simulation

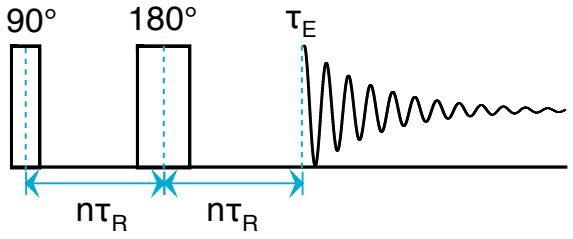

(a) The centred method

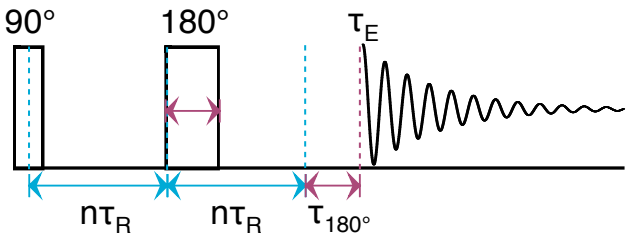

(b) The shifted method

FIGURE 5.2: Two methods of rotor synchronisation have been used in spin echo simulations and experiments.

was 6 μs, corresponding to a B_1 field strength of 41.7 kHz. The evolution of the density matrix was calculated in incremental progressions of 0.1 μs for the simulation in dashed lines, while a time increment of 2.0 μs was used for the solid line simulation. It can be seen that in this case that the increment of 2.0 μs is too large to provide a good approximation for calculating the time-dependent behaviour of the system. In the simulations throughout the rest of the chapter, each rotor period is divided into at least 1000 time increments (thus giving a 1.0 μs increment for calculations employing a spinning rate of $\nu_R = 1$ kHz, a 0.1 μs increment for calculations employing a spinning rate of $\nu_R = 10$ kHz, etc.)

5.3 Rotor synchronisation

Two different schemes of rotor synchronisation have been considered in the spin-echo simulations and experiments. These are illustrated in Figure 5.2. The first method, shown in Figure 5.2(a), is often used in MAS experiments: an integer number of rotor periods forms the time interval between the centre of the excitation pulse and the centre of the refocusing pulse. The echo should reach its maximum after a delay of the same

length, again timed from the centre of refocusing pulse. This rotor synchronisation scheme shall be referred to as the "centred method."

The second approach, which shall be termed the "shifted method", times an interval of an integer number of rotor periods between the centre of the excitation pulse and the start of the refocusing pulse. As shown in Figure 5.2(b), the signal is acquired an integer number of rotor periods after the end of the refocusing pulse. This is a novel approach to rotor synchronisation, and we will see that in some circumstances it offers significant advantages over the centred method in spin-echo experiments.

5.4 Simulations

Figure 5.3 plots the evolution of the I_y magnetisation for a spin-echo pulse sequence during MAS using either a simple 180° refocusing pulse or one of two dual-compensated composite pulses from the ASBO-9 family. The simulation follows the magnetisation over three rotor periods and includes powder averaging of orientations. The simulations use an initial state σ_{initial} of $-I_y$ (the result of a perfect 90° pulse on an equilibrium state I_z). After a perfect spin echo, we would expect the magnetisation to be fully aligned with the same intensity along the I_y axis. The MAS speed, ν_R, used in the simulations was equal to 10 kHz, giving a rotor period of $1/\nu_R = 0.1$ ms. The simulations were carried out with three rf field strengths: $\nu_1 = 250$, 125 and 62.5 kHz. The corresponding pulse lengths for a 180° pulse are 2, 4 and 8 μs, and for an ASBO-9 refocusing pulse 18, 36 and 72 μs.

The left-hand column of results shows the spin-echo sequence with the centred rotor synchronisation scheme. The refocusing pulse is timed such that the middle of the pulse coincides with the start of the second rotor period. The dashed vertical line indicates where the peak of the spin echo is expected to form at time τ_E. Using a simple spin-echo sequence with a 180° refocusing pulse, the magnetisation is fully refocused at 0.2 ms as expected for all rf strengths simulated here. However, in the simulations employing ASBO composite pulses, a deterioration in signal intensity is apparent at the echo time as the pulse lengthens. For the sequences using ASBO-9(B_1) and ASBO-9(7A), the magnetisation is refocused with almost full intensity at 0.2 ms with the strongest rf field strength, but raising the total pulse length to 36 μs results in a significant drop in

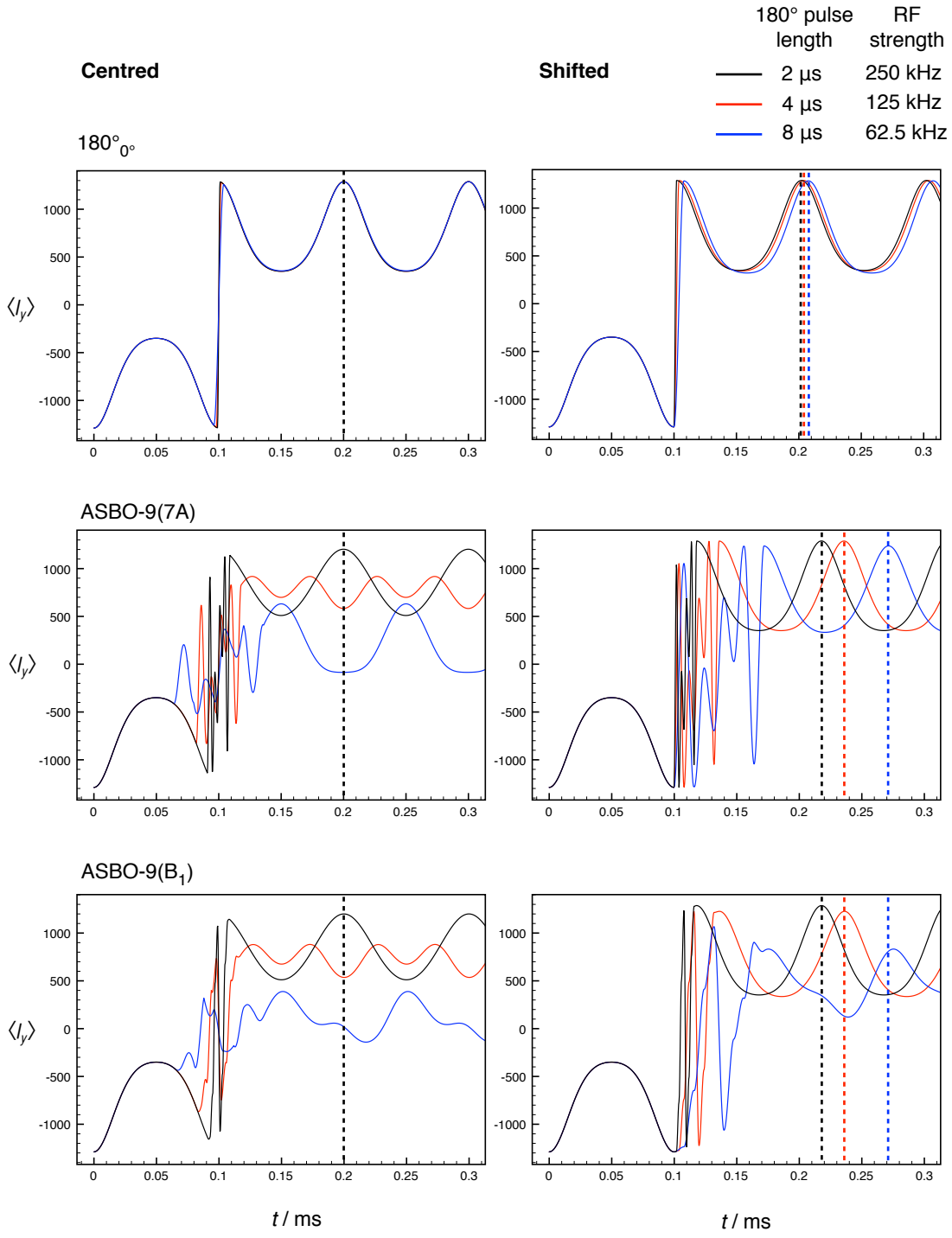

FIGURE 5.3: Simulation showing the refocusing of the I_y magnetisation for a powder under MAS using simple and composite refocusing pulses. The left-hand column uses centred rotor synchronisation, while the shifted method is employed in right-hand column. The 180° pulse lengths used in the simulation were 2 µs, 4 µs and 8 µs, corresponding to B_1 field strengths of 250 kHz, 125 kHz and 62.5 kHz, respectively. Other parameters used in the simulation were $\nu_{\Delta CS}^{PAS} = 10$ kHz and $\nu_R = \omega_R/2\pi = 10$ kHz (thus one rotor period is equal to 0.1 ms). The dashed vertical lines indicate where echo formation is expected.

I_y intensity, and with a pulse length of 72 μs the echo signal at time τ_E diminishes to almost zero.

The right-hand column of results in Figure 5.3 uses the shifted method of rotor synchronisation. Here the refocusing pulse is started at 0.1 ms, after a full rotor period has elapsed. The echo occurs at a time $\tau_E = \tau_R + \tau_P$ after the start of the pulse, where τ_R is the length of a single rotor period and τ_P is the total length of the refocusing pulse. Again, the dashed vertical lines indicate where the echo time occurs – as this varies according to pulse duration, each plot shows one vertical line for each rf field strength simulated and is coloured according to the key shown.

As before, the 180° pulse refocuses the $-I_y$ magnetisation fully. With shifted rotor synchronisation, the spin echo with ASBO-9(7A) perfectly refocuses the magnetisation for the two highest rf field strengths, while only a small reduction is intensity is seen with the longest pulse length simulated. Similar results are found for ASBO-9(B_1), except with a more noticeable decline in the the I_y intensity at the expected echo time with the rf strength of 62.5 kHz. The shifted rotor synchronisation method is clearly advantageous for forming spin echoes with long composite pulses, while for the simple spin echo both the shifted and centred schemes yield perfect echoes.

Figure 5.4 plots the individual trajectories of the I_y magnetisation for a selection of single-orientation nuclear spins during the application of the ASBO-9(B_1) composite pulse in the echo sequences described. The spinning rate is equal to 10 kHz, and the total composite pulse length is 36 μs. In the case of centred rotor synchronisation, the nuclear spins fan out during the first echo delay and there is little coherence between the magnetisation pathways as the pulse is applied. In the powder simulations this manifests as a decrease in the expected signal. Next, considering the shifted case, the rotary echo formed at 0.1 ms brings the various orientations back into alignment before the refocusing pulse is applied.

The plots in Figure 5.5 show how the I_y intensity formed at the expected echo time varies as a function of MAS rate between 1 kHz and 15 kHz (experiments presented later in this chapter will employ these MAS rates) using a number of composite pulses that are listed in Table 5.1. The refocused intensity resulting from the simple spin-echo experiment does not vary with spinning speed with either rotor synchronisation method. The performances of the shorter pulses – LF, SP and TS – are not significantly

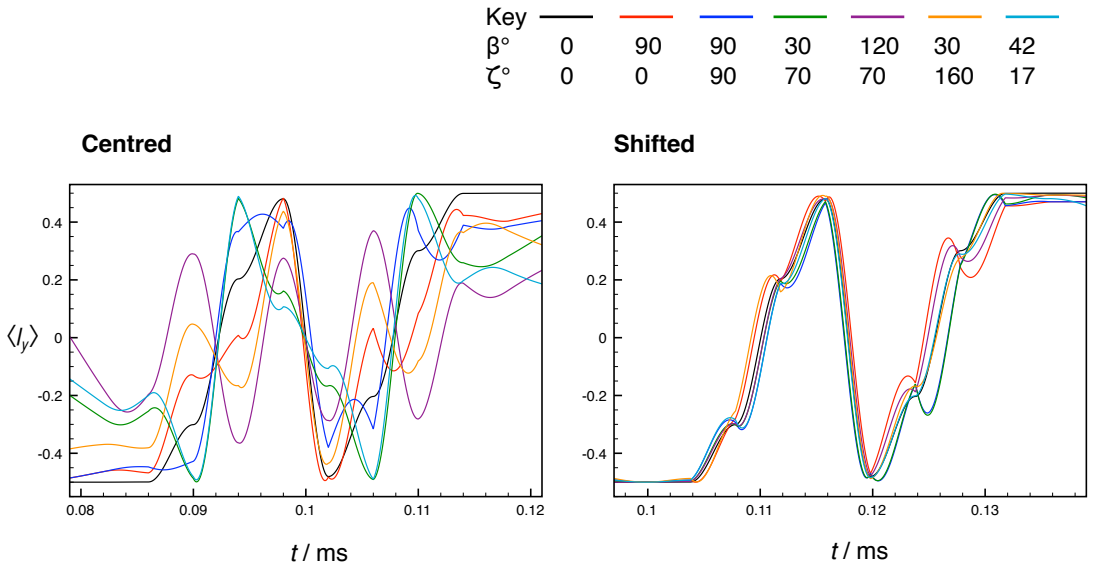

FIGURE 5.4: Simulation showing the evolution of I_y magnetisation for a various crystallite orientations under MAS using the composite refocusing pulse ASBO-9(B_1), contrasting centred and shifted rotor synchronisation. The 180° pulse length used in the simulation was 4 μs, corresponding to a field strength of $\nu_1 = \omega_1/2\pi = 125$ kHz and a total duration of 36 μs for the composite pulse. Other parameters used in the simulation were $\nu_{\Delta CS}^{PAS} = 10$ kHz and $\nu_R = 10$ kHz. Only the time range corresponding to the application of the composite pulse has been plotted.

TABLE 5.1: Total pulse lengths in degrees and microseconds (for an rf field strength $\nu_1 = 125$ kHz) for the refocusing pulses simulated in Figure 5.5.

Pulse	Total length / °	Total length / μs
$180°_{0°}$	180	4
ASBO-9(B_1)	1620	36
ASBO-9(7A)	1620	36
ASBO-11(Ω)	1980	44
OW	2340	52
LF	360	8
SP	420	9.33
TS	540	12
F_1	900	20

affected by sample spinning. However, when using centred rotor synchronisation for the longer composite pulses (the ASBO family and OW), degradation of the refocusing performance is apparent as the MAS rate increases. The decline in I_y intensity with increasing spinning speed is more rapid as the pulse length increases. In contrast, the shifted rotor synchronisation yields consistent performance across this range of MAS speeds for the ASBO pulses, and improved performance for OW and F_1.

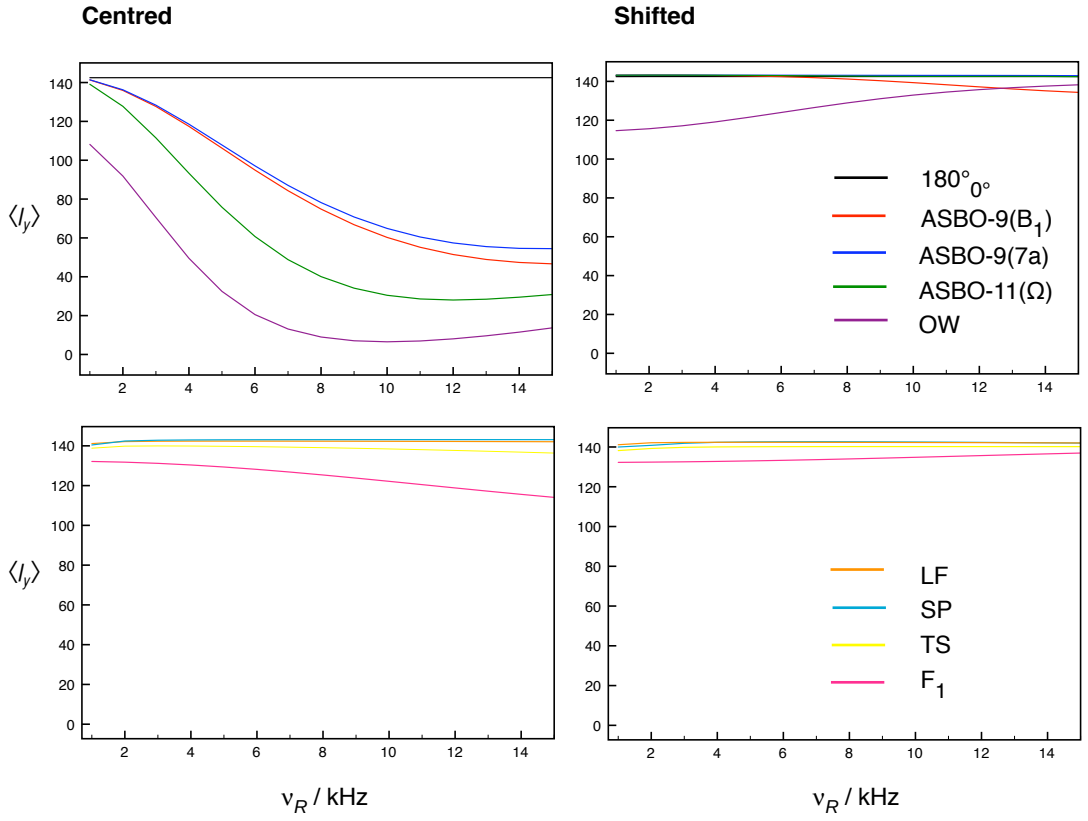

FIGURE 5.5: Simulations showing the change in refocused I_y intensity as a function of MAS rate, ν_R, for a powder using simple and composite refocusing pulses in a spin echo experiment. The left-hand column uses centred rotor synchronisation, while the shifted method is employed in right-hand column. The 180° pulse length used in the simulation was 4 µs, corresponding to a B_1 field strength of 125 kHz. Other parameters used in the simulation were $\nu_{\Delta CS}^{PAS} = 10$ kHz, and the simulation included Exorcycle phase cycling.

5.4.1 Faster MAS

The simulations in Figure 5.6 show the performance of the composite pulse spin-echo experiments up to a MAS rate of 70 kHz. Although we initially see a rapid decline in the echo amplitude with centred rotor synchronisation for the longer composite pulses, the I_y intensity then starts to recover as the spinning speed is raised. As ν_R approaches $2/\tau_P$, where τ_P is the total duration of the composite pulse, the echo amplitude reaches a maximum. In this regime the two rotor synchronisation methods are equivalent.

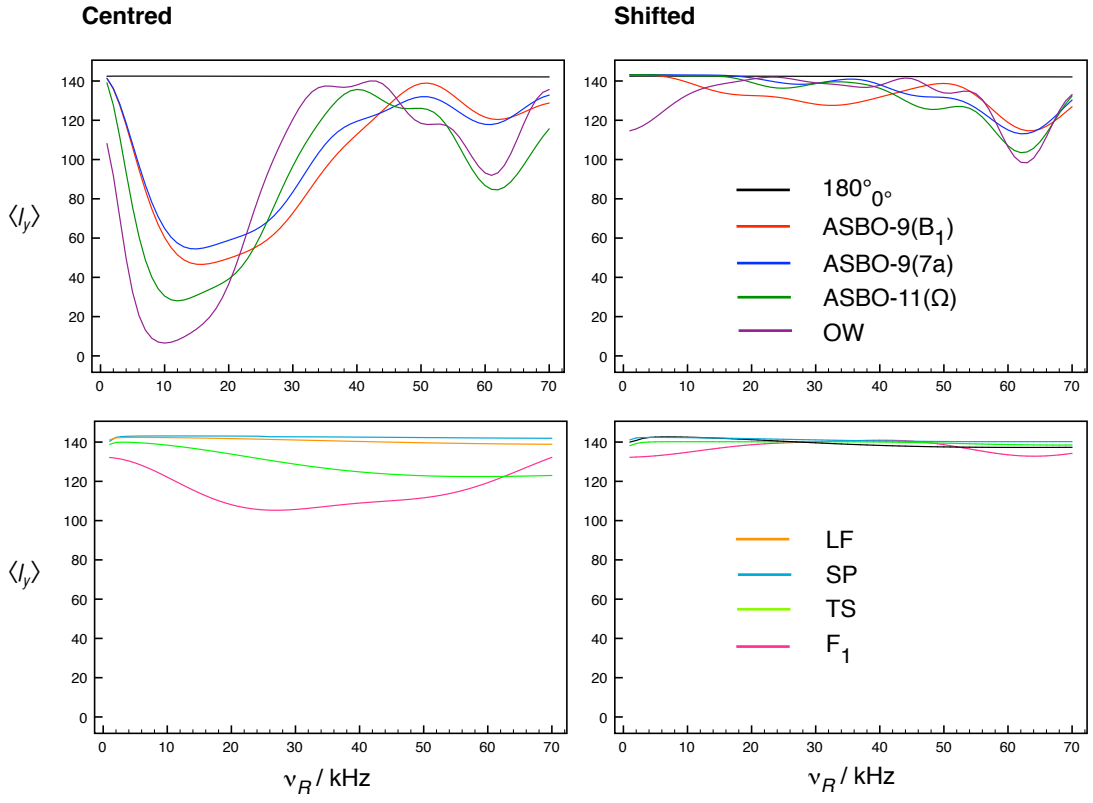

FIGURE 5.6: Simulations showing the change in refocused I_y intensity as a function of MAS rate, ν_R, for a powder using simple and composite refocusing pulses in a spin-echo experiment. The left-hand column uses centred rotor synchronisation, while the shifted method is employed in right-hand column. The 90° pulse length used in the simulation was 2 µs, corresponding to a B_1 field strength of 125 kHz. Other parameters used in the simulation were $\nu_{\Delta CS}^{PAS} = 10$ kHz, and the simulation included Exorcycle phase cycling.

5.4.2 B_1 inhomogeneity

The solenoidal coil used in solid-state NMR produces an inhomogeneous rf field that weakens at each end of the coil. Since the rotor containing the sample is longer than the coil surrounding it, the sample experiences a B_1 field which varies with position in the rotor. In the two-dimensional contour plots in Figure 5.7 the ability of the composite pulse to compensate for B_1 inhomogeneity can be assessed with regard to the MAS rate. The amount of in-phase I_y magnetisation present at echo time τ_E is shown on contour labels as a percentage of the amount present at the start of the simulation. The MAS rate varies between 1 and 15 kHz, while the normalised B_1 field strength ranges from 1 to 0. The contour plot shows that a pulse has good compensation for B_1 inhomogeneity if the pink colour extends downwards, and good refocusing with higher spinning speeds if the pink colour extends horizontally. We can thus see how the composite pulses

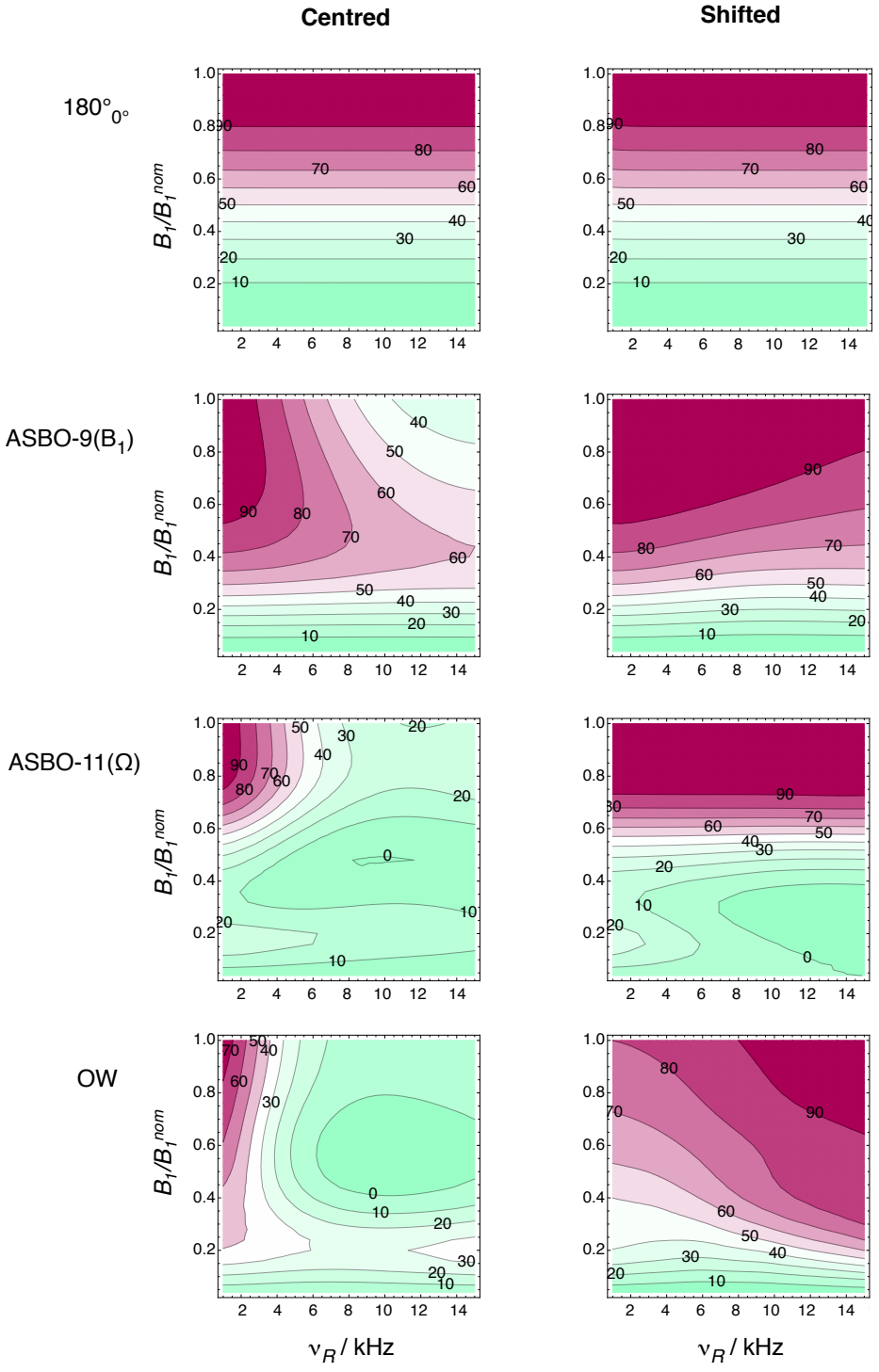

FIGURE 5.7: Two-dimensional contour plots showing the percentage of I_y magnetisation that is refocused in a spin-echo experiment as a function of MAS rate, ν_R, and the normalised B_1 field strength, B_1/B_1^{nom}) for a powder and employing Exorcycle phase cycling. Other parameters used in the simulation were $\nu_{\Delta\text{CS}}^{\text{PAS}} = 10$ kHz and a nominal B_1 field strength of 125 kHz. In addition to a simple 180° pulse of duration 4 μs, the composite pulses ASBO-9(B_1), ASBO-11(Ω) and OW-13 are simulated – these have overall pulse durations of 36, 44 and 52 μs, respectively.

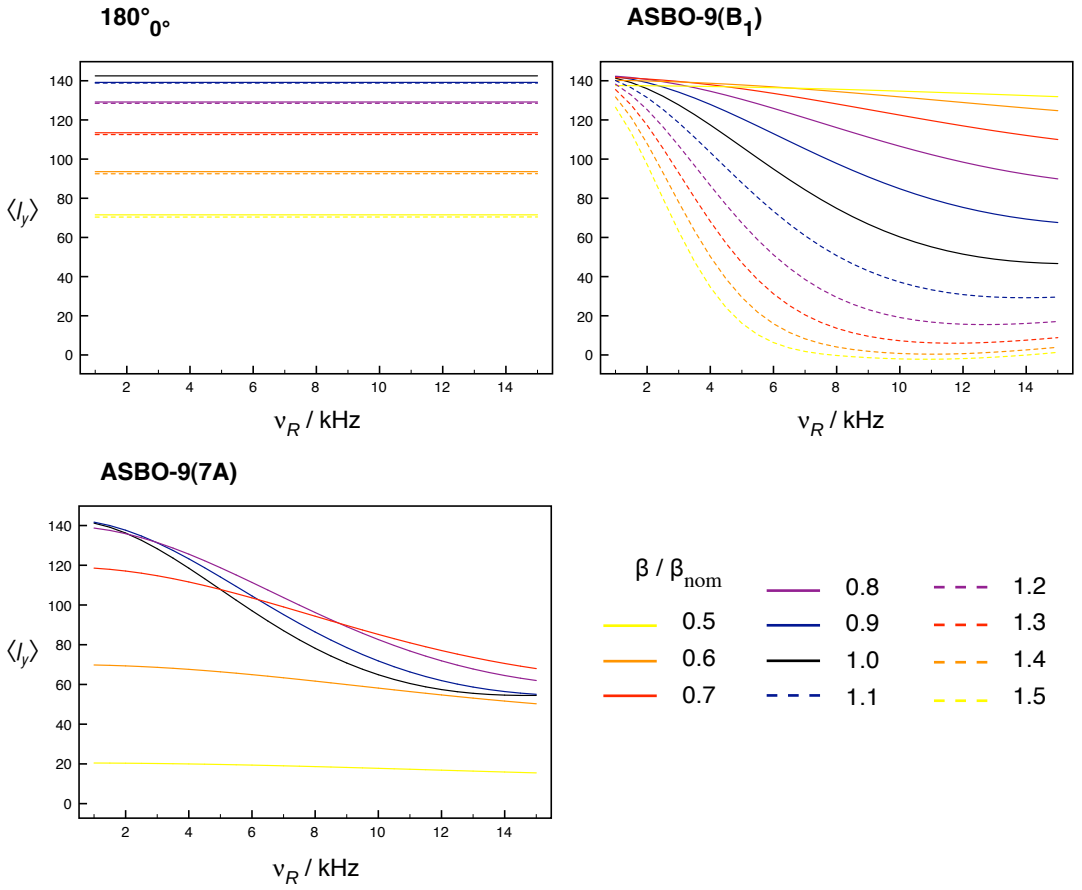

FIGURE 5.8: Simulations showing the change in refocused I_y intensity as a function of MAS rate, ν_R, for a powder and employing Exorcycle phase cycling. In addition to a simple 180°, the composite pulses ASBO-9(B_1) and ASBO-9(7A) are simulated. The flip angle misset β/β^{nom} is varied from 1.5 (pulse lengths increased by 50%) to 0.5 (halved pulse lengths). For clarity, the ASBO-9(7A) plot only shows simulations for β/β^{nom} varied from 1 (no error) to 0.5. Other parameters used in the simulation were $\nu_{\Delta\text{CS}}^{\text{PAS}} = 10$ kHz and a B_1 field strength of 125 kHz. Centred rotor synchronisation was used.

compensate well for B_1 inhomogeneity at low spinning speeds in the case of centred rotor synchronisation, and how this degrades with higher sample spinning rates to give poorer performance than the simple spin echo. In contrast, the composite pulse echoes with shifted rotor synchronisation are able to maintain better B_1 compensation than the simple echo, even as the MAS rate increases.

5.4.3 Misset flip angles

Another error which can affect the outcome of a spin-echo experiment is the missetting of the pulse durations, where poor calibration by the experimentalist means that pulses that are longer or shorter than the correct length are applied. MAS spin echoes with centred rotor synchronisation have been simulated taking the effect of incorrect pulse lengths into account. Figure 5.8 shows for each of the pulse sequences how the I_y magnetisation formed at time τ_E varies in amplitude as the spinning rate is increased from 1 kHz to 15 kHz. The simulations were carried out with flip angle misset parameter β/β^{nom} varying from 1.5 (pulse durations incorrectly set to be 50% longer, i.e., a 180° pulse becomes 270°) to 0.5 (halved pulse lengths, i.e., a 90° pulse is applied instead of a 180° pulse). The initial state was kept as $-I_y$ and the calculations run with all elements of the refocusing pulse shortened or lengthened according to the value of the misset parameter.

The results for the simple spin echo are as expected: the I_y amplitude follows a sine response, decreasing as the flip angle of the refocusing pulse is reduced from its nominal length for a 180° rotation and leading to halved signal intensity with halved pulse length. The extent of signal loss is identical whether the pulse is applied for a proportionately longer or shorter time. This response is unaffected by the MAS rate.

Next, considering the response of the ASBO-9(B_1) echo, we find that as the refocusing pulse is incorrectly set to shorter durations, the I_y amplitude becomes less prone to attenuation with increasing MAS speed. As demonstrated in the previous chapter, this composite pulse is very tolerant of deviations of the flip angle from the nominal value. Coupling this good compensatory ability with the reduction in overall pulse length compared to τ_R leads to an improvement in the echo signal intensity. In contrast, when the pulse is made longer (simulations in dashed lines), a marked decline in performance with sample spinning is seen.

ASBO-9(7A), which was shown in Chapter 4 to have a narrower bandwidth than ASBO-9(B_1) for correcting deviations from the nominal flip angle, shows increasing refocused I_y intensity across the MAS speeds simulated as the pulses are shortened to $\beta/\beta^{\text{nom}} = 0.8$. With $\beta/\beta^{\text{nom}} = 0.6$, the I_y intensity at $\nu_R = 14$ kHz is lower than that created by a

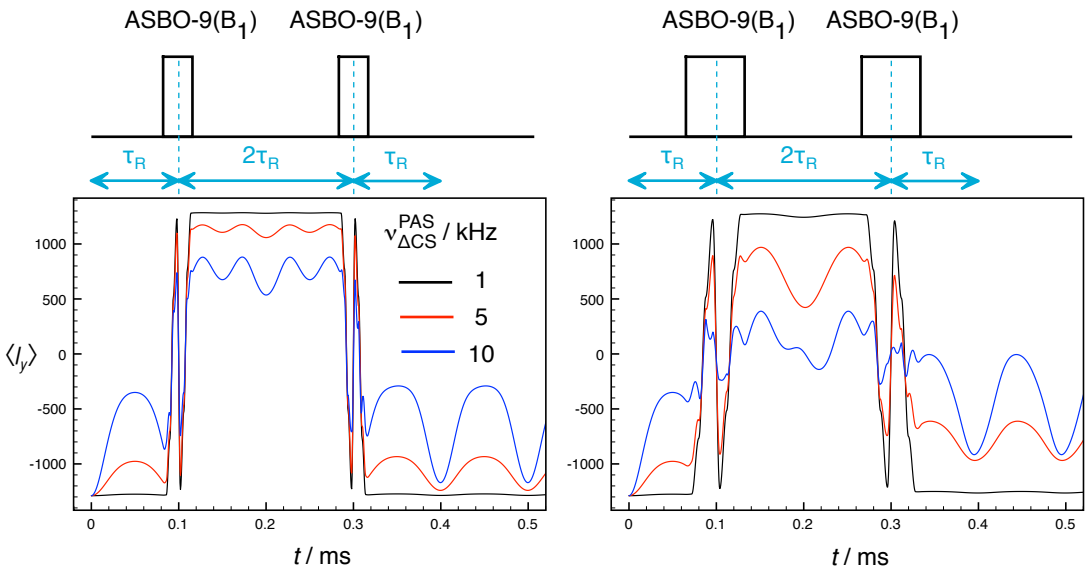

(a) Evolution of I_y magnetisation with two composite refocusing pulses ASBO-9(B_1)

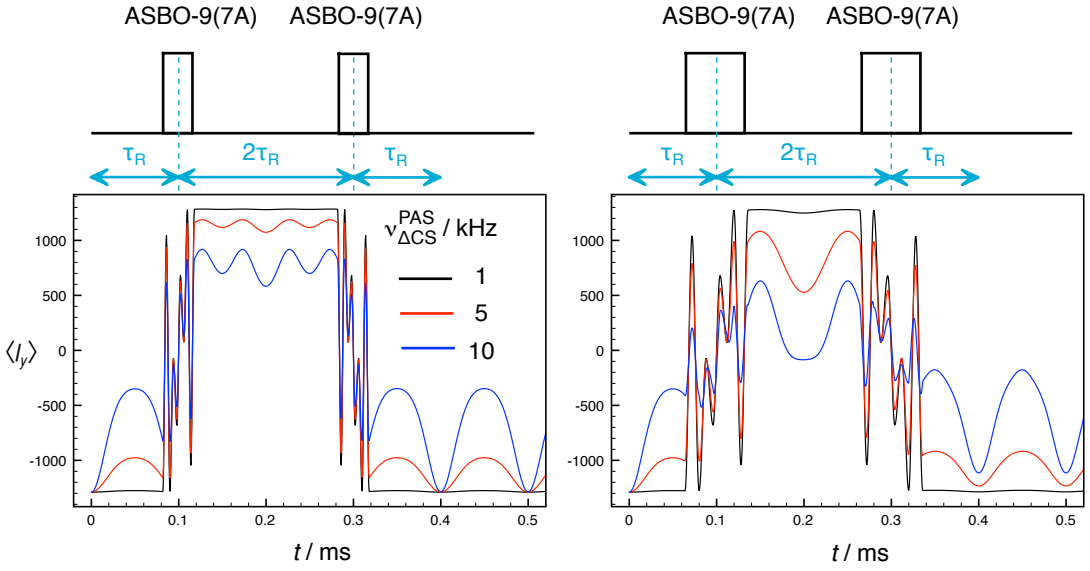

(b) Evolution of I_y magnetisation with two composite refocusing pulses ASBO-9(7A).

FIGURE 5.9: Evolution of I_y magnetisation with two composite refocusing pulses ASBO-9(B_1) at τ_R and $3\tau_R$, giving echo formation at $4\tau_R$. Simulation parameters were: ν_1 of 125 kHz or 62.5 kHz (total composite pulse length of 36 μs or 72 μs), ν_R of 10 kHz, $\nu_{\Delta CS}^{PAS}$ of 1, 5 and 10 kHz.

simple spin echo under the same conditions, or by ASBO-9(7A) with correctly calibrated pulses.

5.4.4 Multiple refocusing

Levitt and Freeman discussed multiple refocusing in solution-state experiments, showing that any error in spin-echo phase caused by a composite pulse can be cancelled out by applying a second echo using the same pulse [73]. Olejniczak, Vega and Griffin analysed magic angle spinning by considering the paths taken by magnetisation vectors in MAS experiments [123]. They stated that if a 180° pulse is applied at time $1/2\tau_R$ after excitation, the amplitude of the echo expected at τ_R is greatly reduced owing to the "scrambling" of the magnetisation vectors from different crystallite orientations which prevents refocusing of the anisotropic shift by further sample rotation. However, this effect can be reversed by applying a second 180° pulse at $3/2\tau_R$, resulting in the formation of a Hahn and a rotational echo at $2\tau_R$.

When applying long composite pulses with centred rotor synchronisation, the pulse starts part of the way through a τ_R period, and a similar scrambling of vectors is seen. We can apply a second echo in our experiments and investigate the perfomance of composite pulse double spin-echo experiments under MAS. Figure 5.9 plots the I_y magnetisation through the double refocusing sequence with the pulses applied centred at times τ_R and $3\tau_R$, forming an echo at $4\tau_R$. The ASBO-9(B_1) double-pulse experiment refocuses the I_y magnetisation with full intensity at $4\tau = 0.4$ ms with $\nu_{\Delta CS}^{PAS} = 1$ kHz. However, a slight reduction in echo intensity is apparent with $\nu_{\Delta CS}^{PAS} = 5$ kHz and 10 kHz. With a longer pulse length (72 μs at $\nu_1 = 62.5$ kHz), both ASBO-9(B_1) (Figure 5.9(a)) and ASBO-9(7A) (Figure 5.9(b)) show deteriorated performance with increasing CSA, with a greater reduction in echo intensity seen in the ASBO-9(B_1) double-pulse experiment. However, the losses are not as significant as those observed in the equivalent simulations with a single echo, indicating that some of the error has been reversed.

5.5 Experiments

Experiments were performed on a Bruker Avance 400 NMR spectrometer equipped with a widebore 9.4 T magnet. The investigation of the effect of spinning rate on composite pulse spin-echo performance was carried out on a sample of titanium pyrophosphate (TiP_2O_7), which was kindly provided by Dr. Gregory Tricot of Université Lille

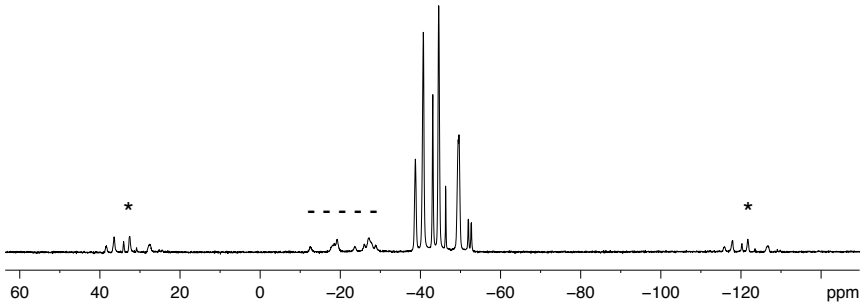

(a) Full spectral width.

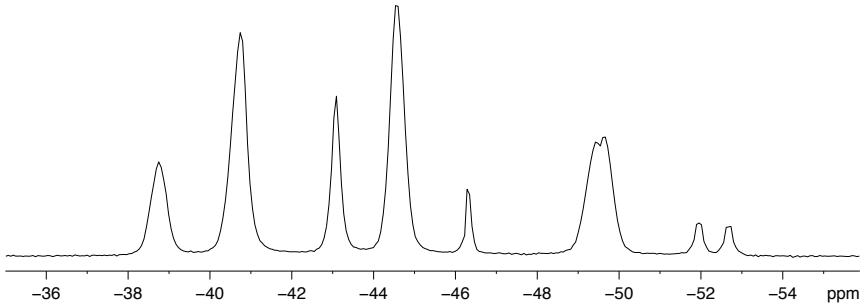

(b) Expansion of centrebands.

FIGURE 5.10: ^{31}P (162 MHz) MAS NMR spectrum of TiP_2O_7 (90° pulse length was 2.5 μs, ν_R of 12.5 kHz, relaxation interval of 180 s, averaging of 16 transients). Spinning sidebands in (a) are marked with asterisks (*), impurity peaks indicated by dashes (–).

de Nord de France. The TiP_2O_7 structure consists of corner-sharing distorted TiO_8 octahedra and PO_4 tetrahedra, giving rise to a structure with eleven crystallographically distinct phosphorus sites [120]. The sample (a white powder) was packed in a 4-mm rotor and the calibrated 90° pulse length was 2.5 μs, corresponding to a nutation rate $\nu_1 = |\gamma B_1|/2\pi = 100$ kHz. The ^{31}P nuclei have a CSA of around $\nu_{\Delta CS}^{PAS} = 10$ kHz at 9.4 T [118].

Figure 5.10 shows the ^{31}P MAS NMR spectrum of TiP_2O_7 obtained with a spinning rate of 12.5 kHz. The spectrum consists of nine resolved peaks between −38 and −53 ppm. A complete assignment of the spectrum is given in reference [118]. The peaks visible between −10 and −30 ppm are attributed to impurities in the sample. Spinning sidebands are present 12.5 kHz on either side of the centrebands in Figure 5.10(a), and an expansion of the centrebands can be seen in Figure 5.10(b).

5.5.1 Phasing of Spinning Sidebands

Figure 5.11 shows spin-echo spectra of TiP_2O_7 obtained using the composite pulse ASBO-9(B_1) at spinning speeds of 4, 6 and 8 kHz. Figures 5.11(a), 5.11(c) and 5.11(e) show spectra obtained with centred rotor synchronisation with increasing MAS rate. In order to phase these spectra, the simple spin-echo was first recorded and phased for each spinning speed. The same phase correction was then applied to the composite pulse spectra before altering the zeroth-order phase correction by a few degrees to optimise the phasing. The outermost sidebands in the spectrum with a MAS rate of 6 kHz (Figure 5.11(c)) are inverted with respect to the centreband, while at 8 kHz (Figure 5.11(e)) all sidebands are inverted. Spectra were also recorded at higher spinning speeds (10, 12 and 14 kHz) and these also showed inversion of all sidebands. It was not possible to bring all the sidebands and the centreband into the correct phase simultaneously. This problem was only observed experimentally for composite pulse echoes. However, simulations suggest that when the rf field strength is much lower and the duration of a simple 180° pulse is very long, the same problem with phasing sidebands can occur in a simple spin-echo experiment.

For the experiments with shifted rotor synchronisation (Figures 5.11(b), 5.11(d) and 5.11(f)) the spectra were phased individually. Unlike the spectra obtained with centred rotor synchronisation, it was always possible to phase the spectra correctly.

5.5.2 Spin-echo spectral intensites

As well as producing a distinctive behaviour in the phase of spinning sidebands in the composite pulse spin-echo experiments, it is interesting to examine the difference in the amplitude of the centrebands and spinning sidebands between the two rotor synchronisation methods. Comparing the spin-echo spectra obtained at spinning speed of 4 kHz (Figure 5.11(a) and Figure 5.11(b)), the centrebands have greater intensity using the centred method. While the shifted method has centrebands of lower intensity, the spinning sidebands are greater, and overall the total integrated intensity of the two spectra are similar.

The difference in centreband signal intensity between the simple pulse spin echo, I_{SP}, and composite pulse echo experiments, I_{CP}, were examined at MAS rates of 4, 6, 8, 10, 12

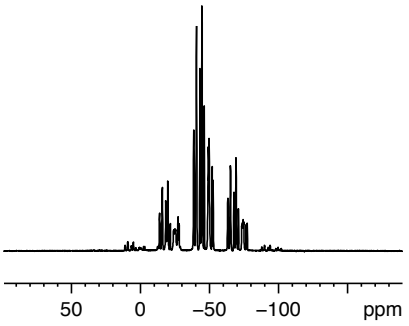

(a) $\nu_R = 4$ kHz, centred rotor synchronisation.

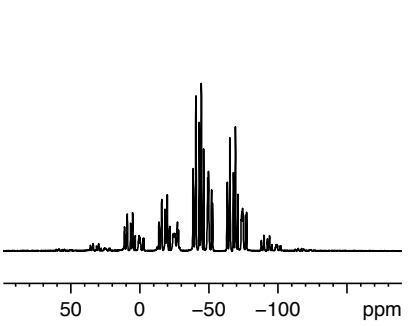

(b) $\nu_R = 4$ kHz, shifted rotor synchronisation.

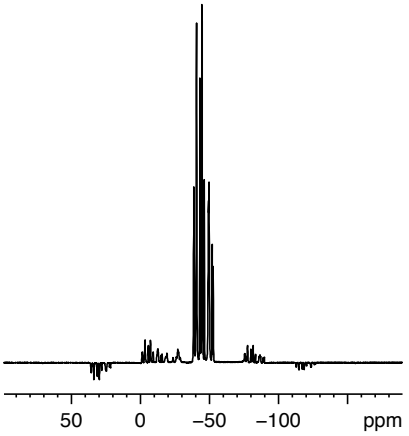

(c) $\nu_R = 6$ kHz, centred rotor synchronisation.

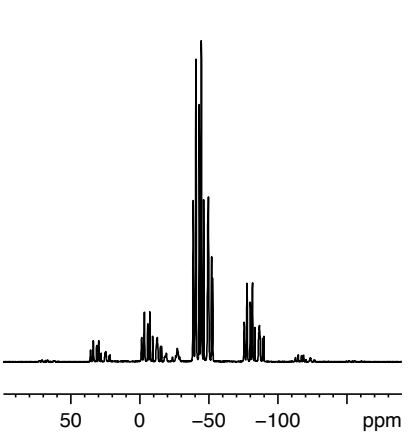

(d) $\nu_R = 6$ kHz, shifted rotor synchronisation.

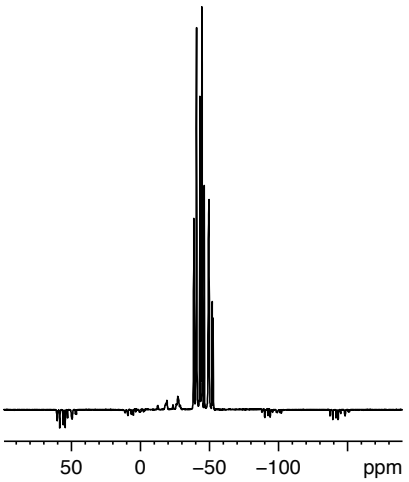

(e) $\nu_R = 8$ kHz, centred rotor synchronisation.

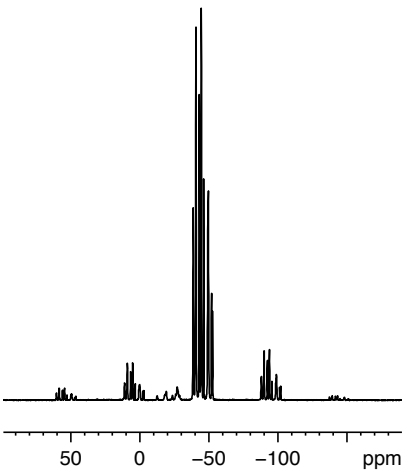

(f) $\nu_R = 8$ kHz, shifted rotor synchronisation.

FIGURE 5.11: ^{31}P (162 MHz) MAS NMR spin-echo spectra of TiP_2O_7 (90° pulse length of 2.5 μs, relaxation interval of 180 s, averaging of 16 transients). The composite pulse ASBO-9(B_1) was used.

and 14 kHz. These have been plotted as a percentage change relative to the simple echo, $\{(I_{CP} - I_{SP})/I_{SP}\} * 100$, at each spinning speed in Figure 5.12. Experiments employing pulses from the ASBO family and OW were carried out using both centred and shifted rotor synchronisation, while the shorter pulses LF, SP and TS were only studied with centred rotor synchronisation as the simulations in Figure 5.5 suggested that both rotor synchronisation methods would yield similar results in this range of MAS speeds. All composite pulse spectra intensities were compared to a simple spin echo with centred rotor synchronisation – again, because the simple echo experiment was not affected by the choice of rotor synchronisation method.

When using the longer composite pulses, the greatest improvement in signal intensity compared to the simple echo is observed with centred rotor synchronisation but only at low spinning speeds. For example, ASBO-9(B_1) gives a 44% increase at $\nu_R = 4$ kHz, yielding the best increase in signal amplitude for any of the composite pulses studied here. However, as the spinning speed increases, the signal enhancement relative to the simple echo diminishes. At $\nu_R = 12$ kHz there is no advantage in using this composite pulse, and at $\nu_R = 14$ kHz the simple echo actually performs better than the composite pulse. Considering the rate of deterioration of composite pulse performance, the relative amplitudes observed using the longer pulses ASBO-11(Ω) and OW fall off more rapidly than the ASBO-9 pulses. The shorter pulses (LF, SP, TS and F_1) do not show much variation in performance with increasing spinning speed.

Using shifted rotor synchronisation, ASBO-9(B_1) only gives a 12% increase at $\nu_R = 4$ kHz. However, the magnitude of the signal enhancement does not vary considerably with MAS rate. From $\nu_R = 10$ kHz and upwards, the shifted rotor synchronisation method performs better than the centred experiments for this pulse sequence. Similarly, the performances of ASBO-9(7A), ASBO-11(Ω) and OW do not vary greatly with MAS rate. These experimental observations reflect the simulations presented in Figure 5.5.

5.5.3 Misset flip angles

Figure 5.13 shows the ^{31}P MAS NMR spin-echo spectra recorded at $\nu_R = 14$ kHz with a simple refocusing pulse as well as ASBO-9(B_1) and ASBO-9(7A). Centred rotor synchronisation was employed in all aquisitions. For each pulse sequence, the experiment was performed with a calibrated duration of 2.5 μs for a 180° rotation (Figures 5.13(a),

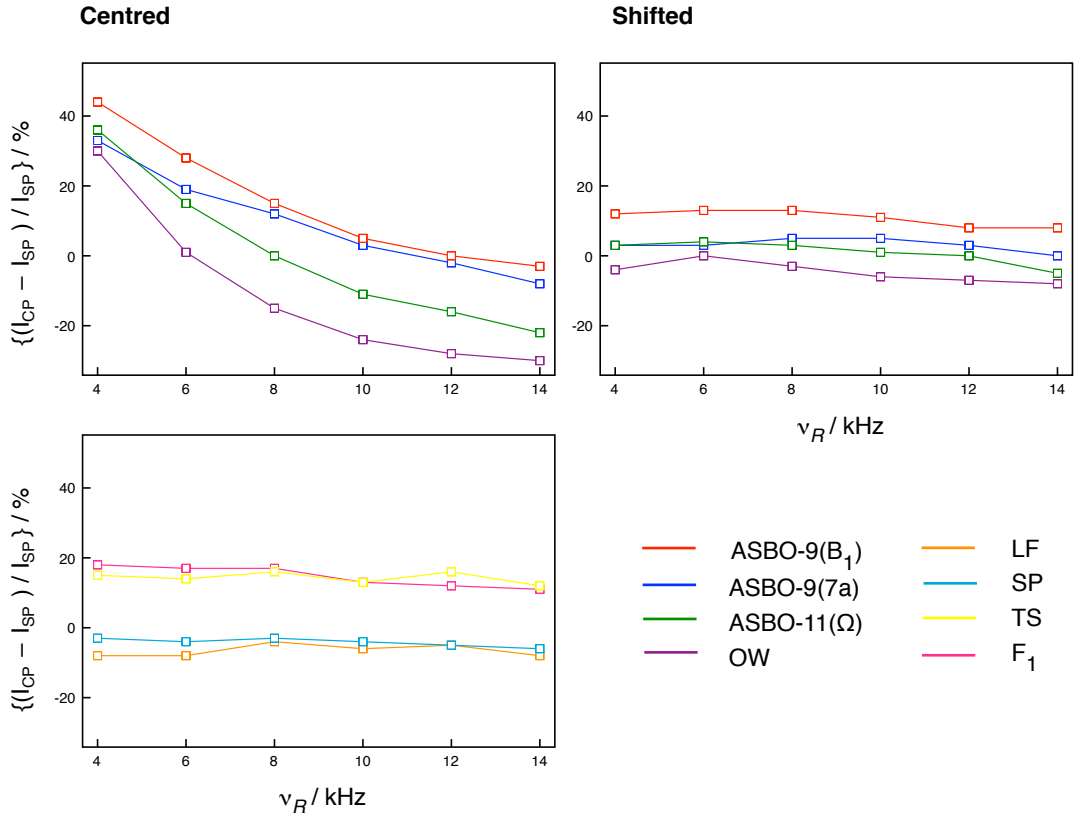

FIGURE 5.12: Plots showing the percentage change in centreband signal intensity of the centreband in ^{31}P spin-echo spectra using composite refocusing pulses compared to a simple spin-echo spectrum. The sample used was TiP_2O_7. The left-hand column uses centred rotor synchronisation, while the shifted method is employed in right-hand column for a selection of longer composite pulses. The calibrated 90° pulse length was 2.5 µs, corresponding to a B_1 field strength of 100 kHz.

5.13(c) and 5.13(e)), and then repeated with the refocusing pulse durations deliberately shortened to 60% of their calibrated values (Figures 5.13(b), 5.13(d) and 5.13(f)).

Considering the simple spin echo first, the spectrum recorded with a misset shows peak amplitudes which are reduced by about 20% compared to the spectrum obtained with a well-calibrated 180° pulse.

Curiously, the missetting of the flip angles results in higher peak amplitudes when ASBO-9(B_1) is used as the refocusing pulse (compare Figure 5.13(c) with Figure 5.13(d)). Coupling the overall reduction in the composite pulse length with the ability of the pulse to compensate for misset flip angles across a large bandwidth results in an improvement of the signal amplitude compared to the experiment carried out with well-calibrated pulse durations. Conversely, with the same extent of error in the pulse length, the ASBO-9(7A) spectrum suffers a loss in centreband intensity (compare Figure 5.13(e)

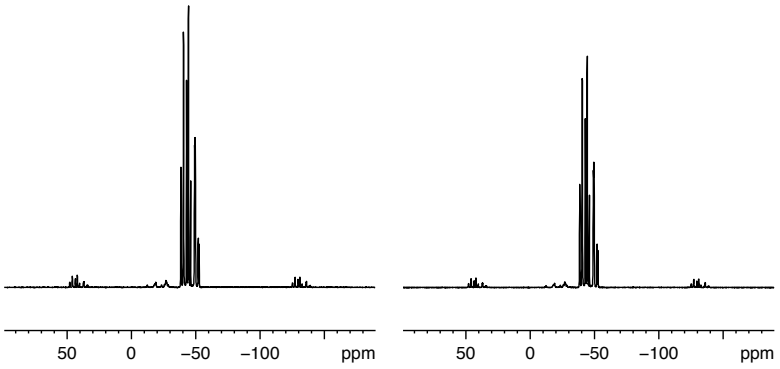

(a) $180^{\circ}_{0^{\circ}}$.

(b) $180^{\circ}_{0^{\circ}}$ with misset.

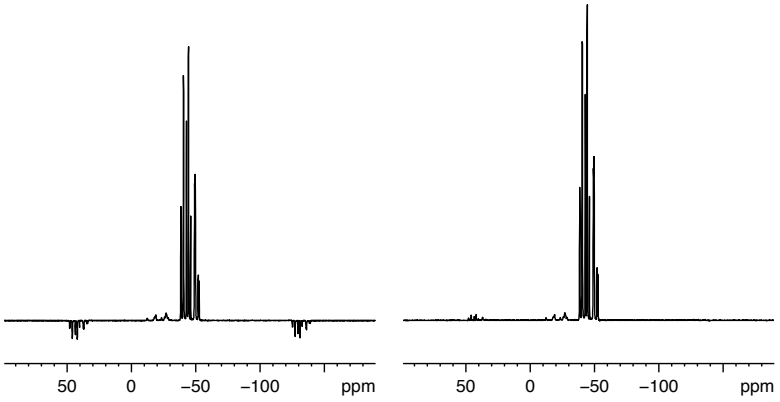

(c) ASBO-9(B_1).

(d) ASBO-9(B_1) with misset.

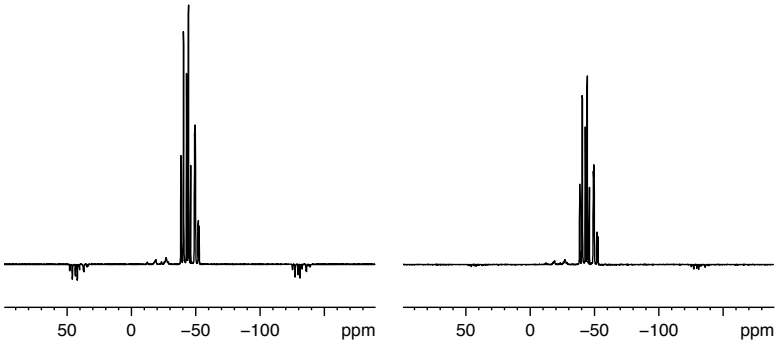

(e) ASBO-9(7A).

(f) ASBO-9(7A) with misset.

FIGURE 5.13: ^{31}P (162 MHz) MAS NMR spin-echo spectra of TiP_2O_7 (90° pulse length of 2.5 μs, relaxation interval of 180 s, averaging of 16 transients, $\nu_R = 14$ kHz). The composite pulses ASBO-9(B_1) and ASBO-9(7A) were used as well as a $180^{\circ}_{0^{\circ}}$ refocusing pulse. In (b), (d) and (f) all elements of the refocusing pulses were misset to 60% of their calibrated duration. Centred rotor synchronisation was used in all of these experiments.

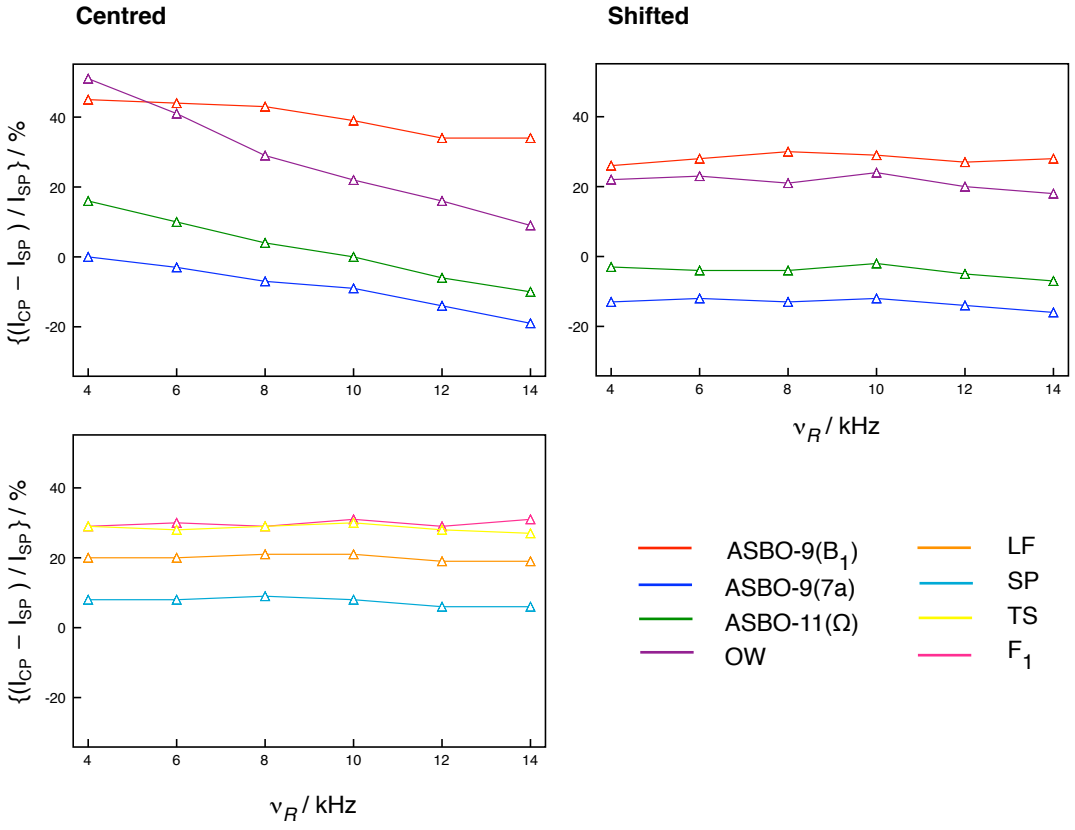

FIGURE 5.14: Plots showing the percentage change in centreband signal intensity of ^{31}P spin-echo spectra using composite refocusing pulses compared to a simple spin-echo spectrum. The left-hand column uses centred rotor synchronisation, while the shifted method is employed in right-hand column for a selection of longer composite pulses. The calibrated 90° pulse length was 2.5 μs, corresponding to a B_1 field strength of 100 kHz. The duration of all elements of the refocusing pulses have been misset to 60% of their calibrated value.

with Figure 5.13(f)). Although dual-compensated with regard to both misset and offset, this composite pulse sequence has a lower tolerance to deviations in flip angle than ASBO-9(B_1). As the extreme error is not compensated, an improvement is not seen despite the decreased pulse length.

Using the refocusing pulses listed in Table 5.1, spin-echo experiments were carried out with the pulse lengths deliberately shortened to a misset of $\beta/\beta^{\text{nom}} = 0.6$. The experiments were performed at $\nu_R = 4$, 6, 8, 10, 12 and 14 kHz and at each MAS speed the centreband intensities of the composite pulse spectra were compared to a simple echo spectrum. The percentage difference in amplitude for each has been plotted in Figure 5.14. Contrasting these with the results in Figure 5.12, where the correct pulse durations were used, we see a particular improvement in the performance of the longer pulses of the ASBO family and OW. The rate of attenuation of the centreband signal

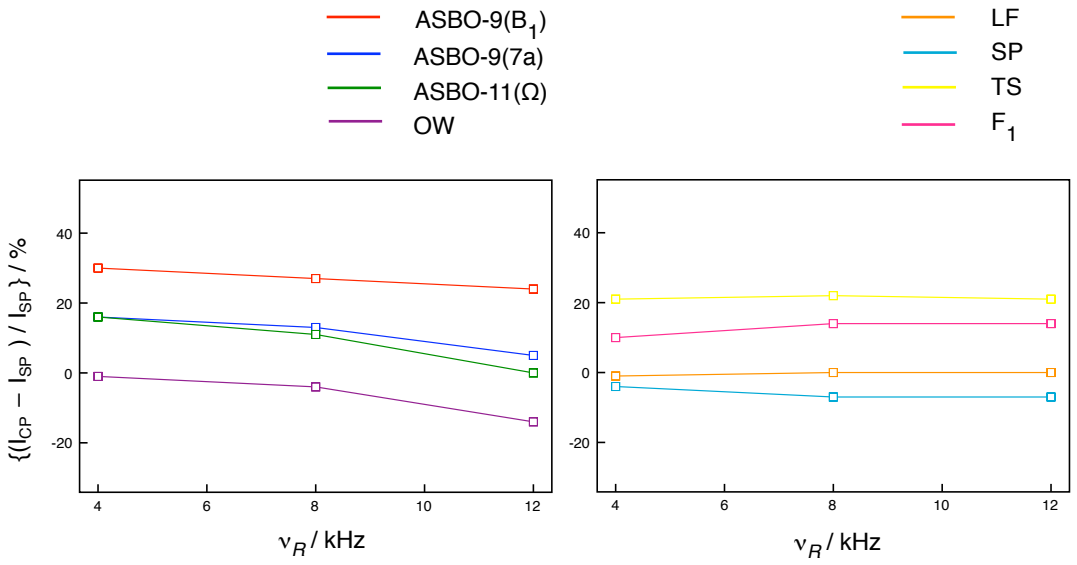

FIGURE 5.15: Plots showing the percentage change in centreband signal intensity of ^{31}P double spin-echo spectra using composite refocusing pulses compared to a double simple spin-echo spectrum. The calibrated 90° pulse length was 2.5 μs, corresponding to a B_1 field strength of 100 kHz. The relaxation interval was 180 s and 64 transients were acquired for each experiment.

with spinning rate using the ASBO pulses with centred rotor synchronisation is noticeably reduced.

5.5.4 Double refocusing experiments

MAS double spin-echo experiments were carried out at $\nu_R = 4$, 8 and 12 kHz. The percentage signal enhancement of the composite pulse echoes compared to the the 180° refocusing experiments are shown in Figure 5.15. Compared to Figure 5.12, we see much less variation in the performance of the composite pulses as a function of MAS rate, indicating that the second echo reverses some of the deleterious effects seen.

5.6 Conclusions

In this Chapter, the effects of MAS on composite pulse performance have been explored, revealing a complex dependence of the outcome of a composite pulse spin-echo sequence on the experimental parameters. Two methods of rotor synchronisation have

been studied (Figure 5.2), with each yielding distinct spectra and different dependencies on the spinning rate. It is clear that the delta pulse approximation is not always valid and the simulations presented, for example in Figure 5.3, do not show the rotations expected of a refocusing pulse. Broadband composite pulses ought to yield improved spectra compared to simple pulses, but we have seen that this is not always the case. Disappointing results have included problems of poor signal amplitude and incorrect phases of spinning sidebands.

In the case of spin echoes with centred rotor synchronisation, the composite pulse begins part way through a rotor period at a time when the magnetisation vectors have fanned out and not been fully refocused by a rotational echo driven by MAS. As described by Olejniczak et al. [123], the application of a refocusing pulse midway through a rotor period scrambles the magnetisation vectors from different crystallite orientations, and further sample rotation will not refocus the anisotropic chemical shift. Destructive interference between magnetisation of different crystallites thus yields a signal of diminished amplitude at time τ_E. As a result of this scrambling phenomenon, centred spin-echo experiments are highly sensitive to the spinning rate, in particular when the total length of the composite pulse necessitates that the rf pulse begins at a point during the rotor period where the magnetisation has dephased significantly under rotation. Thus, the experiment is highly dependent on the sample as well as the composite pulse, as the extent of dephasing at a given MAS rate is governed by the magnitude of the various anisotropic interactions present. With the refocusing ability of a composite pulse compromised even without other pulse errors present, it is not surprising that the compensation for B_1 field strength errors suffers as shown in Figure 5.7.

It is interesting that the presence of a flip angle miscalibration has the potential to improve the performance of a composite pulse spin echo experiment if the flip angles are set lower than their nominal value. Figure 5.13 demonstrates that a decrease in the overall pulse length can lead to spectra of greater signal amplitude. This effect is crucially dependent on the size of the misset and the bandwidth the composite pulse possesses to deal with variations in flip angle. Conversely, if the flip angles are miscalibrated longer than their nominal value, further deterioration in their performance is seen. This is clearly a problem, as one would apply a composite pulse in the hope of relieving problems of misset flip angles, rather than worsening their effects.

In general, we do not wish to replace a single echo with multiple echoes, as this restricts the B_1 bandwidth (as seen in the Depth implementation of spin echoes in Chapter 3). In addition, more signal is lost by transverse relaxation during the spin echo intervals. However, it is noted that, as pointed out by Levitt and Freeman [73] and Olejniczak et al. [123], a second echo has the potential to correct phase problems generated by the first. Figure 5.15 shows that the amplitude enhancement provided by the composite pulse compared to the simple refocusing pulse shows less variation with MAS rate in double echo experiments.

The shifted method of rotor synchronisation times the start of the refocusing pulse with the completion of an integer number of rotor periods, and takes the length of the composite pulse into account in predicting when the echo will reach its maximum. Although the centred method seems to yield spectra with greater centreband intensity at low spinning speeds, a crossover exist at a point depending on the overall pulse duration and the MAS rate. Beyond this, the shifted rotor synchronisation method yields greater amplitudes as is seen in Figure 5.12. Furthermore, the shifted method generates spectra with spinning sidebands with correct phase.

Although the shifted method seems to show some level of success in the single spin-echo experiment, one would express caution in employing these pulse timings in other, more complex experiments. For example, in the refocused INADEQUATE experiments introduced in Chapter 4, the spin-echo intervals must be equal to an integer number of rotor periods to remove the homonuclear dipolar couplings. Attempts to implement the shifted rotor synchronisation scheme would introduce artefacts in the two-dimensional spectrum.

In summary, we have seen that MAS introduces extra complexity to the outcome of a composite pulse spin-echo experiment. Regardless of the choice of rotor synchronisation method, the overall amplitude of the signal depends not only on the bandwidth of the pulse to compensate for experimental imperfections such as B_1 strength errors and resonance offset, but is also hinged on a complicated interplay of the magnitude of the anisotropic interactions in the sample, the MAS rate and the total duration of the composite pulse sequence. It is worth remembering that the problems we have seen here will not necessarily impair all applications of composite pulses in MAS, and that

compensating pulse sequences have been used with success in solid-state NMR experiments, both in this thesis and elsewhere in the literature. However, it is clear that unlike solution-state experiments, a degree of uncertainty exists in their performance under MAS.

Chapter 6

Far off-resonance spin-locking of half-integer quadrupolar nuclei

6.1 Introduction

Moving on from the topics covered in the previous Chapters, we will now examine a completely different theme in solid-state NMR. NMR spin-locking involves the application of a long radiofrequency pulse along the bulk magnetisation vector, with the effect of locking the vector in place for up to several seconds. No further evolution takes place under the influence of resonance offsets, J coupling or dipolar coupling while the magnetisation is spin-locked, as the radiofrequency field strength ($\omega_1 = |\gamma B_1|$) is much stronger than any of these interactions. This spin-locking is an essential part of many experiments in NMR, most notably in the cross-polarisation (CP) experiment where the spin-locking pulse is used to transfer polarisation from abundant spins to dilute nuclei in the sample.

Although the simple vector model picture given above is valid for spin $I = 1/2$ nuclei, the spin-locking behaviour of quadrupolar nuclei in solids is more challenging to understand. The quadrupolar splitting parameter, ω_Q, may be much larger than the radiofrequency field strength, resulting in rapid evolution of the magnetisation on a time

scale of $1/\omega_Q$ before the system settles into a spin-locked state of single- and multiple-quantum coherences as well as non-equilibrium population states. Experiments performed under MAS will be more complex, with a time-dependent quadrupolar splitting parameter and final spin-locked states which vary with rotor phase $\omega_R t$. [124–127]

Previously, a simple theoretical model was given by Ashbrook and Wimperis to describe the creation and evolution of coherences in a spin-locking experiment involving half-integer quadrupolar nuclei [128]. Subsequently, the effects of second-order quadrupolar interactions and small resonance offsets were considered [129]. Here, a study of the far off-resonance case will be presented. The magnetisation is left directed along the z-axis of the rotating frame before the spin-locking pulse is applied. Since the pulse is applied well away from the Larmor frequency, there is a significant z component to the effective field B_{eff} (see Figure 1.2(c)) [130].

The first sections of this Chapter will cover the theoretical model of spin-locking. Computer simulations employing this model will then be presented, as well as exact density matrix calculations for spin $I = 3/2$ and $I = 5/2$. These simulations, together with experimental NMR results, will give insight into the spin-locking phenomenon for half-integer quadrupolar nuclei in the solid state.

6.2 Pulse sequences for spin-locking

Figure 6.1 shows the pulse sequences for the far off-resonance experiments described in this Chapter. The magnetisation is left directed along the z-axis of the rotating frame before the spin-locking pulse is applied. Unlike conventional on (or near) resonance spin-locking, no initial pulse is required. Since the pulse is applied far off the Larmor frequency, there is a significant z component to the effective field B_{eff}. For observing the spin-locking of the central transition, a single pulse of duration τ is used, as shown in Figure 6.1(a). This pulse sequence is modified as shown in Figure 6.1(b) to allow the observation of the multiple-quantum coherences. In this case the second pulse is phase cycled [26] to convert the desired multiple-quantum coherence into the observable single-quantum state.

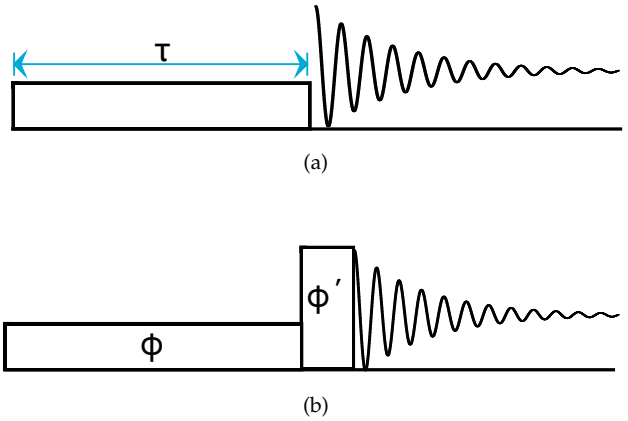

FIGURE 6.1: Spin-locking pulse sequences for observing (a) single-quantum coherences and (b) triple-quantum coherences.

6.3 Theoretical model of spin-locking

As explained in Reference [128], the rotating-frame Hamiltonian during an off-resonance spin-locking pulse is defined as

$$H = H_{\text{rf}} + H_{\text{quad}} + H_{\Omega}, \tag{6.1}$$

where the radiofrequency pulse Hamiltonian (H_{rf}), the first-order quadrupolar Hamiltonian (H_{quad}) and the offset Hamiltonian (H_{Ω}) are given by,

$$H_{\text{rf}} = \omega_1 I_x, \tag{6.2}$$

$$H_{\text{quad}} = \frac{\omega_{\text{Q}}^{\text{PAS}}}{2}(3\cos^2\theta - 1)\{I_z^2 - \frac{1}{3}I(I+1)\}, \tag{6.3}$$

$$H_{\Omega} = \Omega I_z. \tag{6.4}$$

When the spin-locking pulse is applied to the initial state $\sigma(0)$, the system begins to evolve under the influence of the Hamiltonian in Equation 6.1, with the time-dependence given by the Liouville-von Neumann equation,

$$\frac{\mathrm{d}}{\mathrm{d}t}\sigma(t) = -i[H, \sigma(t)]. \tag{6.5}$$

Assuming that H is time-independent (and therefore ignoring any effects of MAS), the solution is

$$\sigma(t) = \exp\{-iHt\}\sigma(0)\exp\{+iHt\} \tag{6.6}$$

as we described in Section 2.2. A unitary transformation V can be used to diagonalise the Hamiltonian,

$$H^D = VHV^{-1}. \tag{6.7}$$

Equation 6.6 can then be written as

$$\sigma(t) = V^{-1} \exp\{-iH^D t\}\, V\sigma(0)V^{-1}\, \exp\{+iH^D t\}V \tag{6.8}$$

or

$$\sigma'(t) = \exp\{-iH^D t\}\, \sigma'(0)\, \exp\{+iH^D t\} \tag{6.9}$$

with

$$\sigma'(t) = V\sigma(t)V^{-1}. \tag{6.10}$$

The initial density operator $\sigma(0)$ is thus transformed by V into the eigenbasis of the spin-locking Hamiltonian, i.e., the frame in which H is diagonal. The off-diagonal elements of $\sigma'(0)$ evolve at rates determined by ω_1 and ω_Q and, when considered across a powder sample where ω_Q will vary according to crystallite orientation, they will dephase rapidly at the start of the spin-locking pulse. The diagonal elements, $\sigma'^D(0)$, are the states which commute with the spin-locking Hamiltonian – these are the states which will be spin-locked. In a static sample these states will remain unchanged for the duration τ of the spin-locking pulse. In the eigenbasis of the spin-locking Hamiltonian these are equivalent to population states. When viewed back in the normal rotating frame using

$$\sigma(\tau) = V^{-1}\sigma'^D(0)V \tag{6.11}$$

the elements of the final density matrix correspond to a range of coherences and population states.

6.3.1 Spin-locking under MAS

During MAS, the quadrupolar splitting parameter ω_Q becomes time dependent:

$$\omega_Q(t) = \frac{\omega_Q^{\mathrm{PAS}}}{2}\{-\sqrt{2}\sin 2\beta\cos(\omega_R t + \xi) + \sin^2\beta\cos 2(\omega_R t + \xi)\} \tag{6.12}$$

where β is the angle between the quadrupolar PAS and the spinning axis and ξ is the initial phase about this axis. The quadrupolar splitting changes sign either two or four times per rotor period depending on β. A measure of whether this rotor-driven behaviour occurs adiabatically or suddenly in the weak field ($\omega_1 \ll \omega_Q$) limit is given by the adiabaticity parameter introduced by Vega [125],

$$\alpha = \frac{\omega_1^2}{2\omega_Q^{\mathrm{PAS}}\omega_R} \tag{6.13}$$

In the sudden limit ($\alpha \ll 1$), the zero-crossing of $\omega_Q(t)$ occurs rapidly, and the final state $\sigma(t)$ remains unchanged by MAS. In this case the spin-locking should be the same as in a static sample. Conversely, in the adiabatic limit ($\alpha \gg 1$) where the zero-crossing occurs slowly, the spin-locked states are time dependent. This can be incorporated into the model by using one unitary transformation, $V(0)$, to produce the initial state in the eigenbasis of the spin-locking Hamiltonian (Equation 6.14) but a different transformation, $V(\tau)$, to view the density matrix in the rotating frame after a spin-locking pulse of duration τ,

$$\sigma(\tau) = V^{-1}(\tau)\sigma'^{D}(0)V(\tau). \tag{6.14}$$

Although the final state $\sigma(\tau)$ varies with rotor phase $\Phi = \omega_R t$ as a result of this time-dependence, the spins remain locked at all times. The third case, when $\alpha \sim 1$, is called the intermediate regime – here, a zero-crossing will partially convert population differences across spin-locking eigenstates into off-diagonal coherences and the spin-locked magnetisation will decay on a timescale of $\sim \omega_R$.

6.4 Spin-locking calculations

6.4.1 Spin-locking model

This simple model of spin-locking has been incorporated into Fortran programs which can be found in Appendix D. The tensor operator $T_{1,0}$, which is proportional to the thermal equilibrium state I_z, forms the initial density matrix. The asymmetry parameter, η, is assumed to equal zero so that Equation 2.59 can be used to calculate the quadrupolar splitting parameter, ω_Q. The spin-locking pulse Hamiltonian is calculated using Equation 6.1. The Hamiltonian is diagonalised using the unitary transformation V which is

found numerically. By setting the off-diagonal elements to equal zero, only the spin-locked, i.e., the diagonal elements of the density matrix are retained. The final density matrix in the rotating frame is obtained using Equation 6.14. The final states are determined by calculating the expectation value of operator Q by taking the trace of the final density matrix elements with the adjoint operator $Q^{\dagger}$,

$$\langle Q \rangle = \mathrm{Tr}\{\sigma(\tau)Q^{\dagger}\}, \tag{6.15}$$

where Q is a spherical tensor operator, $T_{l,p}$.

6.4.2 Exact density matrix method

In order to illustrate that the results of the simple spin-locking model are valid, calculations have also been carried out using an exact density matrix approach similar to that detailed in Section 5.2. The total experimental time is broken into small divisions and the Hamiltonian is assumed to be time-independent during each small step, thus allowing the time evolution of the density operator to be calculated using the solution of the Liouville-von Neumann equation.

6.5 Simulations

6.5.1 Spin $I = 3/2$ in a static solid

Using the model of spin-locking described, the expectation values of the spin $I = 3/2$ spherical tensor operators created by the rapid dephasing of the initial state $\sigma(0) = T_{1,0}$ were calculated as a function of radiofrequency field strength, ω_1, and resonance offset, Ω. Figure 6.2 shows the results as three-dimensional surface plots. The quadrupolar splitting parameter $\omega_{\mathrm{Q}}^{\mathrm{PAS}}$ was 200 kHz and a single orientation was chosen ($\beta = 0°$, hence $\omega_{\mathrm{Q}} = \omega_{\mathrm{Q}}^{\mathrm{PAS}}$. Expectation values are presented for the central transition and for simplicity only tensor operators with positive values of p are shown (although tensors with negative p will also be present since the the density matrix is Hermitian).

First considering $T_{1,0}$, the expectation value is at a maximum when $\omega_1 = 0$ Hz, i.e., there is no evolution of the states when no pulse is applied. As ω_1 increases, $T_{1,0}$ decreases as

the spin-locking pulse creates other coherences and population states. The extent of the falloff with ω_1 decreases as the resonance offset increases. At offsets equal to around 0, ω_Q^{PAS} and $2\omega_Q^{\mathrm{PAS}}$ there are local dips in the $T_{1,0}$ surface plot corresponding to the creation of other states.

The central transition intensity is equal to zero when either $\omega_1/2\pi = 0$ (no pulse) or $\Omega = 0$ (the on-resonance pulse does not excite the equilibrium z-magnetisation). The amount of CT spin-locked increases as both ω_1 and Ω increase, with a dip in intensity at $\Omega/2\pi = 200$ kHz. The population states $T_{2,0}$ and $T_{3,0}$ are created with most efficiency at low rf field strengths (near 0) with offsets equal to multiples of the quadrupolar splitting: $\Omega/2\pi \approx 0, 200$ kHz for $T_{2,0}$ and $\Omega/2\pi \approx 0, 200, 400$ kHz for $T_{3,0}$. In contrast, the single-quantum states $T_{1,1}$, $T_{2,1}$ and $T_{3,1}$ are zero at these conditions of $\Omega/2\pi \approx 0, 200, 400$ kHz and $\omega_1/2\pi \approx 0$ kHz, instead forming between these offsets and at higher rf fields. The amount of $T_{1,1}$ increases as ω_1 and Ω increase. $T_{2,1}$ reaches a maximum at $\Omega/2\pi = 85$ kHz and $\omega_1/2\pi = 205$ kHz. $T_{3,1}$ is most abundant at $\Omega/2\pi = 320$ kHz and $\omega_1/2\pi = 100$ kHz. Next considering the double-quantum coherences $T_{2,2}$ and $T_{3,2}$, both peak at $\omega_1/2\pi = 35$ kHz, inverting in sign at $\Omega/2\pi = 200$ kHz to give most intensity just above and below this offset. Finally, looking at the triple-quantum coherence $T_{3,3}$, we see that it is created mostly at low offsets, with a maximum at $\Omega/2\pi = 5$ kHz and $\omega_1/2\pi = 105$ kHz.

The three-dimensional surface plots in Figure 6.3 show the equivalent results for a powder sample. Here, the contribution of crystallites with differing values of ω_Q according to orientation gives rise to modified behaviour – in particular, interesting features in the plots no longer arise only at offsets around ω_Q^{PAS} and $2\omega_Q^{\mathrm{PAS}}$.

The $T_{1,0}$ plot is similar to the one seen before – the magnitude decreases as ω_1 increases, with a more rapid falloff at lower offsets. A slight dip is seen at $\Omega/2\pi \approx 120$ kHz. $T_{2,0}$ is created with most intensity at $\Omega/2\pi = 90$ kHz and $\omega_1/2\pi = 50$ kHz, while $T_{3,0}$ is abundant at lower resonance offsets and rf strengths, with a maximum at $\Omega/2\pi = 5$ kHz and $\omega_1/2\pi = 10$ kHz.

As before, $T_{1,1}$ is zero when ω_1 and $\Omega = 0$, and as these are both increased, more $T_{1,1}$ is created. $T_{2,1}$ is at a maximum when $\Omega/2\pi = 30$ kHz and $\omega_1/2\pi = 65$ kHz. Both $T_{2,1}$ and $T_{3,1}$ feature dips at $\Omega/2\pi \approx 100$ kHz at weak rf field strengths.

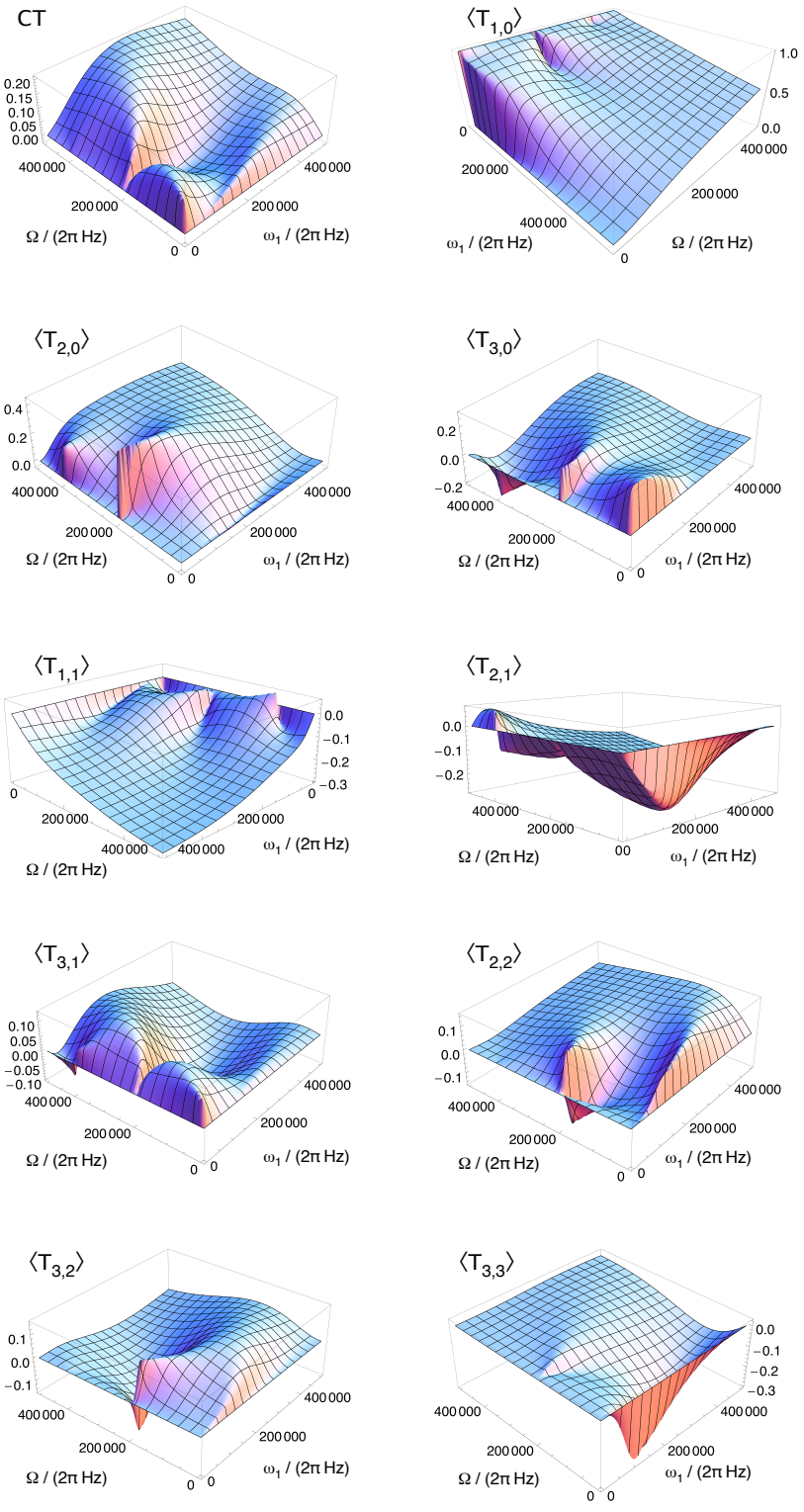

FIGURE 6.2: Three-dimensional surface plots of the spin $I = 3/2$ expectation values of spherical tensor operators, $T_{l,p}$ and the central transition (CT) created by rapid dephasing of initial state $T_{1,0}$ under a spin-locking Hamiltonian, as a function of ω_1 and Ω. Results are plotted for a single orientation ($\theta = 0°$) with $\omega_Q^{PAS}/2\pi = 200$ kHz.

The sign and magnitude of the $T_{2,2}$ expectation value has a varied dependence on the resonance offset and rf field strength, with a maximum at $\Omega/2\pi = 110$ kHz and $\omega_1/2\pi = 47.5$ kHz. Most $T_{3,2}$ is created at $\Omega/2\pi = 40$ kHz and $\omega_1/2\pi = 97.5$ kHz. As seen in the single orientation plots, $T_{3,3}$ is created mostly at low offsets, with a maximum at $\Omega/2\pi = 5$ kHz and $\omega_1/2\pi = 65$ kHz.

Figure 6.4 plots cross-sections of these expectation values as a function of ω_1 with a constant resonance offset of 100 kHz. Here it is clearer to see the relative contribution of each spherical tensor operator to the overall spin-locked magnetisation. As the amount of $T_{1,0}$ decreases, $T_{1,1}$ increases to a maximum around $\omega_1/2\pi = 200$ kHz before falling off again. $T_{2,0}$ and $T_{3,0}$ also make a significant contribution, peaking at $\omega_1/2\pi = 50$ kHz and 125 kHz respectively. $T_{3,1}$, $T_{3,2}$ and $T_{3,2}$ all peak at low rf field strength (around 30 kHz) before passing through zero at 100 kHz and peaking again at higher ω_1. $T_{3,2}$ only becomes significant at stronger rf field strengths, peaking at around $\omega_1/2\pi = 200$ kHz.

As a measure of the extent of the initial rapid dephasing, we can examine the change in the norm of the density operator,

$$\mathrm{Tr}\{\sigma(\tau)\}^2 = \sum_l \sum_p \mathrm{Tr}\{\sigma(\tau) T_{l,-p}\}^2 \tag{6.16}$$

Under a unitary transformation, this quantity is conserved. However, as the initial rapid dephasing represents a non-unitary transformation, we can gauge the efficiency of the spin-locking from changes in the norm. Figure 6.5 plots the norm as a function of rf field strength for a range of resonance offsets from 0 to 250 kHz. For all offsets, a decrease in the magnitude of the norm is observed as the rf strength increases, reflecting the decreasing efficiency of the spin-locking pulse. As the resonance offset increases, the spin-locking efficiency at higher rf strength increases.

Spin-locking simulations for $I = 5/2$ in a static solid can be found in Appendix F.

6.5.2 Spin $I = 3/2$ under MAS

Sample rotation under MAS leads to more complex spin-locking behaviour as the sign and magnitude of the quadrupolar splitting parameter change, with the outcome dependent on whether the zero-crossing occurs adiabatically or suddenly. Figure 6.6

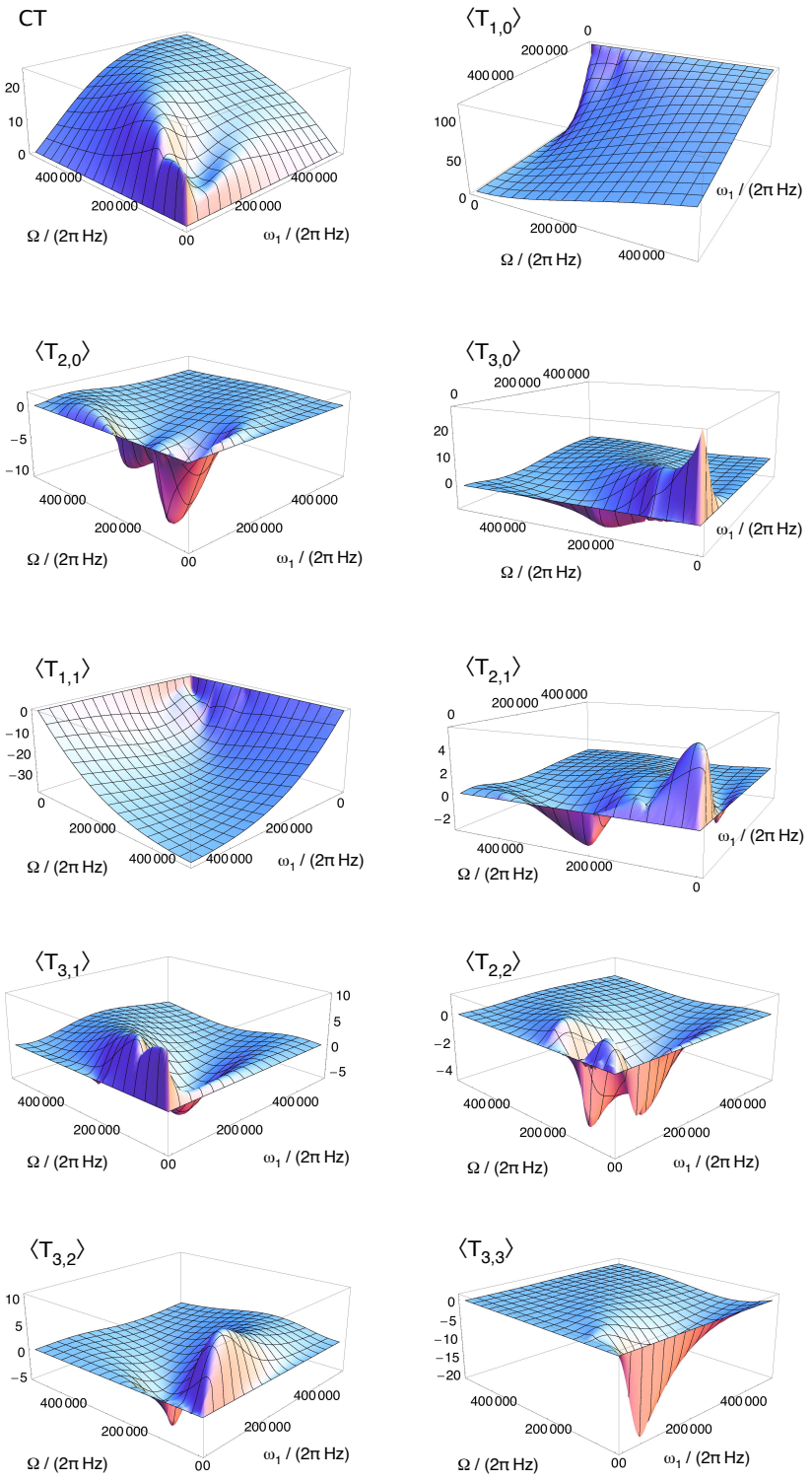

FIGURE 6.3: Three-dimensional surface plots of the spin $I = 3/2$ expectation values of spherical tensor operators, $T_{l,p}$ and the central transition (CT) created by rapid dephasing of initial state $T_{1,0}$ under a spin-locking Hamiltonian, as a function of ω_1 and Ω. Results are plotted for a powder sample with $\omega_Q^{\mathrm{PAS}}/2\pi = 200$ kHz.

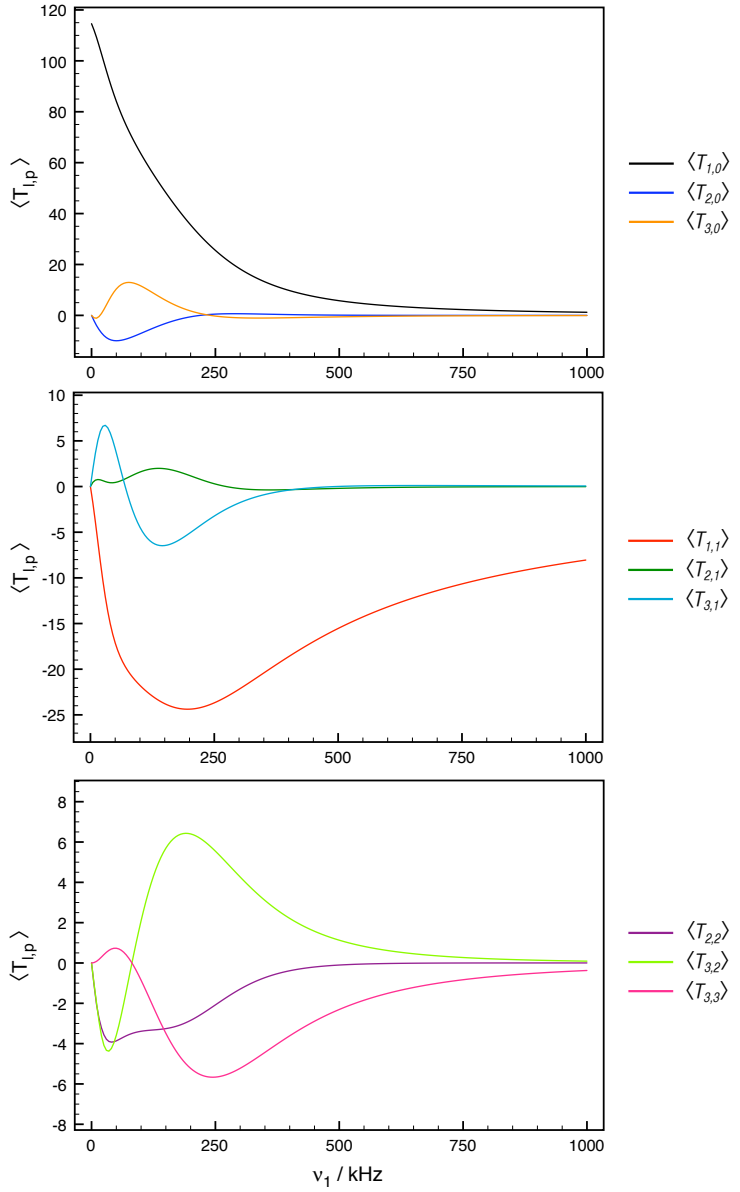

FIGURE 6.4: Expectation values of $I = 3/2$ spherical tensor operators, $T_{l,p}$ created by rapid dephasing of initial state $T_{1,0}$ under a spin-locking Hamiltonian, as a function of $\nu_1 = \omega_1/2\pi$. Results are plotted for a powder with $\omega_Q^{PAS}/2\pi = 200$ kHz and $\Omega/2\pi = 100$ kHz.

shows the expectation values of the $I = 3/2$ spherical tensor operators formed by initial rapid dephasing as a function of time through one complete rotor period at resonance offsets of $\Omega/2\pi = 50$ kHz and 100 kHz. The spin-locking field strength used in these simulations was $\omega_1/2\pi = 75$ kHz and the quadrupolar splitting given by $\omega_Q^{PAS}/2\pi = 200$ kHz. A single crystallite orientation was chosen with $\beta = 90°$ and an initial phase angle of $\xi = 180°$, giving a value of $\omega_Q/2\pi = 100$ kHz at the start of the rotor period.

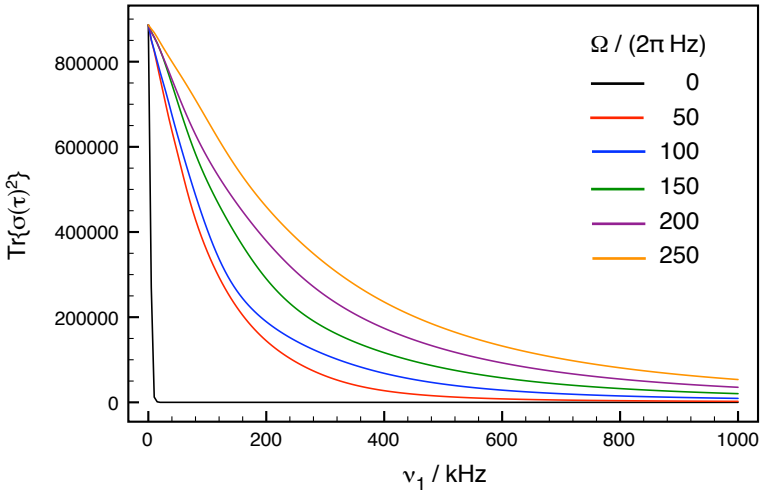

FIGURE 6.5: The norm of the spin $I = 3/2$ density operator created by rapid dephasing of initial state $T_{1,0}$ under a spin-locking Hamiltonian, as a function of $\nu_1 = \omega_1/2\pi$. Results are plotted for a powder with $\omega_Q^{PAS}/2\pi = 200$ kHz and $\Omega/2\pi = 50, 100, 150, 200$ and 250 kHz.

Looking first at Figure 6.6(a), $T_{1,0}$ is most abundant at the start of the rotor period, along with a significant amount of $T_{2,1}$, $T_{2,0}$ and $T_{3,0}$. As the sample rotates, the amount of $T_{1,0}$ decreases then rises again slightly forming a local maximum after a quarter turn of the rotor. This is mirrored by the next quarter turn, returning $T_{1,0}$ to its original amplitude. The same cycle is observed for the second half of the rotor period. Similar behaviour is seen for $T_{2,0}$. The intensity of $T_{1,1}$, $T_{3,1}$ and $T_{2,2}$ correspondingly rises as the population states decline, giving maxima after a quarter turn and minima at a half turn. Both $T_{3,2}$ and $T_{3,3}$ cycle to a maximum after an eight of a turn before falling to a minimum after another equal time period.

Next, considering the plots in Figure 6.6(b), we see that there is less modulation of the spin-locked states compared to the lower offset. At the start of the rotor period, the population states $T_{1,0}$, $T_{2,0}$ and $T_{3,0}$ are present in greatest amplitude in order of decreasing rank. The decrease of these leads to the rotor-driven interconversion with the higher-order coherences, with $T_{1,1}$, $T_{2,1}$ and $T_{2,2}$ being the most significant. A large decline is observed in the amount of $T_{3,1}$, $T_{3,2}$ and $T_{3,3}$ compared to the simulations for $\Omega/2\pi = 50$ kHz.

A density matrix calculation confirms the validity of the results found using the spin-locking model. In Figure 6.7, the spin $I = 3/2$ expectation values for a powder have been calculated for two rotor periods using (a) the spin-locking model and (b) an exact

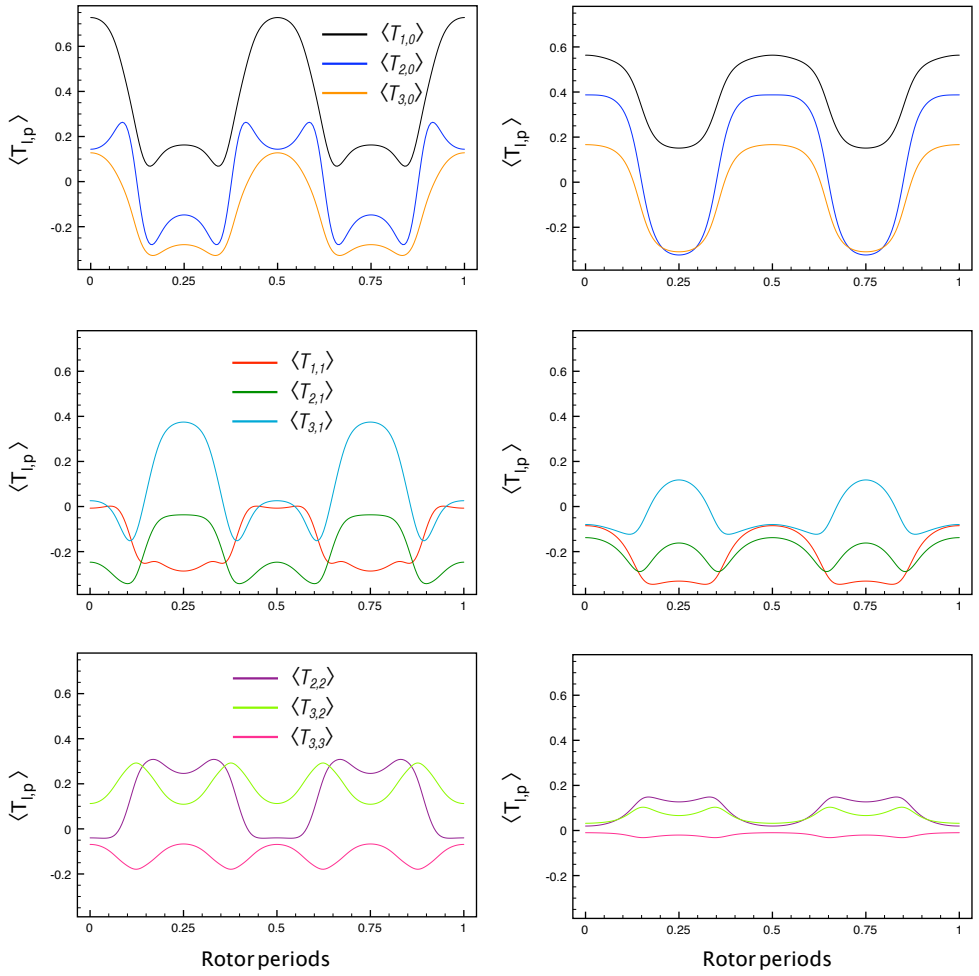

(a) $\Omega/2\pi = 50$ kHz (b) $\Omega/2\pi = 100$ kHz

FIGURE 6.6: Expectation values under MAS of $I = 3/2$ spherical tensor operators, $T_{l,p}$, created by rapid dephasing of initial state $T_{1,0}$ under a spin-locking Hamiltonian, as a function of ν_1. Results are plotted for a single orientation ($\beta = 90°$ and $\xi = 180°$) with $\omega_Q^{\mathrm{PAS}}/2\pi = 200$ kHz.

density matrix approach. The oscillations seen before in Figure 6.6 are strongly dependent on the crystallite orientation as defined in Equation 6.12, while here the summation of the states over a range of β and ξ values are a more realistic representation of a typical experiment. After a period of initial rapid dephasing, the states settle into a periodic interconversion of spin-locked states in Figure 6.7(b). The calculation using the simple model (Figure 6.7(a)) shows excellent agreement in predicting the evolution of the spin-locked states.

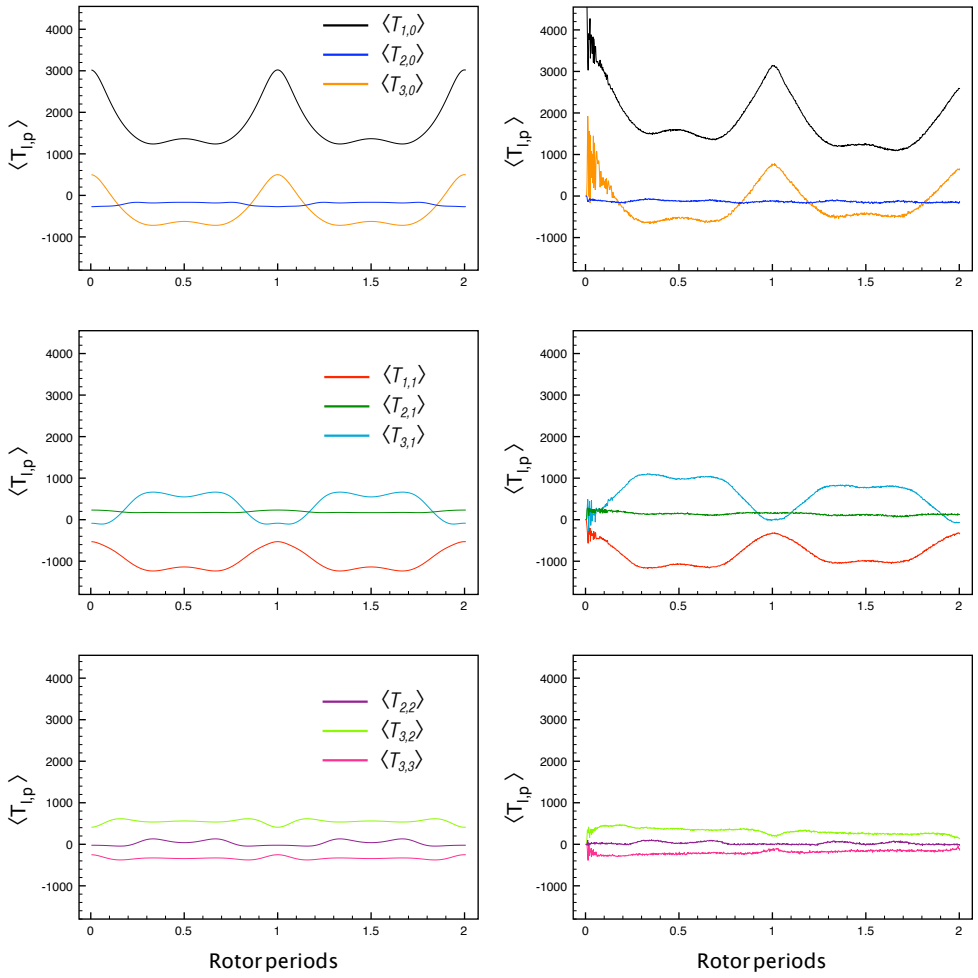

(a) Spin-locking model (b) Exact density matrix

FIGURE 6.7: Evolution of expectation values of $I = 3/2$ spherical tensor operators, $T_{l,p}$, under MAS. Results are plotted for a powder with $\omega_Q^{\mathrm{PAS}}/2\pi = 200$ kHz, $\omega_1/2\pi = 75$ kHz and $\Omega/2\pi = 50$ kHz. Results are shown for (a) the spin-locking model and (b) an exact density matrix calculation. The MAS rate in (b) was $\nu_R = 10$ kHz.

6.5.3 Spin $I = 5/2$ under MAS

A comparison of the results of the model with an exact density matrix calculation is presented in Figure 6.8. Here the evolution of the spin-locked states has been calculated for the duration of two complete turns of the rotor. The same simulation parameters are used as described for the corresponding spin $I = 3/2$ simulation (Figure 6.7), giving an adiabaticity parameter of $\alpha = 1.4$ for the density matrix calculation. For the population states and single-quantum coherences, a good qualitative agreement can be seen between the model and the exact density matrix simulations. However, for the higher order coherences, the magnitude of the spin-locked states decays on the timescale of

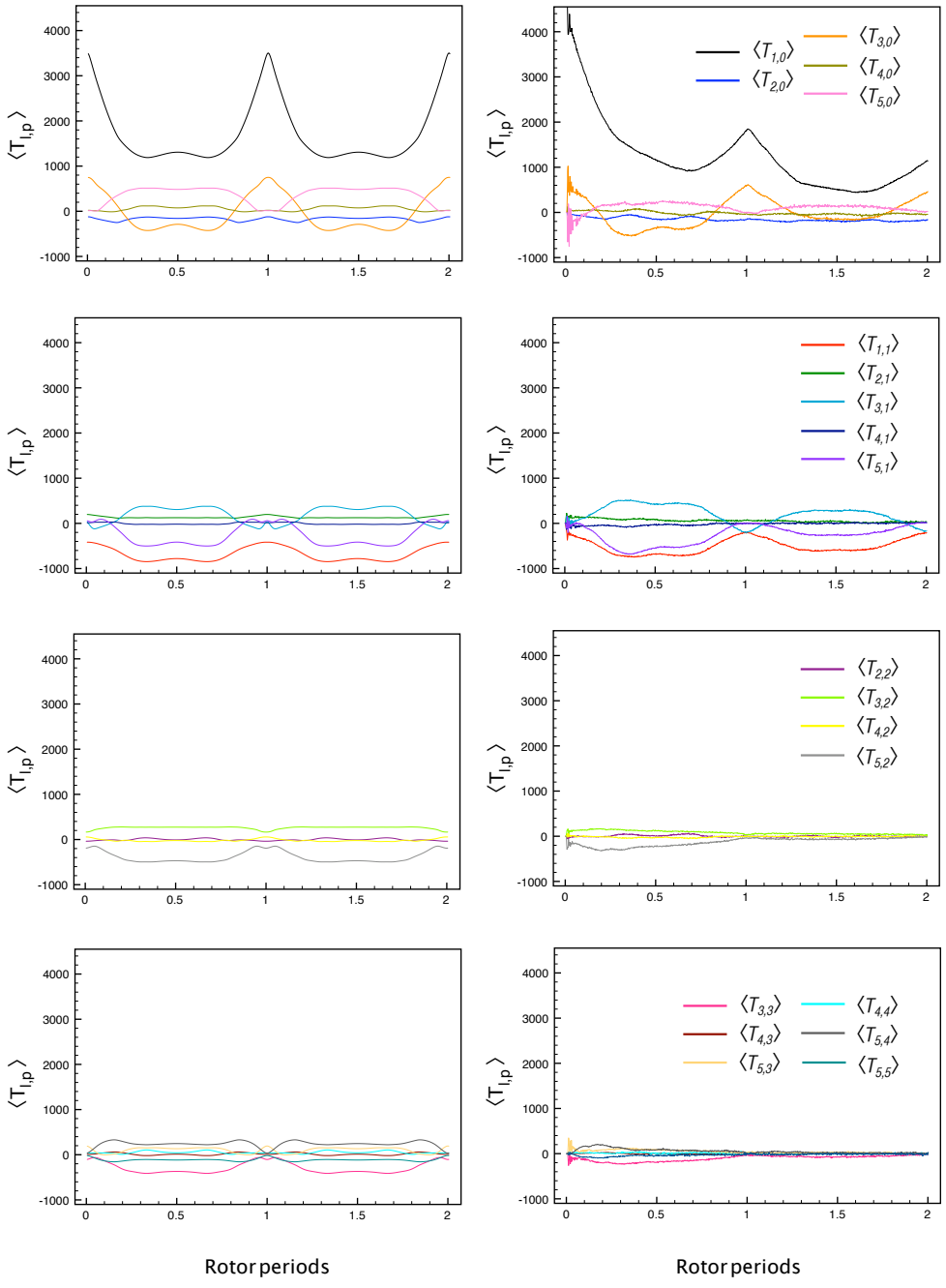

(a) Spin-locking model

(b) Exact density matrix

FIGURE 6.8: Evolution of expectation values of $I = 5/2$ spherical tensor operators, $T_{l,p}$, under MAS. Results are plotted for a powder with $\omega_Q^{\mathrm{PAS}}/2\pi = 200$ kHz, $\omega_1/2\pi = 75$ kHz and $\Omega/2\pi = 50$ kHz. Results are shown for (a) the spin-locking model and (b) an exact density matrix calculation. The MAS rate in (b) was $\nu_R = 10$ kHz.

around $1/\omega_R$ in the density matrix simulations, such that there is little magnetisation spin-locked in these states during the second rotor period. This is a consequence of the adiabaticity parameter being close to 1 – in this intermediate regime, spin-locking

is not efficient under MAS. Appendix F contains further simulations of spin-locking of $I = 5/2$ nuclei under MAS.

6.6 Experiments

6.6.1 Experimental details

Experiments were carried out on a Bruker Avance 400 spectrometer equipped with a widebore 9.4 T magnet operating at a Larmor frequency of $\omega_0/2\pi = 105.8$ kHz for ^{23}Na ($I = 3/2$) and $\omega_0/2\pi = 104.3$ kHz for ^{27}Al ($I = 5/2$). As the size of the quadrupolar interaction of a nucleus becomes comparable to the rf field strength, the pulse response becomes non-sinusoidal, thus making calibration of the rf field difficult for many compounds [131]. The rf field strength was determined by calibrating the 180° pulse length on sodium chloride – owing to the octahedral coordination of chloride ions around the sodium cation, the ^{23}Na quadrupolar interaction is zero. ^{23}Na NMR studies were carried out using two compounds: sodium nitrite ($NaNO_2$) and sodium nitrate ($NaNO_3$), while ^{27}Al experiments were carried out on aluminum acetylacetonate ($Al(acac)_3$). All three compounds were obtained commercially as powdered solids and were packed in 4-mm rotors for both static and MAS experiments. In order to limit the effects of rf inhomogeneity on the experimental results, the samples were packed to a depth of around 1 cm only in the centre of the rotor (the remaining volume of the rotor was packed with powdered boron phosphate as a spacer material). Each of the three compounds possesses a single crystallographically-distinct cation site, with $\omega_Q^{PAS}/2\pi = 84$ kHz for $NaNO_3$ [132]; $\omega_Q^{PAS}/2\pi = 275$ kHz and $\eta = 0.109$ for $NaNO_2$ [133]; and $\omega_Q^{PAS}/2\pi = 225$ kHz and $\eta = 0.15$ for $Al(acac)_3$ [134].

6.6.2 Spin $I = 3/2$ in a static solid

Figure 6.9 shows the ^{23}Na central-transition intensity of static sodium nitrate and sodium nitrite as a function of increasing offset of the rf transmitter from the central transition frequency at three different spin-locking field strengths. The experiments were recorded using the pulse sequence introduced in Figure 6.1(a), with a spin-locking pulse length equal to 300 μs. A recycle interval of 10 s was employed in the $NaNO_3$

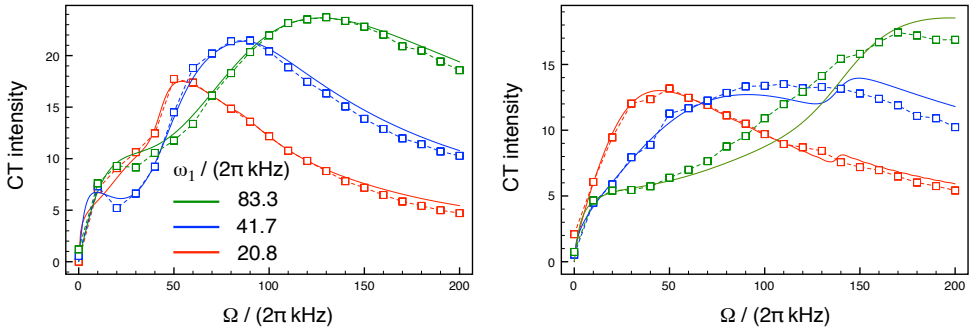

(a) $NaNO_3$ (b) $NaNO_2$

FIGURE 6.9: ^{23}Na central-transition NMR signal intensity in (a) $NaNO_3$ and (b) $NaNO_3$ recorded using the pulse sequence in Figure 6.1(a) as a function of resonance offset. The spin-locking pulse length was 300 μs in each case. Experimental points are shown by squares joined by a dashed line, while the spin-locking intensities calculated using the spin-locking model are shown by a solid line. The intensities of all experimental points were multiplied by the same empirical constant to allow comparison with the simulations.

experiments, while a shorter delay of 1 s was used in the $NaNO_2$ experiments. The experimentally-derived spin-locking intensities (datapoints shown by squares joined by a dashed line) have been empirically scaled to allow a comparison with the simulation results of the spin-locking model (shown by solid lines). The same scaling factor was applied to all experimental data points shown in Figures 6.9 and 6.10.

In Figure 6.9(a), the spin-locked CT intensity of $NaNO_3$ increases to a maximum at $\Omega/2\pi = 50$ kHz before falling off again with the rf field strength equal to $\omega_1/2\pi = 20.8$ kHz. With $\omega_1/2\pi = 41.7$ kHz, the CT intensity rises as the offset increases, dipping at $\Omega/2\pi = 20$ kHz before rising to a maximum at $\Omega/2\pi = 90$ kHz. At the strongest spin-locking field, the CT amplitude rises with increasing offset, dipping very slightly at $\Omega/2\pi = 30$ kHz and reaching a maximum at $\Omega/2\pi = 130$ kHz, before falling off gradually. As ω_1 increases, the maximum amount of spin-locked CT obtained also increases. The experimental results and the model show an excellent agreement at all three rf strengths for $NaNO_3$. While a simulation using density matrix theory would, of course, reflect the experimental results, we see here that calculations employing the simplified model of spin-locking are highly successful in predicting the experimental outcome.

Figure 6.9(b) shows an increase in spin-locked CT magnetisation of $NaNO_2$ up to $\Omega/2\pi=$ 50 kHz with $\omega_1/2\pi = 20.8$ kHz before falling off again with further increase in the resonance offset. At $\omega_1/2\pi = 41.7$ kHz, the amount of CT spin-locked builds up slowly

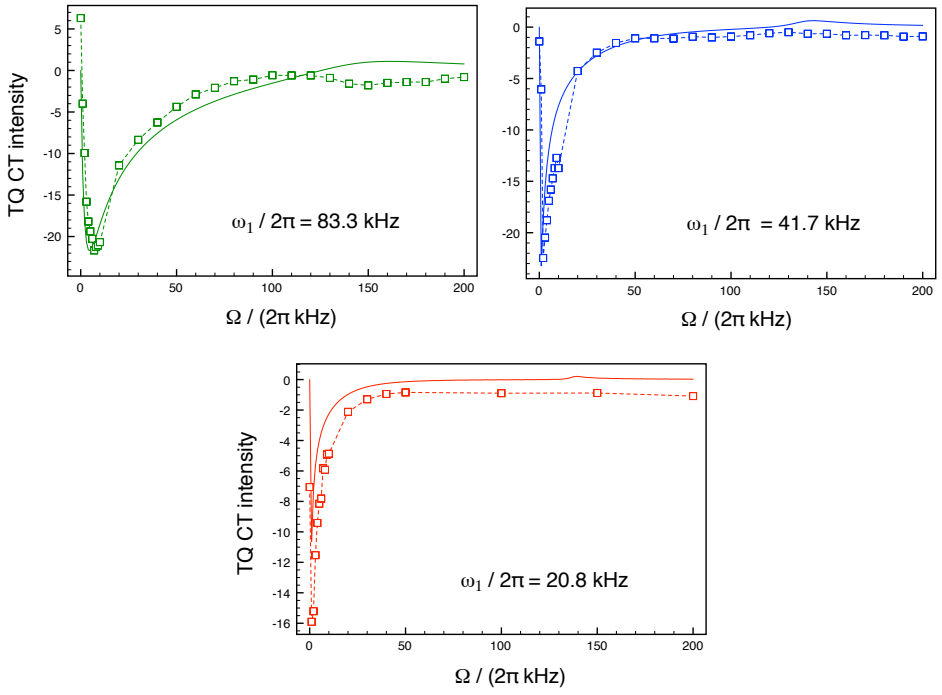

FIGURE 6.10: ^{23}Na triple quantum-filtered central-transition NMR signal intensity in $NaNO_2$ recorded using the pulse sequence in Figure 6.1(b) as a function of resonance offset. The spin-locking pulse length was 300 μs in each case. Experimental points are shown by squares joined by a dashed line, while the spin-locking intensities calculated using the spin-locking model are shown by a solid line.

to a maximum around $\Omega/2\pi = 100$ kHz, and remains fairly steady before decreasing at offsets greater than 140 kHz. At the strongest rf field strength, the build up of the spin-locked CT intensity as the offset increases is slower. A maximum is reached at $\Omega/2\pi = 170$ kHz. A near-perfect agreement between the experimental data and model is seen with $\omega_1/2\pi = 20.8$ kHz, although a greater error is seen for the higher rf strengths. It is possible that the relaxation interval was not sufficient, affecting the intensities measured in the experimental results.

Figure 6.10 shows plots demonstrating the experimentally-obtained spin-locking intensities for the triple-quantum filtered central transition intensity of sodium nitrite as a function of resonance offset and compares them to the expectation value of the triple-quantum coherence $T_{3,3}$ calculated using the simple model of spin-locking. The pulse sequence illustrated in Figure 6.1(b) was used with a spin-locking pulse duration of 300 μs. The length of the second pulse was optimised for the conversion of the triple-quantum coherences back into observable single-quantum coherence (1.6 μs at $\omega_1/2\pi = 166.7$ kHz).

With the spin-locking field strength set to 83.3 kHz, the amount of triple-quantum coherence rises rapidly as the offset increases up to $\Omega/2\pi = 7$ kHz. The intensity then declines as the offset is raised further, with a very slight increase again at $\Omega/2\pi = 150$ kHz. Halving the rf strength to 41.7 kHz, the maximum amount of triple-quantum coherence is created at a lower offset of $\Omega/2\pi = 2$ kHz. When the field strength is lowered further to 20.8 kHz, the occurrence of triple-quantum coherence is again shifted to lower offset, with a maximum at $\Omega/2\pi = 1$ kHz.

For the two strongest rf strengths, the calculations closely match the experimental results, although slightly underestimate the amount of spin-locked magnetisation present at higher offset. The calculation carried out with $\omega_1/2\pi = 20.8$ kHz also significantly underestimates the amount of spin-locked triple-quantum magnetisation created at low offsets. However, the general trend is still reflected accurately. A change in the tuning of the probe could be responsible for this result, as this would affect the scaling factor between experiments.

6.6.3 Spin $I = 5/2$ in a static solid

The creation of various population states and coherences as predicted in the simulations in Appendix F.1 has been observed in ^{27}Al ($I = 5/2$) spin-locking experiments and is demonstrated using coherence-counting experiments [128]. Two-dimensional spectra were recorded using the pulse sequence shown in Figure 6.1(b) with the phase of the spin-locking pulse incremented in place of any incremental time dimension. By varying the phase in $2n$ steps from 0° to 360°, a maximum of n coherence orders may be observed [135, 136]. Here, the phase was incremented in twelve steps of 30°, thus six coherence orders may be seen. As there is no t_1 dimension, the steps from 0° to 360° are repeated (in this case 16 times) and a weighting function applied to build an interferogram before Fourier transformation of the data. Signals in the F_1 projections from the resulting spectrum then correspond to separate coherence orders, with the nth line representing the nth coherence order. As well as being used previously to investigate spin-locked magnetisation [128], this experiment has been used to investigate the build-up of multiple-quantum coherences in multiple-spin correlation experiments [137] and in spin-counting applications in studies of dipolar-coupled proton networks [138, 139].

The spin-locking duration was 300 μs with $\omega_1/2\pi = 83.3$ kHz and the relaxation interval was 10 s in all ^{27}Al experiments performed. Whereas in Figure 6.10 the duration of the second pulse was optimised for the conversion of triple-quantum coherences back into observable 1Q coherence, the pulse here was chosen to be able to simultaneously observe a variety of coherences.

Figure 6.11 shows the results of the spin-locking coherence-counting experiment performed on Al(acac)$_3$ at two resonance offsets, $\Omega/2\pi = 10$ and 50 kHz. As expected from the three-dimensional surface plots presented in Figure F.2, the $p = 0$ amplitude increases as the offset is raised, mainly owing to the contribution of $T_{1,0}$. Similarly, the simulations showed a noticeable increase in $T_{1,1}$ with greater offset, reflected experimentally in the $p = 1$ amplitude. The $p = 2$ signal of the coherence-counting spectrum also increases as the offset is increased to 50 kHz, while higher coherence orders either decrease or remain at a similar intensity.

6.6.4 Spin $I = 3/2$ under MAS

^{23}Na spin-locking experiments have been carried out under MAS on sodium nitrite, confirming the complex rotor-driven dynamics predicted by theory. Figure 6.12 shows experimental ^{23}Na central-transition signal intensities as a function of the spin-locking pulse length, where the maximum pulse length was equal to five full rotor periods (500 μs at a MAS rate of $\omega_R/2\pi = 10$ kHz). In Figure 6.12 the spin-locking field strength used was 83.3 kHz, giving an adiabaticity parameter of $\alpha = 1.26$. In this adiabatic regime, the rotor-driven modulation is clear. As the rotor turns, the CT intensity increases, reaching a maximum after a half turn. This is followed by a decrease during the second half of the rotor period as the various crystallites experience zero-crossings. At the end of each rotor period, the crystallites have experienced either two or four zero-crossings, and the original signal intensity is re-established.

In Figure 6.12(b), the spin-locking field strength was reduced to 20.8 kHz, yielding $\alpha = 0.08$. In these experiments, the modulation of the eigenstates falls under the sudden regime and the effect of sample rotation on the spin-locked states is less pronounced.

Similar effects are seen in Figure 6.13, where the triple-quantum coherence is monitored as a function of spin-locking duration under (a) the adiabatic regime and (b) the sudden

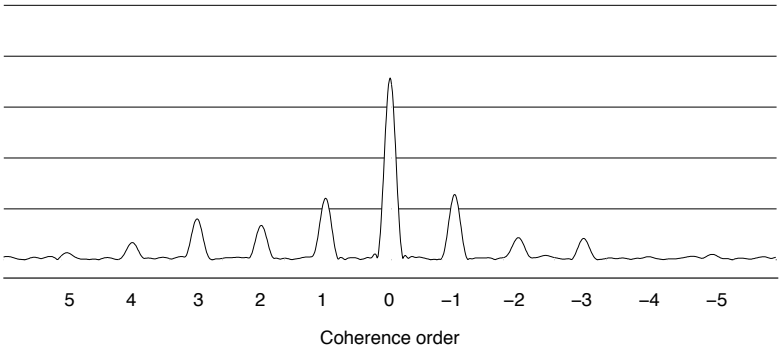

(a) $\Omega/2\pi = 10$ kHz

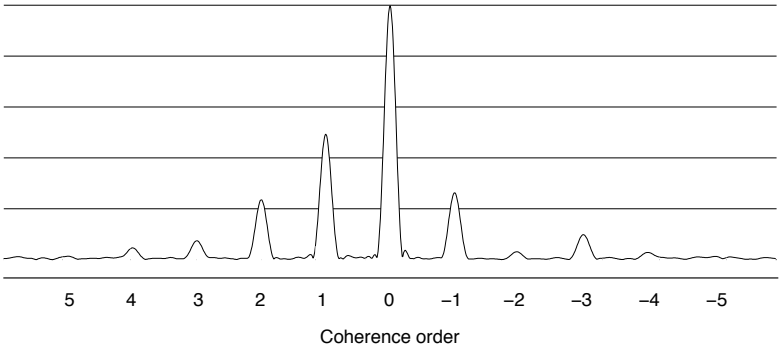

(b) $\Omega/2\pi = 50$ kHz

FIGURE 6.11: ^{27}Al NMR coherence-counting experiments, showing the amplitude of different coherence orders present during the spin-locking of Al(acac)$_3$ at resonance offsets of (a) 10 kHz and (b) 50 kHz. Rows were extracted from the F_1 dimension of two-dimensional spectra recorded using the pulse sequence shown in Figure 6.1(b), with a 30° increment in the phase of the spin-locking pulse. The strength of the spin-locking field was 83.3 kHz.

limit. Under the adiabatic limit, a clear modulation of the magnetisation is observed, with minima at integer rotor periods. This corresponds to the simulations where population states are most abundant at the start of each rotor period, and sample rotation induces coherence-transfer to higher order states. When performed at a lower spin-locking field strength, there is no clear modulation of the amplitude with rotation.

6.6.5 Spin $I = 5/2$ under MAS

The ^{27}Al coherence-counting experiment has been used to examine the dependence of the spin-locked states on sample rotation. Figure 6.14 shows the coherence orders present at various points through a rotor period with the transmitter frequency offset by 50 kHz from resonance. The spin-locking field strength was $\omega_1/2\pi = 83.3$ kHz and

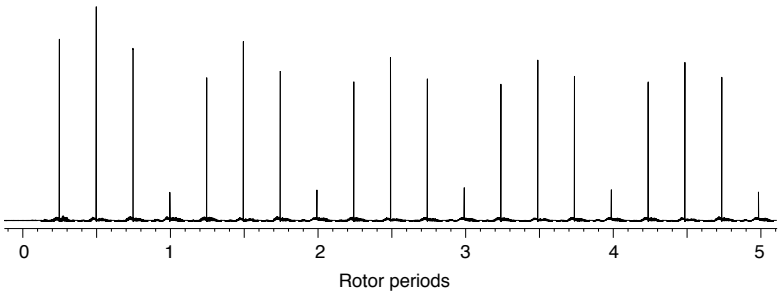

(a) $\omega_1/2\pi = 83.3$ kHz

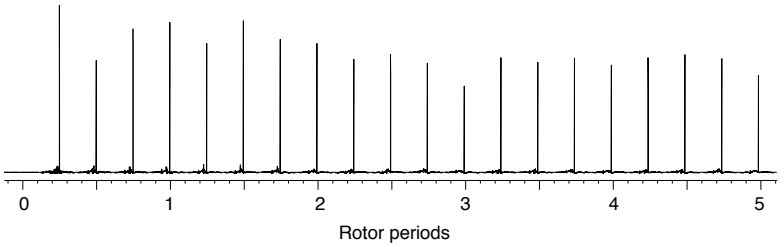

(b) $\omega_1/2\pi = 20.8$ kHz

FIGURE 6.12: ^{23}Na MAS NMR experiments, showing the signal intensity of the 1Q central transition during the spin-locking of $NaNO_2$ at a resonance offset of 50 kHz with varying spin-locking durations. The MAS rate was $\omega_R/2\pi = 10$ kHz, giving adiabaticity parameters of (a) $\alpha = 1.26$ and (b) $\alpha = 0.08$.

the the MAS rate was $\omega_R/2\pi = 10$ kHz, giving an adiabaticity parameter of $\alpha = 1.26$. In Figure 6.14(a), where the spin-locked states are observed after half a rotor period, magnetisation is present in most abundance with coherence orders $p = 1$, 0 and -1. Some double- and triple-quantum coherences are also observed. As in the $I = 3/2$ case, rotor-driven interconversion of states occurs and the spin-locked states vary throughout the rotor period. In Figure 6.14(b), where $\tau = 0.8\tau_R$, the amount of $p = 0$ has declined along with $p = -2$ and $p = 3$. In Figure 6.14(c), we see that further rotation of the sample has further decreased the amount of multiple-quantum coherences present in the spin-locked magnetisation. This corresponds to the minima observed at integer rotor periods in the calculated spin-locked states in Figure 6.8. Whereas in the static spin-counting experiments the spin-locked states do not change during the pulse, here it is shown that a time-dependent modulation of the spin-locked states under MAS exists.

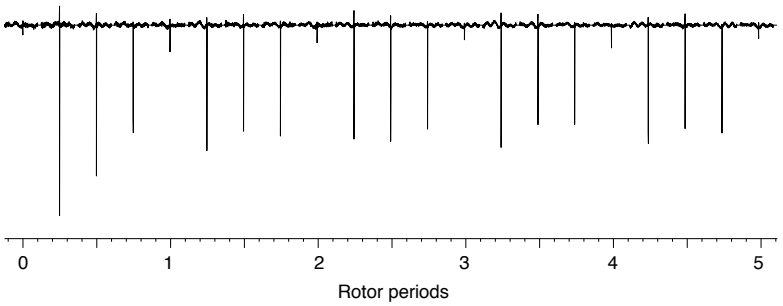

(a) $\omega_1/2\pi = 83.3$ kHz

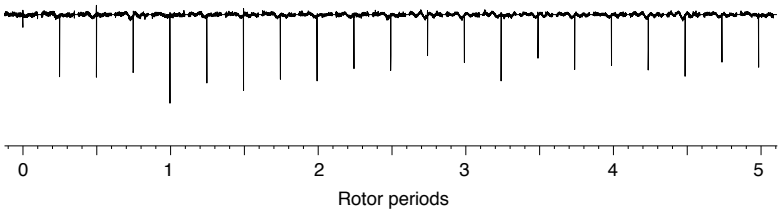

(b) $\omega_1/2\pi = 20.8$ kHz

FIGURE 6.13: ^{23}Na MAS NMR experiments, showing the signal intensity of the 3Q central transition during the spin-locking of $NaNO_2$ at a resonance offset of 50 kHz with varying spin-locking durations. The MAS rate was $\omega_R/2\pi = 10$ kHz, giving adiabaticity parameters of (a) $\alpha = 1.26$ and (b) $\alpha = 0.08$.

6.7 Conclusions

Using the model of quadrupolar spin-locking introduced by Ashbrook and Wimperis [128] which predicts the spin-locked state after an initial period of rapid dephasing, we have investigated the far off-resonance case of spin locking for spin $I = 3/2$ and $I = 5/2$ nuclei. Since the offset is large, there is a significant z-component to the effective field B_{eff} and so the magnetisation is left directed along the rotating-frame z-axis before the pulse is applied.

Three-dimensional surface plots showing the creation of a range of different coherences as a function of offset and spin-locking field strength have been presented. In the plots for single-orientation nuclear spin, features occur in the plots an integer multiples of ω_Q^{PAS} (see Figure 6.2), while more complicated behaviour is observed in the powder simulations (Figure 6.3).

Calculations using the simple model were found to be successful in predicting the results of single-quantum and triple-quantum experiments carried out on $NaNO_2$ and

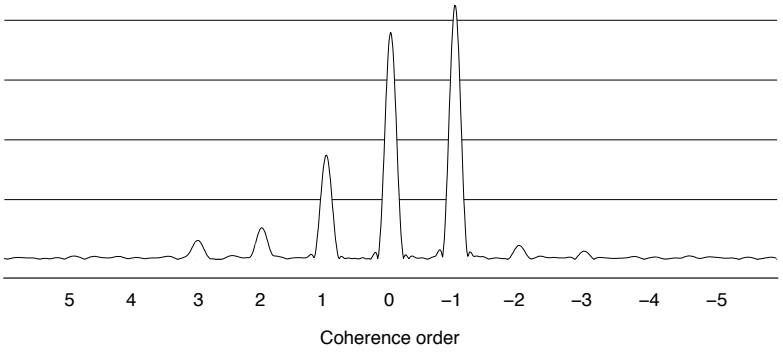

(a) $\tau = 0.5\tau_R = 50\ \mu s$

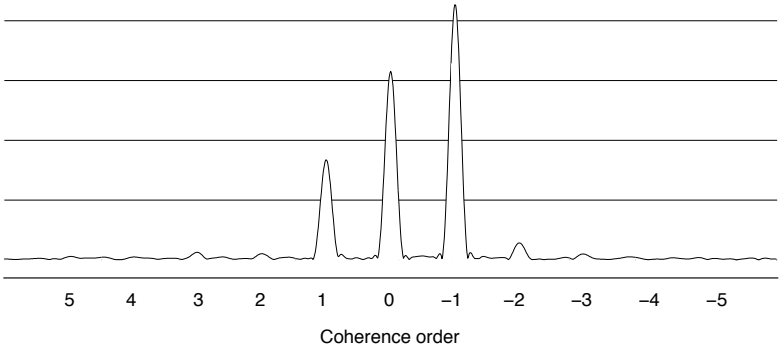

(b) $\tau = 0.8\tau_R = 80\ \mu s$

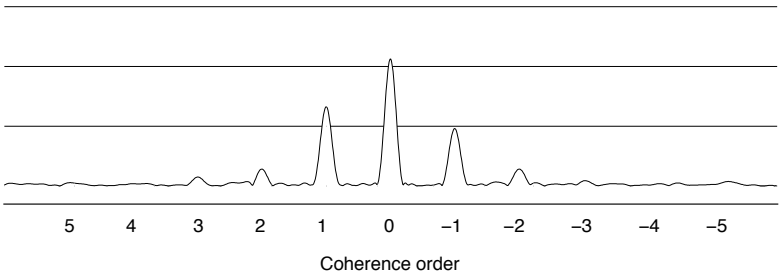

(c) $\tau = \tau_R = 100\ \mu s$

FIGURE 6.14: ^{27}Al MAS NMR coherence-counting experiments, showing the amplitude of different coherence orders present during the spin-locking of $Al(acac)_3$ at a resonance offset of 50 kHz with varying spin-locking durations, τ. The MAS rate was 10 kHz. Rows were extracted from the F_1 dimension of two-dimensional spectra recorded using the pulse sequence shown in Figure 6.1(b), with a 30° increment in the phase of the spin-locking pulse. The strength of the spin-locking field was 83.3 kHz.

$NaNO_3$ (Figures 6.9 and 6.10), while coherence-counting experiments on $Al(acac)_3$ confirmed the creation of a variety of multiple quantum coherences which vary with offset (Figure 6.11).

Under MAS, a time dependence is introduced to the quadrupolar splitting parameter,

and the spin-locking behaviour under a weak field limit ($\omega_1 \ll \omega_Q$) falls into different regimes according to the value of the adiabaticity parameter as defined by Vega [125]. In the adiabatic limit, the spin-locked states also acquire a time dependence. The rotor-driven interconversion of eigenstates predicted by the model calculations are reflected by the brute-force density matrix simulations in Figures 6.7 and 6.8, while Figure 6.14 shows an experimental demonstration of the variation of the spin-locked eigenstates of $Al(acac)_3$ under MAS conditions.

In the sudden limit, the spin-locked states under MAS are expected to be similar to those found in static solids. This was found in Figures 6.12(b) and 6.13(b), where experiments on $NaNO_2$ show little variation in the spin-locked single- or triple-quantum central transition amplitudes with MAS.

Chapter 7

Conclusions

This study has focused on two areas:

1. Composite pulse spin-echo methods for spin $I = 1/2$ nuclei. New pulse sequences have been presented which can be used in both solution- and solid-state NMR

2. NMR spin-locking of half-integer quadrupolar nuclei in the solid state, in the case where the transmitter frequency is far off-resonance

We will summarise our key findings for each of these topics in turn.

7.1 Spin $I = 1/2$ composite pulse spin echoes

The Hahn spin-echo sequence, $90^\circ_{0^\circ} - \tau - 180^\circ_{0^\circ} - \tau$, is one of the most well-known experiments in NMR and an integral feature of many other more complex experiments. Many spectra suffer from the effects of pulse imperfections inherent in NMR experiments, such as the inhomogeneity of the B_1 field, which reduces the effective flip angle of spins in the sample, or an offset of the transmitter from the resonance frequency. The 180° refocusing pulse in the spin-echo experiment is particularly sensitive to these errors. The consequences of such errors include reduced signal and phase distortions in the resulting spectra. With appropriate selection of the echo coherence pathway, phase errors can be removed. However, as we have seen using a product operator analysis,

a strong dependence of the signal amplitude on the flip angle and offset remains. It is therefore tempting to replace the simple refocusing pulse in the spin-echo experiment with a composite pulse to try to improve the signal amplitude. Importantly, the composite pulse must have an *antisymmetric* phase scheme, otherwise phase errors will be reintroduced into the signal despite the coherence selection with phase cycling (Exorcycle) or pulsed field gradients.

In Chapter 3 we investigated the use of composite pulses in the Depth method for ^{1}H background suppression in MAS NMR. The Depth method, consisting of a 90° pulse followed by N 180° pulses, achieves suppression of the signal originating from background ^{1}H spins by spatial localisation, and with the common implementation with two refocusing pulses ($N = 2$), signal is only acquired from the centre of the rotor. However, owing to the inhomogeneity of the B_1 field, signal from the ends of the rotor is also eliminated. Using novel passband composite pulses in an $N = 1$ Depth sequence to compensate for the B_1 inhomogeneity in the region of the rf coil, we found it was possible to excite more signal from within the rotor as well as achieving a degree of suppression equal to or better than that achieved by the simple $N = 2$ Depth sequence. With each of the APB$_n$ passband pulses in an $N = 1$ Depth experiment, we found a signal-to-noise ratio was approximately doubled compared to the simple $N = 2$ Depth sequence.

Using a two-dimensional nutation experiment, it was possible to gain further insight into the origin of the background signal as well as allowing further analysis of the Depth sequences. This experiment can be performed on any MAS probe. In the particular probe used in our experiments, the background signal was found to originate approximately 60 mm below the centre of the sample, which is well below the coil, rotor and stator block. Another interesting finding of the nutation experiment was that the nutation rate of the packed sample at each end of the rotor in fact overlapped with the range of nutation rates of the background signal. Thus, although we observed an improvement in the signal amplitude from the sample using the APB$_n$ pulses in the Depth sequence, it is evident that it is not possible to retain the full signal intensity from the sample using any background suppression method which exploits the B_1 distribution of signals.

Stimulated by our recognition of the importance of using antisymmetric refocusing sequences, novel families of broadband composite 180° pulses were introduced in Chapter 4. All pulses in the ASBO families, consisting of either 9 or 11 consecutive 180° rotations, are dual-compensated to simultaneously correct for both B_1 inhomogeneity and resonance offset. Unlike most existing dual-compensated composite pulses found in the literature, the ASBO pulses are antisymmetic and thus well suited to forming spin echoes without phase distortion. The pulses were designed using a graphical interpretation of average Hamiltonian theory and experimentally verified using solid-state static ^{31}P spin-echoes and, under MAS, refocused INADEQUATE experiments. It is expected that these pulses will also prove useful in solution-state NMR experiments.

In Chapter 5, we examined the effects of MAS on composite pulse performance. Sample rotation introduces a time dependence to the internal spin interactions such as the chemical shift anisotropy, dipolar couplings and for spin $I > 1/2$, quadrupolar interaction. The resonance offset of each crystallite in a powder will therefore vary over the course of a rotor period. We explored the problem with density matrix calculations and ^{31}P spin-echo experiments using two different schemes of rotor synchronisation and found that as the total duration of a composite refocusing pulse becomes comparable to the length of a rotor period, undesirable effects can result. With centred rotor synchronisation, the ability of the composite pulse to form a spin echo of full intensity deteriorated with increasing MAS speed, and unusual inversion of spinning sidebands was observed experimentally. The ability of the composite pulses to compensate for B_1 inhomogeneity and misset flip angles is also much more complicated than the simpler behaviour in an analogous solution-state spin-echo experiment would be. Using shifted rotor synchronisation, the outcome of the experiment showed less dependency on the MAS rate, and no problems were encountered in the phasing of spinning sidebands. It is clear that MAS introduces a complexity into the experiment, and it is difficult to predict how successful a composite refocusing pulse will be under such conditions. Whichever rotor synchronisation method is chosen, the outcome of the composite pulse spin-echo experiment depends not only on the bandwidth of the pulse, but on the pulse length, MAS rate and the magnitude of the anisotropic interactions present in the sample.

7.2 Far off-resonance spin-locking of half-integer quadrupolar nuclei

In NMR, spin-locking involves the application of a radiofrequency pulse with a long duration along the bulk magnetisation vector. In spin $I = 1/2$, this has the effect of locking the magnetisation vector in place for up to several seconds. The spin-locking pulse is a vital component of many experiments in NMR, including the famous cross-polarisation experiment. However, this vector model picture is not valid for quadrupolar nuclei, where the magnitude of the quadrupolar interaction may be much greater than the radiofrequency field strength. In order to help understand spin-locking of half-integer quadrupolar nuclei, Ashbrook and Wimperis developed a simple theoretical model of spin locking. After transforming the initial density operator into the eigenbasis of the spin-locking Hamiltonian, only elements which commute with the spin-locking Hamiltonian will be spin-locked – in this frame, these correspond to population states. When transformed back into the normal rotating frame, these elements correspond to population states and coherences. This model has been used to investigate the far off-resonance case of spin-locking, where the effective rf field has a significant z component and can be used on the equilibrium state I_z.

Calculations incorporating the theoretical model predicted the creation of a range of different populations and coherences depending on the radiofrequency field strength and resonance offset. These agreed well with single- and multiple-quantum ^{23}Na ($I = 3/2$) and ^{27}Al ($I = 5/2$) spin-locking experiments carried out, both under static conditions and showing the time-dependence of the spin-locked states under MAS. In addition, a comparison with an exact density matrix calculation proved the robustness of the simple model in predicting the off-resonance spin-locking behaviour of half-integer quadrupolar nuclei.

Appendix A

Matrix representations of spin angular momentum operators

A.1 $I = 1/2$

$$I_x = \frac{1}{2}\begin{pmatrix} 0 & 1 \\ 1 & 0 \end{pmatrix} \qquad I_y = \frac{i}{2}\begin{pmatrix} 0 & -1 \\ 1 & 0 \end{pmatrix} \qquad I_z = \frac{1}{2}\begin{pmatrix} 1 & 0 \\ 0 & -1 \end{pmatrix}$$

A.2 $I = 3/2$

$$I_x = \frac{1}{2}\begin{pmatrix} 0 & \sqrt{3} & 0 & 0 \\ \sqrt{3} & 0 & 2 & 0 \\ 0 & 2 & 0 & \sqrt{3} \\ 0 & 0 & \sqrt{3} & 0 \end{pmatrix} \qquad I_y = \frac{i}{2}\begin{pmatrix} 0 & -\sqrt{3} & 0 & 0 \\ \sqrt{3} & 0 & -2 & 0 \\ 0 & 2 & 0 & -\sqrt{3} \\ 0 & 0 & \sqrt{3} & 0 \end{pmatrix}$$

$$I_z = \frac{1}{2}\begin{pmatrix} 3 & 0 & 0 & 0 \\ 0 & 1 & 0 & 0 \\ 0 & 0 & -1 & 0 \\ 0 & 0 & 0 & -3 \end{pmatrix}$$

A.3 $I = 5/2$

$$I_x = \frac{1}{2}\begin{pmatrix} 0 & \sqrt{5} & 0 & 0 & 0 & 0 \\ \sqrt{5} & 0 & \sqrt{8} & 0 & 0 & 0 \\ 0 & \sqrt{8} & 0 & 3 & 0 & 0 \\ 0 & 0 & 3 & 0 & \sqrt{8} & 0 \\ 0 & 0 & 0 & \sqrt{8} & 0 & \sqrt{5} \\ 0 & 0 & 0 & 0 & \sqrt{5} & 0 \end{pmatrix}$$

$$I_y = \frac{i}{2}\begin{pmatrix} 0 & -\sqrt{5} & 0 & 0 & 0 & 0 \\ \sqrt{5} & 0 & -\sqrt{8} & 0 & 0 & 0 \\ 0 & \sqrt{8} & 0 & -3 & 0 & 0 \\ 0 & 0 & 3 & 0 & -\sqrt{8} & 0 \\ 0 & 0 & 0 & \sqrt{8} & 0 & -\sqrt{5} \\ 0 & 0 & 0 & 0 & \sqrt{5} & 0 \end{pmatrix}$$

$$I_z = \frac{1}{2}\begin{pmatrix} 5 & 0 & 0 & 0 & 0 & 0 \\ 0 & 3 & 0 & 0 & 0 & 0 \\ 0 & 0 & 1 & 0 & 0 & 0 \\ 0 & 0 & 0 & -1 & 0 & 0 \\ 0 & 0 & 0 & 0 & -3 & 0 \\ 0 & 0 & 0 & 0 & 0 & -5 \end{pmatrix}$$

Appendix B

Matrix representations of irreducible spherical tensor operators

B.1 $I = 3/2$

	$l = 0$	$l = 1$	$l = 2$	$l = 3$
$p = +3$				$\begin{pmatrix} 0 & 0 & 0 & -1 \\ 0 & 0 & 0 & 0 \\ 0 & 0 & 0 & 0 \\ 0 & 0 & 0 & 0 \end{pmatrix}$
$p = +2$			$\frac{1}{\sqrt{2}} \begin{pmatrix} 0 & 0 & 1 & 0 \\ 0 & 0 & 0 & 1 \\ 0 & 0 & 0 & 0 \\ 0 & 0 & 0 & 0 \end{pmatrix}$	$\frac{1}{\sqrt{2}} \begin{pmatrix} 0 & 0 & 1 & 0 \\ 0 & 0 & 0 & -1 \\ 0 & 0 & 0 & 0 \\ 0 & 0 & 0 & 0 \end{pmatrix}$
$p = +1$		$\frac{1}{\sqrt{10}} \begin{pmatrix} 0 & -\sqrt{3} & 0 & 0 \\ 0 & 0 & -2 & 0 \\ 0 & 0 & 0 & -\sqrt{3} \\ 0 & 0 & 0 & 0 \end{pmatrix}$	$\frac{1}{\sqrt{2}} \begin{pmatrix} 0 & -1 & 0 & 0 \\ 0 & 0 & 0 & 0 \\ 0 & 0 & 0 & 1 \\ 0 & 0 & 0 & 0 \end{pmatrix}$	$\frac{1}{\sqrt{5}} \begin{pmatrix} 0 & -1 & 0 & 0 \\ 0 & 0 & \sqrt{3} & 0 \\ 0 & 0 & 0 & -1 \\ 0 & 0 & 0 & 0 \end{pmatrix}$
$p = 0$	$\frac{1}{2} \begin{pmatrix} 1 & 0 & 0 & 0 \\ 0 & 1 & 0 & 0 \\ 0 & 0 & 1 & 0 \\ 0 & 0 & 0 & 1 \end{pmatrix}$	$\frac{1}{\sqrt{20}} \begin{pmatrix} 3 & 0 & 0 & 0 \\ 0 & 1 & 0 & 0 \\ 0 & 0 & -1 & 0 \\ 0 & 0 & 0 & -3 \end{pmatrix}$	$\frac{1}{2} \begin{pmatrix} 1 & 0 & 0 & 0 \\ 0 & -1 & 0 & 0 \\ 0 & 0 & -1 & 0 \\ 0 & 0 & 0 & 1 \end{pmatrix}$	$\frac{1}{\sqrt{20}} \begin{pmatrix} 1 & 0 & 0 & 0 \\ 0 & -3 & 0 & 0 \\ 0 & 0 & 3 & 0 \\ 0 & 0 & 0 & -1 \end{pmatrix}$
$p = -1$		$\frac{1}{\sqrt{10}} \begin{pmatrix} 0 & 0 & 0 & 0 \\ \sqrt{3} & 0 & 0 & 0 \\ 0 & 2 & 0 & 0 \\ 0 & 0 & \sqrt{3} & 0 \end{pmatrix}$	$\frac{1}{\sqrt{2}} \begin{pmatrix} 0 & 0 & 0 & 0 \\ 1 & 0 & 0 & 0 \\ 0 & 0 & 0 & 0 \\ 0 & 0 & -1 & 0 \end{pmatrix}$	$\frac{1}{\sqrt{5}} \begin{pmatrix} 0 & 0 & 0 & 0 \\ 1 & 0 & 0 & 0 \\ 0 & -\sqrt{3} & 0 & 0 \\ 0 & 0 & 1 & 0 \end{pmatrix}$
$p = -2$			$\frac{1}{\sqrt{2}} \begin{pmatrix} 0 & 0 & 1 & 0 \\ 0 & 0 & 0 & 1 \\ 0 & 0 & 0 & 0 \\ 0 & 0 & 0 & 0 \end{pmatrix}$	$\frac{1}{\sqrt{2}} \begin{pmatrix} 0 & 0 & 0 & 0 \\ 0 & 0 & 0 & 0 \\ 1 & 0 & 0 & 0 \\ 0 & -1 & 0 & 0 \end{pmatrix}$
$p = -3$				$\begin{pmatrix} 0 & 0 & 0 & 0 \\ 0 & 0 & 0 & 0 \\ 0 & 0 & 0 & 0 \\ 1 & 0 & 0 & 0 \end{pmatrix}$

B.2 $I = 5/2$

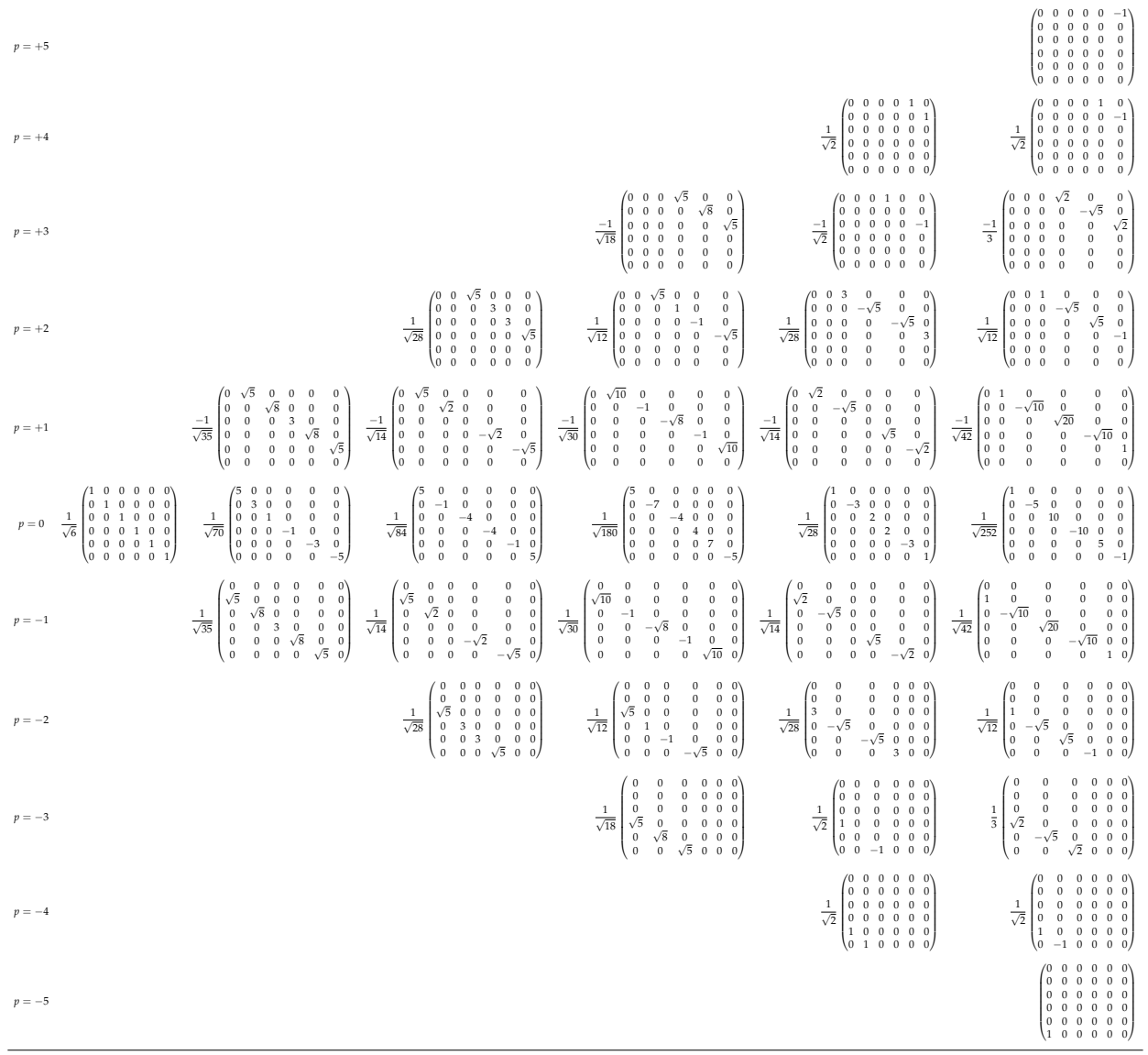

Appendix C

Quaternions

C.1 Quaternions as a tool for analysing composite pulses

If the effects of relaxation and spin-spin interactions may be neglected over the course of an rf pulse, the evolution of the spin density operator may be described as a pure rotation in three-dimensional space. A composite pulse, which is a sequence of rf pulses of varying flip and phase, may be analysed by determining its overall flip angle and rotation axes. The mathematical solution to determining the overall rotation of a sequence of rotations was first described by Hamilton in 1843 using the quaternion formalism [140]. Blümich and Speiss were the first to apply the theory to composite pulses in NMR [141], and soon after Counsell et al. introduced the following formalism which avoids the use of matrix multiplication [70].

If a rotation about the axis $\mathbf{n_1}$ through an angle β_1 is followed by a second rotation about an axis $\mathbf{n_2}$ through an angle β_2 , then the overall rotation axis is through an angle β_{12} about an axis $\mathbf{n_{12}}$ given by the equations

$$c_{12} = c_1 c_2 - s_1 s_2 \mathbf{n_1} \cdot \mathbf{n_2} \tag{C.1}$$

$$s_{12}\mathbf{n_{12}} = s_1 c_2 \mathbf{n_1} + c_1 s_2 \mathbf{n_2} - s_1 s_2 \mathbf{n_1} \times \mathbf{n_2} \tag{C.2}$$

where

$$c_i = \cos(\beta_i/2) \tag{C.3}$$

$$s_i = \sin(\beta_i/2) \tag{C.4}$$

$$c_{12} = \cos(\beta_{12}/2) \tag{C.5}$$

$$s_{12} = \sin(\beta_{12}/2) \tag{C.6}$$

These equations may be extended to three or more non-commuting rotations.

Appendix D

Source code

Example Fortran program code for simulations presented in this thesis.

D.1 Composite pulse B_1 bandwidths

```
      PROGRAM COMPPLOT5c
C
C     CALCULATES X, Y, Z, XY
    MAGNETISATION CREATED BY COMPOSITE
C     PULSE AS A FUNCTION OF B1/B1NOM
C     WITH PHASECYCLE
C
      IMPLICIT DOUBLE PRECISION (A-H,O-Z
    )
      DOUBLE PRECISION Z(501,64),X
    (501,64),Y(501,64)
      DOUBLE PRECISION U(501,64),V
    (501,64),W(501,64)
      REAL*16 XAXIS(501),TEMPRY(501,64),
    TEMPRX(501,64)
      REAL*16 RX(501),RY(501),RZ(501),
    RXY(501)
      CHARACTER*12 TITLEX,TITLEY,TITLEZ,
    TITLEXY
      PI=4.0*DATAN(1.0D0)
 70   DO 50 I=1,501
      RZ(I)=0.0
      RX(I)=0.0
      RY(I)=0.0
      DO 50 J=1,64
      Z(I,J)=0.0
      X(I,J)=0.0
 50   Y(I,J)=0.0
      WRITE(*,100)
 100  FORMAT(1H ,'INIT. MAGN. IS Z(
    ANSWER 0), X(1), Y(2) OR -Y(3)?')
      READ *,INIT
      IF (INIT.EQ.0) THEN
       DO 51 J=1,501
       DO 51 K=1,64
 51    Z(J,K)=1.0
      ELSE IF (INIT.EQ.1) THEN
       DO 52 J=1,501
       DO 52 K=1,64
 52    X(J,K)=1.0
      ELSE IF (INIT.EQ.2) THEN
       DO 53 J=1,501
       DO 53 K=1,64
 53    Y(J,K)=1.0
      ELSE
       DO 54 J=1,501
       DO 54 K=1,64
 54    Y(J,K)=-1.0
      ENDIF
      PRINT *,'NUMBER OF PULSES?'
      READ *,N
      PRINT *,'MAXIMUM NORMALISED FIELD
    STRENGTH?'
      READ *,STRENMAX
      PRINT *,'STEPS IN PHASE CYCLE'
      READ *,IPCS
      DO 20 I=1,N
      WRITE(6,*) '**** FLIP ANGLE FOR
    PULSE',I,' ****'
      READ *,F
      DO 10 K=1,IPCS
      WRITE(6,*) 'RF PHASE FOR PULSE',I
    ,'AND STEP',K
      READ *,P
      D=(F*PI)/180.0
      B=(P*PI)/180.0
      G=0.002*D*STRENMAX
      A=-G
      DO 10 J=1,501
```

```
      A=A+G
      CA=DCOS(A)
      SA=DSIN(A)
      CB=DCOS(B)
      SB=DSIN(B)
      S2B=DSIN(2.0*B)
      SA2=DSIN(0.5*A)
      U(J,K)=Z(J,K)*CA-X(J,K)*SA*SB+Y(J
   ,K)*SA*CB
      V(J,K)=Z(J,K)*SA*SB+X(J,K)*(CA*SB
   *SB+CB*CB)+Y(J,K)*SA2*SA2*S2B
      W(J,K)=-Z(J,K)*SA*CB+X(J,K)*SA2*
   SA2*S2B+Y(J,K)*(CA*CB*CB+SB*SB)
      Z(J,K)=U(J,K)
      X(J,K)=V(J,K)
      Y(J,K)=W(J,K)
 10   CONTINUE
 20   CONTINUE
      DO 66 K=1,IPCS
      WRITE(6,*) 'RECEIVER PHASE FOR
   STEP',K,'?'
      READ *,RPD
      RP=(RPD*PI)/180.0
      DO 66 J=1,501
      TEMPRX(J,K)=X(J,K)*DCOS(RP)+Y(J,K)
   *DSIN(RP)
      TEMPRY(J,K)=Y(J,K)*DCOS(RP)-X(J,K)
   *DSIN(RP)
      RZ(J)=RZ(J)+Z(J,K)
      RX(J)=RX(J)+TEMPRX(J,K)
      RY(J)=RY(J)+TEMPRY(J,K)
 66   XAXIS(J)=0.004*(J-1)
       DO 390 I=1,501
 390   RXY(I)=SQRT((RX(I)**2.0)+(RY(I)
   **2.0))
C
C     OUTPUT RESULTS
C
       TITLEX='X'
       OPEN(1,FILE=TITLEX,STATUS='
   UNKNOWN')
       DO 300 I=1,501
          WRITE(1,635) XAXIS(I),RX(I)
 300   CONTINUE
       CLOSE(1)
       TITLEY='Y'
       OPEN(2,FILE=TITLEY,STATUS='
   UNKNOWN')
       DO 301 I=1,501
          WRITE(2,635) XAXIS(I),RY(I)
 301   CONTINUE
       CLOSE(2)
       TITLEZ='Z'
       OPEN(3,FILE=TITLEZ,STATUS='
   UNKNOWN')
       DO 302 I=1,501
          WRITE(3,635) XAXIS(I),RZ(I)
 302   CONTINUE
       CLOSE(3)
       TITLEXY='XY'
       OPEN(4,FILE=TITLEXY,STATUS='
   UNKNOWN')
       DO 303 I=1,501
          WRITE(4,635) XAXIS(I),RXY(I)
 303   CONTINUE
       CLOSE(4)
 635  FORMAT (F28.18,5X,F30.20)
      PRINT *,'NEW SEQUENCE (1), OR QUIT
   (2)?'
      READ *,NOPT
      IF (NOPT.EQ.1) THEN
       GOTO 70
      ELSE
       STOP
      ENDIF
      END
```

D.2 Overall flip angles and rotation axes of composite pulses

```
      PROGRAM QUATCOMPROFF1
C
C     CALCULATES BETA (OVERALL ROTATION
     ANGLE), PHI (PHASE) AND THETA
C     (TILT FROM Z AXIS) OF A COMPOSITE
     PULSE USING QUATERNIONS
C     AS FUNCTION OF RESONANCE OFFSET (
     ROFF PARAMETER = -1 -> 1)
C
      IMPLICIT REAL*8 (A-H,O-Z)
C
C     SET UP ARRAYS
C
      REAL*8 A(25),B(25),S1N1(3),S2N2(3)
     ,CF(501),BETA(501)
      REAL*8 ROFF(501),S1N1NEW(3),THETA
     (501),FL(11)
      REAL*8 PHII(11),PHI(501),SFNF
     (501,3),X(50)
      REAL*4 XRES(501),YRES(501)
      CHARACTER*12 TITLEX,TITLEY,TITLEB,
     TITLEP,TITLET
C
C     INPUT VARIABLES
C
      PI=3.1415926536
 70   PRINT *,'NUMBER OF PULSES?'
      READ *,NPULSE

      DO 60 I=1,NPULSE
      PRINT *,'FLIP ANGLE FOR PULSE',I
      READ *,F
      FL(I)=(F*PI)/180.0
      PRINT *,'RF PHASE FOR PULSE',I
      READ *,PHII(I)
      PHII(I)=PHII(I)*PI/180.0
 60   CONTINUE
C
C     CALCULATE OVERALL FLIP ANGLE AND
     ROTATION AXIS
C
      DO 80 I=1,501
      ROFF(I)=-1.0+0.004*(I-1)
      THETAONE=ATAN(ROFF(I))
      BETAONE=(FL(1)/COS(THETAONE))
      COSONE=COS(0.5*BETAONE)
      SINONE=SIN(0.5*BETAONE)
      S1N1(1)=SINONE*COS(THETAONE)*COS(
     PHII(1))
      S1N1(2)=SINONE*COS(THETAONE)*SIN(
     PHII(1))
      S1N1(3)=SINONE*SIN(THETAONE)
      DO 90 J=2,NPULSE
      THETATWO=ATAN(ROFF(I))
      BETATWO=(FL(J)/COS(THETAONE))
      COSTWO=COS(0.5*BETATWO)
      SINTWO=SIN(0.5*BETATWO)
      S2N2(1)=SINTWO*COS(THETATWO)*COS(
     PHII(J))
      S2N2(2)=SINTWO*COS(THETATWO)*SIN(
     PHII(J))
      S2N2(3)=SINTWO*SIN(THETATWO)
      COSNEW=COSONE*COSTWO-S1N1(1)*S2N2
     (1)-S1N1(2)*S2N2(2)
       +      -S1N1(3)*S2N2(3)
      S1N1NEW(1)=COSTWO*S1N1(1)+COSONE*
     S2N2(1)
       +          -S1N1(2)*S2N2(3)+S1N1(3)
     *S2N2(2)
      S1N1NEW(2)=COSTWO*S1N1(2)+COSONE*
     S2N2(2)
       +          +S1N1(1)*S2N2(3)-S1N1(3)
     *S2N2(1)
      S1N1NEW(3)=COSTWO*S1N1(3)+COSONE*
     S2N2(3)
       +          -S1N1(1)*S2N2(2)+S1N1(2)
     *S2N2(1)
      DO 100 K=1,3
 100  S1N1(K)=S1N1NEW(K)
 90   COSONE=COSNEW
      DO 110 K=1,3
 110  SFNF(I,K)=S1N1(K)
 80   CF(I)=COSONE
C
C     CONVERT TO NORMAL COORDINATES
C
      DO 120 I=1,501
      BETA(I)=2.0*ACOS(CF(I))
      PHI(I)=ATAN(SFNF(I,2)/SFNF(I,1))
      IF (SFNF(I,1).LT.0) PHI(I)=PHI(I)+
     PI
      RNORM=SQRT(SFNF(I,1)**2+SFNF(I,2)
     **2+SFNF(I,3)**2)
 120  THETA(I)=ACOS(SFNF(I,3)/RNORM)
C
C     CALCULATE EXCITATION PROFILES
C
      DO 130 I=1,501
      SA=SIN(BETA(I))
      CB=COS(PHI(I))
      SB=SIN(PHI(I))
      SC=SIN(THETA(I))
      SA2=SIN(0.5*BETA(I))
      S2C=SIN(2.0*THETA(I))
      XRES(I)= SA*SB*SC+SA2*SA2*CB*S2C
 130  YRES(I)=-SA*CB*SC+SA2*SA2*SB*S2C

      DO 140 I=1,501
      BETA(I)=BETA(I)*180.0/PI
      PHI(I)=PHI(I)*180.0/PI
 140  THETA(I)=THETA(I)*180.0/PI
C
C     OUTPUT RESULTS
C
       TITLEX='X'
       OPEN(1,FILE=TITLEX,STATUS='
     UNKNOWN')
       DO 300 I=1,501
          WRITE(1,635) ROFF(I),XRES(I)
 300   CONTINUE
       CLOSE(1)

       TITLEY='Y'
       OPEN(2,FILE=TITLEY,STATUS='
     UNKNOWN')
       DO 301 I=1,501
          WRITE(2,635) ROFF(I),YRES(I)
 301   CONTINUE
       CLOSE(2)

       TITLEB='BETA'
```

```
      OPEN(3,FILE=TITLEB,STATUS='
   UNKNOWN')
      DO 302 I=1,501
         WRITE(3,635) ROFF(I),BETA(I)
302   CONTINUE
      CLOSE(3)

      TITLEP='PHI'
      OPEN(4,FILE=TITLEP,STATUS='
   UNKNOWN')
      DO 303 I=1,501
         WRITE(4,635) ROFF(I),PHI(I)
303   CONTINUE
      CLOSE(4)

      TITLET='THETA'
      OPEN(4,FILE=TITLET,STATUS='
   UNKNOWN')
      DO 304 I=1,501
         WRITE(4,635) ROFF(I),THETA(I)
304   CONTINUE
      CLOSE(4)

635  FORMAT (F10.6,5X,F10.6)
     PRINT *,'NEW SEQUENCE (1), OR QUIT
   (2)?'
     READ *,NOPT
     IF (NOPT.EQ.1) THEN
      GOTO 70
     ELSE
      STOP
     ENDIF
     END
```

D.3 Passband composite pulse design

```
C
C       GRIDSEARCH2
C
C       GRIDSEARCH ATTEMPTS TO MINIMISE
    AN EQUATION BY A
C       BRUTE-FORCE GRID SEARCH
C      FOR ANTISYMMETRIC SEQUENCE OF
    SEVEN 180 DEGREE
C         PULSES TO FIND A PASSBAND
    COMPOSITE PULSE
C
C       INITIALIZE ARRAYS AND THE LIKE
C
        IMPLICIT REAL*8 (A-H,O-Z)
        REAL*8 Z(13),X(13),Y(13),U(13),V
    (13),W(13)
        REAL*8 P(9)
        PI=4.0*DATAN(1.0D0)
C
C       CALCULATION
C
        RMIN=10000.0
        DO 10 I=0,360,6
        DO 10 J=0,360,6
        DO 10 K=0,360,6
        E=REAL(I)
        F=REAL(J)
        G=REAL(K)
        P(1)=E*0.0174532925D0
        P(2)=F*0.0174532925D0
        P(3)=G*0.0174532925D0
        P(4)=0.0
        P(5)=-P(3)
        P(6)=-P(2)
        P(7)=-P(1)
C
        DO 50 II=1,13
        Z(II)=1.0
        X(II)=0.0
 50     Y(II)=0.0
        DO 20 II=1,7
        G=0.1*PI
        A=-G
        DO 30 JJ=1,13
        A=A+G
        CA=DCOS(A)
        SA=DSIN(A)
        CB=DCOS(P(II))
        SB=DSIN(P(II))
        S2B=DSIN(2.0*P(II))
        SA2=DSIN(0.5*A)
        U(JJ)=Z(JJ)*CA-X(JJ)*SA*SB+Y(JJ)
    *SA*CB
        V(JJ)=Z(JJ)*SA*SB+X(JJ)*(CA*SB*
    SB+CB*CB)+Y(JJ)*SA2*SA2*S2B
        W(JJ)=-Z(JJ)*SA*CB+X(JJ)*SA2*SA2
    *S2B+Y(JJ)*(CA*CB*CB+SB*SB)
        Z(JJ)=U(JJ)
        X(JJ)=V(JJ)
        Y(JJ)=W(JJ)
 30     CONTINUE
 20     CONTINUE
C
C
        CURRENT=(4.0-Z(1)-Z(2)-Z(3)-Z(4)
    )-(-8.0-Z(6)-Z(7)-Z(8)-Z(9)
     C  -Z(10)-Z(11)-Z(12)-Z(13))
        IF (CURRENT.LE.RMIN) THEN
         RMIN=CURRENT
         AA=P(1)/0.0174532925D0
         BB=P(2)/0.0174532925D0
         CC=P(3)/0.0174532925D0
         DD=P(4)/0.0174532925D0
         WRITE (6,*) RMIN
         WRITE (6,*) AA
         WRITE (6,*) BB
         WRITE (6,*) CC
         WRITE (6,*) DD
         WRITE (6,*)
        ELSE
         GOTO 10
        ENDIF
 10     CONTINUE
        STOP
        END
```

D.4 Spin $I = 1/2$ spin echo under MAS

```
C
C     PROGRAM SPINV10
C
C     CALCULATES Iy CREATED BY (INIT=-Iy
     )-T-180-T AS A
C     FUNCTION OF TIME THROUGH SEQUENCE
     (2 ROTOR PERIODS)
C     FOR A I = 1/2 SINGLE CRYSTALLITE
C
C     INITIALIZE ARRAYS AND OTHER SUCH
     THINGS
C
      IMPLICIT REAL*8 (A-H,O-Z)
      REAL*8 EIGVEC(2,2),RESULT(2001),
     RES(2001),SPINRATE,TIME(2001)
      REAL*8 PULHAM(2,2),DELHAM(2,2),
     RESULTX(2001),RESULTZ(2001)
      COMPLEX*16 EXOPER(2,2),DENMAT(2,2)
     ,RMZ(2,2),RMX(2,2),RMY(2,2)
      COMPLEX*16 WORKZERO(2,2),WORKONE
     (2,2),WORKTWO(2,2),PROPAG(2,2)
      REAL*8 DIAG(2,2),DIAGT(2,2),CSA
     (2001)
      COMPLEX*16 PHSHOP(2,2)
      INTEGER NBETA,NPHI,NPOINTS,IS,
     PSTART,PEND,RP
      CHARACTER TITLEY,TITLEX,TITLEZ,
     TITLEC
      PI=4.0*DATAN(1.0D0)
C
C     ANGLES AND NUMBER OF TO POINTS TO
     CALCULATE
C
      PHI=0.0
      PHI=PHI*PI/180.0
      THETA=0.955316
C
C     READ IN DATA
C
 4    PRINT *,'90 DEGREE PULSE LENGTH IN
      MICROSECONDS'
      READ *,PLENGTH
      OMEGA=1570796.3267/PLENGTH
      WRITE(*,6) OMEGA/(6.28318531*1000)
 6    FORMAT(1H ,'B1 FIELD STRENGTH (IN
     KHZ) IS ',F15.3)
      PLENGTH=PLENGTH/1000000.0
      PRINT *,'BETA?'
      READ *,BETA
      BETA=BETA*(2.0*PI/360.0)
      PRINT *,'MAX. CSA IN KHZ'
      READ *,CSAMAX
      CSAMAX=2.0*PI*CSAMAX*1000.0
      PRINT *,'SPINNING SPEED IN KHZ'
      READ *,SPINRATE
      SPINRATE=SPINRATE*1000.0
      ROTINC=1.0/(SPINRATE*1000)
      RP=NINT(PLENGTH/ROTINC)
      PSTART=1001-RP
      PEND=1000+RP
      WRITE(*,9) PLENGTH,ROTINC
 9    FORMAT(F15.8)
      WRITE(*,8) RP,PSTART,PEND
 8    FORMAT(I5)
      SPINRATE=SPINRATE*2.0*PI
C
C     PRE-CALCULATE OBSERVABLES
C
      DO 540 J=1,2
      DO 540 K=1,2
      RMX(J,K)=CMPLX(0.0,0.0)
      RMZ(J,K)=CMPLX(0.0,0.0)
 540  RMY(J,K)=CMPLX(0.0,0.0)
      RMX(1,2)=CMPLX(0.5,0.0)
      RMX(2,1)=CMPLX(0.5,0.0)
      RMY(1,2)=CMPLX(0.0,-0.5)
      RMY(2,1)=CMPLX(0.0,0.5)
      RMZ(1,1)=CMPLX(0.5,0.0)
      RMZ(2,2)=CMPLX(-0.5,0.0)
C
C     THE LOOP (PHI)
C
C      DO 28 III=1,NPHI
C      PHI=(III-1)*2.0*PI/NPHI
C
C     CONSTRUCT EQUILIBRIUM DENSITY
     MATRIX -Iy
C
      DO 5 J=1,2
      DO 5 K=1,2
 5    DENMAT(J,K)=CMPLX(0.0,0.0)
      DENMAT(1,2)=CMPLX(0.0,0.5)
      DENMAT(2,1)=CMPLX(0.0,-0.5)
C
C     THE LOOP (ROTOR INCREMENTS)
C
      DO 25 I=1,2001
      TIME(I)=(I-1)*ROTINC

      CSA(I)=CSAMAX*(0.5*(3.0*(COS(THETA
     )**2.0)-1.0)
     +                          *(3.0*(
     COS(BETA)**2.0)-1.0)
     +    -1.5*SIN(2.0*THETA)*SIN(2.0*
     BETA)
     +                 *COS(SPINRATE*
     TIME(I)+PHI)
     +    +1.5*(SIN(THETA)**2.0)*(SIN(
     BETA)**2.0)
     +                 *COS(2.0*(
     SPINRATE*TIME(I)+PHI)))
      NOPT=2
      IF (I.GE.PSTART) THEN
      IF (I.LE.PEND) THEN
      NOPT=1
      ELSE
      ENDIF
      ELSE
      ENDIF
C
      IF (NOPT.EQ.1) THEN
C
C      THE PULSE OPTION
C      180   PULSE
C
C     ASSEMBLE THE PULSE HAMILTONIAN
C
      PULHAM(1,1)=0.5*CSA(I)
      PULHAM(1,2)=0.5*OMEGA
      PULHAM(2,1)=0.5*OMEGA
      PULHAM(2,2)=-0.5*CSA(I)
```

```
C
C     DIAGONALIZE THE PULSE HAMILTONIAN
C
      ALPH=0.5*ATAN(2*PULHAM(1,2)/(
     PULHAM(1,1)-PULHAM(2,2)))
      DIAG(1,1)=DCOS(ALPH)
      DIAG(1,2)=SIN(ALPH)
      DIAG(2,1)=-DSIN(ALPH)
      DIAG(2,2)=DCOS(ALPH)
      DIAGT(1,1)=DCOS(ALPH)
      DIAGT(1,2)=-DSIN(ALPH)
      DIAGT(2,1)=DSIN(ALPH)
      DIAGT(2,2)=DCOS(ALPH)
      DO 400 J=1,2
      DO 400 K=1,2
      WORKONE(J,K)=DIAG(J,K)
 400  WORKTWO(J,K)=PULHAM(J,K)
      CALL MATMULT(WORKONE,WORKTWO,
     WORKZERO)
      DO 402 J=1,2
      DO 402 K=1,2
 402  PULHAM(J,K)=WORKZERO(J,K)
      DO 401 J=1,2
      DO 401 K=1,2
      WORKONE(J,K)=DIAGT(J,K)
 401  WORKTWO(J,K)=PULHAM(J,K)
      CALL MATMULT(WORKTWO,WORKONE,
     WORKZERO)
      DO 403 J=1,2
      DO 403 K=1,2
 403  PULHAM(J,K)=WORKZERO(J,K)
C      CONSTRUCT THE PULSE PROPAGATOR
C
       DO 55 J=1,2
       DO 55 K=1,2
 55    EXOPER(J,K)=CMPLX(0.0,0.0)
       DO 70 J=1,2
       EXOPER(J,J)=CMPLX(0.0D0,PULHAM(J,
     J))
 70    EXOPER(J,J)=EXP(-ROTINC*EXOPER(J,
     J))
C
C      CONSTRUCT PHASE SHIFT PROPAGATOR
C
       PHASE=0.0
       PHASE=0.0174532925*PHASE
       DO 80 J=1,2
       DO 80 K=1,2
 80    PHSHOP(J,K)=CMPLX(0.0D0,0.0D0)
       PHSHOP(1,1)=CMPLX(0.0D0,0.5*PHASE
     )
       PHSHOP(2,2)=CMPLX(0.0D0,-0.5*
     PHASE)
       PHSHOP(1,1)=EXP(-PHSHOP(1,1))
       PHSHOP(2,2)=EXP(-PHSHOP(2,2))
C
C      MULTIPLY MATRICES TOGETHER
C
       DO 100 J=1,2
       DO 100 K=1,2
       WORKONE(J,K)=DIAG(J,K)
 100   WORKTWO(J,K)=PHSHOP(J,K)
       CALL MATMULT(WORKTWO,WORKONE,
     WORKZERO)
       DO 110 J=1,2
       DO 110 K=1,2
 110   PROPAG(J,K)=WORKZERO(J,K)
       DO 130 J=1,2
       DO 130 K=1,2
       WORKONE(J,K)=EXOPER(J,K)
 130   WORKTWO(J,K)=PROPAG(J,K)
       CALL MATMULT(WORKTWO,WORKONE,
     WORKZERO)
       DO 140 J=1,2
       DO 140 K=1,2
 140   PROPAG(J,K)=WORKZERO(J,K)
       DO 160 J=1,2
       DO 160 K=1,2
       WORKONE(K,J)=DIAG(J,K)
 160   WORKTWO(J,K)=PROPAG(J,K)
       CALL MATMULT(WORKTWO,WORKONE,
     WORKZERO)
       DO 170 J=1,2
       DO 170 K=1,2
 170   PROPAG(J,K)=WORKZERO(J,K)
       DO 190 J=1,2
       DO 190 K=1,2
       WORKONE(J,K)=CONJG(PHSHOP(J,K))
 190   WORKTWO(J,K)=PROPAG(J,K)
       CALL MATMULT(WORKTWO,WORKONE,
     WORKZERO)
       DO 200 J=1,2
       DO 200 K=1,2
 200   PROPAG(J,K)=WORKZERO(J,K)
       DO 220 J=1,2
       DO 220 K=1,2
       WORKONE(J,K)=DENMAT(J,K)
 220   WORKTWO(J,K)=PROPAG(J,K)
       CALL MATMULT(WORKTWO,WORKONE,
     WORKZERO)
       DO 230 J=1,2
       DO 230 K=1,2
 230   WORKONE(K,J)=CONJG(WORKTWO(J,K))
       CALL MATMULT(WORKZERO,WORKONE,
     WORKTWO)
       DO 240 J=1,2
       DO 240 K=1,2
 240   DENMAT(J,K)=WORKTWO(J,K)
C
C      DELAY OPTION
C
       ELSE IF (NOPT.EQ.2) THEN
       DELHAM(1,1)=0.5*CSA(I)
       DELHAM(1,2)=0.0
       DELHAM(2,1)=0.0
       DELHAM(2,2)=-0.5*CSA(I)
       DO 420 J=1,2
       DO 420 K=1,2
 420   EXOPER(J,K)=CMPLX(0.0,0.0)
       DO 430 J=1,2
       EXOPER(J,J)=CMPLX(0.0,DELHAM(J,J)
     )
 430   EXOPER(J,J)=EXP(-ROTINC*EXOPER(J,
     J))
       DO 450 J=1,2
       DO 450 K=1,2
       WORKONE(J,K)=DENMAT(J,K)
 450   WORKTWO(J,K)=EXOPER(J,K)
       CALL MATMULT(WORKTWO,WORKONE,
     WORKZERO)
       DO 460 J=1,2
       DO 460 K=1,2
 460   PROPAG(J,K)=WORKZERO(J,K)
       DO 480 J=1,2
       DO 480 K=1,2
       WORKONE(J,K)=CONJG(EXOPER(J,K))
 480   WORKTWO(J,K)=PROPAG(J,K)
       CALL MATMULT(WORKTWO,WORKONE,
     WORKZERO)
       DO 490 J=1,2
       DO 490 K=1,2
 490   DENMAT(J,K)=WORKZERO(J,K)
```

```
      ENDIF
C
C     TRACE CALCULATION
C
      CALL MATMULT(RMY,DENMAT,WORKONE)
      DO 626 J=1,2
 626  RESULT(I)=RESULT(I)+WORKONE(J,J)

      CALL MATMULT(RMX,DENMAT,WORKONE)
      DO 627 J=1,2
 627  RESULTX(I)=RESULTX(I)+WORKONE(J,J)

      CALL MATMULT(RMZ,DENMAT,WORKONE)
      DO 628 J=1,2
 628  RESULTZ(I)=RESULTZ(I)+WORKONE(J,J)

 25   CONTINUE

C
C     OUTPUT RESULTS
C
      DO 44 P=1,2001
      TIME(P)=TIME(P)*1000
 44   CONTINUE
      TITLEY='Y'
      OPEN(1,FILE=TITLEY)
       DO 630 I=1,2001
 630   WRITE(1,635) TIME(I),RESULT(I)
      CONTINUE
      CLOSE(1)

      TITLEX='X'
      OPEN(2,FILE=TITLEX)
       DO 631 I=1,2001
 631   WRITE(2,635) TIME(I),RESULTX(I)
      CONTINUE
      CLOSE(2)

      TITLEZ='Z'
      OPEN(3,FILE=TITLEZ)
       DO 632 I=1,2001
 632   WRITE(3,635) TIME(I),RESULTZ(I)
      CONTINUE
      CLOSE(3)

      TITLEC='CSA'
      OPEN(4,FILE=TITLEC)
       DO 633 I=1,2001
 633   WRITE(4,635) TIME(I),CSA(I)
      CONTINUE
      CLOSE(4)

 635   FORMAT(F30.10,5X,F30.10)

      STOP
      END

C
C     MATRIX MULTIPLICATION
C
      SUBROUTINE MATMULT(A,B,C)
      COMPLEX*16 A(2,2),B(2,2),C(2,2)
      DO 10 I=1,2
      DO 10 K=1,2
      C(I,K)=CMPLX(0.0,0.0)
      DO 10 J=1,2
 10   C(I,K)=C(I,K)+A(I,J)*B(J,K)
      RETURN
      END
C
```

D.5 Spin-locking model

```
      PROGRAM VSPINLOCK6

C     THIS PROGRAM CALCULATES THE
     AMOUNT OF EACH TENSOR PRESENT AFTER
C     THE SPINLOCKING OF A STATIC
     SAMPLE FOR SPIN I=3/2 AS A FUNCTION
     OF
C     SPIN-LOCKING FIELD STRENGTH
C     POWDER SAMPLE
C
C    DECLARATION OF VARIABLES

      REAL*8   RES10(201),VALZ(201),
     TRACE,TV(4,4),V(4,4)
      REAL*8   REST(201),WORKONE(4,4),
     RES31(201),TEN32(4,4)
      REAL*8   IDM(4,4),FDM(4,4),MDM
     (4,4),WORKZERO(4,4)
      REAL*8   RES20(201),RES30(201),
     RES11(201),RES21(201)
      REAL*8   RESCT(201),TEN30(4,4),
     TEN33(4,4),TEN20(4,4)
      REAL*8   RES22(201),RES32(201),
     RES33(201),TEN10(4,4)
      REAL*8   TEN11(4,4),TEN21(4,4),
     TEN31(4,4),TEN22(4,4)
      REAL*8   TENCT(4,4),THETA,
     INTHETA, ROFFH,ROFF,QUADIR,INOMEGA
      REAL*8   PULHAM(4,4),EIGTEMP
     (4,4),OMEGA,QUAD,QUADI,PI,THETAI
      INTEGER  I,J,INOP,NZ,K,QD,NTHETA
      CHARACTER*12 TITLE10, TITLE20,
     TITLE30, TITLE11, TITLE21,TITLE31
      CHARACTER*12 TITLE22, TITLE32,
     TITLE33, TITLECT, TITLET, TITLEVALZ
      PI=3.1415926536
C
C    INPUT DATA
C
      PRINT*, 'RESONANCE OFFSET (HZ)?'
      READ*,ROFFH
      PRINT*, 'QUADRUPOLAR SPLITTING,
     VQPAS (HZ)?'
      READ*,QUADI
      DO 12 I=1,4
      DO 12 J=1,4
 12   IDM(I,J)=0.0
      IDM(1,1)=3.0/SQRT(20.0)
      IDM(2,2)=1.0/SQRT(20.0)
      IDM(3,3)=-1.0/SQRT(20.0)
      IDM(4,4)=-3.0/SQRT(20.0)
      DO 13 I=1,4
      DO 13 J=1,4
      TEN10(I,J)=0.0
      TEN20(I,J)=0.0
      TEN30(I,J)=0.0
      TEN11(I,J)=0.0
      TEN21(I,J)=0.0
      TEN31(I,J)=0.0
      TEN22(I,J)=0.0
      TEN32(I,J)=0.0
      TEN33(I,J)=0.0
 13   TENCT(I,J)=0.0
      TEN10(1,1)=3/SQRT(20.0)
      TEN10(2,2)=1/SQRT(20.0)
      TEN10(3,3)=-1/SQRT(20.0)
      TEN10(4,4)=-3/SQRT(20.0)
      TEN20(1,1)=0.5
      TEN20(2,2)=-0.5
      TEN20(3,3)=-0.5
      TEN20(4,4)=0.5
      TEN30(1,1)=1/SQRT(20.0)
      TEN30(2,2)=-3/SQRT(20.0)
      TEN30(3,3)=3/SQRT(20.0)
      TEN30(4,4)=-1/SQRT(20.0)
      TEN11(1,2)=-SQRT(0.3)
      TEN11(2,3)=-SQRT(0.4)
      TEN11(3,4)=-SQRT(0.3)
      TEN21(1,2)=-SQRT(0.5)
      TEN21(3,4)=SQRT(0.5)
      TEN31(1,2)=-SQRT(0.2)
      TEN31(2,3)=SQRT(0.6)
      TEN31(3,4)=-SQRT(0.2)
      TEN22(1,3)=SQRT(0.5)
      TEN22(2,4)=SQRT(0.5)
      TEN32(1,3)=SQRT(0.5)
      TEN32(2,4)=-SQRT(0.5)
      TEN33(1,4)=-1.0
      TENCT(2,3)=1.0
C
C     CALCULATION
C
      OMEGA=0.0
      ROFF=ROFFH*2.0*PI
      INTHETA=2.0*PI/360.0
      QUADIR=QUADI*2.0*PI
      INOMEGA=5000*2.0*PI
      DO 100 NZ=1,201
      THETA=0.0
         DO 200 NTHETA=0,180
         QUAD=QUADIR*0.5*(3.0*(DCOS(
     THETA)**2.0)-1.0)
         PULHAM(1,1)=QUAD+1.5*ROFF
         PULHAM(1,2)=0.8660254035*
     OMEGA
         PULHAM(1,3)=0.0
         PULHAM(1,4)=0.0
         PULHAM(2,1)=0.8660254035*
     OMEGA
         PULHAM(2,2)=-QUAD+0.5*ROFF
         PULHAM(2,3)=OMEGA
         PULHAM(2,4)=0.0
         PULHAM(3,1)=0.0
         PULHAM(3,2)=OMEGA
         PULHAM(3,3)=-QUAD-0.5*ROFF
         PULHAM(3,4)=0.8660254035*
     OMEGA
         PULHAM(4,1)=0.0
         PULHAM(4,2)=0.0
         PULHAM(4,3)=0.8660254035*
     OMEGA
         PULHAM(4,4)=QUAD-1.5*ROFF
C
C     DIAGONALIZE THE PULSE HAMILTONIAN
C
       CALL HDIAG(PULHAM,EIGTEMP,4)
       CALL EIGSORT(PULHAM,EIGTEMP,4)
       DO 99 J=1,4
       DO 99 K=1,4
 99    V(J,K)=EIGTEMP(K,J)
       DO 11 I=1,4
```

```
        DO 11 J=1,4
 11     TV(I,J)=V(J,I)
        CALL MATMULT(V,IDM,WORKZERO)
        CALL MATMULT(WORKZERO,TV,MDM)
        MDM(1,2)=0.0
        MDM(1,3)=0.0
        MDM(1,4)=0.0
        MDM(2,1)=0.0
        MDM(2,3)=0.0
        MDM(2,4)=0.0
        MDM(3,1)=0.0
        MDM(3,2)=0.0
        MDM(3,4)=0.0
        MDM(4,1)=0.0
        MDM(4,2)=0.0
        MDM(4,3)=0.0
        CALL MATMULT(TV,MDM,WORKONE)
        CALL MATMULT(WORKONE,V,FDM)
        RES10TEMP=TRACE(FDM,TEN10)
        RES20TEMP=TRACE(FDM,TEN20)
        RES30TEMP=TRACE(FDM,TEN30)
        RES11TEMP=TRACE(FDM,TEN11)
        RES21TEMP=TRACE(FDM,TEN21)
        RES31TEMP=TRACE(FDM,TEN31)
        RES22TEMP=TRACE(FDM,TEN22)
        RES32TEMP=TRACE(FDM,TEN32)
        RES33TEMP=TRACE(FDM,TEN33)
        RESCTTEMP=TRACE(FDM,TENCT)
        RESTTEMP=RES10(NZ)**2.0+RES20(NZ
    )**2.0+RES30(NZ)**2.0
     +  +2.0*(RES11(NZ)**2.0)+2.0*(RES31
    (NZ)**2.0)+2.0*(RES21(NZ)**2.0)
     +  +2.0*(RES22(NZ)**2.0)+2.0*(RES32
    (NZ)**2.0)+2.0*(RES33(NZ)**2.0)
        RES10(NZ)=RES10(NZ)+(RES10TEMP*
    SIN(THETA))
        RES20(NZ)=RES20(NZ)+(RES20TEMP*
    SIN(THETA))
        RES30(NZ)=RES30(NZ)+(RES30TEMP*
    SIN(THETA))
        RES11(NZ)=RES11(NZ)+(RES11TEMP*
    SIN(THETA))
        RES21(NZ)=RES21(NZ)+(RES21TEMP*
    SIN(THETA))
        RES31(NZ)=RES31(NZ)+(RES31TEMP*
    SIN(THETA))
        RES22(NZ)=RES22(NZ)+(RES22TEMP*
    SIN(THETA))
        RES32(NZ)=RES32(NZ)+(RES32TEMP*
    SIN(THETA))
        RES33(NZ)=RES33(NZ)+(RES33TEMP*
    SIN(THETA))
        RESCT(NZ)=RESCT(NZ)+(RESCTTEMP*
    SIN(THETA))
        REST(NZ)=REST(NZ)+RESTTEMP
        THETA=THETA+INTHETA
 200    CONTINUE
        VALZ(NZ)=OMEGA/QUADI
        OMEGA=OMEGA+INOMEGA
 100    CONTINUE
C
C      WRITES RESULT TO A FILE
C
        TITLEVALZ="W P"
        OPEN(37,FILE=TITLEVALZ,STATUS='
    UNKNOWN')
        DO 337 I=1,201
           WRITE(37,*) VALZ(I)
  337   CONTINUE
        CLOSE(37)
        TITLE10="T10 P"
        OPEN(1,FILE=TITLE10,STATUS='
  UNKNOWN')
        DO 300 I=1,201
           WRITE(1,450) VALZ(I),RES10(I)
300     CONTINUE
        CLOSE(1)
        TITLE20="T20 P"
        OPEN(2,FILE=TITLE20,STATUS='
  UNKNOWN')
        DO 301 I=1,201
           WRITE(2,450) VALZ(I), RES20(I
  )
301     CONTINUE
        CLOSE(2)
        TITLE30="T30 P"
        OPEN(3,FILE=TITLE30,STATUS='
  UNKNOWN')
        DO 302 I=1,201
           WRITE(3,450) VALZ(I), RES30(I
  )
302     CONTINUE
        CLOSE(3)
        TITLE11="T11 P"
        OPEN(4,FILE=TITLE11,STATUS='
  UNKNOWN')
        DO 303 I=1,201
           WRITE(4,450) VALZ(I), RES11(I
  )
303     CONTINUE
        CLOSE(4)
        TITLE21="T21 P"
        OPEN(9,FILE=TITLE21,STATUS='
  UNKNOWN')
        DO 304 I=1,201
           WRITE(9,450) VALZ(I), RES21(I
  )
304     CONTINUE
        CLOSE(9)
        TITLE31="T31 P"
        OPEN(10,FILE=TITLE31,STATUS='
  UNKNOWN')
        DO 305 I=1,201
           WRITE(10,450) VALZ(I), RES31(
  I)
305     CONTINUE
        CLOSE(10)
        TITLE22="T22 P"
        OPEN(11,FILE=TITLE22,STATUS='
  UNKNOWN')
        DO 306 I=1,201
           WRITE(11,450) VALZ(I),RES22(I
  )
306     CONTINUE
        CLOSE(11)
        TITLE32="T32 P"
        OPEN(12,FILE=TITLE32,STATUS='
  UNKNOWN')
        DO 307 I=1,201
           WRITE(12,450) VALZ(I),RES32(I
  )
307     CONTINUE
        CLOSE(12)
        TITLE33="T33 P"
        OPEN(13,FILE=TITLE33,STATUS='
  UNKNOWN')
        DO 308 I=1,201
           WRITE(13,450) VALZ(I),RES33(I
  )
308     CONTINUE
        CLOSE(13)
        TITLECT="CT P"
```

```
        OPEN(33,FILE=TITLECT,STATUS='
     UNKNOWN')
        DO 414 I=1,201
           WRITE(33,450) VALZ(I),RESCT(I
     )
  414   CONTINUE
        CLOSE(33)
        TITLET="T P"
        OPEN(36,FILE=TITLET,STATUS='
     UNKNOWN')
        DO 417 I=1,201
           WRITE(36,450) VALZ(I), REST(I
     )
  417   CONTINUE
        CLOSE(36)

  450   FORMAT (F30.18,5X,F30.20)

        END

*MATRIX MULTIPLICATION ROUTINE

      SUBROUTINE MATMULT(A,B,C)
      INTEGER I,J,K
      REAL*8 A(4,4),B(4,4),C(4,4)
      DO 10 I=1,4
      DO 10 K=1,4
      C(I,K)=0.0
      DO 10 J=1,4
 10   C(I,K)=C(I,K)+(A(I,J)*B(J,K))
      RETURN
      END


*TRACE ROUTINE

      REAL*8 FUNCTION TRACE(A,B)
      REAL*8 A(4,4),B(4,4)
      INTEGER I,J
      TRACE=0.0
      DO 10 I=1,4
      DO 10 J=1,4
 10   TRACE=TRACE+(A(I,J)*B(J,I))
      RETURN
      END

C
C     MATRIX DIAGONALIZATION
C
      SUBROUTINE HDIAG(G,X,N)
      IMPLICIT REAL*8 (A-H,O-Z)
      REAL*8 G(4,4),X(4,4),R(5),B(5),C
     (5),CS(5),SN(5),P(5)
      EQUIVALENCE (P,C)
      DO 43 I=1,5
 43   B(I)=0.0
      DO 1 I=1,N
      DO 1 J=1,N
 1    X(I,J)=0.0
      DO 2 I=1,N
 2    X(I,I)=1.0
      FNORM=0.0
      BABSB=0.0
      N1=N-2
      DO 3 K=1,N1
      R(K)=G(K,K)
      SIGMA=0.0
      K1=K+1
      DO 4 I=K1,N
 4    SIGMA=SIGMA+G(I,K)*G(I,K)
      T=BABSB+ABS(R(K))
      BABSB=SQRT(SIGMA)
      TTA=T+BABSB
      FNORM=DMAX1(FNORM,TTA)
      ALPHA=G(K+1,K)
      IF (ALPHA) 5,6,6
 5    BETA=BABSB
      GOTO 7
 6    BETA=-BABSB
 7    B(K1)=BETA
      IF (SIGMA) 8,3,8
 8    GAMMA=1.0/(SIGMA-ALPHA*BETA)
      G(K1,K)=ALPHA-BETA
      DO 10 I=K1,N
      T=0.0
      DO 11 J=K1,I
 11   T=T+G(I,J)*G(J,K)
      IF (I-N) 12,10,10
 12   I1=I+1
      DO 13 J=I1,N
 13   T=T+G(J,I)*G(J,K)
 10   P(I)=GAMMA*T
      T=0.0
      DO 14 I=K1,N
 14   T=T+G(I,K)*P(I)
      T=0.5*GAMMA*T
      DO 15 I=K1,N
 15   P(I)=P(I)-T*G(I,K)
      DO 16 I=K1,N
      DO 16 J=K1,I
 16   G(I,J)=G(I,J)-G(I,K)*P(J)-P(I)*G(J
     ,K)
      DO 17 I=2,N
      T=0.0
      DO 18 J=K1,N
 18   T=T+X(I,J)*G(J,K)
 17   P(I)=GAMMA*T
      DO 19 I=2,N
      DO 19 J=K1,N
 19   X(I,J)=X(I,J)-P(I)*G(J,K)
 3    CONTINUE
      R(N-1)=G(N-1,N-1)
      R(N)=G(N,N)
      B(N)=G(N,N-1)
      T=ABS(B(N))
      TTA=BABSB+ABS(R(N-1))+T
      TTB=T+ABS(R(N))
      FNORM=DMAX1(FNORM,TTA,TTB)
      EPS=FNORM*1.0E-8
      B(1)=0.0
      AMU=0.0
      M=N
 20   IF (M) 21,21,22
 21   RETURN
 22   I=M-1
      K=I
      M1=I
      IF (ABS(B(K+1))-EPS) 23,23,24
 23   G(M,M)=R(M)
      M=K
      GOTO 20
 24   IF (ABS(B(K))-EPS) 26,26,25
 25   K=K-1
      GOTO 24
 26   B0=B(M1+1)
      B0=B0*B0
      R1=R(M1)-R(M)
      R1=SQRT(R1*R1+4.0*B0)
      T=R(M1)*R(M)-B0
      R0=R(M1)+R(M)
      IF (R0) 28,27,27
 27   AMDA=0.5*(R0+R1)
```

```
      GOTO 29
 28   AMDA=0.5*(R0-R1)
 29   T=T/AMDA
      IF (ABS(T-AMU)-0.5*ABS(T))
     30,31,31
 30   AMDA=T
      GOTO 34
 31   IF (ABS(AMDA-AMU)-0.5*ABS(AMDA))
     32,33,33
 32   AMU=AMDA
      GOTO 35
 33   AMDA=0.0
 34   AMU=T
 35   R(K)=R(K)-AMDA
      BETA=B(K+1)
      DO 36 J=K,M1
      R0=R(J)
      R1=R(J+1)-AMDA
      B0=B(J+1)
      T=SQRT(R0*R0+BETA*BETA)
      CASIN=R0/T
      CS(J)=CASIN
      SANE=BETA/T
      SN(J)=SANE
      R(J)=CASIN*R0+SANE*BETA
      R(J+1)=-SANE*B0+CASIN*R1
      B(J+1)=CASIN*B0+SANE*R1
      BETA=B(J+2)
      B(J+2)=CASIN*BETA
 36   C(J+1)=SANE*BETA
      B(K)=0.0
      C(K)=0.0
      DO 37 J=K,M1
      SANE=SN(J)
      CASIN=CS(J)
      R0=R(J)
      B0=B(J+1)
      B(J)=B(J)*CASIN+C(J)*SANE
      R(J)=R0*CASIN+B0*SANE+AMDA
      B(J+1)=-R0*SANE+B0*CASIN
      R(J+1)=R(J+1)*CASIN
      DO 37 I=1,N
      X0=X(I,J)
      X1=X(I,J+1)
      X(I,J)=X0*CASIN+X1*SANE
 37   X(I,J+1)=-X0*SANE+X1*CASIN
      R(M)=R(M)+AMDA
      GOTO 20
      END
*
      SUBROUTINE EIGSORT(D,V,N)
      IMPLICIT REAL*8 (A-H,O-Z)
      REAL*8 D(N,N),V(N,N)
      DO 1 I=1,N-1
      K=I
      P=D(I,I)
      DO 2 J=I+1,N
      IF (D(J,J).GE.P) THEN
       K=J
       P=D(J,J)
      ENDIF
 2    CONTINUE
      IF (K.NE.I) THEN
       D(K,K)=D(I,I)
       D(I,I)=P
       DO 3 J=1,N
       P=V(J,I)
       V(J,I)=V(J,K)
 3     V(J,K)=P
      ENDIF
 1    CONTINUE
      RETURN
      END
```

Appendix E

ASBO composite pulse trajectories

Figure E.1 illustrates the simulated $I_y- > -I_y$ inversion trajectories of magnetisation vectors for the ASBO pulses given in Table 4.1 under ideal conditions ($B_1/B_1^{nom} = 1, \Delta B/B_1^{nom} = 0$).

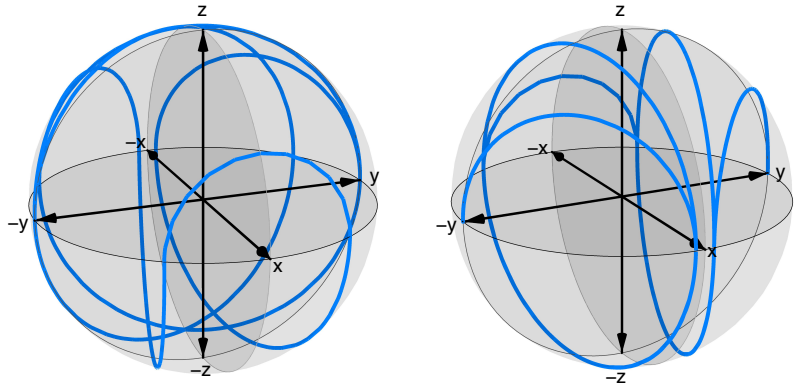

(a) ASBO-9(7A)

(b) ASBO-9(7B)

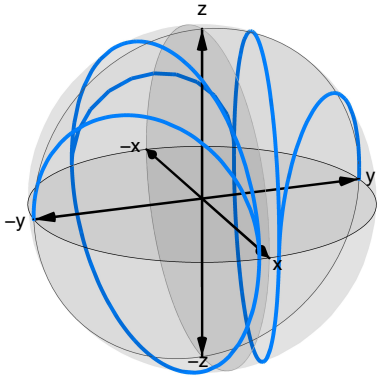

(c) ASBO-9(7C)

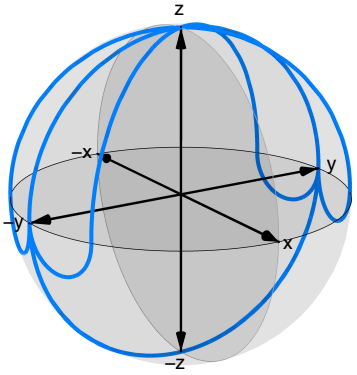

(d) ASBO-9(7D)

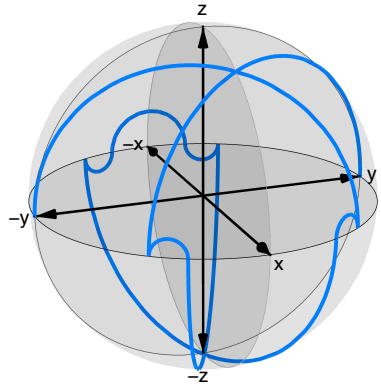

(e) ASBO-9(B_1)

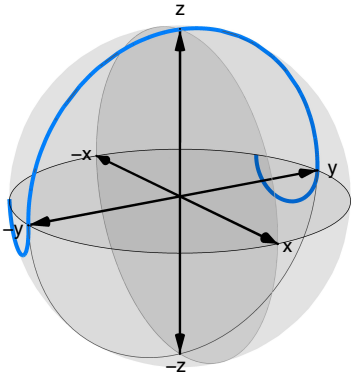

(f) ASBO-9(Ω)

FIGURE E.1: "Grapefruit plots" showing the trajectories of magnetisation vectors under the 9-pulse ASBO composite pulses given in Table 4.1. Simulated with Spin Dynamica [2] with $B_1/B_1^{nom} = 1$ and $\Delta B/B_1^{nom} = 0$ (continued on next page…)

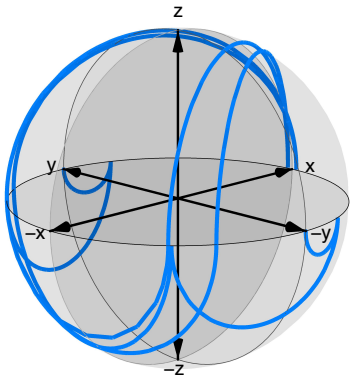

(a) ASBO-11(B_1)

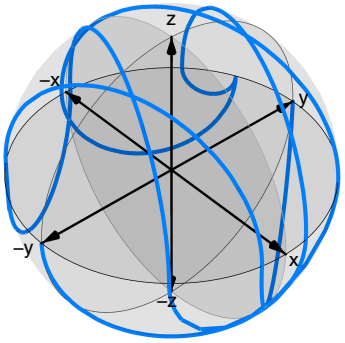

(b) ASBO-11(Ω)

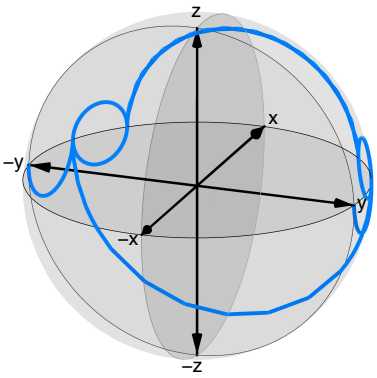

(c) TPG

FIGURE E.1: (continued) "Grapefruit plots" showing the trajectories of magnetisation vectors under the 11-pulse ASBO composite pulses given in Table 4.1 and TPG. Simulated with Spin Dynamica [2] with $B_1/B_1^{nom} = 1$ and $\Delta B/B_1^{nom} = 0$.

Appendix F

Spin-locking simulations of $I = 5/2$ nuclei

F.1 Spin $I = 5/2$ in a static solid

The spin-locking model has also been used to examine the creation of coherences and populations for spin $I = 5/2$. Figure F.1 shows the expectation values of the $I = 5/2$ spherical tensor operators as three-dimensional surface plots as a function of varying ω_1 and Ω for a single orientation nuclear spin ($\beta = 0^\circ$).

Considering the inital state $T_{1,0}$ first, we find that the amount decreases as the field strength of the spin-locking pulse increases. Again we see dips in the surface plot when the resonance offset is equal to multiples of the quadrupolar splitting: at 0, 200, 400, 600 and 800 kHz furrows of decreasing depth are present, corresponding to the creation of other states.

The population states $T_{2,0}$, $T_{3,0}$, $T_{4,0}$ and $T_{5,0}$ are created at these offsets, even at very low ω_1. In contrast, the single-quantum states are not formed under these conditions, only occuring as the field strength is raised and with maxima in between these offsets. This reflects the results seen for spin $I = 3/2$.

Next, considering the double-quantum coherences, we see interesting features in the surface plots at around $\Omega/2\pi = 0, 200, 400$ and 600 kHz. The plots for coherence orders

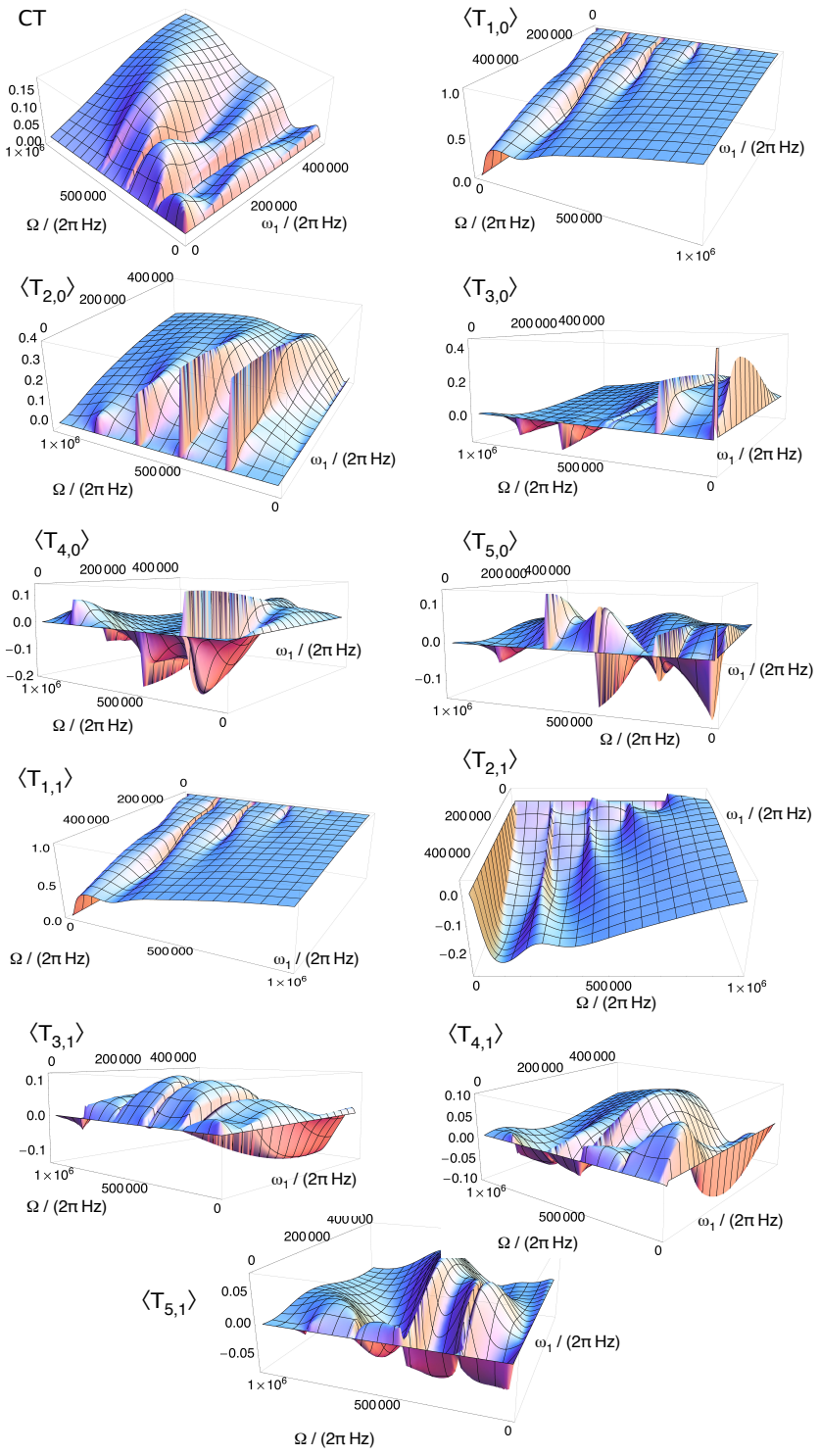

FIGURE F.1: Three-dimensional surface plots of the spin $I = 5/2$ expectation values of spherical tensor operators, $T_{l,p}$ and the central transition (CT) created by rapid dephasing of initial state $T_{1,0}$ under a spin-locking Hamiltonian, as a function of ω_1 and Ω. Results are plotted for a single orientation ($\theta = 0°$) with $\omega_Q^{PAS}/2\pi = 200$ kHz

(continued on next page...)

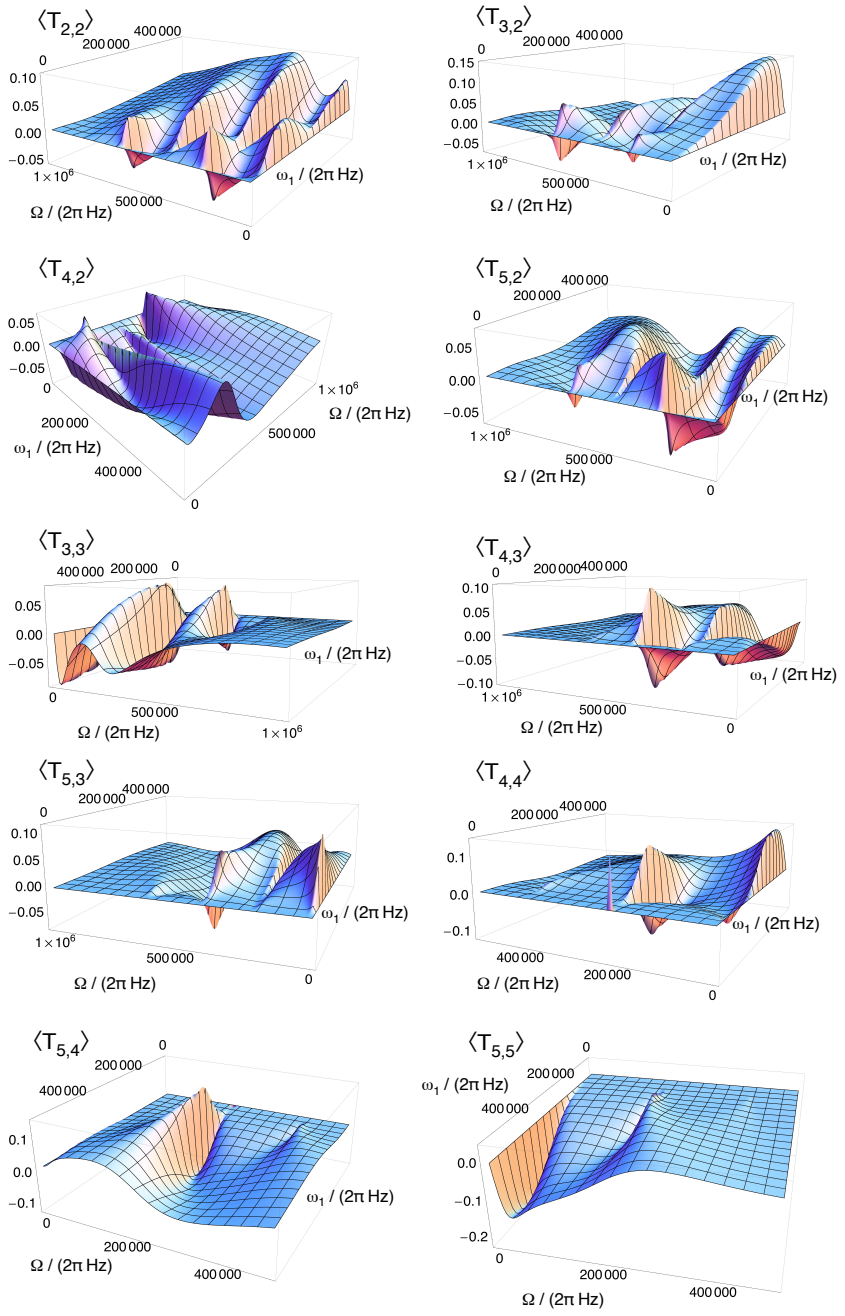

FIGURE F.1: (continued) Three-dimensional surface plots of the spin $I = 5/2$ expectation values of spherical tensor operators, $T_{l,p}$ and the central transition (CT) created by rapid dephasing of initial state $T_{1,0}$ under a spin-locking Hamiltonian, as a function of ω_1 and Ω. Results are plotted for a single orientation ($\theta = 0°$) with $\omega_Q^{\mathrm{PAS}}/2\pi = 200$ kHz.

3 and 4 feature peaks around $\Omega/2\pi = 0, 200$ and 400 kHz, while the $T_{5,5}$ is mostly present at lower offsets around $\Omega/2\pi = 0$ and 200 kHz.

Again, we expect these trends to be different in the case of a powder sample. These are explored in the three-dimensional surface plots in Figure F.2. $T_{1,0}$ decreases as the

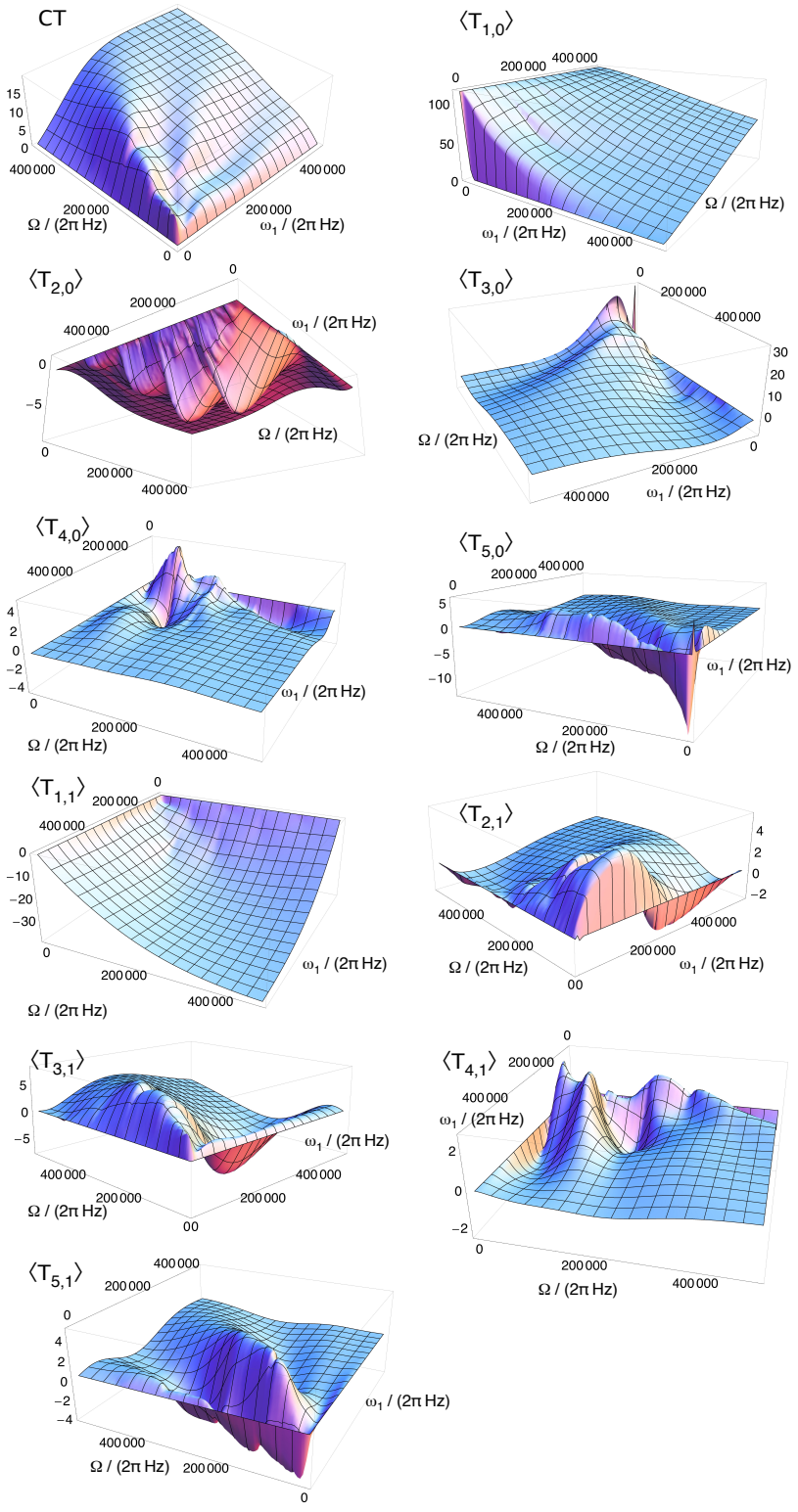

FIGURE F.2: Three-dimensional surface plots of the spin $I = 5/2$ expectation values of spherical tensor operators, $T_{l,p}$ and the central transition (CT) created by rapid dephasing of initial state $T_{1,0}$ under a spin-locking Hamiltonian, as a function of ω_1 and Ω. Results are plotted for a powder with $\omega_Q^{PAS}/2\pi = 200$ kHz (continued on next page...)

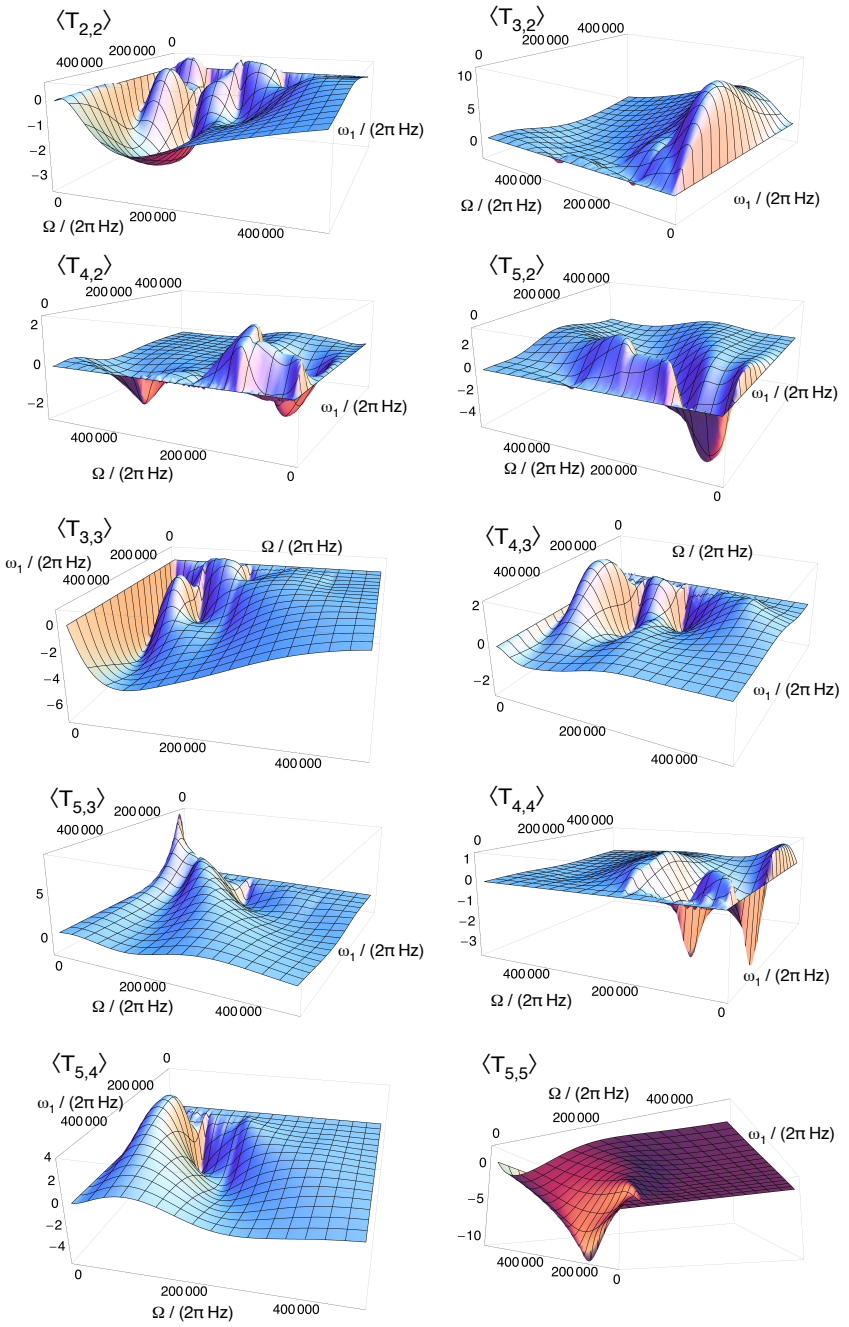

FIGURE F.2: (continued) Three-dimensional surface plots of the spin $I = 5/2$ expectation values of spherical tensor operators, $T_{l,p}$ and the central transition (CT) created by rapid dephasing of initial state $T_{1,0}$ under a spin-locking Hamiltonian, as a function of ω_1 and Ω. Results are plotted for a powder with $\omega_Q^{\mathrm{PAS}}/2\pi = 200$ kHz.

rf field strength is raised, and the falloff is more rapid at lower offsets. $T_{2,0}$ shows three ridges along $\Omega/2\pi = 100, 200$ and 300 kHz, which peak around $\omega_1/2\pi = 100$ kHz. The $T_{3,0}$ plot is similar to the corresponding spin $I = 3/2$ plot, with most creation at low ω_1 and Ω. $T_{4,0}$ is produced when either ω_1 or Ω are small, with a maximum at $\omega_1/2\pi = 30$

kHz and $\Omega = 90$ kHz. $T_{5,0}$ is also mostly created at low ω_1 and Ω.

Looking at the double-quantum coherences, $T_{2,2}$ has ridges along $\Omega = 100$ and 200 kHz, while $T_{3,2}$ is present at mostly at offsets under 100 kHz. $T_{3,3}$ has a maximum at $\omega_1/2\pi = 40$ kHz and $\Omega = 5$ kHz, and all the triple-quantum coherences feature a dip in intensity at $\Omega = 100$ and 200 kHz, as well as at 300 kHz for $T_{4,3}$. The $T_{4,4}$ surface plot features ridges in between offsets of 0 and 100 kHz, 100 and 150 kHz and 150 and 300 kHz, while the $T_{5,4}$ is mainly created between offsets of 0 and 100 kHz and 100 and 200 kHz. $T_{5,5}$ is created mostly at low resonance offsets, with a maximum in the plot at $\omega_1/2\pi = 165$ kHz and $\Omega = 5$ kHz.

Figure F.3 shows the cross sections at $\Omega/2\pi = 100$ kHz for these simulations. The expectation value for $T_{1,0}$ falls off as the rf strength is increased, as $T_{2,0}$, $T_{3,0}$, $T_{1,1}$ form in significant amounts. When $\omega_1/2\pi$ is raised between 0 and 200 kHz, the multiple quantum coherences $T_{3,3}$,$T_{5,3}$ and $T_{5,4}$ peak, while at higher field strengths (around 300 kHz) $T_{2,2}$ and $T_{5,2}$ form.

The changes in the norm, presented in Figure F.4, reflect the results seen for spin $I = 3/2$: the magnitude decreases as the field strength increases, and as the resonance offset is raised, the rate of the falloff decreases.

F.2 Spin $I = 5/2$ with MAS

The rotor-driven modulation of the eigenstates of the spin $I = 5/2$ nucleus under adiabatic conditions has also been studied. Figure F.5 presents the expectation values of spherical tensor operators for a single crystallite formed by initial rapid dephasing. The same simulation parameters have been employed as in Figure 6.6. Considering the plots for $\Omega/2\pi = 50$ kHz, $T_{1,0}$ is most abundant at the start of the rotor period, along with $T_{3,0}$, $T_{3,0}$ and $T_{2,1}$. As the rotor turns, these states decrease as coherence transfer takes place, leading to increased amounts of $T_{2,0}$, $T_{3,1}$ and $T_{4,2}$ being created at 0.1 rotor periods. Further rotor-driven modulation leads to $T_{1,1}$, $T_{5,1}$ and $T_{2,2}$ being present in more significant amounts after a quarter turn of the rotor is completed. The second half of the rotor period repeats the same cycle of the spin-locked states.

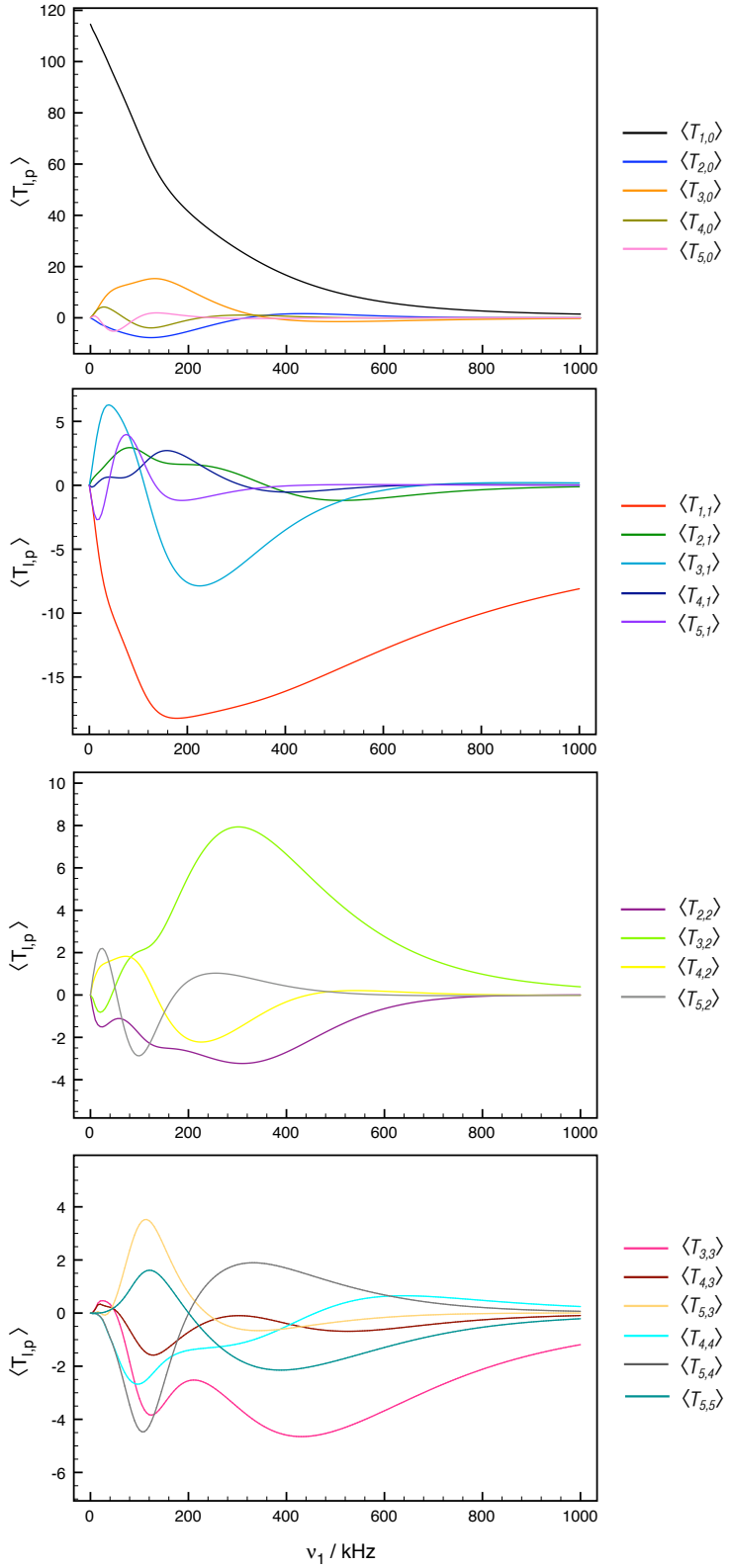

FIGURE F.3: Expectation values of $I = 5/2$ spherical tensor operators, $T_{l,p}$ created by rapid dephasing of initial state $T_{1,0}$ under a spin-locking Hamiltonian, as a function of ν_1. Results are plotted for a powder with $\omega_Q^{\mathrm{PAS}}/2\pi = 200$ kHz and $\Omega/2\pi = 100$ kHz.

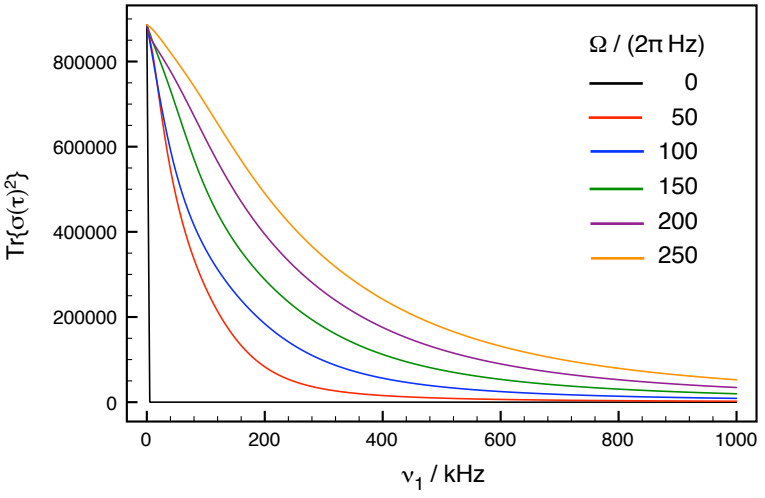

FIGURE F.4: The norm of the spin $I = 5/2$ density operator created by rapid dephasing of initial state $T_{1,0}$ under a spin-locking Hamiltonian, as a function of ν_1. Results are plotted for a powder with $\omega_Q^{PAS}/2\pi = 200$ kHz and $\Omega/2\pi = 50, 100, 150, 200$ and 250 kHz.

As in the spin $I = 3/2$ case, we observe a decrease in the extent of the eigenstate modulation when the offset is increased to 100 kHz in Figure F.5(b). At the start of the rotor period, the population states are again most abundant in order of decreasing rank. The decrease in the amplitude of the population states leads to the creation of single- and multiple-quantum coherence states, with increasingly higher order coherences being formed in lower amounts. After 0.2 rotor periods, $T_{2,1}$, $T_{2,2}$ and $T_{3,2}$ are formed, along with small amounts of $T_{3,3}$ and $T_{4,3}$. $T_{1,1}$ and $T_{3,1}$ are at a maximum at a quarter turn. All states return to their original amplitude after a half turn is completed, and the second half of the rotor period repeats the behaviour of the first half.

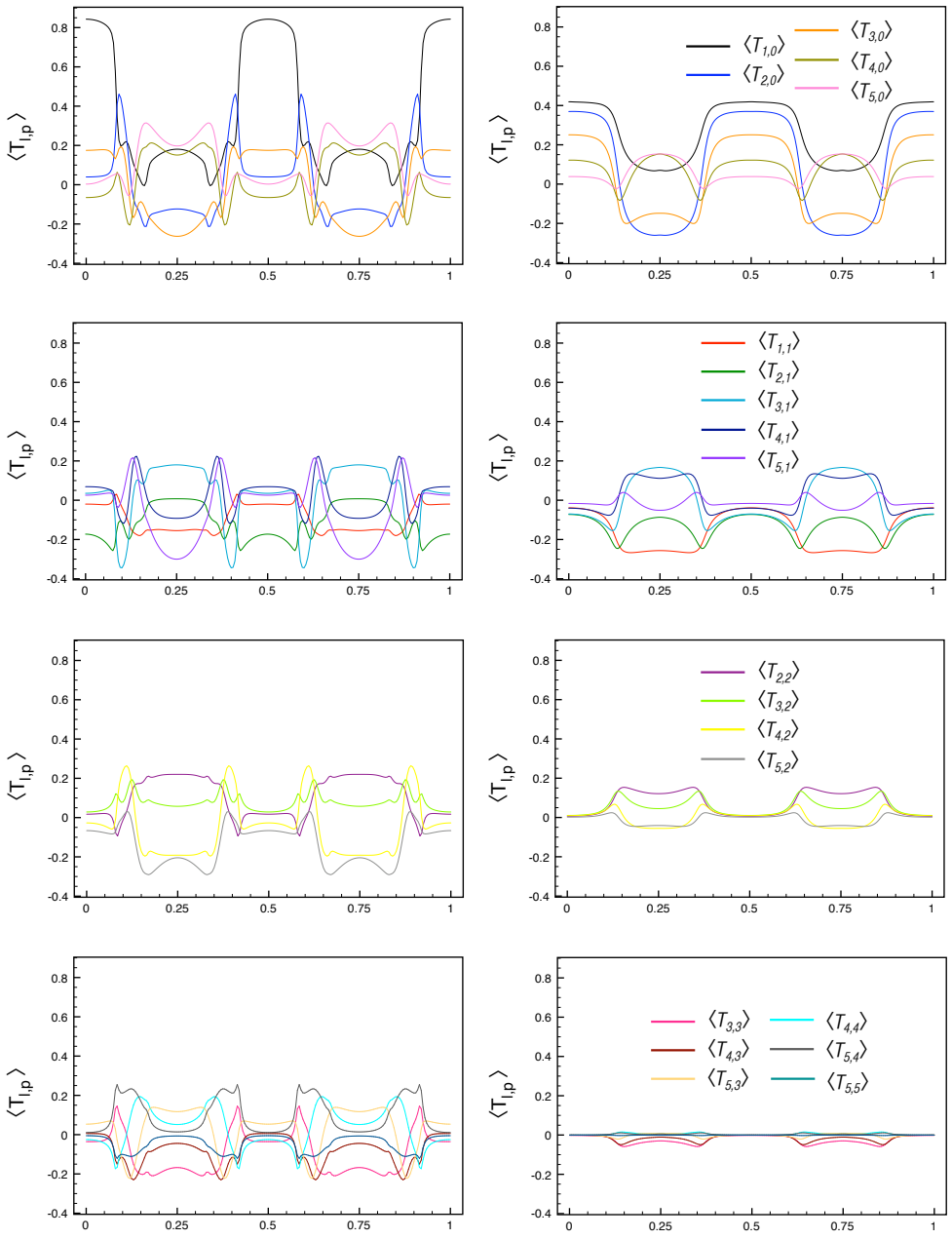

(a) $\Omega/2\pi = 50$ kHz (b) $\Omega/2\pi = 100$ kHz

FIGURE F.5: Expectation values under MAS of $I = 5/2$ spherical tensor operators, $T_{l,p}$ created by rapid dephasing of initial state $T_{1,0}$ under a spin-locking Hamiltonian, as a function of ν_1. Results are plotted for a single orientation ($\beta = 90°$ and $\xi = 180°$) with $\omega_Q^{PAS}/2\pi = 200$ kHz.

Appendix G

List of chemicals used

The following chemicals have been used in the experimental parts of this work:

Substance	Chemical formula	Purity (%)	Supplier
Adamantane	$C_{10}H_{16}$	99	Sigma Aldrich
L-Alanine	CH_3CHCO_2H	99	Sigma Aldrich
Aluminum acetylacetonate	$Al(acac)_3$	99	Sigma Aldrich
Boron phosphate	BPO_4	99.995	Sigma Aldrich
Oxalic acid dihydrate, nominally perdeuterated (96% ^2H)	$HO_2CCO_2H \cdot 2H_2O$	98	Sigma Aldrich. Deuterated by Wimperis Group.
Poly(methyl methacrylate) (PMMA), nominally perdeuterated (99% ^2H)	$(C_5O_2H_8)_n$	-	Adrian Brunsdon, Bruker
Sodium chloride	NaCl	99.9	AnalaR
Titanium pyrophosphate	TiP_2O_7	95	Dr. Gregory Tricot of Université Lille de Nord de France

Bibliography

[1] S. Patel. Latex thesis template. Available at http://www.sunilpatel.co.uk/thesis-template.

[2] M. H. Levitt, J. Rantaharju, and A. Brinkmann. SpinDynamica code for Wolfram Mathematica. Available at www.SpinDynamica.soton.ac.uk.

[3] S. Odedra and S. Wimperis. Use of composite refocusing pulses to form spin echoes. *Journal of Magnetic Resonance*, 214:68–75, 2012.

[4] S. Odedra and S. Wimperis. Improved background suppression in ^{1}H MAS NMR using composite pulses. *Journal of Magnetic Resonance*, 221:41–50, 2012.

[5] S. Odedra and S. Wimperis. Imaging of the B_1 distribution and background signal in a MAS NMR probehead using inhomogeneous B_0 and B_1 fields. *Journal of Magnetic Resonance*, 231:95–99, 2013.

[6] S. Odedra, M. J. Thrippleton, and S. Wimperis. Dual-compensated antisymmetric composite refocusing pulses for NMR. *Journal of Magnetic Resonance*, 225:81–92, 2012.

[7] W. Gerlach and O. Stern. Das magnetische moment des silberatoms. *Zeitschrift für Physik*, 8:353–355, 1922.

[8] G. E. Uhlenbeck and S. Goudsmit. Ersetzung der Hypothese vom unmechanischen Zwang durch eine Forderung bezüglich des inneren Verhaltens jedes einzelnen Elektrons. *Die Naturwissenschaften*, 13:953–954, 1925.

[9] W. Pauli. Zuschriften und vorläufige Mitteilungen. *Die Naturwissenschaften*, 12:741–743, 1924.

[10] I. Estermann and O. Stern. Über die magnetische Ablenkung von Wasserstoffmolekülen und das magnetische Moment des Protons. II. *Zeitschrift fr Physik*, 85(1-2):17–24, 1933.

[11] R. Frisch and O. Stern. Über die magnetische Ablenkung von Wasserstoffmolekülen und das magnetische Moment des Protons. I. *Zeitschrift für Physik*, 85(1-2):4–16, 1933.

[12] I. I. Rabi. Space quantization in a gyrating magnetic field. *Physical Review*, 51:652–654, 1937.

[13] I. J. Lowe. Free induction decays of rotating solids. *Physical Review Letters*, 2:285–287, 1959.

[14] R. R. Ernst and W. A. Anderson. Application of Fourier transform spectroscopy to magnetic resonance. *Review of Scientific Instruments*, 37:93–102, 1966.

[15] R. Freeman. *Spin Choreography*. Oxford University Press, 1998.

[16] R. R. Ernst, G. Bodenhausen, and A. Wokaun. *Principles of Nuclear Magnetic Resonance in One and Two Dimensions*. Oxford University Press, 1987.

[17] D. I. Hoult and B. Bhakar. NMR signal reception: Virtual photons and coherent spontaneous emission. *Concepts in Magnetic Resonance*, 9:277–297, 1997.

[18] D. I. Hoult. The origins and present status of the radio wave controversy in NMR. *Concepts in Magnetic Resonance Part A*, 34:193–216, 2009.

[19] M. J. Duer. *Introduction to Solid-State NMR Spectroscopy*. Blackwell Publishing, 2004.

[20] J. Keeler. *Understanding NMR Spectroscopy*. John Wiley and Sons, 2005.

[21] N. E. Jacobsen. *NMR Spectroscopy Explained*. John Wiley and Sons, 2007.

[22] M. H. Levitt. *Spin Dynamics*. John Wiley and Sons, 2001.

[23] P. Plateau, C. Dumas, and M. Guéron. Solvent-peak-suppressed NMR: Correction of baseline distortions and use of strong-pulse excitation. *The Journal of Magnetic Resonance*, 54:46–53, 1983.

[24] W. P. Aue, E. Bartholdi, and R. R. Ernst. Two-dimensional spectroscopy. Application to nuclear magnetic resonance. *Journal of Chemical Physics*, 64:2229–2246, 1976.

[25] A. Bax, P. G. De Jong, A. F. Mehlkopf, and J. Smidt. Separation of the different orders of NMR multiple-quantum transitions by the use of pulsed field gradients. *Chemical Physics Letters*, 69:567–570, 1980.

[26] G. Bodenhausen, H. Kogler, and R. R. Ernst. Selection of coherence transfer pathways in NMR pulse experiments. *The Journal of Magnetic Resonance*, 58:370–388, 1984.

[27] O. W. Sørensen, G. W. Eich, M. H. Levitt, G. Bodenhausen, and R. R. Ernst. Product operator formalism for the description of NMR pulse experiments. *Progress in NMR Spectroscopy*, 16:163–192, 1983.

[28] P. J. Hore, J. A. Jones, and S. Wimperis. *NMR: The Toolkit*. Oxford University Press, 2000.

[29] N. Müller, G. Bodenhausen, and R. R. Ernst. Relaxation-induced violations of coherence transfer selection rules in nuclear magnetic resonance. *Journal of Magnetic Resonance*, 75:1297–334, 1987.

[30] C. E. Hughes. *New techniques in NMR spectroscopy*. PhD thesis, Oxford University, 1998.

[31] I. Solomon. Relaxation processes in a system of two spins. *Physical Review*, 99:559–565, 1955.

[32] G. E. Pake. Nuclear resonance absorption in hydrated crystals: Fine structure of the proton line. *Journal of Chemical Physics*, 16:327–336, 1948.

[33] J. H. Van Vleck. The dipolar broadening of magnetic resonance lines in crystals. *Physical Review*, 74:1168–1183, 1948.

[34] N. S. Barrow. *Homonuclear Correlationin Solid-State NMR: Developing Experiments for Half-Integer Quadrupolar Nuclei*. PhD thesis, The University of Warwick, 2009.

[35] S. Ashbrook and S. Wimperis. Quadrupolar coupling: An introduction and crystallographic aspects. In *Encyclopedia of Magnetic Resonance*, pages 1–15. John Wiley and Sons, 2007.

[36] A. Abragam. *Principles of Nuclear Magnetism*. Oxford University Press, 1961.

[37] E. Andrew, A. Bradbury, and R. G. Eades. Nuclear magnetic resonance spectra from a crystal rotated at high speed. *Nature*, 182:1659, 1958.

[38] M.M. Maricq and J. S. Waugh. NMR in rotating solids. *The Journal of Chemical Physics*, 70(7):3300–3316, 1979.

[39] D. Apperley, P. Hodgkinson, and R. K. Harris. *Solid State NMR: Basic Principles and Practice*. Momentum Press, 2012.

[40] H. A. Buckmaster. Tables of angular momentum transformation matrix elements. *Canadian Journal of Physics*, 42(2):386–391, 1964.

[41] M. Mehring. *High Resolution NMR Spectroscopy in Solids*. Springer-Verlag, 1976.

[42] E. L. Hahn. Spin echoes. *Physical Review*, 80:580–594, 1950.

[43] H. Y. Carr and E. M. Purcell. Effects of diffusion on free precession in nuclear magnetic resonance experiments. *Physical Review*, 94:630–638, 1954.

[44] J. H. Davis, K. R. Jeffrey, M. Bloom, and M. I. Valic. Quadrupolar echo deuteron magnetic resonance spectroscopy in ordered hydrocarbon chains. *Chemical Physics Letters*, 42:390–394, 1976.

[45] S. Antonijevic and S. Wimperis. Refocusing of chemical and paramagnetic shift anisotropies in ^{2}H NMR using the quadrupolar-echo experiment. *The Journal of Magnetic Resonance*, 164:343–350, 2003.

[46] G. Bodenhausen, R. Freeman, and D. L. Turner. Suppression of artifacts in two-dimensional J spectroscopy. *The Journal of Magnetic Resonance*, 27:511–514, 1977.

[47] G. Bodenhausen, R. Freeman, R. Niedermeyer, and D. L. Turner. Double fourier transformation in high-resolution NMR. *The Journal of Magnetic Resonance*, 26:133–164, 1976.

[48] G. Bodenhausen. Reflections of pathways: A short perspective on 'selection of coherence transfer pathways in NMR pulse experiments'. *The Journal of Magnetic Resonance*, 213:295–297, 2011.

[49] S. Wimperis. Broadband, narrowband and passband composite pulses for use in advanced NMR experiments. *Journal of Magnetic Resonance, Series A*, 109:221–231, 1994.

[50] M. H. Levitt and R. Freeman. NMR population inversion using a composite pulse. *The Journal of Magnetic Resonance*, 33:473–476, 1979.

[51] R. Freeman, S. P. Kempsell, and M. H. Levitt. Radiofrequency pulse sequences which compensate their own imperfections. *The Journal of Magnetic Resonance*, 38:453–479, 1980.

[52] M. H. Levitt. Short perspective on NMR population inversion using a composite pulse by M.H. Levitt and R. Freeman. *The Journal of Magnetic Resonance*, 213:274–275, 2011.

[53] M.H. Levitt. Symmetrical composite pulse sequences for NMR population inversion. I. Compensation of resonance offset. *Journal of Magnetic Resonance*, 50:95–110, 1982.

[54] M. H. Levitt. Symmetrical composite pulse sequences for NMR population inversion. II. Compensation of radiofrequency field inhomogeneity. *Journal of Magnetic Resonance*, 48:234–264, 1982.

[55] M.H. Levitt and R.R. Ernst. Composite pulses constructed by a recursive expansion procedure. *Journal of Magnetic Resonance*, 55:247–254, 1983.

[56] R. Tycko. Broadband population inversion. *Physical Review Letters*, 51:775–777, 1983.

[57] A.J. Shaka and R. Freeman. Composite pulses with dual compensation. *Journal of Magnetic Resonance*, 55:487–493, 1983.

[58] R. Tycko and A. Pines. Iterative schemes for broadband and narrowband population inversion in NMR. *Chemical Physics Letters*, 111:462–467, 1984.

[59] R. Tycko, H.M. Cho, E. Schneider, and A. Pines. Composite pulses without phase distortion. *Journal of Magnetic Resonance*, 61:90–101, 1985.

[60] R. Tycko, A. Pines, and J. Guckenheimer. Fixed point theory of iterative excitation schemes in NMR. *Journal of Chemical Physics*, 83:2775–2802, 1985.

[61] R. Tycko. Iterative methods in the design of pulse sequences for NMR excitation. *Advances in Magnetic and Optical Resonance*, 15:1–49, 1990.

[62] S. Wimperis. Iterative schemes for phase-distortionless composite 180° pulses. *Journal of Magnetic Resonance*, 93:199–206, 1991.

[63] J. A. Jones. Quantum computing with NMR. *Progress in NMR Spectroscopy*, 59:91–120, 2011.

[64] M. Bando, T. Ichikawa, Y. Kondo, and M. Nakahara. Concatenated composite pulses compensating simultaneous systematic errors. *Journal of the Physical Society of Japan*, 82(1), 2013.

[65] J.A. Jones. Designing short robust not gates for quantum computation. *Physical Review A - Atomic, Molecular, and Optical Physics*, 87(5), 2013.

[66] S. Husain, M. Kawamura, and J.A. Jones. Further analysis of some symmetric and antisymmetric composite pulses for tackling pulse strength errors. *Journal of Magnetic Resonance*, 230:145–154, 2013.

[67] G. S. Kupriyanova, V. V. Molchanov, E. A. Severin, and I. G. Mershiev. Composite pulses in inhomogeneous field NMR. In *Magnetic Resonance Detection of Explosives and Illicit Materials*, NATO Science for Peace and Security Series B: Physics and Biophysics, pages 137–147. Springer Netherlands, 2014.

[68] H.P. Hetherington and D.L. Rothman. Phase cycling of composite refocusing pulses to eliminate dispersive refocusing magnetization. *Journal of Magnetic Resonance (1969)*, 65(2):348 – 354, 1985.

[69] A.J. Shaka and A. Pines. Symmetric phase-alternating composite pulses. *The Journal of Magnetic Resonance*, 71:495–503, 1987.

[70] C. Counsell, M. H. Levitt, and R. R. Ernst. Analytical theory of composite pulses. *Journal of Magnetic Resonance*, 63:133–141, 1985.

[71] A.J. Shaka and R. Freeman. Spatially selective radiofrequency pulses. *Journal of Magnetic Resonance*, 59:169–176, 1984.

[72] J. S. Waugh. Systematic procedure for constructing broadband decoupling sequences. *Journal of Magnetic Resonance*, 49:517–521, 1982.

[73] M. H. Levitt and R. Freeman. Compensation for pulse imperfections in NMR spin-echo experiments. *The Journal of Magnetic Resonance*, 81:65–80, 1981.

[74] T.-L. Hwang and A.J. Shaka. Water suppression that works. Excitation sculpting using arbitrary waveforms and pulse field gradients. *Journal of Magnetic Resonance, Series A*, 112:275–279, 1995.

[75] A. Lesage. Recent advances in solid-state NMR spectroscopy of spin $I = 1/2$ nuclei. *Physical Chemistry Chemical Physics*, 11:6876–6891, 2009.

[76] V. E. Zorin, S. P. Brown, and P. Hodgkinson. Origins of linewidth in ^{1}H magic-angle spinning NMR. *The Journal of Chemical Physics*, 125(14):–, 2006.

[77] S. Brown. Probing proton-proton proximities in the solid state. *Progress in NMR Spectroscopy*, 50:199–251, 2007.

[78] P. Hodgkinson. High-resolution ^{1}H NMR spectroscopy of solids. In *Annual Reports on NMR Spectroscopy*, volume 72, pages 185–223. Academic Press, 2011.

[79] E. Vinogradov, P.K. Madhu, and S. Vega. Proton spectroscopy in solid state nuclear magnetic resonance with windowed phase modulated Lee-Goldburg decoupling sequences. *Chemical Physics Letters*, 354(3-4):193 – 202, 2002.

[80] A. Lesage, D. Sakellariou, S. Hediger, B. Elna, P. Charmont, S. Steuernagel, and L. Emsley. Experimental aspects of proton NMR spectroscopy in solids using phase-modulated homonuclear dipolar decoupling. *Journal of Magnetic Resonance*, 163(1):105 – 113, 2003.

[81] S. P. Brown. Applications of high-resolution ^{1}H solid-state NMR. *Solid State Nuclear Magnetic Resonance*, 41(0):1 – 27, 2012.

[82] Q. Chen, S.S. Hou, and K. Schmidt-Rohr. A simple scheme for probehead background suppression in one-pulse ^{1}H NMR. *Solid State Nuclear Magnetic Resonance*, 26(1):11 – 15, 2004.

[83] C. Jaeger and F. Hemmann. EASY: A simple tool for simultaneously removing background, deadtime and acoustic ringing in quantitative NMR spectroscopy – part I: Basic principle and applications. *Solid State Nuclear Magnetic Resonance*, 5758:22 – 28, 2014.

[84] M. R. Bendall and R. E. Gordon. Depth and refocusing pulses designed for multipulse NMR with surface coils. *Journal of Magnetic Resonance*, 53:365–385, 1983.

[85] M. R. Bendall and D. T. Pegg. Theoretical description of depth pulse sequences, on and off resonance, including improvements and extensions thereof. *Magnetic Resonance in Medicine*, 2(2):91–113, 1985.

[86] M. R. Bendall and D. T. Pegg. Further comparisons of simple and composite depth pulses. *Journal of Magnetic Resonance (1969)*, 68(2):252 – 262, 1986.

[87] D. G. Cory and W. M. Ritchie. Suppression of signals from the probe in Bloch decay spectra. *Journal of Magnetic Resonance*, 80:128–132, 1988.

[88] D. G. Cory and W. M. Ritchie. Suppression of signals from the probe in NMR T_1 measurements. *Spectroscopy Letters*, 21:551–558, 1988.

[89] J. White, L. W. Beck, D. B. Ferguson, and J. F. Haw. Background suppression in MAS NMR. *Journal of Magnetic Resonance*, 100:336–341, 1992.

[90] A. Bax. A spatially selective composite 90° radiofrequency pulse. *Journal of Magnetic Resonance*, 65:142–145, 1985.

[91] E. M. Purcell. *Electricity and Magnetism*. McGraw-Hill, 1985.

[92] D. I. Hoult. The NMR receiver: A description and analysis of design. *Concepts in Magnetic Resonance*, 12:41–77, 1978.

[93] S. Wimperis. Composite pulses with rectangular excitation and inversion profiles. *Journal of Magnetic Resonance*, 83:509–524, 1989.

[94] H. M. Cho, R. Tycko, A. Pines, and J. Guckenheimer. Iterative maps for bistable excitation of two-level systems. *Physical Review Letters*, 56:1905–1908, 1986.

[95] H. Cho, J. Baum, and A. Pines. Iterative maps with multiple fixed points for excitation of two-level systems. *Journal of Chemical Physics*, 86:3089–3106, 1987.

[96] E. Díez-Peña, I. Quijada-Garrido, J. M. Barrales-Rienda, I. Schnell, and H. W. Spiess. Advanced ^{1}H solid-state NMR spectroscopy on hydrogels, 1. *Macromolecular Chemistry and Physics*, 205(4):430–437, 2004.

[97] K. Landfester, C. Boeffel, M. Lambla, and H. W. Spiess. Characterization of interfaces in coreshell polymers by advanced solid-state NMR methods. *Macromolecules*, 29(18):5972–5980, 1996.

[98] I. Schnell, A. Lupulescu, S. Hafner, D. E. Demco, and H. W. Spiess. Resolution enhancement in multiple-quantum MAS NMR spectroscopy. *Journal of Magnetic Resonance*, 133(1):61 – 69, 1998.

[99] S. P. Brown and H. W. Spiess. Advanced solid-state NMR methods for the elucidation of structure and dynamics of molecular, macromolecular, and supramolecular systems. *Chemical Reviews*, 101(12):4125–4156, 2001.

[100] A. Lesage, L. Duma, D. Sakellariou, and L. Emsley. Improved resolution in proton NMR spectroscopy of powdered solids. *Journal of the American Chemical Society*, 123(24):5747–5752, 2001.

[101] H. Heise, D. Sakellariou, C. A. Meriles, A. Moulé, and A. Pines. Two-dimensional high-resolution NMR spectra in matched B_0 and B_1 field gradients. *Journal of Magnetic Resonance*, 156:146–151, 2002.

[102] S. Antonijevic and S. Wimperis. High-resolution NMR spectroscopy in inhomogeneous B_0 and B_1 fields by two-dimensional correlation. *Chemical Physics Letters*, 381:634–641, 2003.

[103] U. Haeberlen and J.S. Waugh. Coherent averaging effects in magnetic resonance. *Physical Review*, 175:454–467, 1968.

[104] U. Haeberlen. High resolution NMR in solids. In *Advances in Magnetic Resonance*. Academic Press, 1976.

[105] J.S. Waugh. Average Hamiltonian theory. In *Encyclopedia of Magnetic Resonance*, pages 849–854. John Wiley and Sons, 2007.

[106] Gustav E.R. Schulze. Die Kristallstruktur von BPO_4 und $BAsO_4$. *Naturwissenschaften*, 21(30):562–562, 1933.

[107] A. Bax, R. Freeman, and S. P. Kempsell. Natural abundance ^{13}C-^{13}C coupling observed via double-quantum coherence. *Journal of the American Chemical Society*, 102(14):4849–4851, 1980.

[108] T. A. Early, B. K. John, and L. F. Johnson. Observation of homonuclear double-quantum correlations in plastic crystals using cross polarization and magic angle spinning. *Journal of Magnetic Resonance*, 75(1):134 – 138, 1987.

[109] R. Benn, H. Grondey, C. Brevard, and A. Pagelot. The detection of connectivities of rare spin-1/2 nuclei in the solid state using natural abundance samples: ^{13}C and ^{29}Si INADEQUATE and COSY type experiments. *Journal of the Chemical Society, Chemical Communications*, pages 102–103, 1988.

[110] C. A. Fyfe, Y. Feng, H. Gies, H. Grondey, and G. T. Kokotailo. Natural-abundance two-dimensional solid-state ^{29}Si NMR investigations of three-dimensional lattice connectivities in zeolite structures. *Journal of the American Chemical Society*, 112(9):3264–3270, 1990.

[111] A. Lesage, M. Bardet, and L. Emsley. Through-bond carbon-carbon connectivities in disordered solids by NMR. *Journal of the American Chemical Society*, 121(47):10987–10993, 1999.

[112] L. J. Mueller and J. J. Titman. Correlation spectroscopy for resonance assignments in solid-state proteins using J-couplings. In *Encyclopedia of Magnetic Resonance*. John Wiley and Sons, 2007.

[113] F. Fayon, I. J. King, R. K. Harris, R. K. B. Gover, J. S. O. Evans, and D. Massiot. Characterization of the room-temperature structure of SnP_2O_7 by ^{31}P through-space and through-bond NMR correlation spectroscopy. *Chemistry of Materials*, 15(11):2234–2239, 2003.

[114] D. Sakellariou, S. P. Brown, A. Lesage, S. Hediger, M. Bardet, C. A. Meriles, A. Pines, and L. Emsley. High-resolution NMR correlation spectra of disordered solids. *Journal of the American Chemical Society*, 125(14):4376–4380, 2003.

[115] H. Kono, T. Erata, and M. Takai. Determination of the through-bond carboncarbon and carbonproton connectivities of the native celluloses in the solid state. *Macromolecules*, 36(14):5131–5138, 2003.

[116] G. De Paëpe, N. Giraud, A. Lesage, P. Hodgkinson, A. Bckmann, and L. Emsley. Transverse dephasing optimized solid-state NMR spectroscopy. *Journal of the American Chemical Society*, 125(46):13938–13939, 2003.

[117] G. Grasso, T. M. de Swiet, and J. J. Titman. Electronic structure of the polymer phase of CsC_{60}: Refocused INADEQUATE experiments. *The Journal of Physical Chemistry B*, 106(34):8676–8680, 2002.

[118] F. Fayon, D. Massiot, M. H. Levitt, J. J. Titman, D. H. Gregory, L. Duma, L. Emsley, and S. P. Brown. Through-space contributions to two-dimensional double-quantum J correlation NMR spectra of magic angle spinning solids. *The Journal of Chemical Physics*, 122:194313, 2005.

[119] F. Fayon, G. Le Saout, L. Emsley, and D. Massiot. Through-bond phosphorus-phosphorus connectivities in crystalline and disordered phosphates by solid-state NMR. *Chemical Communications*, 122:1702–1703, 2002.

[120] S.T. Norberg, G. Svensson, and J. Albertsson. A TiP_2O_7 superstructure. *Acta Crystallographica Section C Crystal Structure Communications*, 57(4):225–227, 2001.

[121] J. Leppert, B. Heise, and R. Ramachandran. Magic angle spinning NMR spectroscopy with composite RF pulses. *Journal of Magnetic Resonance*, 139(2):382 – 388, 1999.

[122] M. Edén. Computer simulations in solid-state NMR. II. Implementations for static and rotating samples. *Concepts in Magnetic Resonance Part A*, 18A(1):1–23, 2003.

[123] E. T. Olejniczak, S. Vega, and R. G. Griffin. Multiple pulse NMR in rotating solids. *The Journal of Chemical Physics*, pages 4804–4817, 1984.

[124] G. Jeschke. Spin locking of I=3/2 nuclei in static and spinning samples: A description by abstract spins and Floquet formalism. *The Journal of Chemical Physics*, 108(3):907–917, 1998.

[125] A. J. Vega. MAS NMR spin locking of half-integer quadrupolar nuclei. *The Journal of Magnetic Resonance*, 96:50–68, 1992.

[126] W. Sun, J. T. Stephen, L. D. Potter, and Y. Wu. Rotation-induced resonance and second-order quadrupolar effects on spin locking of half-integer quadrupolar nuclei. *Journal of Magnetic Resonance*, 116:181–188, 1995.

[127] Y. Zhang, F. Deng, J. Qui, and C. Ye. Spin-locking mechanism of spin $I = 3/2$ quadrupolar nuclei undergo magic angle spinning. *Solid State Nuclear Magnetic Resonance*, 15:209–216, 2000.

[128] S. Ashbrook and S. Wimperis. Spin-locking of half-integer quadrupolar nuclei in nuclear magnetic resonance of solids: Creation and evolution of coherences. *The Journal of Chemical Physics*, 120:2719–2731, 2004.

[129] S. Ashbrook and S. Wimperis. Spin-locking of half-integer quadrupolar nuclei in nuclear magnetic resonance of solids: Second-order quadrupolar and resonance offset effects. *The Journal of Chemical Physics*, 131:194509, 2009.

[130] S. Odedra. NMR spin-locking of half-integer quadrupolar nuclei: The far off-resonance case. Honours thesis, University of Glasgow, 2010.

[131] T. L. Spencer, G. R. Goward, and A. D. Bain. Complete description of the interactions of a quadrupolar nucleus with a radiofrequency field. Implications for data fitting. *Solid State Nuclear Magnetic Resonance*, 53:20–26, 2013.

[132] A. P. M. Kentgens. A practical guide to solid-state NMR of half-integer quadrupolar nuclei with some applications to disordered systems. *Geoderma*, 80:271–306, 1997.

[133] E. Kundla, A. Samoson, and E. Lippmaa. High-resolution NMR of quadrupolar nuclei in rotating solids. *Chemical Physics Letters*, 83:229–232, 1981.

[134] P. J. Barrie. Distorted powder lineshapes in ^{27}Al CP / MAS NMR spectroscopy of solids. *Chemical Physics Letters*, 208:486–490, 1993.

[135] D. N. Shykind, J. Baum, S.-B. Liu, and A. Pines. Phase-incremented multiple-quantum NMR experiments. *Journal of Magnetic Resonance*, 76:149–154, 1988.

[136] G. Jaccard, S. Wimperis, and G. Bodenhausen. Multiple-quantum NMR spectroscopy of $S = 3/2$ spins in isotropic phase: A new probe for multiexponential relaxation. *Journal of Chemical Physics*, 85:6282–6293, 1986.

[137] A. Lupulescu, S. P. Brown, and H. W. Speiss. Rotor-encoded heteronuclear MQ MAS NMR spectroscopy of half-integer quadrupolar and spin $I = 1/2$ nuclei. *Journal of Magnetic Resonance*, 154:101–129, 2002.

[138] J. Baum, M. Munowitz, A. N. Garroway, and A. Pines. Multiple-quantum dynamics in solid state NMR. *Journal of Chemical Physics*, 83:2015–2025, 1985.

[139] C. Hughes. Spin counting. *Progress in Nuclear Magnetic Resonance Spectroscopy*, 45:301–313, 2004.

[140] W. R. Hamilton. On a new species of imaginary quantities connected with a theory of quaternions. *Proceedings of the Royal Irish Academy*, 2:424–434, 1844.

[141] B. Blümich and H. W. Speiss. Quaternions as a practical tool for the evaluation of composite pulses. *Journal of Magnetic Resonance*, 61:356–362, 1985.